# Complex Magnetized Plasmas


UNIVERSITY OF LIVERPOOL

Department of Electrical Engineering and Electronics

Thesis submitted in accordance with the requirements of the University of Liverpool

*Doctor of Philosophy*

Matthew Alexander Smith

September 2021

# Contents

# List of Figures

# List of Tables

**Abstract**

The presence of dust is commonly observed in industrial, fusion and astrophysical plasmas. This dust may perturb plasmas in several ways which is of particular importance to manufacturing and fusion plasmas. For example, dust deposition on a substrate will interfere with film deposition and sufficient dust mobilised into the core of a fusion plasma may terminate it. An important parameter in studying dusty plasmas is the dust charge, which influences several plasma phenomena. This research is concerned with the dust charge parameter and how charging dynamics change in magnetised plasmas. Simulations have been performed in the literature which predict the charge on a dust grain will deviate from that given by conventional unmagnetised OML theory when the electron Larmor radius ($r_{Le}$) becomes $\approx 10$ times the dust radius ($r_d$). The validity of conventional theory within this limit was investigated experimentally in this thesis. Experiments were performed in a 13.56 MHz capacitively coupled RF plasma with an applied magnetic field of 0 - 50 mT. Dust charge depends on, among other factors, bulk plasma parameters and the electric field in the sheath so a reliable method of measuring these properties in magnetised plasmas was needed. An optical imaging spectroscopy diagnostic, based on the work of a previous post - doctorate using the Corona model, was developed to measure electron density and temperature which are key parameters in calculating dust charge. The OIS diagnostic had to be calibrated with an RF - compensated Langmuir probe before being used in magnetised plasmas, where conventional Langmuir probe theory breaks down.

To determine dust charging dynamics, the levitation height of a 9.47 $\mu$m diameter Melamine Formaldehyde (MF) particle was measured in experiments. When the dust levitates at a constant height, there is a balance of forces, principally those of the electrostatic, ion drag and gravitational forces. The electrostatic force is dependent on the dust charge, so if the other forces are known the charge can be calculated from this force balance. The levitation height was measured using a camera (with a calibration procedure to convert pixels to mm) and compared to the predicted height using the force balance equation and OML theory with a shifted Maxwellian distribution. The ion drag force was calculated using the conventional unmagnetised theory of Khrapak *et. al.* [1]. The electric field in the sheath at the location of the dust levitation was obtained from a sheath potential profile measured by a novel emissive probe method. When a magnetic field up to 30 mT is applied the plasma collimates, the sheath width

decreases and the dust was found to levitate in the presheath region. Good agreement was found between the predicted and measured levitation heights, which provides experimental verification to the theoretical prediction. In addition, as the use of a magnetic field causes the dust to levitate in the presheath, conditions of microgravity or a strong thermophoretic force (which influence the force balance equation) are not required to experimentally ensure the relatively simply OML theory is applicable in dusty plasma studies.

There are therefore two main objectives of this thesis: (i) to investigate experimentally the theoretical prediction that dust charge deviates from orbital motion limited (OML) theory when $r_{Le} < 10r_d$. This will require accurate measurements of parameters in the RF plasma used in this thesis, so (ii) is to describe a comprehensive method of determining the level of passive RF compensation of a Langmuir probe which is often overlooked in the literature. Measurements of plasma potential, floating potential, electron temperature and density obtained from Langmuir probe IV curves (along with the first and second derivatives) are used to determine the level of RF compensation.

In addition, as mentioned, a novel emissive probe method was also developed in this research in order to determine the sheath potential profile. Emissive probes are often used to obtain spatially resolved potential measurements in RF or DC plasmas. When used in the sheath, where density is low, the signal to noise ratio decreases. This novel method, using a signal generator and audio power amplifier, was found to greatly reduce noise and decreased the measurement time relative to the conventional methods commonly used in the literature.

# Chapter 1

# Introduction

## 1.1 Overview of Plasmas

Often referred to as the fourth state of matter, a plasma can be thought of in the most simple terms as an ionised gas [2]. Plasmas are common in the observable universe as the sun and every other star is composed primarily of plasma in the form of ionised hydrogen and helium (among others). Terrestrial plasmas exist both in nature, such as during lightning strikes, and artificial systems in which they are used for a variety of purposes in industry and medicine. Among these are the manufacture of microchips by sputtering (the emission of material by high energy particle impact on a surface) and deposition of thin films. Applications of medical plasmas include the destruction of cancer cells and pathogens without damage to healthy cells [3] using reactive oxygen and nitrogen species at atmospheric pressure. A key potential use of plasmas is for the generation of relatively clean electricity from fusion of atomic nuclei, similar to the process which occurs in stars, and considerable experimental and theoretical effort for this goal is ongoing [4].

In order to be classified as a plasma, a gas must have a sufficiently large number of charges ($\gg 1$) surrounding each charged particle within a volume known as the Debye sphere. The charge density must be large enough that the central charge is screened outside of this Debye sphere. There is consequently the macroscopic absence of electric fields, but at length scales smaller than the Debye length ($\lambda_D$) electrical interactions can become important. In 3D the Debye sphere has a volume given by $(4/3)\pi\lambda_D^3$. There is an implicit assumption that there is a large number of charges outside the Debye sphere, so the Debye length must be smaller than the size of the plasma (the system size). Another way plasmas are distinct from ionised gases

is that plasmas exhibit collective behaviour owing to electrical interactions between charged particles. The motion of charged particles in the bulk generates microscopic electromagnetic fields which affect the motion of other charged particles within the Debye sphere. This motion propagates through the plasma and thus particle motion can influence (and be influenced by) distant particles (i.e. outside the Debye sphere) in forms such as waves. Plasmas, especially low temperature plasmas, also exhibit quasineutrality which is the near equivalence of electron and ion density within the plasma bulk which means the plasma is overall approximately neutral.

Another key concept of plasmas is that of the sheath. Because of the greater mobility of electrons compared to ions, when a plasma is created within a vessel the walls obtain a net negative charge. This generates an electric field between the plasma bulk and the walls which acts to repel electrons and accelerate ions. This sets up a "sheath" region between the wall and the plasma and the wall which is populated only by ions and a small number of high energy electrons that can overcome the potential barrier. Between the sheath and the bulk is a region known as the presheath where quasineutrality approximately holds, but small electric fields are present which accelerate the ions to a minimum velocity to enter the sheath known as the Bohm velocity $v_B = (k_b T_e/m_i)^{1/2}$. This is derived from Poisson's equation (equation 1.1) assuming a Maxwellian distribution of electrons [5].

$$\frac{d^2\phi}{dx^2} = \frac{e}{\varepsilon_0}(n_i - n_e) \tag{1.1}$$

As the wall charges negatively due to the more mobile electrons, the plasma bulk becomes slightly positively charged with respect to the walls. The potential the plasma bulk acquires is called the plasma potential ($V_p$). This is an important parameter in several plasma phenomena which will be described in later chapters. Although most plasmas exhibit the previously described behaviour, they can be divided in several ways based on parameters of those plasmas.

### 1.1.1 Low Temperature Plasmas

A common way of generating a plasma is by applying an electric field to a gas, or mixture of gasses, within a sealed chamber. The electric field is then increased until the dielectric strength of the gas is exceeded. An initial ionisation event occurs in which an electron is generated and is accelerated to the positive electrode. This electron will undergo collisions which will cause

further ionisation events which in turn generate more free electrons. This process is called the Townsend avalanche and occurs when the breakdown criterion $1-\zeta(e^{\alpha d}-1)=0$ is met. Here $\zeta e^{\alpha d}$ is the number of generated electrons per incident electron. The plasma can be generated by either direct or alternating current at radio frequency (RF). Although in DC discharges a conduction current is generated compared to a displacement current in RF discharges, the power is in both cases more efficiently coupled to the electrons than the ions. There is consequently a difference between the energy, or temperature, of these two species. Even in weakly ionised low temperature plasmas, the electrons are mostly responsible for processes such as ionisation, excitation and molecular dissociation producing chemically reactive species. The power from the heating mechanism is most efficiently coupled to the smaller, more mobile electrons.

The temperature of a plasma is an important parameter because it determines electron and ion thermal energy and the energy distribution functions. Electron temperatures in plasmas are usually expressed in electron volts (eV) such that $T_e(eV)=k_bT_e(K)/e$ where $k_b$ is Boltzmann's constant and $e$ is electron charge. This means that 1 eV $\approx$ 11,600 K. Plasmas may be categorised as either low or high temperature. In high temperature plasmas the electrons and ions are in thermal equilibrium with each other and is often the case in fusion plasmas. Low temperature plasmas typically have electron temperature ($T_e$) much greater than ion temperature ($T_i$) where $T_e$ is usually of the order 3 eV while ions and neutrals remain at room temperature (0.025 eV). Whether a plasma is "low" or "high" temperature is determined by the ionisation fraction. If a large number of the plasma particles are neutral (i.e. a low ionisation fraction) the electrons and ions will not be in thermal equilibrium with each other and so be classed as low temperature. Technological plasmas can therefore be broadly defined in terms of temperature. Industrial plasmas are used in manufacturing, for instance by sputtering of a desired substrate to deposit a thin film to create microchips for electronic circuits [6]. Industrial plasmas can be driven by either DC or RF signals, the latter often at 13.56 MHz frequency or its harmonics [7]. Low temperature plasmas may be generated by capacitively coupled discharges (CCP), inductively coupled discharges (ICP), magnetrons and arc discharges. Most low temperature plasmas also have a low degree of ionisation, so the majority of plasma species are not ionised. An example of a capacitively coupled RF discharge schematic is shown in figure 1.1. The chamber walls are typically grounded or held at a given potential while either one electrode is powered and one grounded (asymmetric discharge) or both electrodes are powered (symmetric discharge). The electrons charge up the driven electrode and the blocking capacitor, which has

a low impedance to the driving frequency, prevents the electrode from discharging. This leads to a DC self - bias on the electrode and is an important parameter in determining properties such as the sheath electric field.

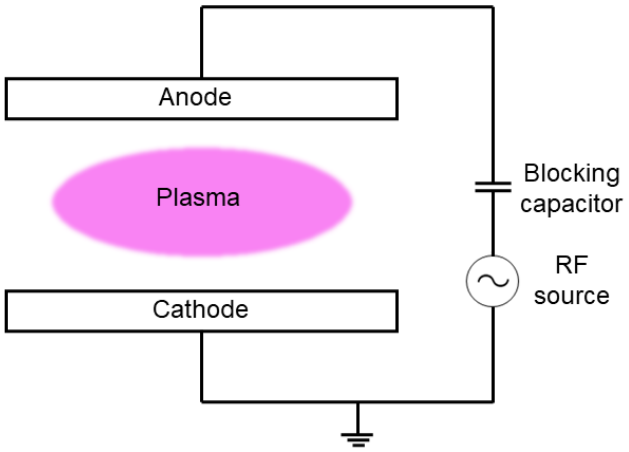


Figure 1.1: Schematic of a typical capacitively coupled RF discharge. A DC discharge would have a positive and negative terminal in place of the RF source and variable resistor in place of the capacitor.

Although RF discharges may appear more complex than DC discharges, there are several reasons to prefer RF plasmas in technological applications. Because a DC current is not required it is possible to process non - conducting surfaces which is desirable in industrial applications. The additional heating mechanism allows for more efficient power coupling to the electrons. Sputtering also has a smaller effect in RF discharges compared to DC discharges as the oscillating sheath potential (given by V = $V_{RF} sin(\omega t)$) decreases the average energy of ions in the sheath.

### 1.1.2 Fusion Plasmas

Fusion plasmas are distinct from low temperature plasmas in that the temperature is usually much higher such that the electrons and ions are in thermal equilibrium with each other. The ionisation fraction is also typically much closer to unity so few, if any, neutral particles are present. Fusion plasmas exist both naturally in stars and in several man - made machines and there are important distinctions between them. In stellar cores, temperatures are sufficiently high so that two hydrogen nuclei (protons) can achieve an energy to overcome the repulsive forces between them to fuse into helium. This releases an amount of energy equal to the change in binding energy between the two nuclei. Although the cross section of hydrogen - hydrogen fusion is small (so the likelihood of fusion occurring is low), the large volume of plasma will

counteract this.

Such conditions are obviously impossible in a reactor on Earth, but fusion can be achieved in a terrestrial plasma if certain conditions are met. These conditions are characterised by several parameters including the density ($n$), temperature, and how effectively the energy is confined within the plasma. The last parameter is defined by the confinement time, $\tau_E = W/P_l$ where $W$ is the thermal energy in the plasma and $P_l$ is the power lost from the plasma. The product $n\tau_E$ is known as the Lawson parameter and gives the requirements for ignition - the condition where fusion releases enough energy to operate without external heating. This occurs at $n\tau_E > \frac{12T}{<\sigma v>E_a}$ where $\sigma$ is the fusion cross section, $v$ is the relative velocity, $E_a$ is the energy of the helium nucleus generated by fusion and $<>$ is an average over the Maxwellian velocity distribution at temperature $T$.

Several methods, reactions and types of machines are used to try and achieve fusion on Earth which can be broadly split into two main procedures for electricity generation. Both of these tend to focus on the fusion of deuterium and tritium (isotopes of hydrogen) nuclei into a helium nucleus and a neutron as this process requires the least heating to achieve a reasonably large cross section (which is a function of particle energy). The first method is Inertial Confinement Fusion (ICF) where a small spherical pellet of high density deuterium - tritium (DT) fuel is compressed by spherically symmetric laser beams or X - rays [8]. The compression increases the density and heats the fuel which (in theory) causes ignition. This method is advantageous in that the high density means that the requirements for confinement time for the Lawson parameter to be satisfied is reasonably low. At present, ICF has not achieved a net energy gain from fusion (the ignition criterion) for numerous reasons, including instabilities in the compressing material which cause the compression to become non-isotropic. Additionally, issues exist in the development of a commercial ICF reactor regarding constructing a powerful enough laser with a high enough pulse rate, combined with the requirement of injecting fuel pellets sufficiently frequently.

The second method, and most important for this thesis, is magnetic confinement fusion (MCF) which aims to achieve steady state plasma operation at high temperature using magnetic fields to confine the electrically charged fuel. The D - T fuel must be confined within the vessel for long enough for a fusion reaction to occur, which imposes stricter requirements on confinement time than in ICF. Magnetic confinement is most often attempted in a tokamak, a doughnut shaped machine in which the electric field is driven by a current through a central

solenoid in order to generate a magnetic field in the plasma. Charged particles are constrained to gyrate around magnetic field lines. If these field lines are densely packed and parallel to each other, the gyrating particles may collide and fuse if they have a sufficiently high temperature.

Other designs such as stellarators, which use complex geometry to better confine the D - T fuel, have also been designed and constructed. The current state of MCF research is focussed on optimising geometry of magnetic fields to achieve a reasonable confinement time and on developing materials capable of withstanding the high temperature plasma within the vessel. This is a major issue, as the plasma requires stable conditions to achieve ignition and as the plasma facing components heat up they will erode material into the plasma which may lead to radiative energy losses or even plasma termination. Safety issues are also a key concern with the newest generation of larger, and higher temperature, MCF reactors such as ITER as the plasma facing components in these reactors will contain beryllium, which is toxic to humans.

## 1.2 Complex Plasmas

Dust is commonly found in industrial, astrophysical and fusion plasmas. Plasmas which contain dust are known as complex plasmas. Complex plasmas are important in astrophysical environments such as planetary rings, nebulae and comet trails which all contain dust [9]. Dust is also important in the formation of planets (and to a lesser extent, stars) as the Jeans criterion ($M_J = [375k_b^3T^3/4\pi m^4G^3n]^{1/2}$) describes the condition which, when met, will lead to the collapse of a gas or dust cloud [10]. In the Jeans criterion $M_J$ is the Jeans mass, $k_b$ is Boltzmann's constant, $T$ is cloud temperature, $G$ is the gravitational constant, $m$ is particle mass and $n$ is particle density. Dust, if present in a cloud, will contribute to the particle mass in the criterion.

In industrial and fusion plasmas dust is a common contaminant which may cause radiative losses through, for example, Bremsstrahlung emission and with enough energy lost may even cause the termination of a plasma [11]. Dust may be generated by the erosion of chamber walls, sputtering of material or as waste material from etching processes. Chemical reactions in Reactive Ion Etching (RIE) plasmas where silicon is used will also generate dust.

In tokamaks dust mobilisation may also present a health concern as plasma facing components in ITER contain beryllium which is toxic. Deposited radioactive tritium may also be re-mobilised or stored in dust. Large amounts of dust can also cause problems on start-up due to radiative cooling. Dust can be released in tokamaks by transient events such as Edge Lo-

calised Modes (ELMs), which release large heat and particle fluxes onto tokamak walls which can erode the plasma facing components.

One of the key parameters for complex plasmas is the dust charge. In typical laboratory plasmas the electrons are more mobile than ions so a larger number of electrons are incident on an isolated dust grain. A micron - scale dust grain will, in the absence of other charging mechanisms (e.g. electron emission from the dust grain), acquire a charge on the order of 10,000 electron charges (e). The dust grain charge will change many plasma parameters by introducing an additional charged species, especially if the charge is fluctuating. These parameters include, for example, the Debye length. The dust grains will, upon becoming charged, modify the background plasma and cause self - consistent coupling between the background plasma and the dust [12].

There are also a number of parameters introduced by having charged dust grains in the plasma. One of these is the Coulomb coupling parameter, $\Gamma$, which is the ratio of the potential energy to thermal energy. In addition, the Lorentz and coulomb drag forces on a moving dust grain depend on its charge [13]. The work in this thesis is therefore motivated by the need for accurate and reliable measurements of dust charge in complex plasmas.

## 1.3 Probe Diagnostics

In order to understand the charging processes of dust a reliable and accurate method of measuring the parameters of the plasma is required. Probe diagnostics are an intrusive method of obtaining local plasma parameters such as electron density ($n_e$), electron temperature ($T_e$), ion density ($n_i$) and plasma potential ($V_p$). The basic methodology of probe diagnostics involves immersing a conducting wire in a plasma and applying a voltage to it. The resulting current, either drawn to the wire or emitted from it, is measured and used to determine plasma parameters. Different kinds of probe diagnostics can be used to obtain different plasma parameters and in various ranges of plasma conditions. Key examples of probes used in this thesis are Langmuir and emissive probes, both of which have been commonly used in low temperature and fusion plasmas [14, 15]. These are relatively simple to construct and the theoretical basis has been worked on for much of the last century [16]. Although the probe setup is relatively simple, multiple analytical and operating techniques exist for the two probe designs [17, 14]. The analysis of such probes is further complicated by the presence of the driving RF signal

(and harmonics which are generated by the non-linear variation of sheath capacitance) [18] and magnetic fields. Accurate measurements of the plasma parameters in these conditions are important because RF and magnetic fields are commonly present in industrial and fusion plasmas.

## 1.4 Objectives of this Thesis

This thesis is divided into two main research topics. The first topic is the investigation of dust charging dynamics in magnetised plasmas. Dust charging in magnetised plasmas has been investigated in simulations [19] but experimental studies are rare in the literature. In order to do this reliable diagnostics that can measure plasma parameters in magnetised are needed, a study of which is provided in this thesis.

The second topic is the removal of RF signals from a Langmuir probe (RF compensation) which is necessary to obtain accurate parameters from IV curves in RF plasmas. The theory behind the effect of RF and several techniques to remove it are commonly discussed in the literature [15, 20, 21], but a comprehensive study of compensation of Langmuir probes is missing in publications. The main research topics in this thesis relating to complex plasmas are described below.

### 1.4.1 RF Compensation of Langmuir Probes

One of the simplest experimental techniques, used for almost a century, to obtain plasma parameters is the Langmuir probe. This is a conducting wire immersed in a plasma and a voltage sweep is applied which draws a current that is recorded at each voltage. Langmuir probes used in RF plasmas are known to produce distorted IV characteristics [22]. Multiple compensation techniques have been developed to remove this distortion such as active compensation [23], where a signal which is phase- and amplitude- matched to the driving frequency is applied to the probe tip to force the probe to follow RF oscillations. The applied signal is tuned until the floating potential reaches a maximum which reduces the voltage drop across the probe sheath and reduces distortion. However, this method requires complex circuitry and the number of harmonics that can be compensated is limited which makes it unsuitable for a comprehensive compensation study. Note that although it is generally unnecessary to compensate multiple harmonics with active compensation, it has been reported that it can become necessary at low

pressures when the given RF harmonic amplitude exceeds $2T_e$ [23]. Passive compensation is the most common alternative and involves installing inductors, with a high impedance to RF and tuned to be self - resonant at the harmonic frequencies, in the probe circuit as close as possible to the tip. This is generally used along with a large surface area ($A > 10A_p$) compensation electrode where $A_p$ is the probe surface area. This is relatively simple both in terms of construction and theory, but the large physical size of the components risks perturbing the plasma. However, this drawback makes passive compensation ideal in the present study as the effect of compensation electrode area on plasma parameters can be investigated experimentally.

### 1.4.2 Dust Charge Study

Several techniques have been used to determine the dust charge in low temperature plasmas, but in the literature there are few experimental studies of dust charging in magnetic field. Knowledge of the dust charging mechanisms in tokamaks is important in understanding the motion, deposition and mobilisation of dust in tokamaks. When dust is present in an electronegative plasma it will acquire a net negative charge from the more mobile electrons which causes a number of forces to act on it. The principle forces are gravity, the ion drag force and the electrical force (only in the sheath) which can cause the dust to levitate in the sheath if these forces balance. Orbital Motion Limited (OML) theory is commonly used to predict the charge of a spherical or cylindrical object immersed in a plasma [16] but it has been predicted in simulations that the charge on a dust grain will deviate from OML theory when $r_{Le} < 10r_d$ where $r_{Le}$ is the electron Larmor radius and $r_d$ is the dust radius [19, 24]. This has not been proven experimentally in the literature so is investigated in this thesis in a magnetised RF plasma, although there have been other dust charging investigations in magnetised plasmas [25, 12]. Dust experiments have been performed in strongly magnetised (up to 4 T) plasmas by Thomas *et. al.* [26]. These experiments observed a number of phenomena in complex plasmas, including magnetically - modified dust acoustic waves and ordered structures. The theoretical prediction of Lange will be verified experimentally by comparing the measured dust levitation heights using a camera with the predicted height using the force balance equation and OML theory (which is modified to take into account ion flow). This requires accurate knowledge of the sheath electric field and plasma parameters in a magnetic field, so a novel emissive probe method and an optical imaging spectroscopy diagnostic were developed to obtain these and described in this work.

Within this thesis, chapter 2 contains a review of the key aspects of theory and the state of the literature. This includes the background of plasma generation, the operation of fusion plasmas and how the presence of dust influences a plasma. Chapter 3 describes the experimental setup and the probe diagnostics used to acquire data in RF plasmas. Experimental results of RF compensated Langmuir probes are described chapter 4. An optical method for measuring plasma parameters in magnetised plasmas where Langmuir probes are unreliable is described in chapter 5 along with experimental results taken with it. Chapter 6 describes a novel setup for emissive probes and experimental data of sheath scans obtained using it, including in magnetic fields. Experimental results of dust in magnetised and unmagnetised plasma sheaths, including the theory and data analysis, are described in chapter 7. Finally, chapter 8 contains conclusions and possibilities of further study.

# Chapter 2

# Literature Review

This chapter will describe the current state of complex plasma research including magnetised plasmas in tokamaks. This review will particularly focus on complex industrial and fusion plasmas although some physics is applicable to astrophysical plasmas. Basic plasma theory and concepts will also be described including the dust charging mechanisms and how this relates to relevant forces on a dust grain. This chapter is divided into two main sections. Section 2.1 describes industrial RF plasma theory. The current state of dust charging theory in low temperature and fusion plasmas is described in section 2.4. The dynamics of dust in fusion plasmas is then described in section 2.5.

## 2.1 Capacitively Coupled Plasmas

Experiments in this thesis are performed in a 13.56 MHz RF capacitively coupled plasma (CCP). A review of the physics of these plasmas is provided in [27, 28, 29]. In CCPs, a schematic of which is shown in figure 1.1, the power is coupled to the plasma by several methods. The principal method is Ohmic heating and, depending on conditions, stochastic heating may contribute significantly as well. Stochastic heating occurs by the expansion and contraction of the sheath in RF plasmas. As the sheath expands, the electrons are accelerated into the plasma by the electric field. This acceleration couples energy to the electrons which can cause further ionisation events and sustain the plasma. The effect of stochastic heating can be determined using a simplified uniform density reflecting wall model. However, this requires the RF current in the plasma to be known and this is likely to be complicated by a significant displacement current which is generated by capacitive coupling to the electrode and is not easily measured [27].

### 2.1.1 Low Temperature Plasma Physics Background

Several parameters are important in determining plasma properties. The degree of ionisation in a plasma is important to the properties which a plasma has and is a ratio of the number of ions to the number of neutrals. In fusion plasmas, almost all the particles are ionised whereas in low temperature capacitively coupled plasmas the degree of ionisation is much lower, at around $10^{-5}$. The degree of ionisation when in thermal equilibrium is given by the Saha equation (equation 2.1) [8] but note that this condition does not hold for all plasma conditions. It is generally a good approximation for low temperature plasmas.

$$\frac{n_i n_e}{n_n} = \frac{(2\pi m_e k_b T_n)^{3/2}}{h^3} \frac{2g_i}{g_n} exp(-\varepsilon_i / k_b T_e) \tag{2.1}$$

Where $n_{n,i,e}$ is the number density of neutrals, ions and electrons respectively, $m_e$ is the electron mass, $k_b$ is the Boltzmann constant, $T_{n,e}$ is the neutral gas or electron temperature, $h$ is the Planck constant, $g$ is the degeneracy and $\varepsilon_i$ is the ionisation energy.

The temperature of plasma species is also a critical parameter in understanding both plasmas in general and dust charging dynamics. In low temperature plasmas, where the coupling of energy to ions is generally weak, the ions remain at approximately the gas temperature (taken as room temperature $T_i \approx T_n \approx 0.025$ eV). This allows the ion temperature to be determined relatively simply in low temperature plasmas (along with the neutral temperature) using the ideal gas law [5]:

$$pV = Nk_b T_{n,i} \tag{2.2}$$

Where $p$ is pressure, $V$ is volume and $N$ is the total number of particles. If the degree of ionisation is low, then $N \approx n_n$ / $V$. The electron temperature $T_e$ is usually much higher ($\approx 3$ eV). Determination of $T_e$ is often complicated and requires one or more diagnostic methods (see section 2.2).

A key aspect of plasmas is the ability to shield the electric field from each individual charged particle by other local charged particles. This is known as Debye shielding, and occurs over a characteristic length called the Debye length given by equation 2.3. Over this distance from a charged particle in 3D space (i.e. a Debye sphere) an electric field exists and quasineutrality does not hold.

$$\lambda_D = \sqrt{\frac{\varepsilon_0 k_b T_e}{n_e e^2}} \tag{2.3}$$

Where $\varepsilon_0$ is the permittivity of free space. On length scales longer than $\lambda_D$, the plasma is electrically neutral [30]. However, if temperature is finite, the shielding is not perfect and particles near the edge of the Debye sphere where the electric field is weakest can escape. If one species of a stationary (cold) plasma is displaced by some distance from their initial position an electric field will be set up between the species. If the perturbed species are then released the particles will accelerate towards each other to attempt to restore the original neutral charge. However, the particles will overshoot their initial position due to their inertia and thus set up a reversed electric field. The motion causes an oscillation of the two species, which are described by a characteristic frequency. This electron plasma frequency is given by [31, 9]:

$$\omega_{pe} = \sqrt{\frac{n_e e^2}{\varepsilon_0 m_e}} \tag{2.4}$$

And similarly the ion plasma frequency is given by:

$$\omega_{ie} = \sqrt{\frac{n_e e^2}{\varepsilon_0 m_i}} \tag{2.5}$$

Ions enter the sheath with a speed known as the Bohm velocity, $v_B$. The energy gained to accelerate ions to this velocity is gained from a small electric field in the presheath [32].

## 2.2 Plasma Diagnostic Techniques Overview

A number of diagnostic techniques have been developed to experimentally measure the important parameters in a plasma. These vary substantially in theoretical and experimental complexity and do not all measure the same parameters in the same conditions. However, they can in general be divided into invasive and non - invasive techniques. Invasive techniques require an instrument to be immersed in a plasma which will result in collection (or repulsion) of plasma particles in the local area which can modify the measured local parameters. This effect must be minimised in order to take accurate measurements. This is done by limiting the physical size of the instrument in the plasma and, where applicable, ensuring a relatively small current is drawn from the plasma.

Non - invasive techniques often, but not always, use window ports and optical methods to

measure photon emission to determine plasma parameters. Mass spectroscopy is an example of a non - invasive, non - optical technique which can be used to give a direct measurement of the ion energy distribution function and the chemical species present in a plasma. Optical techniques are often based on the scattering of photons by electrons. Laser light is shone through a diagnostic port in a plasma chamber and the photons are scattered by either the free electrons in the plasma (Thomson scattering), the bound electrons in atoms (Rayleigh scattering), or the bound electrons in molecules (Raman scattering). In Thomson scattering the electric field of a photon from the laser accelerates a free plasma electron which in turn releases a scattered photon. These scattered photons can be released in a different direction to the initial laser light which can be detected with, for example, an iCCD. The number of detected photons is proportional to the density of the free electrons. This allows Thomson scattering to have a relatively simple method to interpret data in several plasma conditions including magnetised plasmas. However, this means very sensitive, complex and expensive equipment is needed to use the Thomson scattering method as the Thomson scattering signal is generally much weaker than the Rayleigh scattering signal [33]. Consequently, probe and optical emission diagnostics (which will be described in Chapter 5) will be used in this thesis due to the ease of construction and installation.

## 2.3 Langmuir Probe Diagnostics

Langmuir probes are the oldest plasma diagnostic [34] as well as one of the most simple to construct. In simple terms, a Langmuir probe is a wire immersed in a plasma and a slowly varying bias is applied. The current is recorded at each bias and the current is plotted against bias voltage to create an IV curve (or IV characteristic). However, interpretation of IV curves can be complex depending on plasma conditions and the presence of a magnetic field will cause electrons to gyrate around field lines. At a sufficiently strong field (when $r_{Le} \approx R_p$) the effective collection area of the probe is modified and conventional theory will no longer apply. Consequently, in this thesis the Langmuir probe will be used to calibrate an optical imaging diagnostic in unmagnetised plasmas which will in turn be used in magnetised plasmas.

### 2.3.1 Acquisition of Langmuir Probe IV Characteristics

Analysis of IV characteristics can yield information on $V_p$, $n_e$, $T_e$, $n_i$ and the electron energy distribution function (EEDF). An example IV curve is shown in figure 2.1 which shows the

important regions of the characteristic. As electrons are negatively charged, they are repelled by negative voltages and attracted at positive voltages. At strongly negative biases, ions are attracted to the probe which is read as negative current by convention. This is indicated on the figure as the ion saturation region. As the bias increases, fewer electrons and more ions are collected by the probe until the ion and electron currents are equal so no net current is drawn which occurs at the floating potential ($V_f$). For more positive biases, the ions are repelled and electrons are collected based on their energy as at smaller biases only the highest energy electrons can be collected. This is described by equation 2.6. This part of the IV curve can be referred to as the transition region although it is also known as the electron retardation region. When the probe bias is increased further still, electron collection is increased until the probe bias matches the plasma potential, at which point a kink or "knee" is observed. Above this potential, in theory, every electron in the sheath is collected so the electron current should saturate and flatten. However, because increasing bias further increases the size of the sheath, the effective collection area of the probe increases so more electrons are collected and the drawn current does not saturate. This region is nevertheless usually known as the electron saturation region. The transition region and electron saturation regions together are known as the electron current region.

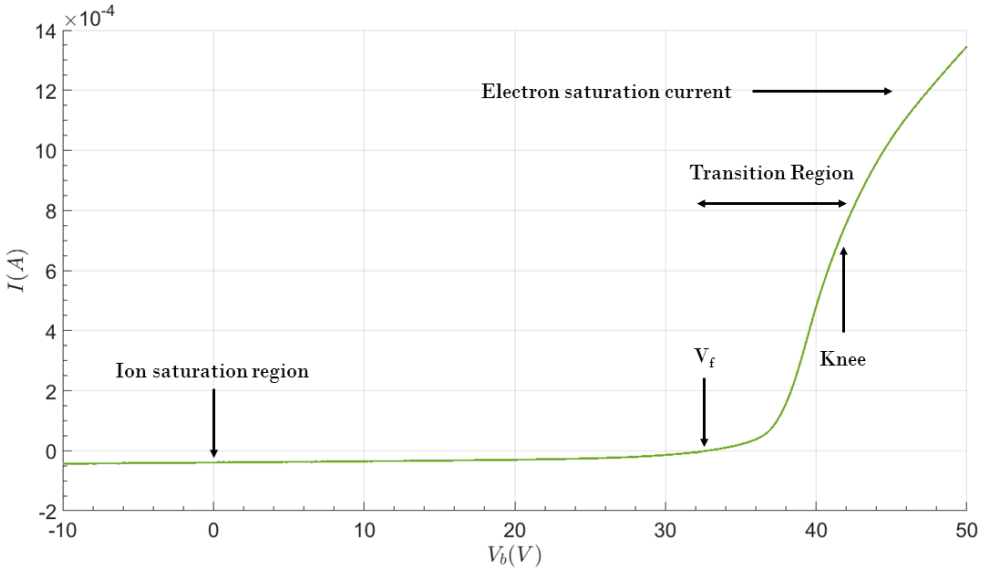


Figure 2.1: *Example IV characteristic taken using a 50 μm diameter Langmuir probe in an unmagnetised RF plasma*

The total drawn current ($I$) is the combination of electron ($I_e$) and ion ($I_i$) currents. The electron current is given by:

$$I_e = I_{es} exp\left(\frac{e(V_b - V_p)}{k_b T_e}\right) \tag{2.6}$$

Where the electron saturation current, $I_{es}$ is:

$$I_{es} = \frac{1}{4} e A_p n_e v_{th,e} = \frac{1}{4} e A_p n_e \sqrt{\frac{8 k_b T_e}{\pi m_e}} \tag{2.7}$$

Where $A_p$ is probe area, $k_b$ is Boltzmann's constant, $v_{th}$ is electron thermal velocity and $e$ and $m_e$ are the electron charge and mass respectively. Equation 2.6 gives the exponential dependence in the transition region shown in figure 2.1. The simplest parameter to obtain from an IV curve is the plasma potential which can be determined from the peak of the first derivative of the characteristic. An example is shown in figure 2.2 with the plasma potential located at approximately 40 V. The peak of the first derivative, or equivalently the zero crossing point of the second derivative, is located at the knee in the IV characteristic [35]. This marks the boundary between the transition and electron saturation regions, so the plasma potential is the point in the IV curve where the current deviates from the exponential in the transition region [36]. The floating potential and the point of zero net current in the IV curve are related by:

$$V_f = V_p - \frac{k_b T_e}{2e} ln\left(\frac{2M}{\pi m_e}\right) \tag{2.8}$$

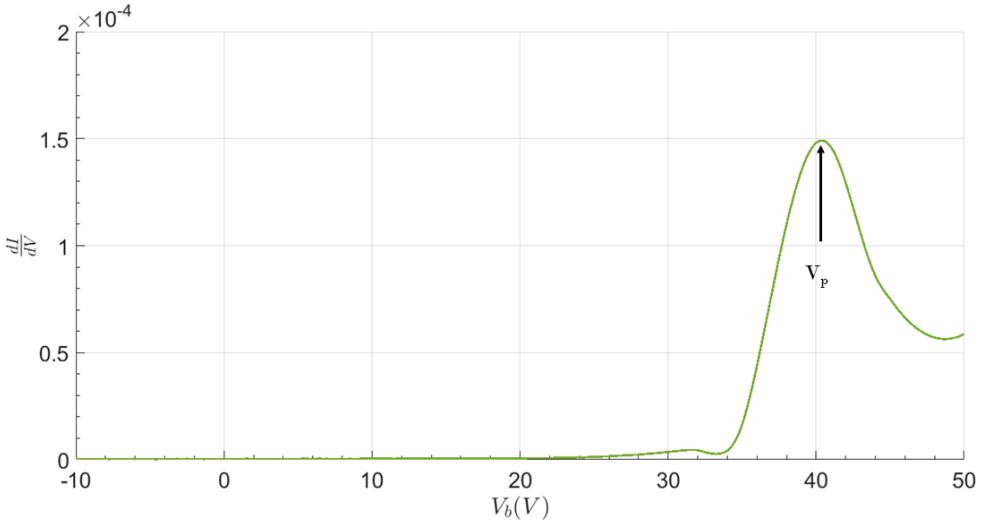


Figure 2.2: *Example IV characteristic first derivative taken by a 50 μm Langmuir probe.*

The electron temperature can be determined from the transition region just below the plasma potential. By taking the natural logarithm of equation 2.6, it is apparent that the gradient of a plot of $\ln(I_e)$ against $V$ is proportional to the inverse of electron temperature. This is true

as long as ion contribution to the current is subtracted and the distribution is Maxwellian [36]. This also assumes no magnetic field and cold ions ($T_e \gg T_i$) and a large ($A_p > \lambda_D$) planar probe. The natural logarithm of equation 2.6 is given by [2]:

$$ln(I_e) = ln(I_{es}) + \frac{e(V_b - V_p)}{k_b T_e} \tag{2.9}$$

$$k_b T_e = \frac{e(V_b - V_p)}{ln(I_e) - ln(I_{es})} \tag{2.10}$$

So a plot of $ln(I_e)$ against $(V_b - V_p)$ will give 1 / $T_e$. For experimental results taken in this chapter, the electron temperature will be plotted against voltage relative to $V_p$ (shown in equation 2.10). In general equation 2.9 may not be linear (or equivalently, equation 2.10 is not constant) over the whole range over the electron retardation region. A small region of constant $T_e$, over about 5 - 10 V, may be present below the plasma potential in which case the temperature will be obtained by taking an average over the near constant region.

The simplest way to measure the density is to measure the current at the knee and use equation 2.11 which is obtained, if $T_e$ is known, by removing the ion current from the IV characteristic and rearranging equation 2.7. It is important to only measure the density at the knee because below the knee the current collected is less than $I_{es}$ and above it, in practice, the electron current does not saturate (as shown in figure 2.1). This will be referred to as the "knee method" and provides a simple but potentially unreliable measure of electron and ion density particularly in RF plasmas as the knee may be rounded and flattened [37].

$$n_e = \frac{4 I_{es} \sqrt{\pi m_e}}{e A_p \sqrt{8 k_b T_e}} \tag{2.11}$$

Alternatively, density can be measured from the ion or electron saturation regions with a suitable probe theory (e.g. Orbital Motion Limited (OML) [17], Allen Boyd and Reynolds (ABR) [38] etc.). These theories take into account different probe geometries and plasma conditions and are described in section 2.3.2 with a focus being on the commonly used OML theory. Regardless of the method used the electron and ion densities should be approximately equal for most low temperature electropositive plasmas because of quasineutrality.

The electron energy distribution function (EEDF) can give several parameters including the relative abundance of electrons at each energy in the plasma, from which the effective

temperature can be calculated. The electron density can also be obtained from the EEDF by integrating over all energies. The EEDF can be determined from the second derivative of an IV characteristic [39] and, if the plasma is Maxwellian, is defined by:

$$f_E(E) = \frac{-m_e^2}{2A_p \pi e^3} \frac{d^2 I}{dV_b^2} \tag{2.12}$$

The shape of the EEDF measured by a Langmuir probe is influenced by particle collisions and RF fields in the plasma. For example, in low pressure discharges the shape of the EEDF becomes non - Maxwellian. In this case, a commonly used distribution function to calculate the EEDF of an isotropic plasma [40, 41] is the Druyvesteyn distribution function given by:

$$f_{ED}(E) = -\frac{1}{e\pi r^2} \left( \frac{-mV_b}{2e} \right)^{1/2} \frac{d^2 I}{dV_b^2} \tag{2.13}$$

The Druyvesteyn method is valid for planar, cylindrical and spherical probe geometries but assumes the velocity distribution is spherically symmetrical [17]. In the simple case of a planar probe ($R_p \gg \lambda_D$) in an unmagnetised DC plasma with a Maxwellian temperature distribution and cold ions (typically in low temperature plasmas $T_i = 0.025eV \ll T_e$) the ion current drawn to an attracting probe is given by:

$$-I_i = -env_B A_p \tag{2.14}$$

Where $v_B = \sqrt{k_b T_e / m_i}$ is the Bohm velocity. The total drawn current, $I$ is the sum of the electron and ion currents, $I_e + I_i$ where the ion current is negative by convention. By varying the probe bias (specifically including the electron retardation region) and removing the ion current from the total current:

$$I - I_i = I_e = \frac{1}{4} env_{eth} A_p exp \left( \frac{V_b - V_p}{T_e} \right) \tag{2.15}$$

The theory given above provides a relatively simple method of obtaining plasma parameters from an IV curve in ideal conditions. However, most laboratory plasmas are not well described by such theories (for example, the measured floating potential, electron saturation current and electron temperature are all affected by RF). A more detailed theory is needed in most real cases.

### 2.3.2 Orbital Motion Limited (OML) Theory

In addition to the simple theory described above, a large number of detailed advanced analysis techniques exist in the literature [17, 38, 42]. These are applicable for different probe sizes and geometries (i.e. spherical & cylindrical), plasma parameters and for different plasma states (e.g. collisionless). Most of these theories are for unmagnetised DC plasmas. A description of the different probe theories and their applicability is given by Bryant [43]. The theories are limited by the two length scale ratios: $r_p$ / $\lambda_D$ and $\lambda_{in,en}$ / $\lambda_D$ Where $r_p$ is the radius of the collector and $\lambda_{in,en}$ is the ion - (electron -) neutral collisional mean free path.

This work is mainly concerned with the commonly used OML theory.

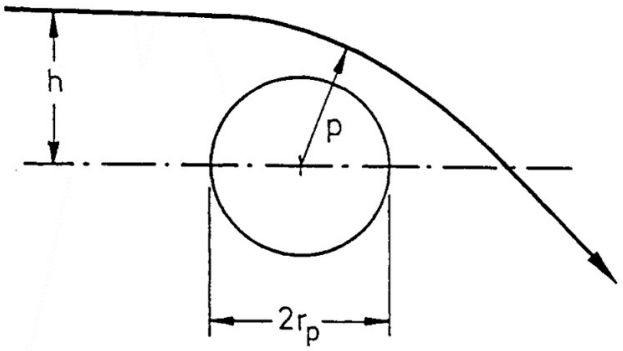


Figure 2.3: Schematic showing closest approach of an ion to an object from Allen [17].

In the following it is assumed that the ions are unmagnetised, do not undergo collisions, are non - thermal and have a Maxwellian distribution of energy. The probe is assumed to be cylindrical with probe radius such that $\lambda_D > R_p$ and of infinite length so that end effects are ignored. For simplicity it is assumed that the potential in the plasma is zero ($V_p = 0$) and the probe potential, $V$, is at a negative value so that ions are attracted and electrons are repelled from the probe. There is also the assumption that the ions are Maxwellian, are initially far from the probe and have initial velocity components $v_\theta$ (angular component) $v_r$ (radial component). It should be noted that a plasma is not required for OML theory.

The corresponding velocities at the probe surface are $v'_r$ and $v'_\theta$, after passing through the sheath of radius $s$. There is also the implicit assumption that the radial potential profile is such that there is no radius within which the electric field is so strong that ions cannot escape (the absorption radius). It is assumed that there is no radial motion so the particle always grazes the surface of the probe. Orbital motion limited theory is based on the conservation of energy and angular momentum:

$$sv_\theta = r_p v'_\theta \tag{2.16}$$

The conservation of energy is given by:

$$\frac{1}{2}m(v_r^2 + v_\theta^2) + eV = \frac{1}{2}m(v_r'^2 + v_\theta'^2) \tag{2.17}$$

Solving these equations for $v'_r$ gives:

$$v_r'^2 = v_r^2 + v_\theta^2 + \frac{2eV}{m} - \frac{s^2}{r_p^2}v_\theta^2 \tag{2.18}$$

which can be set to zero given the assumption that every ion is collected, giving:

$$v_{\theta 0} = \left(\frac{v_r^2 + 2eV/m}{s^2/r_p^2 - 1}\right)^{1/2} \tag{2.19}$$

The current can be calculated by integrating the flux $nv_r$ over the distribution function, which is assumed to be Maxwellian, but the integration requires complicated manipulation of error functions so some simplifications can be made:

$$\frac{a}{s} \ll 1 \tag{2.20}$$

$$v_r^2 \ll \frac{eV}{m} \tag{2.21}$$

$$v_{\theta 0}^2 \ll \frac{eT_i}{m_i} \tag{2.22}$$

Assuming a Maxwellian distribution:

$$f(v_r, v_\theta) = \frac{m_{i,e}}{2\pi k_b T_{i,e}} exp\left(\frac{-m_{i,e}(v_r^2 + v_\theta^2)}{2k_b T_{i,e}}\right) \tag{2.23}$$

Where $m_i$ is the ion mass and $m_e$ is the electron mass. The resulting integral of the radial flux over the distribution function can be evaluated using the prior assumptions to obtain:

$$I = -2\pi sneL \int_{-\inf}^{0} v_r\, dv_r \int_{-v_{\theta 0}^2}^{v_{\theta 0}^2} f(v_r, v_\theta)\, dv_\theta \tag{2.24}$$

By evaluating this integral using the prior assumption the electron or ion saturation current

is obtained (denoted by subscripts $e$ and $i$ respectively):

$$I = 2enr_p l \left(\frac{2eV}{m_{i,e}}\right)^{1/2} \tag{2.25}$$

And rearranged to:

$$n = \frac{I}{(2er_p l)} \left(\frac{2eV}{m_{i,e}}\right)^{-1/2} \tag{2.26}$$

From equation 2.25, it can be seen that a plot of $I^2$ against probe bias should be a straight line where the gradient is related to the density if the assumptions of OML are met. This is independent of the temperature of the relevant species (which can be electrons or ions). Note that $V$ here was taken with $V_p = 0$ but is actually the difference between the plasma potential and probe bias. In order to use this to measure $n_{i,e}$ from IV curves the current contribution from only one species is needed. Ion contribution can be separated by extrapolating the ion saturation region to the floating potential and subtracting this from the IV curve. An alternative derivation of OML is given by Conde [44] and is derived from particle motion, but this requires more complex mathematical manipulation of error functions [45].

## 2.4 Complex Plasmas

Many plasmas both in nature and industry are composed not only of ions, electrons and neutral species, but also of dust grains. These typically have a characteristic size which are much larger (on the order of nm - $\mu$m) than the other plasma particles. A dusty plasma can be defined as a plasma in which the dust radius ($r_d$) is much less than the dust inter - grain distance ($a$), and $a$ is greater than $\lambda_D$ [9]. Dusty plasmas also require the dust density to be sufficiently high. The presence of dust can have a major effect on the operation of industrial and fusion plasmas [46] which may include early plasma termination [11] in fusion plasmas or contamination of a surface in material fabrication.

Dust may become present either by thermal or chemical processes or sputtering (assuming it is not deliberately injected). In fusion plasmas, desorption, arcing and sublimation processes can become important as well due to the high temperature plasma and wall coatings [9, 47]. Dust grains of nm length scales are commonly grown in silane based discharges which are often used in industrial processing [48]. Dust is also commonly present naturally in astrophysical

plasmas. Despite the great differences in length and time scales, materials, and interactions with the plasma the dust charging process remains an important factor in investigating complex plasmas.

The effect of dust on plasmas has been studied for much of the last 50 years due to the common presence of dust in astrophysical, industrial and fusion plasmas [49]. Laboratory studies of astrophysical plasmas can be difficult due to the much restricted length scales of laboratory plasmas compared to, for example, nebulae. Additionally, the presence of gravitational forces on Earth can make replicating astrophysical plasmas difficult.

Dust charge ($q_d$) is an important parameter in understanding dust motion within a plasma [50]. In low temperature industrial plasmas, dust typically charges to around 20,000e. The electrons in a plasma are much more mobile than ions, so dust grains typically acquire a negative charge in an electropositive plasma [51]. One possible way to determine the dust charge is to use the force balance equation:

$$q_d E = m_d g + m_d \mu_{di}[u_i(E) - v_d] + F_{th} + F_n \tag{2.27}$$

Where $F_{th}$ is the thermophoretic force, $\mu_{di}$ is the ion mobility, $u_i(E)$ is the ion velocity and $F_n$ is the neutral drag. Equation 2.27 can be used to determine $q_d$ if the other forces are known. The thermophoretic force occurs when there is a temperature gradient ($\Delta T$) in a discharge. The particles in the higher temperature region have larger thermal velocities than those in the lower temperature region which will result in a net transfer of momentum to particles in the lower temperature region [52]. The thermophoretic force is given by [53]:

$$F_{th} = -\frac{8\sqrt{2\pi} r_d^2}{15 v_{th,n}} \left(1 + \frac{5\pi}{32}(1-\alpha)\right) \kappa_T \Delta T \tag{2.28}$$

Where $\kappa$ is the thermal conductivity of the neutral particles and $v_{th,n}$ is the thermal velocity of the neutrals. The parameter $\alpha$ is the accommodation coefficient which is approximately unity when the temperature is less than 500 K. The neutral drag force $F_n$ occurs as a result of momentum transfer from the neutral gas particles to the dust grain through collisions [54].

$$F_n = \delta \frac{4\pi}{3} r_d^2 n_n m_n v_{th} v_n \tag{2.29}$$

Where $n_n$ is the number density of the neutral gas particles, $m_n$ is the gas particle mass, $v_{th}$

is the gas particle's average thermal speed and $v_n$ is the velocity of the dust particle relative to the neutral gas particle. The coefficient $\delta$ (on the order of unity) accounts for the mechanism of the collision between the neutral gas and the dust. Another important parameter in complex plasmas is the Coulomb coupling parameter ($\Gamma_c$) [55]. The Coulomb coupling parameter is the ratio of the dust potential energy to the thermal energy [56]. The thermal energy is the kinetic energy obtained from the thermal velocity, $\phi_{th} = 0.5 m_d v_{th,d}$. The potential energy is simply the Coulomb potential between two charges (the dust particles) separated by a distance, $d$ which can be given by:

$$W_E = \frac{1}{4\pi\varepsilon_0}\frac{Q_1 Q_2}{r^2} \tag{2.30}$$

The Coulomb coupling parameter determines the level of interaction between nearby dust particles and thus a dusty plasma can be in different states depending on the coupling parameter [57]. Some terrestrial dusty plasma experiments use the thermophoretic force to adjust the dust levitation height into the plasma bulk to allow OML to be used [58]. However, an alternative method has been developed on the international space station which takes advantage of the free-falling conditions to increase the levitation height of the dust [59, 60]. This counteracts $m_d g$ in equation 7.8 which causes the dust to levitate higher up. If this is high enough (in the presheath), and if the pressure is sufficiently low that collisions are not important, then conventional OML theory can be used.

### 2.4.1 Dust Charging Theory

Several aspects of dust interaction with plasmas have been studied in the literature, including charging [61, 62, 50], dust kinetics (e.g dust acoustic waves) [63] and the formation of voids (large areas of relatively little dust) in microgravity plasmas on the international space station [60]. Because most of the dusty plasma phenomena are dependent on charge, the dust charge (and charging mechanisms) are critical in understanding dusty plasmas. The main charging processes of dust grains are due to the absorption of photons, electrons and ions [61, 62]. Due to the higher mobility of electrons the majority of charged particles incident on an initially uncharged dust grain are negative. This will charge the grain negatively relative to the plasma. This negative potential in turn attracts positive ions and acts to repel electrons, which sets up a floating condition when ion and electron currents (collision rates) become approximately equal. This typically results in a charge (in low temperature plasmas) on the order of $10^2$

- $10^4$ electron charges [9] depending mainly on particle size and electron temperature. In other charging processes, high energy incident ions can collide with (and transfer energy to) electrons on the dust grain which can then be emitted in a process known as secondary electron emission. Similarly, if an electron on the grain absorbs a photon, the electron can be emitted into the plasma. This results in the grain becoming more positively charged. These processes tend to occur in fusion and some astrophysical plasmas.

If a dust grain is isolated (inter - grain distance, a $\gg \lambda_D$) and levitating in the plasma bulk (either by microgravity or using thermophoresis) then OML is likely to be a good approximation. If the dust density becomes too large, then shielding will occur between the particles and OML will assumptions will break down. If the dust is levitating in the sheath, where the electric field will create ion flow, then a modification to OML theory that takes this into account is needed.

Sickafoose *et. al.* [50] have investigated levitation and charging of dust grains in order to determine the validity of OML theory. An unmagnetised DC 0.02 Pa argon plasma, which was assumed to be Maxwellian, was used in their experiments. Several different types of dust were used including glass microballons (diameter up to 38 $\mu$m), lunar regolith simulant (diameters up to 25 $\mu$m) and polystyrene spheres (diameter 10 $\mu$m). Emissive probes were used to measure the potential profile in the sheath in order to ascertain dust charge. The charge was calculated using $Q_d = CV_d$ where $C = 4\pi\varepsilon_0 r_d(V_d - V_s)$. The authors found that the grain floating potentials in the plasma sheath agreed with the OML theory for all dust types and sizes. However, the ion drag force was not taken into account in the model but was calculated to be around $10^4$ times smaller than gravity. This is a reasonable assumption in the bulk where the electric field is weak but will likely fail in the sheath. The authors of that paper also did not measure the sheath width directly, but calculated it using the Bohm model. There is therefore some doubt over the applicability of the model. The calculated sheath width was compared to the width determined by a sheath potential profile measured by an emissive probe (see chapter 6), but the edge of the sheath was not clearly defined.

## 2.5 Complex Plasmas in Fusion

Nuclear fusion is the process by which two smaller nuclei, having overcome the Coulomb potential barrier separating them, merge to form a single, heavier nucleus. This occurs when

the nuclei are close enough for the strong nuclear force to overcome the Coulomb potential. The difference in binding energy between the product nucleus and the component nuclei is released as thermal energy. This process takes place in stars (most commonly protons fusing into a helium nucleus) and several methods exist which attempt to replicate the process on Earth as a means of generating electricity. Several possible reactions and methods exist to achieve this, of which the easiest energetically and the most well developed theoretically is deuterium - tritium fusion.

Given the high temperatures in fusion plasmas it is critical to make a reactor out of materials which are resilient to such conditions. This is particularly important as several kinds of instabilities can occur in tokamaks such as edge localised modes (ELMs) in which large heat and particle fluxes are incident on the reactor walls.

One of several issues preventing viable commercial fusion energy is that of dust. As MCF plasmas use magnetic fields for confinement then dust mobilised into an MCF reactor will create a complex plasma system. In addition to the issues discussed previously, dust in tokamaks can cause safety concerns as the walls of large tokamaks can contain beryllium which is toxic and tritium fuel in D - T fusion is radioactive. Dust may be generated in such plasmas due to arcing, sputtering, thermal sublimation of wall material and desorption [9]. The understanding of charging dynamics, described in section 2.4, is important in determining the motion of the dust in tokamaks which in turn determines the effect dust will have on the plasma.

It has been shown by several authors, such as De Temmerman *et. al.* [11] that the presence of dust was found to lead to premature termination of plasmas in the Tore Supra tokamak [64]. In addition, the dust material was found to have an effect on dust motion in that tungsten dust was found to move slower but with an increased component in the direction of the plasma core than carbon dust. Those results were used to provide experimental verification of the Dust in Tokamaks (DTOKS) code which is commonly used to simulate dust dynamics [24]. This includes simulations which gave rise to the prediction that dust charge deviates from OML when $r_{Le} < 10 r_d$.

# Chapter 3

# Experimental Apparatus

Experiments were done in a capacitively coupled RF plasma chamber shown schematically in figure 3.1. The chamber is placed inside the bore of an electromagnet arranged into a Helmholtz coil. The chamber and electromagnet stacks are mounted on an aluminium frame as shown in figure 3.2. The electromagnets create a linear vertical field in the chamber. A local DC generator powers the electromagnets. Chilled water is pumped through the stacks to provide cooling. All of the experimental apparatus shown in figures 3.1 and 3.2 was constructed and set up prior to the beginning of the present research.

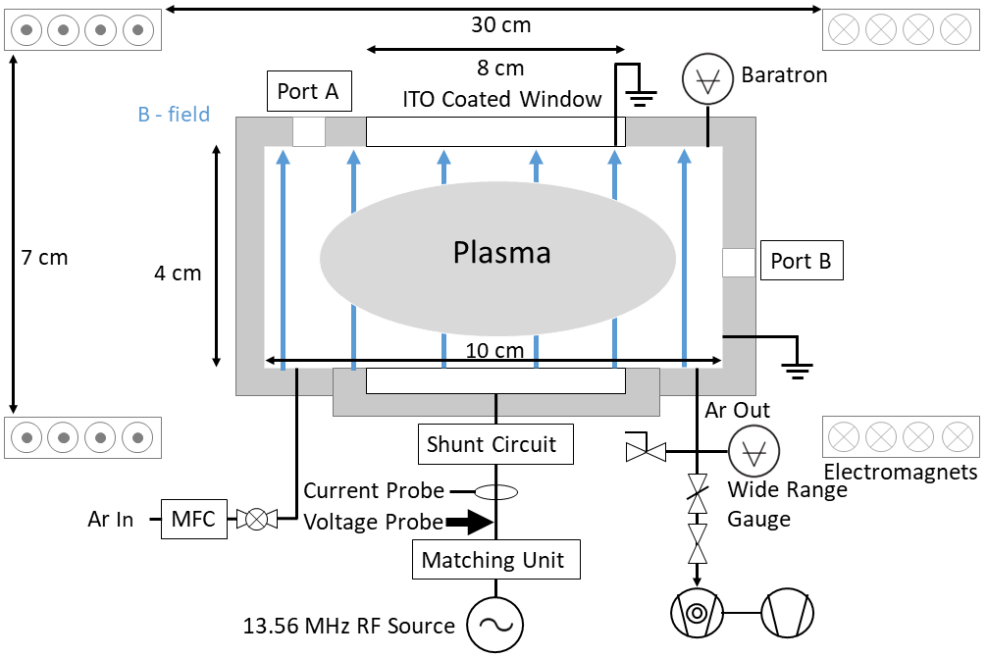


Figure 3.1: Basic schematic of the plasma chamber. Langmuir probes, sensors or other diagnostics may be mounted in the ports. (WRG ≡ wide range gauge)

Several diagnostics including Langmuir and emissive probes, pressure gauges, a dust injection system and windows for optical diagnostics can be installed on the top and side of the

chamber. Electrical power and argon gas are supplied from beneath the chamber to generate the plasma. Gas is pumped out of the chamber through a butterfly and gate valve leading to a turbo pump backed by a rotary vane pump. A separate optical table positioned to one side of the frame contains a laser system to illuminate dust in the chamber and diagnostics for Optical Imaging Spectroscopy (OIS).

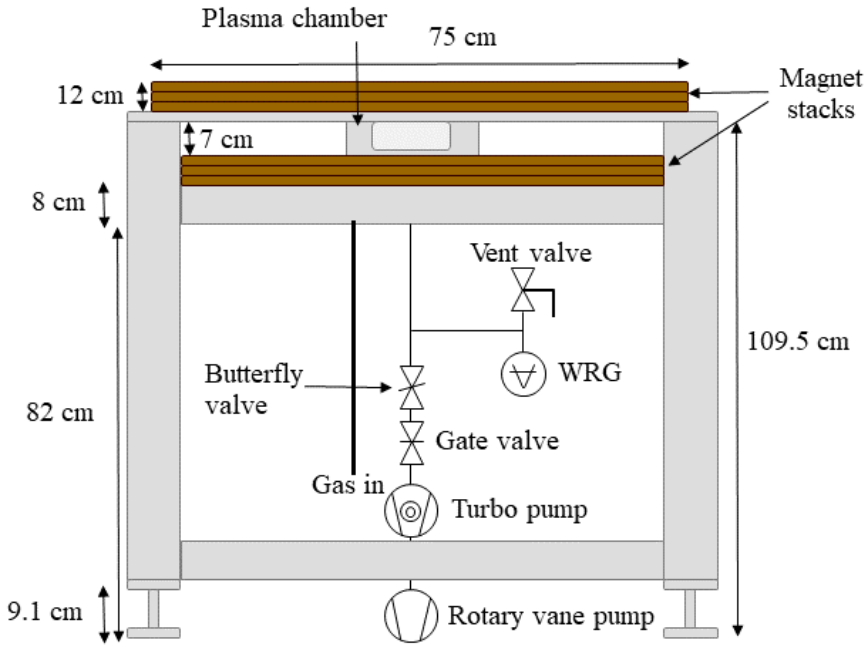


Figure 3.2: RF Plasma chamber, Helmholtz coil stacks and supporting frame. The valves and wide range gauge (WRG) are also shown.

In the following sections the equipment used to acquire experimental results is described in detail. The pumping system, gas supply system, plasma chamber, RF power supply, and electro-magnet set-up are described in section 3.1. The construction and installation of Langmuir and emissive probe diagnostics and the retarding field analyser are described in section 3.2. The dust injection system, laser system and optical imaging diagnostics are described in section 3.3.

## 3.1 Experimental Setup

### 3.1.1 Electro-Magnet System

Copper tubes encased in phenolic resin are arranged into a Helmholtz coil above and below the chamber to generate a linear magnetic field, which are shown in figure 3.2. The DC current through the Helmholtz coil generates a magnetic field in the direction shown in figure 3.1. A

Prüftechnik DC power supply provides up to 1638 A at 120 V to the coils. This is done by converting the 3 phase input supply to DC with a variable step-down transformer coupled to a power diode bridge rectifier. The field is uniform to within 0.3 % horizontally and 0.6 % vertically in the chamber [65]. The field strength varies linearly with current with 1638 A = 1 T in chamber centre. Because of the high current maximum, overheating limits the time that can be spent at 800 A (800 A = 0.5 T) to about 15 minutes (even with cooling) as after this time the stacks reach a temperature of around 70 °C. The heating causes an increase in the resistance of the coil which limits the current. Chilled water is pumped through them to provide cooling to 12 °C with no current through the coils. The temperature is measured using two thermocouples attached to the outside of the copper outlet tubes of the upper and lower stacks. Two shut off valves, one on the upper and one on the lower stack, can be used to stop the flow should a leak occur. A flow interlock is inserted in the inlet/outlet line which shuts down the DC power supply in the event of a leak or chiller malfunction.

### 3.1.2 Plasma Chamber & Gas Supply System

The vacuum chamber is made of aluminium with inner dimensions of 100 × 100 mm and a height (electrode gap) of 40 mm. The chamber has a wall thickness of 20 mm. The powered electrode is a 70 mm diameter stainless steel disk of 8 mm thickness. A polytetrafluoroethylene (PTFE) ring of 10 mm thickness isolates the adjacent grounded surfaces from the powered electrode. The powered electrode can be replaced by a 40 mm diameter disk with a corresponding PTFE ring. The ground electrode is an indium tin oxide (ITO) coated glass disk of 80 mm diameter and 10 mm thickness. The ground electrode is mounted into a detachable chamber lid which is screwed into the rest of the chamber. Two copper rings are compressed between the ground electrode and the chamber lid and an aluminium mounting is screwed into the lid which secures the lid in place. For some tests in DC the ITO window was replaced by a moveable stainless steel electrode. This was a 70 mm diameter disk of 10 mm thickness that is screwed into a 30 cm long, 6 mm diameter stainless steel rod. This is mounted on the top of the chamber, using a linear O-ring seal, in a stainless steel flange of the same dimensions as the ITO coated window. This allows the position of the ground electrode above the driven electrode to be adjusted from 0 - 40 mm. The chamber set-up is shown schematically in figure 3.1 (also shown in figure 3.3) with ports in the side of the chamber for OIS and probe diagnostics, and in the top of the chamber for emissive and Langmuir probes. A top view of the chamber is shown

in figure 3.4. A ball pen probe can be mounted only in port B, which can measure $V_p$ when fields of above 200 mT are used. Quartz windows (40 $\times$ 70 mm) are mounted in the other two side ports.

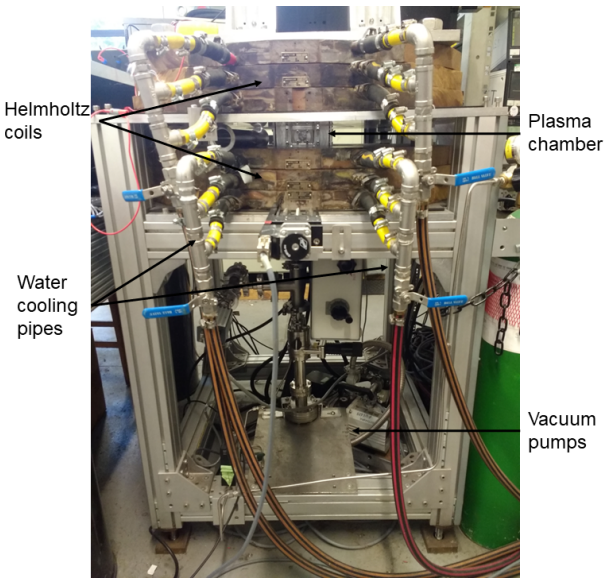


Figure 3.3: RF plasma chamber photo including the pumping system and magnetic stacks.

Argon gas is introduced into the chamber through a 1/4 inch stainless steel tube from a pressurised gas cylinder through a two stage regulator. Stainless steel was used to minimise water vapour contamination. BOC research grade (99.9995% purity) argon gas is stepped down from a pressure of around 200 bar through a two stage BOC regulator (HP 1701B) to about 1 bar. An argon plasma is used because it is commonly worked with and well understood and due to the low chemical reactivity. An MKS 1179A Mass-Flo$^{TM}$ Controller (MFC) was positioned between the regulator and the chamber, which was typically set to around 2 sccm. The flow rate is displayed and adjusted by an MKS PR4000B interface unit connected to the MFC. A ball valve placed immediately after the MFC can also be used to stop the gas flow if necessary. A gate valve between the chamber and the pumps can be used to isolate the chamber from the pumping system. A butterfly valve located above the gate valve is used to increase the pressure in the chamber and reduce the flow rate in the chamber. The vacuum system consists of a Leybold TRIVAC E2 rotary pump acting as a backing pump for a Leybold TURBOVAC 50 turbomolecular pump. Copper gaskets are used to create the vacuum seal around the turbo pump while connections elsewhere in the chamber are done with O - rings. Copper gaskets are not required throughout the chamber as thin film deposition is not done in this chamber so the vacuum requirements are less strict. The pumping system is shown in figure 3.1. This pumping system can achieve a minimum base pressure of $2 \times 10^{-5}$ mbar in the chamber. The turbo pump

is positioned 1 m below the chamber in a region of diverging magnetic field to avoid magnetic induced stresses. The turbo pump slows down in magnetic fields which limits the maximum magnetic field it can be operated in to 7 mT or less [66]. An MKS 627B Baratron is mounted on top of the plasma chamber (port 3 in figure 3.4) and is used in the working range of $1 \times 10^{-5}$ mbar to $1 \times 10^{-1}$ mbar. The Baratron is used because it has no gas dependence and has a linear response over a relatively wide working range. A separate wide - range gauge (WRG, Leybold ITR-90), incorporating a Pirani and Bayard-Alpert gauge, measures the base pressure when pumping down from atmospheric pressure. The gauge automatically switches between the Bayard-Alpert Gauge and the Pirani. The Bayard-Alpert gauge is used for pressures $< 2.0 \times 10^{-2}$ mbar and the Pirani gauge is used above $5.5 \times 10^{-3}$ mbar. The Pirani gauge is gas dependant with a calibration factor in Argon of 0.8. This is mounted between the turbo pump and the plasma chamber. The gas dependency of the gauge means it is only used when pumping down and venting. The WRG is manually deactivated when the magnetic field is applied as the field affects the reading displayed on the sensor.

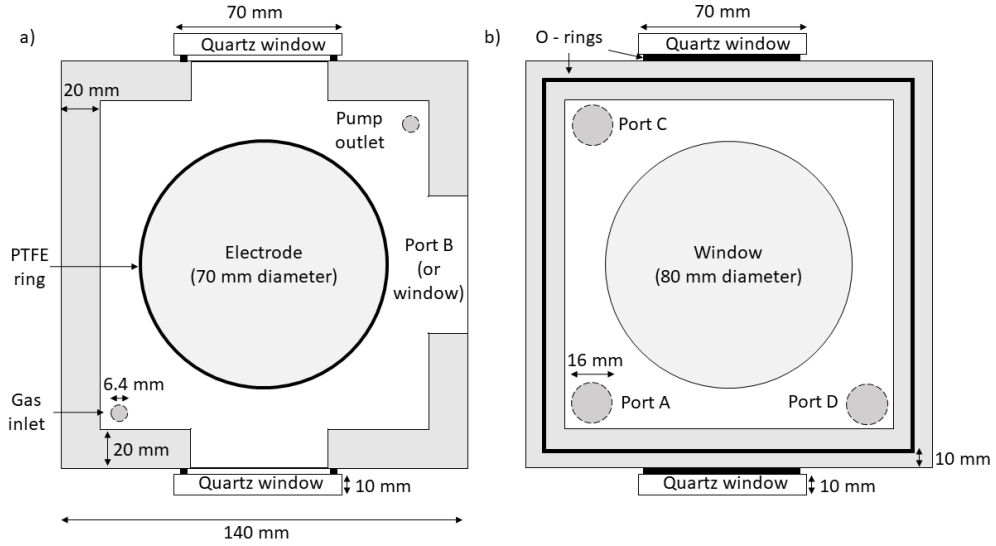


Figure 3.4: Inside view (top) of a) the lower and b) the upper surfaces of the vacuum chamber. The ports in the upper surface can be used for probe diagnostics or pressure sensors.

### 3.1.3 RF Power Supply

The plasma is generated by an 13.56 MHz RF power supply (Dressler CESAR Model 136) providing a maximum power of 600 W. The RF generator was used to provide up to 50 W to the driven (lower) electrode in the experiments. This is connected to a matching unit, consisting of two variable capacitors in an L - network. This allows matching of the impedance of the RF source to the chamber and plasma to reduce reflected RF power. The reflected power

is adjusted manually and is typically no more than 1 - 2 W. A separate shunt circuit is placed between the matching unit and the powered electrode which allows a direct measurement of the plasma current by cancelling out the parasitic impedances of the chamber through the method described by Sobolewski [67]. The variable capacitance of the shunt circuit was adjusted so that the DC offset of the current probe was at a minimum (approximately 1 mA on the scope). A voltage and a current probe (Pearson 2877) are mounted 25 cm below the driven electrode as shown in figure 3.1 and connected to a a Tektronix MDO 3054 Oscilloscope which also displays the DC bias voltage on the electrode, the RF voltage and the plasma current.

## 3.2 Electrical Plasma Diagnostics

Probe diagnostics are used to obtain information such as $n_e$, $T_e$, $V_p$ [68] and the electron energy distribution function (EEDF) [69]. Langmuir probes can be used to measure $n_e$, $T_e$, and $V_p$ in the bulk but not in the sheath. Emissive probes can only measure local potential but can be used in the bulk or sheath and in magnetic fields. This section will provide an overview of the construction, installation and electronics of the probes.

### 3.2.1 Langmuir Probes

A Langmuir probe tip is a metal wire or disk immersed in a plasma. Langmuir probes are one of the most commonly used diagnostics due to their simple construction [16]. A voltage ramp is applied to the tip and the current drawn by the probe is measured. A plot of the applied voltage (V) against the measured current (I) is known as an IV characteristic. This characteristic contains information on $n_e$, $n_i$, $T_e$, $V_p$ and the EEDF. Analysis of these probe characteristics is not straightforward primarily due to RF distortions of the IV curve. For more details of probe theory and RF perturbations see Chapter 4.

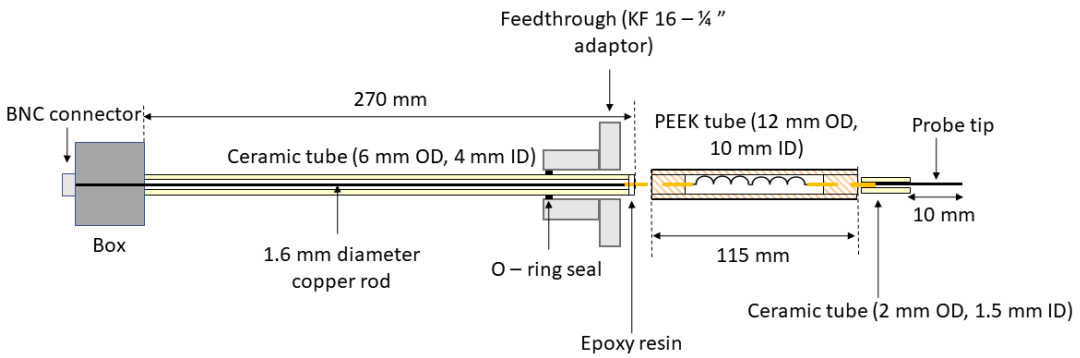


Figure 3.5: Schematic of RF compensated Langmuir probe with inductors and PEEK holder.

The Langmuir probe used in experiments is shown in figure 3.5. The Langmuir probe was a 1 cm long tungsten (W) tip of 99.95 % purity (Goodfellow W 005135). The diameters used were 25, 50 and 100 $\mu$m. These were used to ensure $R_p < \lambda_D$ so Orbital Motion Limited theory can be used [70] in the electron saturation region. Typical parameters are $T_e$ = 3 eV and $n_e$ = $10^{15} m^{-3}$, which results in $\lambda_D$ = 1.2 $\times 10^{-4}$ m and the inequality is satisfied. The probe tip was constructed by connecting the wire to a gold-plated pin using solder (tungsten cannot be soldered, so this was done just to form an electrical contact) and supported mechanically with epoxy resin. The wire was then inserted into a 10 mm long alumina ceramic tube (Precision Ceramics Ltd. Birmingham) of 3.1 mm outer diameter (O.D.). A smaller alumina tube of 2 mm O.D. and 40 mm in length (Friatec-Degussit Ltd. Hertford) was then inserted into the larger tube and joined with Epoxy resin leaving only 1 cm of tungsten exposed. The probe stem, which was fed through the flange, was a 270 mm long (6 mm O.D.) alumina tube. A 1.6 mm diameter copper rod was passed through the stem and soldered to a BNC connector (in a plastic box) at one end. The copper rod was threaded through both ends of the tube and small 3.1 cm O.D. ceramic tubes at each end of the main tube to keep the rod centred.

A hollow polyetheretherketone (PEEK) tube 115 mm long and 10 mm O.D. with corresponding pins connects the tip to the probe stem. The PEEK tube was used to hold the RF chokes which connect the probe tip to the stem for passive RF compensation. The probe stem can be inserted through a feed through on port B or port A into the chamber as shown in figure 3.1. Either an L-shaped or straight probe tip could be used depending on whether the probe was mounted horizontally or vertically.

The Langmuir probe is connected to a Hiden Langmuir probe acquisition system (ESPIon) via a 1.5 m BNC cable to the BNC connector on the probe stem. An external low pass RF filter (cut-off frequency 1 MHz) is connected between the probe stem and the Hiden unit. This is designed to block RF currents which will cause over-current errors (level shifting the IV curve along the current axis) and potential damage to the Hiden unit. A voltage sweep is applied in 0.1 V increments (used in all experiments) and the current drawn by the probe is measured across a 1 - 1000 $\Omega$ internal resistor depending on the current range selected. Typically the maximum current that can be measured by the Hiden unit was 1000 mA but usually the current was limited to lower than this. Unless otherwise stated IV curves were averaged over 1000 scans. The Langmuir probe was cleaned approximately weekly by gently scraping the wire with a knife before inserting into the chamber and then biased to -40 V in a plasma for 5 - 10

minutes for ion cleaning. Ion cleaning was generally chosen over electron cleaning because the risk of breaking the filament with large currents is lower but electron cleaning was done monthly.

### 3.2.2 Emissive Probes

The emissive probe consists of a pair of parallel or 'V' - shaped ceramic tubes 6 cm long with an O.D. of 2 mm. Each tube contains a conducting NiCr rod. At the open end of each tube, a thoriated tungsten wire (Goodfellow W 055200 0.6 %) is formed into a filament 1 cm long and wrapped around the rods and crimped. Thoriated tungsten is used as it has a work function much lower than tungsten or oxides of tungsten which are produced by the heating process (2.6 eV compared to 4.6 eV) [71]. The 'V' - shaped probe was used to avoid the effect of overlapping probe sheaths that develop around the ceramic tubes. This can be a problem at low plasma densities or in the sheath where the sheaths can expand rapidly. These effects can be minimized by increasing the distance between the ends of the ceramic tubes. The 'V' shape probe can be used at lower densities than the loop probe (made with parallel ceramic tubes). This method is accurate within a density range of $10^5$ - $10^{12}$ $cm^{-3}$ [72]. Below this limit, the electron sheath surrounding the tube significantly overlaps the filament. Above this limit, the filament temperature required is too high [14]. This makes the 'V' probe suitable for use in a plasma sheath [72]. However, because the taught filament wire is in contact with the end of the ceramic tubes a hot spot can develop at high heating current and break the filament. The filaments used were 25 or 50 microns in diameter. The thin filament perturbs the plasma to a smaller extent, but is more vulnerable to overheating and breaking than the thicker filament. The filament size also determined the maximum magnetic field the probe could be used in. This is determined by $r_{Le} = R_p$. This gives a maximum field strength of 530 mT (12.5 $\mu$m wire) and 260 mT (25 $\mu$m wire) assuming $T_e$ = 3 eV.

The position of the emissive probe could be adjusted vertically and horizontally to an accuracy of approximately $\pm$ 0.5 mm and $\pm$ 5 degrees respectively. The positioning system is shown in figure 3.6. The positioning system is attached to a vertical translation stage with a micrometer to allow precise vertical movement of the emissive probe. An aluminium block is screwed into the back plate (attached to the translation stage) to hold the micrometer in place. The head of the micrometer is clamped to the end of the track of the translation stage. An aluminium pointer is grub screwed to the probe stem above a protractor to provide a measurement

of the rotational movement of the probe.

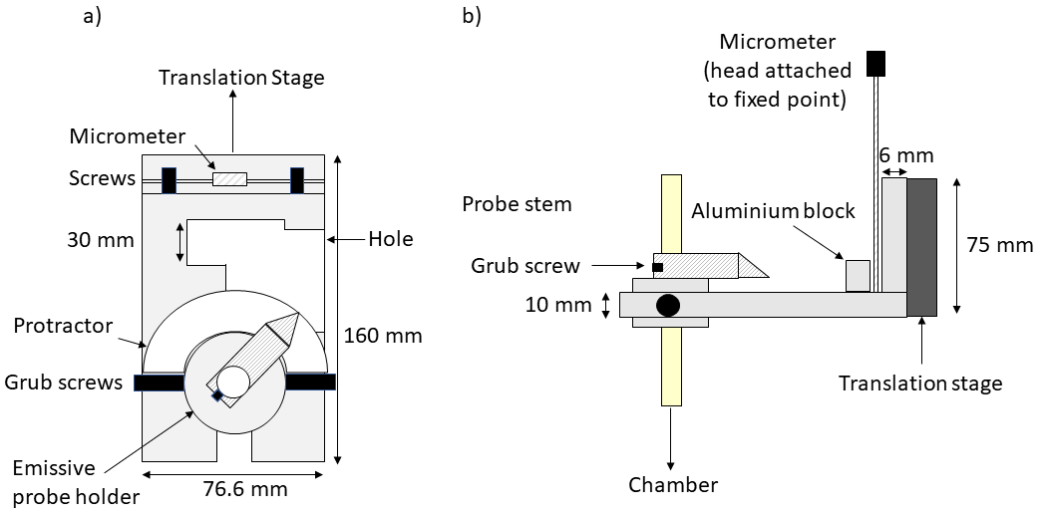


Figure 3.6: Top (a) and side (b) view of the emissive probe positioning system. The probe stem can be allowed to rotate or fixed in place with the grub screws.

The position is calibrated by measuring the distance between the filament and the bottom of the probe tip outside the chamber with a micrometer. The probe was then mounted into the chamber and the height adjusted until the probe tip touched the bottom of the chamber. After taking into account the difference between the position of the filament and the bottom of the probe tip, this is taken to be zero as measured by the micrometer. This position was checked against camera images (see section 3.3) of the probe with a known pixel/distance ratio. The angle was calibrated by using a dummy probe tip which was designed such that it would touch the chamber wall at a reading of 90° on the protractor. The pointer was fixed to this position and then the emissive probe tip was installed.

Emissive probes can be considered more accurate than collecting probes in measuring $V_p$ as the former has a measured potential dependent on filament temperature and the latter has a measured potential dependent on electron temperature [73]. The filament temperature is typically around 0.3 eV compared to electron temperatures of approximately 3 eV in low temperature non-thermal plasmas. Additionally, multiple measurements taken with the inflection point method (see section 6.2) give more accurate values of $V_p$ than cold probes. However, emissive probes are mainly only used to determine $V_p$, with special techniques needed to measure $T_e$ [74]. Emissive probes can also measure electric fields such as those found in sheaths or a vacuum [75] whereas Langmuir probes cannot [76]. Emissive probes are also self-cleaning when heated [77] and have been used in deposition-heavy environments and in magnetised plasmas [78]. They can also be used to measure the RF amplitude in plasmas [14].

## 3.3 Dust Imaging System

Dust (given by the manufacturer as 9.42 $\pm$ 0.02 $\mu$m diameter melamine formaldehyde (MF)) is injected into the chamber from a dust dropper held in port C with an identical feed through to the Langmuir probe (see figure 3.5). The dropper consists of a 30 cm long 1/4" steel rod which is bent at 90° inside the chamber. At the end of the rod is a PEEK container with a 5 mm radius hole in the bottom. A nylon mesh of 50 $\mu m^2$ holes is held in place over the hole with an aluminium covering with dimensions of 2 $\times$ 10 $\times$ 5 mm with a hole matching that of the PEEK container. A steel confinement ring 2 mm thick and 40 mm in diameter rests on the driven electrode directly below the PEEK holder to modify the potential profile to confine the dust. Dust was injected into the chamber by impacting the steel rod with a solenoid actuator (Mecalectro 8.M14.02.62) attached to the emissive probe positioning system (see figure 3.6). The rod is tapped by the actuator until dust is imaged by a Photron Fastcam with a 50 mm diameter 532 nm filter (Edmund Optics, 10 nm bandwidth) mounted with a Sigma EX 105 mm macro lens. The camera images the dust through a quartz window (see figure 3.4). The dust is illuminated by a laser sheet from a 532 $\pm$ 1 nm LD pumped solid state laser (CNI MGL-III-532, 300 mW). Dust crystals are imaged using a laser system based on that of Samsonov *et. al.* [79]. A system of lenses and mirrors create a laser sheet that can be swept vertically or horizontally over the dust crystal allowing the dust grains to be imaged by a camera. The setup is shown in figure 3.7.

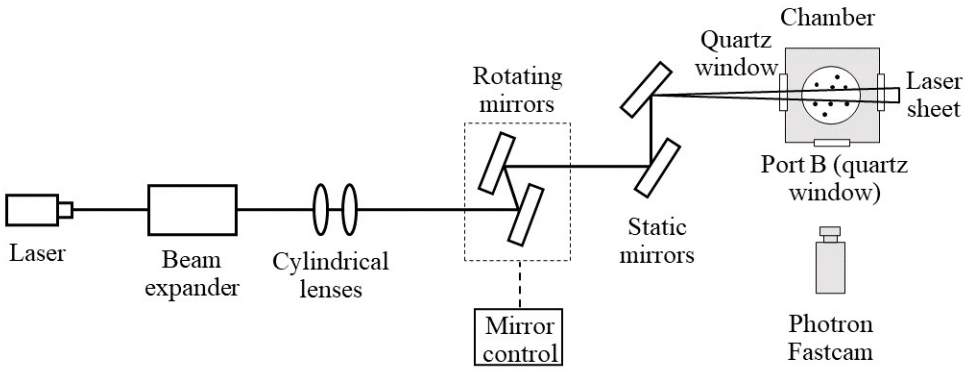


Figure 3.7: Schematic of the laser system for dust imaging. The camera can be placed above the chamber or view the crystal through port B.

Once emitted from the laser, the light travels 8 cm to a beam expander. The beam expander increases the diameter of the laser beam by a factor of ten to around 1.4 cm. The beam then passes through a pair of cylindrical lenses (focal length 1.5 m) which convert the expanded

beam into a laser sheet. The distance between the cylindrical lenses and the beam expander can be varied to change the height and width of the laser sheet. A pair of galvanometer - driven rotating mirrors were used to sweep the laser sheet vertically or horizontally depending on their orientation. The mirrors rotate synchronously by a custom - made control unit which could rotate the mirrors in 256 discrete steps. This allowed the sheet position to be chosen consistently between experiments, but with the lens and mirror positions and sheet thickness chosen to allow for smooth motion of the laser sheet in the chamber between steps. The two additional static mirrors in figure 3.7 are used to adjust the height and angle of the sheet in the chamber. Two PEEK blocks, of the same dimensions as the chamber window, were pushed into the outside of the window frames (with the window installed) on both sides of the chamber (The quartz windows in figure 3.4). The PEEK blocks had a grid of $3 \times 3$ 1 mm diameter holes. The height and angle of the laser sheet was adjusted so that the laser light passed through the same hole positions in both PEEK blocks. This would ensure the laser sheet was at a uniform height in the chamber. The sheet illuminates levitating dust in the chamber which is imaged by the Photron camera through the 532 nm bandpass filter.

The laser sheet thickness was calibrated using the method described by Samsonov *et. al.* [79] with a 5 cm long glass slide consisting of a grid of $0.48 \times 0.48$ $mm^2$ squares. The slide is placed on an incline of $6^\circ$ in the plasma chamber with the Photron camera positioned above it looking down. The laser sheet illuminates the cells on the grid, from which the laser sheet thickness could be determined using simple trigonometry to be $1.3 \pm 0.1$ mm.

# Chapter 4

# Passive RF Compensation of Langmuir Probes

## 4.1 Introduction

Langmuir probes are commonly used, in both DC and RF plasmas, as an invasive electric probe diagnostic which can measure local values of bulk plasma potential ($V_p$), electron and ion density ($n_e$ and $n_i$ respectively) and electron temperature ($T_e$), but not ion temperature ($T_i$) [80, 32]. These values are obtained from a probe IV characteristic (or IV curve) which is a plot of applied voltage against current drawn from the plasma. To obtain an IV curve, a slowly varying voltage ramp is applied to a probe tip in the plasma bulk and the current drawn from the plasma is measured at each voltage. In DC plasmas, standard probe theory and techniques can be used to obtain the plasma parameters (for example, $n_i$, $n_e$, $T_e$) from an IV curve including Orbital Motion Limited (OML) theory and the second derivative method. In RF plasmas, the electron collection regions of an IV characteristic becomes distorted so these theories cannot be used to accurately obtain the plasma parameters in the electron collection regions. Langmuir probes which have this distortion are known as uncompensated probes. Several compensation methods have been developed (such as active compensation or the use of a compensation electrode) to recover the undistorted curve, from which standard probe theory can be used to obtain the plasma parameters. Accurate values of these parameters is important in several fields, including sputtering and deposition in industrial plasmas. It is also vital in fusion devices where RF heating is used, as these RF fields can affect the plasma potential [81].

The purpose of this chapter is to present results from an in - depth study of passive compensation of Langmuir probes in small RF plasmas. In particular, how the key plasma parameters change with the level of RF compensation. It is shown that passive RF compensation with a compensation electrode can significantly perturb small plasmas.

The RF plasma chamber and equipment used for generating the plasma are described in Chapter 3 including the probe design in section 3.2.1. The standard analytical techniques of IV curves from Langmuir probes have been discussed in section 2.3.1. Orbital motion limited theory, which is used to determine density in these experiments, was discussed in section 2.3.2. Section 4.2 details the theoretical background of RF influence on a probe and compensation techniques. The experimental conditions are described in section 4.3. An LT SPICE model has been developed and used to calculate the circuit impedance at the harmonic frequencies and is described in section 4.4. Experimental results showing the change in level of compensation of a probe with only a chain of inductors are described in section 4.5. The effect of adding a compensation electrode is described in section 4.6. Conclusions are presented in section 4.7.

## 4.2 RF Compensation Theory

When RF is used to generate a plasma multiple harmonics of the fundamental frequency are generated mainly in the driven sheath regions. In higher pressure plasmas the fundamental frequency (13.56 MHz) is typically dominant, with the first few harmonics also having significant voltage amplitudes relative to the fundamental [82, 23]. With decreasing pressure, the shielding provided by charged particles in the plasma decreases and other harmonics may dominate [83]. Harmonics arise as a result of the non - linear structure of the sheath as the electron density decreases exponentially. A more detailed discussion of the origin of harmonics in CCP discharges is given in [27]. The harmonics cause an oscillation of the plasma potential which affects probe measurements. The distortion is primarily due to the dominant fundamental frequency and decreases with higher order harmonics. The contribution of the first and second order harmonics depends on the plasma pressure. Harmonics of higher than the third order typically have a small contribution to the distortion [84]. An oscillating RF voltage drop across the probe sheath results in a ”stretching” effect on the IV characteristic because of the non-linearity of the probe sheath [22, 85]. This effect is caused by the oscillation of the plasma potential which consists of the fundamental oscillation and its harmonics. The transition re-

gion of the IV curve is a function of the difference $V_b - V_p$, so will oscillate around a central potential. This effect is illustrated in figure 4.1 [2]. The instantaneous IV curve oscillates over the regions where electrons are collected. The time average over all the instantaneous curves will give the green curve. RF fluctuations particularly affect the electron collecting regions of the IV curve, as the heavier ions respond more slowly to RF oscillations. Consequently, it may seem more convenient to measure density from the ion current region and assume quasineutrality [86] and while this may be the case there are several limitations on using the ion current region. For example, Allen, Boyd and Reynolds' theory of radial ion collection requires the electron temperature to be known and the plasma must be sufficiently low density for OML to apply.

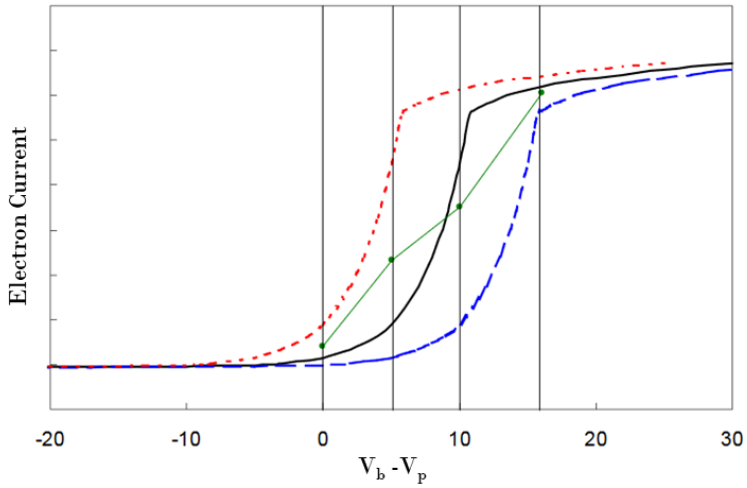


Figure 4.1: Example IV characteristic with RF distortion [2] ($V_p$ is the plasma potential, $V_b$ is probe potential). The red and blue curves are the instantaneous IV characteristics at the limits of the RF oscillation. The green dotted line is the time averaged IV curve. The black curve is the undistorted IV characteristic.

The floating potential in an RF plasma is shifted negatively according to equation 4.1 [87] if no harmonics are present and if electrons are retarded throughout the entire period. This shift is typically on the order of a few $T_e$ [88] (typical $T_e$ = 3 eV).

$$V_f = \frac{k_b T_e}{2e}\left[ln\left(\frac{2\pi m_e}{m_i}\right) - ln\left[I_0\left(\frac{eV_{RF}}{k_b T_e}\right)\right]\right] \tag{4.1}$$

Where $k_b$ is the Boltzmann constant, $V_{RF}$ is the RF voltage amplitude across the sheath, $T_e$ is electron temperature, $e$ is electron charge, $m_e$ and $m_i$ are electron and ion masses respectively and $I_0$ is the modified zero - order Bessel function. The second term on the right hand side of

equation 4.1 indicates the shift in floating potential. The DC floating potential can be recovered when $V_{RF}$ is less than $T_e$ as the second term on the right hand side tends to zero.

The distortion of the electron retardation region results in an overestimate of $T_e$ [85], which could be up to 20 eV, and $n_e$ [89] by an order of magnitude or more. Plasma potential is not generally affected by RF, although electron - neutral collisions will reduce the magnitude of electron saturation current [2]. This tends to flatten the IV curve which makes determination of $V_p$ more difficult.

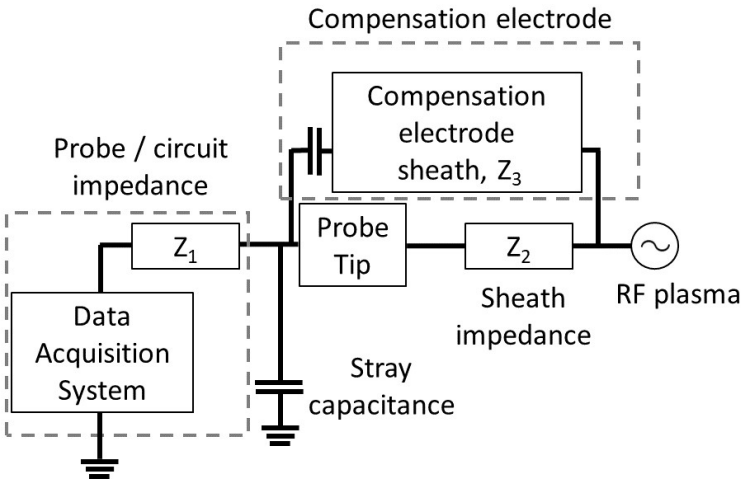


Figure 4.2: Passively compensated Langmuir probe circuit diagram including a compensation electrode. Note that this assumes collisionless sheaths.

The probe - plasma system may be modelled as a potential divider circuit which is shown in figure 4.2 where in the case of a compensation electrode $Z_2$ and $Z_3$ are in parallel. Note that this representation is simplified in that resistive effects caused by collisions in the sheath are ignored. In addition, the sheath capacitance varies non - sinusoidally in time due to sheath oscillations [20]. However, in this model it is simplified by assuming the capacitance to be a constant value. The compensation electrode ($Z_3$) is capacitively coupled to the probe circuit as this will allow high frequency RF signals to pass to the probe tip (thus decreasing the probe tip impedance to RF) while blocking DC signals to prevent these from contributing to the measured IV curve.

The corresponding potential divider equation is given by:

$$V_O = \frac{V_{RF} Z_1}{Z_1 + 1/[1/Z_2 + 1/Z_3]} \tag{4.2}$$

Where $V_O$ is output voltage, $V_{RF}$ is the voltage amplitude of the dominant harmonic and $Z_1$ is the impedance of the inductance chain, external filter and data acquisition system, $Z_2$ is the

probe sheath impedance and $Z_3$ is the impedance of the compensation electrode sheath. When $Z_1 \gg Z_2 \,//\, Z_3$ the sheath voltage ($V_s = V_{RF} - V_0$) across the sheath becomes small [90]. Due to the relation of frequency and impedance, the electron (and ion) plasma frequency becomes important when the RF fluctuation frequency ($\omega$) is large compared to the plasma frequency. In this case the impedance $Z_1 \gg 1/\omega C_s$ where $C_s$ is the constant value of the sheath capacitance as used in the model. The ions can only respond to the time averaged RF oscillations so ions are ignored for the purposes of the RF model [91] so $Z$ refers to electron impedance.

The compensation electrode is designed to have a low impedance to RF due to its relatively large surface area (on the order of 10 $A_p$) and is capacitively coupled to the probe tip. This allows the probe tip to follow the RF fluctuations in the plasma which will in turn minimise $V_s$ as the electrode lowers the probe's impedance to RF. Godyak and Piejak [90] and Chen [92] report that undistorted IV characteristics are obtained when:

$$\frac{Z_{sh}}{Z_{tot}} \leq (0.3 - 0.5)\frac{T_e}{V_{RF}} \tag{4.3}$$

Where $Z_{tot}$ is total RF circuit impedance, $Z_{sh}$ is sheath RF impedance, $T_e$ is electron temperature and $V_{RF}$ is the RF voltage amplitude. Similarly, Godyak and Popov [93] and Dyson *et. al.* [23] have shown that if $V_{RF} < T_e$, the effect of RF can no longer be distinguished from errors in the probe method.

In order to use equation 4.3, the factors within it must be known. Electron temperature can be measured relatively easily, for instance by using an optical method. $Z_{tot}$ can be measured but usually must be done *in situ* as the stray capacitance to ground introduced by the chamber is usually significant. $V_{RF}$ is more complicated to measure, but can be done with a capacitive probe [94]. $Z_{sh}$ is very hard to measure experimentally so equation 4.3 is not trivial to use in practice.

As direct measurements of sheath impedance are difficult, other indicators of compensation are preferable. Most of the key parameters measured using Langmuir probes are affected by the presence of RF so the values of $n_e$, $T_e$ and $V_f$ can be used to determine the level of RF compensation. Another method would be to observe the amplitudes of RF harmonics on a spectrum analyser connected to the output of the probe filter to make qualitative measurements of RF harmonic amplitudes.

### 4.2.1 RF Compensation Methods

The methods developed to remove RF distortion and allow standard DC probe theories to be used to obtain correct values of $n_e$ and $T_e$ can broadly be divided into three categories. The first of these is active compensation in which a signal, phase and amplitude matched to the local RF potential, is applied to the probe tip [84, 95]. The matched signal results in the removal of the RF voltage across the probe sheath as when both the probe and plasma are oscillating with matched phase and amplitude the impedance between the plasma and the probe (which have become coupled) becomes infinite.

The active method was developed by Braithwaite [95] who performed experiments in a parallel plate discharge at 3 Pa with a 13.56 MHz signal used to generate the plasma. The same signal was passed into the probe circuit, which consisted of a phase matcher, an amplitude matcher and a tantalum probe. A voltage sweep was applied to the probe to measure IV characteristics. As an RF signal will shift the floating potential more negatively, the phase and amplitude of the externally applied signal were adjusted such that the most positive floating potential was measured. This criterion was originally suggested by Sabadil and Klagge [96] and used by Braithwaite [95]. This method achieved reasonably good compensation for the fundamental frequency. More recent developments in active compensation have been to use phase locked loops, which are control circuits which generate an output signal at the same phase as an input signal [23]. These have since been used to actively compensate the fundamental, second and third harmonics [83, 23] in a low pressure asymmetric CCP. In the work of Dyson *et. al.* [23] the pressure and driving voltage were adjusted to increase the strength of harmonic signals which were measured by connecting the probe to a spectrum analyser. The authors of that paper report achieving good compensation, and determine that compensation of the second harmonic was not necessary at high pressure. At low pressure, when the second harmonic amplitude became approximately $2T_e$, the active compensation successfully compensated the probe. The active method was also used by Cox *et. al.* [97] to measure the EEDF in an RF driven plasma. Only the fundamental frequency was applied and the signal was varied until the floating potential was maximised. This adjustment does not require physically changing the probe unlike in passive compensation, but no comparison was made in this paper between the active method and an undriven probe to determine the level of compensation.

In summary, advantages of the active compensation method include no modification to the probe design being needed, such as the addition of a large compensation electrode (CE), which

allows for greater spatial resolution. Another advantage is that the plasma will not be perturbed by a large area compensation electrode. The active method can also be used to measure the local $V_{RF}$ by "tuning" the applied signal to the local oscillations [82]. The active method comes with the drawback of requiring expensive and complex circuitry, such as phase shifters and RF amplifiers, to generate the compensation signals. This complexity increases with each compensated harmonic.

Passive compensation methods can be divided into two types: intrinsic or extrinsic. The intrinsic method uses inductors, with a large impedance to RF, placed in the probe stem near the probe tip. This ensures a greater RF voltage drop across the probe circuit ($Z_1$ in figure 4.2) than the probe sheath [98]. These inductors are limited by constraints in physical size as well as requiring large self - resonant frequencies. In practice inductors alone are not usually sufficient to reduce RF distortions enough so that DC theory can be used. A compensation electrode, which has a large surface area, is capacitively coupled to the probe tip (see CE in figure 4.2) which couples the RF to the tip and reduces the RF sheath voltage drop [94]. This forces the probe to follow the local RF oscillations by reducing the potential difference between the oscillating plasma potential and the (now also oscillating) probe potential. The coupling capacitance between the CE and the probe must have as low impedance as possible in order to be effective.

Gagné and Cantin [94] originally added an additional electrode to the probe system to reduce RF fluctuations. In their work a capacitively coupled RF plasma was generated in a cylindrical bottle made by joining two Pyrex tubes (7.5 cm inner diameter). Regarding the probe, as well as compensating inductors, the compensation system included a conducting electrode of large surface area (3000 $\times$ probe area) which was AC coupled to the probe tip. The authors note that this electrode must not be so large as to perturb the plasma. An optically coupled capacitive probe was used to measure the RF voltage level. The density from microwave interferometry measurements was used to determine the level of compensation of the probe, and the two methods were found to agree to within 15 % and the compensation electrode was found to offer closer agreement than with inductors alone. Several other geometries of compensation electrode have been developed including a large ring centred on the probe tip, such as that used by Annaratone *et. al.* [99], a wire wrapped around the probe tip or a "sleeve" which was used by Chatterton *et. al.* [100]. Chatterton *et. al.* investigated the effect of varying the surface area of a compensation electrode on IV characteristics. In their design they used metal sleeves as

compensation electrodes which had different surface areas. In this work, which used a modified Reactive Ion Etching system in a 40 mTorr (5.3 Pa) argon plasma, it was found that $V_f$ gradually increased with compensation electrode area up to around 4 $cm^2$, after which $V_f$ is generally unaffected by increasing area. Paranjpe *et. al.* [98] used a copper rod encased in a glass tube in series with the probe tip to provide coupling between the probe and the RF oscillations and report similar improvement over uncompensated probes. Sudit and Chen [15] have recognised that compensation electrodes may perturb small plasmas. They have also found that their compensation electrode and inductance chain reduced the measured $T_e$ of a Langmuir probe by 1.6 eV compared to a probe without a compensation electrode in an RF helicon plasma, which implies a compensation electrode did not perturb their plasma.

Annaratone *et. al.* [82] have compared the active (with only the fundamental compensated) and intrinsic passive methods. This was performed experimentally in a 1 Pa, 13.56 MHz argon plasma with parallel plate electrodes (applied RF voltage amplitude of 100 V, electrode separation 70 mm) They note that when non-sinusoidal potentials are present, the passive method better follows the RF fluctuations. The passive method also gave a lower $T_e$ and larger $V_f$ than the active method. The inductances used in that paper were such that the self-resonant frequency was chosen to be 45 MHz. However, the authors do not investigate the improvement either method gives compared to an uncompensated probe. The effect of changing the inductance and capacitance values, and therefore the level of compensation, were also not investigated. Consequently, it is not possible to determine whether their probe system was optimally compensated. The intrinsic passive method was also used by Dilecce *et. al.* [101] to measure the EEDF in a capacitively coupled, parallel plate plasma at a fundamental frequency of 27 MHz. They report a factor 2 increase in RF blocking compared to without compensation, but also do not report plasma parameters measured with increasing levels of compensation and do not report the level of compensation. The values of inductance and stray capacitances in the experiment were not given. Mahony *et. al.* have used the intrinsic passive compensation method in an asymmetric, capacitively coupled discharge [102] and similarly report an increase in floating potential compared to without compensation but do not give many details as to the level of compensation.

An alternative intrinsic method involves using transmission lines and has been used Shimizu *et. al.* [103]. This method uses a series of inverse L - networks of coaxial cables each containing two coaxial cables of identical length. By choosing the length of these cables, the trans-

mission line input impedance of the filter can be made theoretically (although not practically) infinite at a chosen characteristic frequency. When an RF voltage is present at the characteristic frequency, the signal is reflected within the filter and is cancelled at the output. These filters can be cascaded to compensate for multiple harmonics. This method has been used to compensate the fundamental, second and third harmonics [103]. The technique is relatively simple to implement and does not perturb the plasma directly. However, a long cable coupled with a high sweep rate of the probe voltage will create a current ($dV_p/dt$) which will offset the IV characteristic [103]. The authors of the paper compared the transmission line method to no compensation and did find significant improvement but did not compare the transmission line method to other compensation techniques or vary the level of compensation to prove the system is optimally compensated.

In the extrinsic method the RF blocking circuit element (e.g. the inductance chain) is positioned outside of the plasma chamber. By placing this blocking element externally the stray capacitance, between the probe stem and the feedthrough, must be incorporated into the design of the filter. Wendt gives an example of three tunable and parallel LC filters with the fundamental filter tuned to incorporate the stray capacitance [104]. By tuning the circuit impedance with variable capacitors, a parallel resonance effect can be created at several frequencies. As each filter is made of only inductors and capacitors, the order of harmonic that can be compensated is limited only by the capacitance and inductance values that can be used with a sufficient Q value and self resonant frequency (as size limitations can be ignored outside the chamber). In Wendt's paper, the fundamental, second and third harmonics were compensated (each with an LC filter tuned to the harmonic frequency) by adjusting the capacitance and taking the maximum in floating potential to be optimum compensation and compared to the transmission line method. Compensation was found to be improved with the lumped elements as the oscillation of the floating potential was found to be almost twice that of the transmission line, implying the lumped component filter was better able to follow potential fluctuations (i.e the input impedance was greater). A similar filter was employed by Mutsukura *et. al.* [105]. Differences in plasma parameters between the compensated and uncompensated probe were not reported as this was not the objective of the paper. However, the authors report a 35 dB reduction in RF voltage on the probe. The external filter method is simple to construct, but can be time - consuming to tune adequately and requires knowledge of the probe stray capacitance to ground.

An alternative method to obtain compensated IV characteristics to analyse with conventional DC probe theory is by using a theoretical approach with uncompensated IV curves. Oksuz *et. al* [89] and separately Linnane and Hopkins [106] performed an analysis on simulated uncompensated probe IV curves with an RF voltage amplitude of 30 V to show it is possible to obtain $T_e$ without using additional circuitry. The resulting $T_e$ agreed to within 3 % of the expected value. The analysis techniques of Oksuz *et. al* were used to obtain accurate $T_e$ values for partially compensated probes. However, this method requires knowledge of $V_{RF}$ in order to measure $T_e$ over the correct part of the electron retardation region which in turn requires a method of measuring the RF amplitude, for instance with a capacitive probe in addition to the Langmuir probe used to take the IV characteristic. Hannemann and Sigeneger [107] have investigated simulated and experimental IV curves (the latter taken in a capacitively coupled, parallel plate 10 W 13.56 MHz argon plasma at 0.02 - 0.5 mbar) and have found that the distorted probe characteristic can be described by a convolution of the undistorted curve with an apparatus function.

The passive technique has been used with both single [82] and double probes [108]. Previous work in the field (to the author's knowledge) does not include a comprehensive work of passive compensation where both compensation electrode area and inductor chain optimisation are investigated simultaneously. Authors have rarely justified experimentally that a Langmuir probe has been optimally compensated.

## 4.3 Experimental Conditions

A voltage sweep of - 10 to + 40 V was typically applied to the probe, in 0.1 V increments, by the Hiden unit. The current range was typically 2.0 mA. The voltage range could be varied depending on where the peak of the 1st derivative was located. IV characteristics were averaged over 1000 scans. A passive RF LC low pass filter, cut-off frequency of 1 MHz, was used in all experiments (see figure 3.5, Chapter 3). This was connected to the output of the box at the end of the probe stem using a BNC connector (see figure 3.5, Chapter 3).

This was done to protect the Hiden unit from large RF currents which can cause over - current errors or damage the current - sensing resistors within the unit. During the experiments, the amplitudes of the RF harmonics were measured with a spectrum analyser (part of the Tektronix MDO Oscilloscope) attached to the output of the low pass filter with a 50 Ω BNC cable.

Unless otherwise stated, IV characteristics were taken in the centre of the plasma chamber in a 6 Pa argon plasma with 10 W RF power supplied to the electrode. This results in 380 V RF amplitude and a DC bias on the powered electrode of approximately -120 V with no magnetic field.

In a series of experiments an inductance chain, placed in the probe stem, was used to vary the level of RF compensation. The inductance chain was made by soldering up to four inductors together (limited by space constraints in the PEEK tube, see figure 3.5). If less than four inductors were used the inductor(s) were soldered to a Nickel-Chromium wire of 1 mm diameter and of sufficient length to connect the inductors to the end of the PEEK tube. An inductor was soldered to a gold-plated female pin in one end of the PEEK tube, and the wire (or another inductor if four were used) were soldered to an identical pin The order of the inductors as well as the combination of values were changed during the experiments. The relevant parameters are shown in table 4.1. The values of inductance used in the chain (as given by the manufacturer EPCOS) were 22 (tolerance $\pm$10%), 100 (tolerance $\pm$20%) and 470 (tolerance $\pm$20%) $\mu$H.

Table 4.1: *Inductor data given by the manufacturer (EPCOS) including calculated inter-turn capacitance of each inductor ($C_L$) and Self - Resonant Frequency (SRF)*

| Inductance ($\mu$H) | SRF (MHz) | $C_L(pF)$ | DC Current Limit (A) | DC resistance ($\Omega$) | Q - Factor |
|---|---|---|---|---|---|
| $22 \pm 2$ | 13 | 6.813 | 0.56 | 0.74 | 55 |
| $100 \pm 18$ | 55 | 0.0837 | 1 | 0.65 | - |
| $470 \pm 54$ | 25 | 0.0862 | 0.3 | 6.5 | - |

The Chapter is organised as follows: In section 4.4, a theoretical model of the inductor chain and filter used in LT SPICE simulations is described. This gives the predicted impedance of each inductor setup used in experiments, which are described in section 4.5.1. In another experiment the proximity of the inductors to the grounded chamber wall, and the resulting change in effect of stray capacitance, was also investigated by retracting or extending the probe in the chamber. This experiment is described in section 4.5.2. In another experiment, two different stainless steel tube diameters were used to change the distance between ground and the inductors and wire. The final experiment in this chapter is described in section 4.6 and shows how the IV curves change in the plasma when a compensation electrode is added. This includes using several geometries and areas of compensation electrode as have been described in the literature.

## 4.4 LT SPICE Simulations

Software simulations such as LT SPICE can be used to calculate the circuit impedance ($Z_1$ in figure 4.2) to determine the effectiveness of the circuit for RF compensation. The most effective compensation occurs at the maximum input impedance. The changes in simulated circuit impedance can also be compared to experimentally observed changes in $n_e$, $T_e$ and $V_f$ which are also a measure of RF compensation. The passive compensation circuit used in experiments was simulated in LT SPICE (Analog Devices, [109]) with the circuit shown in figure 4.3. This was used to obtain the circuit impedance at RF frequencies as well as to understand the circuit behaviour. An attempt was made to experimentally measure the impedance response of the probe in the chamber with increasing frequency using a network analyser, but this was not possible as the probe was not impedance matched to the analyser.

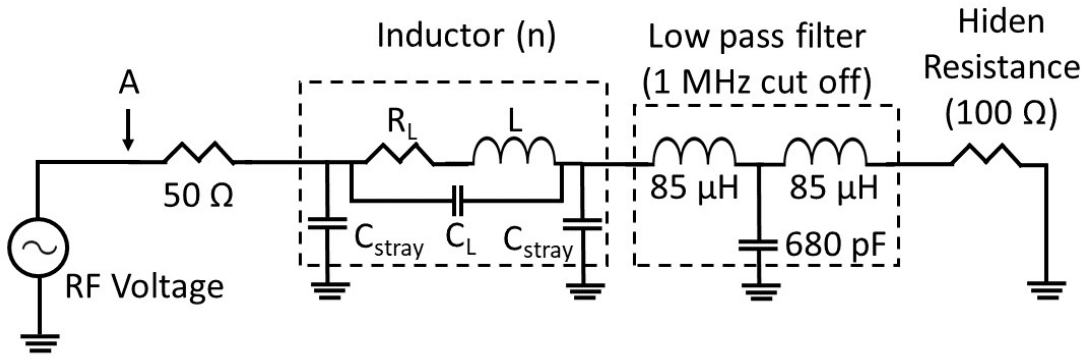


Figure 4.3: *Basic LT SPICE circuit model with up to n inductors in series. The sheath impedance was not included in the model.*

The RF voltage source in the figure represents the plasma oscillations and was swept in frequency with a constant amplitude of 100 V in simulations. The 50 Ω resistor connected to the voltage source does not represent any physical element of the probe - plasma system, but is only used in the simulation to record the current collected by the probe. The sheath impedance was not included because it was not possible to accurately model a time varying, non linear sheath capacitance in the software. The compensation electrode was also not included for this reason.

The inductors were modelled as an equivalent circuit consisting of an ideal inductance ($L$), resistance ($R_L$) and inter-turn capacitance ($C_L$) as shown in the dotted box in figure 4.3. The inductor DC resistances used in the model, given by the manufacturer, are shown in table 4.1 but the actual resistance may be higher due to the skin effect at RF frequencies. This resistance

was also measured with a multimeter and was found to be within 10 % of the given value. The capacitance $C_L$ was calculated from the given self resonant frequency (SRF, $f_{SRF}$) with the inductance $L$ as shown in table 4.1 using equation 4.4.

$$f_{SRF} = \frac{1}{2\pi\sqrt{LC_L}} \tag{4.4}$$

The value of $L$ was also measured experimentally using a Tinsley LCR bridge (at its maximum frequency of 300 kHz). These measured values of inductances were found to vary from the stated value by as much as 12 % (but within the stated tolerance of the 100 and 470 $\mu$H inductors). Only the manufacturer values of inductance were used in simulations, but the importance of the actual values used in experiments will be explained in section 4.5.1. The number of inductors (n) was varied between 0 - 4 to be consistent with the experiments. Capacitors $C_{stray}$ represent the stray capacitance of the inductors and wires to ground through the probe feedthrough. Each inductor contributes two $C_{stray}$ located at either end of the inductor as shown in the figure as it was not possible to distribute the capacitance over the inductance in the software. $C_{stray}$ accounts for both the capacitance between the wire ($C_{wire}$) and the inductor ($C_{Ind}$) to ground. The total capacitance is given by:

$$\frac{1}{C_{stray}} = \frac{1}{C_{Ind}} + \frac{1}{C_{Wire}} \tag{4.5}$$

The capacitances $C_{Ind}$ and $C_{Wire}$ were calculated using the cylindrical capacitance equation:

$$C_{Ind,Wire} = \frac{2\pi\varepsilon_0 L_{Ind,Wire}}{ln(b/a_{Ind,Wire})} \tag{4.6}$$

The stray capacitance on one side of the inductor is calculated from $L_{Ind,Wire}$, being half the length of either the inductor (27 / 2 mm = 13.5 mm) or the wire between two inductors (8 / 2 mm = 4 mm) as measured by a micrometer. If less than 4 inductors were present, a wire connecting the final inductor to the pin at the filter side end of the PEEK tube (see figure 3.5) was added. The inner and outer radii are given by $a_{Ind,Wire}$ and $b$ respectively. In this case, $a_{Ind,Wire}$ is the radius of the inductor (4 mm) or the wire (0.9 mm) which was also measured using a micrometer. The inductors were inside a 10 cm long stainless steel tube (flange KF 16) with radius $b = 8$ mm installed in port B (shown in section 3.1). With these numbers $C_{stray} = 0.18$ pF. The steel tube is attached to the feedthrough of the chamber which does not

change the value of $b$. Because half of the first inductor, nearest to the plasma, was always protruding into the chamber, this inductor contributed only half the capacitance of the others.

The low pass filter, which is installed outside the chamber, is included in the model as shown in figure 4.3. The cut off frequency of the filter with the components shown is 1 MHz. The resistance of the Hiden unit is also included which could be changed from 1 - 1000 Ω when changing the current range. The typical value used in experiments was 100 Ω corresponding to a 10 mA current range as was used in the simulations.

An example plot of the input impedance against frequency (100 kHz to 100 MHz), using 4 × 470 $\mu$H inductors, is shown in figure 4.4. For simplicity, the 470 $\mu$H inductors are referred to as n L, where n is the index (1 - 4) and L = 470 $\mu$H. The inductor closest to the probe tip is referred to as $L_1$, followed by inductors up to $L_n$. The input impedance was calculated from the ratio of voltage between point A and ground (in figure 4.3) to the current through the 50 Ω resistor. At DC (not shown in the figure) the impedance is 178 Ω due to the 50 Ω resistor, the DC resistance of each inductor (7 Ω) and the Hiden resistance (100 Ω). Whilst the 50 Ω is not a part of the real plasma system, the impedance at higher frequencies (such as used in figure 4.4) it will not significantly affect results. This is the reason the frequency range is above 100 kHz in the figure.

The impedance increases with frequency until around 3 MHz, after which peaks occur at 3.9, 11.6 and 19 MHz and minima are observed at 8.1 and 14.0 MHz. When frequency is increased beyond the peak at 19 MHz the impedance decreases. The fundamental frequency is located between the 11.6 MHz peak and the 14.0 MHz minimum giving an impedance of 41.5 kΩ indicated by the vertical line on the figure. The initial impedance peak (3.9 MHz) is likely the result of a parallel resonance between the final $C_{stray}$ (closest to the filter), the filter capacitance (680 pF) and the 85 $\mu$H inductor in the filter shown in figure 4.3. This was calculated using equation 4.4 with $C_L$ given by $(C_{stray}^{-1} + C_{680}^{-1})^{-1}$. Since $C_{680} \gg C_{stray}$ then $C_L$ can be replaced by $C_{stray}^{-1}$ which gives a frequency of 3.86 MHz. The peaks in the figure will all be because of parallel resonances between the inductors and capacitors in the circuit while the minima will be because of series LC resonances. The impedances at the fundamental frequency and several harmonics for all the inductors used in experiments are shown in table 4.2.

The inclusion of $C_L$ has the effect of reducing the magnitude of peaks and minima in figure 4.4 but does not shift their position on the frequency axis. Changing the value of $C_{stray}$ changes some of the peak positions in the figure, so impedance at the harmonic frequencies is a sensitive

function of $C_{stray}$. This is particularly important for the fundamental as this is on a rising edge of an impedance peak as shown in figure 4.4. If all $C_{stray}$ values were ignored, the impedance at 13.56 MHz would be 234 kΩ which is almost a factor of 5 greater than with $C_{stray}$. It is therefore important to include the stray capacitance in the model. The phase angle is also plotted on figure 4.4. This alternates between + 90 ° and - 90 ° over the frequency range, indicating when the circuit is inductive and capacitive respectively. The phase angle, as is expected, tends towards 0 for very low frequencies.

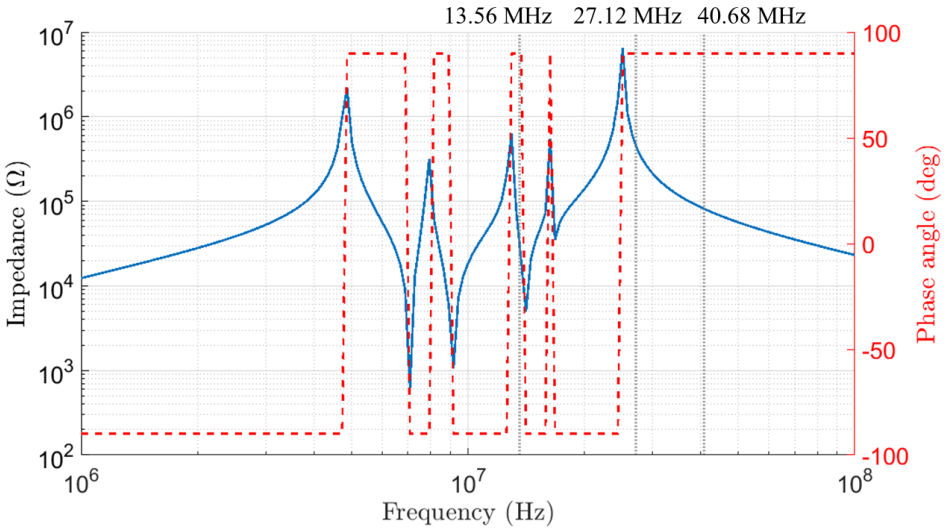


Figure 4.4: *Example trace of the LT SPICE simulation with four 470 μH inductors. The dashed lines indicate the positions of the 13.56, 27.12 and 40.68 MHz frequencies. The phase angle is plotted on the secondary y - axis*

Table 4.2: *Impedance calculated by LT SPICE at harmonic frequencies for each ideal inductance. The measured inductances and their position in the inductance chain are also included.*

| Inductance (μH) | 13.56 MHz Impedance (kΩ) | 27.12 MHz Impedance(kΩ) | 40.68 MHz Impedance (kΩ) | Measured Inductance (μH) | L Index |
|---|---|---|---|---|---|
| 0 | 11.5 | 22.3 | 2.03 | 0 | |
| 22 | 8.43 | 94.4 | 3.34 | 22 | |
| 100 | 2.116 | 93.2 | 145 | 98 | |
| 2 × 100 | 45.6 | 17.2 | 228 | 196 | |
| 1 L | 52.8 | 51.9 | 25.8 | 450 | $L_1$ |
| 2 L | 42.4 | 52.0 | 26.2 | 460 | $L_2$ |
| 3 L | 67.3 | 52.0 | 26.3 | 429 | $L_3$ |
| 4 L | 62.3 | 52.0 | 26.3 | 453 | $L_4$ |

The model was used to determine the impedance at the fundamental frequency and first two harmonics by increasing the inductance of the inductor chain. The impedance values for each inductance are shown in table 4.2 and plotted in figure 4.5. At 13.56 MHz, the impedance decreases from 11.5 kΩ with no inductor to a minimum of 2.12 k Ω at 100 μH before increasing to about 55 kΩ at 1 - 4 L. The impedance over 1 - 4 L varies from this average value by around ± 15 kΩ. With no inductor, the first harmonic has an impedance of 22.3 kΩ but then increases to a

maximum (around 95 kΩ) over 22 - 100 $\mu$H, which corresponds with the minimum impedance at the fundamental. The impedance then drops to a nearly constant value of 52 kΩ over 1 - 4 L, which is approximately the same as at the fundamental. The second harmonic, initially at an impedance of 2.03 kΩ, reaches a maximum of 220 kΩ at 2 $\times$ 100 $\mu$H, which is significantly higher than the fundamental and first harmonic, before rapidly decreasing to a near constant value of 26 kΩ over 1 - 4 L which is about half of the fundamental and first harmonic.

The impedances at the harmonics change due to the shifting positions of the peaks and minima when inductors are added. When changing the inductance from 22 $\mu$H to the 100 $\mu$H the impedance peak closest to the fundamental (see figure 4.4) shifts to the right, so the minimum is closer to the fundamental frequency, which results in a decrease of impedance. The first and second harmonics lie on the falling edge of the peak in impedance at 20 MHz in figure 4.4. When the inductance is increased, this peak will move towards the higher frequencies which increases the impedance for both harmonics which results in the impedance peak. When inductance is increased further, the peak shifts away from the higher frequencies leading to a decreasing impedance. In the range 1 - 4 L, the impedance peaks shift both towards and away from the fundamental frequency which results in the variation of impedance (see figure 4.5). At the first and second harmonics, the 20 MHz peak does not move which results in a nearly constant impedance.

From the model and the calculated impedances in table 4.2 it can be predicted that the best compensated probe can be obtained at 1 - 4 L where the impedance reaches a plateau assuming the fundamental frequency dominates which is a reasonable assumption at the pressure used in experiments. The worst compensation according to the model occurs at 100 $\mu$H due to the minimum in impedance at 13.56 MHz. The impedance at the first and second harmonics are much greater at lower inductances which should give a good level of compensation if these harmonics become comparable to the fundamental (for example at low pressure).

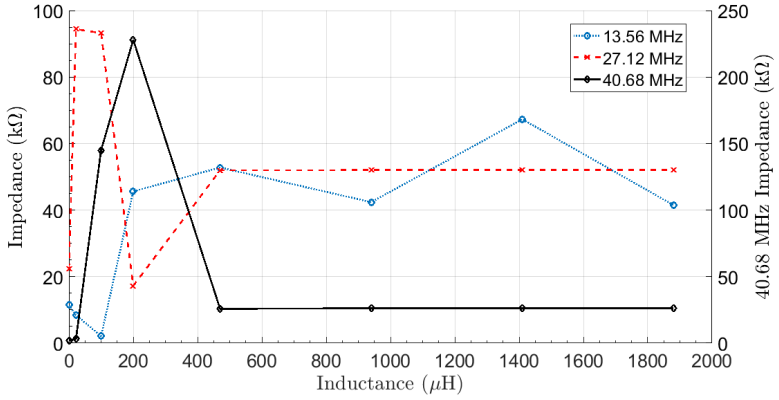


Figure 4.5: *LT SPICE calculated impedances at the fundamental frequency and first two harmonics with increasing inductance.*

The LT SPICE model cannot account for the impedance of the probe sheath and consequently changing of probe sizes. The sheath impedance is therefore assumed to be negligible compared to the circuit impedance in the model. The effect of changing probe radius on compensation must therefore be measured experimentally using values of $V_f$, $T_e$ and $n_e$. All plasma conditions and inductor configurations must be kept constant during these experiments.

## 4.5 IV Characteristic Measurements in RF Plasmas

### 4.5.1 Effect of Inductance Chain on IV Curves

In these experiments the measured inductances, which differed from the manufacturer's values, are shown in table 4.2 with $L_1$ being closest to the probe tip. This order was kept constant throughout the experiments. The notation n L will be used to refer to a chain of inductors in the order $L_1$ up to $L_n$. Figures 4.6 to 4.8 show the effect of increasing inductance on the IV curves using a 1 cm long Langmuir probe of several diameters (25, 50 and 100 $\mu$m) in the centre of the chamber in the plasma bulk. Current-voltage characteristics were also taken without inductors, which are shown as the black dashed curves in the figures. In figure 4.6 (a), the floating potential $V_f$ is initially at 24 V with no inductor and decreases by 15 V to around 8 V for both the 22 and 100 $\mu$H inductors. As the floating potential decreases, the electron current increases in the electron current region ($V > V_f$) for the 22 and 100 $\mu$H inductors. A maximum in the electron current occurs for the 100 $\mu$H inductor which implies this has the lowest impedance to RF. The floating potential then increases for the 1 L by approximately 20 V to 33 V which is consistent with increasing RF impedance in the literature [82, 23]. The

electron current decreases for 1 L which implies an increasing impedance to RF and also gives a much sharper kink compared to the other inductances. The increase in $V_f$, the reduction in electron current and the sharper kink are all consistent with increasing RF impedance predicted by equations 4.1 and 4.2. In figure 4.6 (b) the floating potential increases slightly from the 1 L case to a maximum of 34.1 V at 2 L then falls by 1 V for the 3 and 4 L. The electron current is greatest in the electron saturation region for 2 L and smallest for the 4 L. The maximum in $V_f$ coincides with the sharpness of the kink which is most pronounced for the 2 L case and least for the 4 L case.

When the probe radius is increased to 50 $\mu$m (figure 4.7) or 100 $\mu$m (figure 4.8) the shape of the IV curves follows the same general trend in $V_f$ and electron saturation current up to 1 L. For all probe sizes used in experiments the 100 $\mu$H inductor has the lowest $V_f$, the highest electron current and the least clearly defined kink. The 22 and 100 $\mu$H inductors both have the worst compensation for all probe sizes. For the 1 - 4 L cases, shown in (b) in the figures, there are some small differences between the probe sizes. For the 25 and 100 $\mu$m probes the sharpest kink and the highest $V_f$ occur at 2 L, but for the 50 $\mu$m probe this occurs at 3 L. For all the probe sizes between 1 - 4 L, the greatest $V_f$ (which only varied by about 1 V) also correlates with the largest electron current in the saturation region. The plasma is reasonably constant between scans and between the different probe sizes as evidenced by the near constant ion current in the saturation region. When changing probe sizes the chamber had to be vented so the constant ion current suggests this did not affect the plasma parameters. In addition, separate tests were carried out in which the chamber was repeatedly pumped to vacuum and vented with an IV scan taken in the plasma each time with no changes to the probe to determine plasma repeatability.

At lower inductances (0 - 100 $\mu$H), the collected current appears to be larger at the plasma potential which will give an overestimate of $n_e$. The LT SPICE model in figure 4.5 and table 4.2 predict a minimum in impedance for 22 $\mu$H and 100 $\mu$H inductances at the fundamental frequency which coincides with the minimum in $V_f$ in the experimental results. This suggests the fundamental is dominant in experiments, as the impedances at the first and second harmonics are much larger than at the fundamental for the 100 $\mu$H inductance. The LT SPICE model also predicts only relatively small changes in impedance over 1 - 4 L which is also seen in experimental results, particularly in the small changes in $V_f$. The results of these tests support the observations reported in the literature that $V_f$ should increase with improving RF compensation, but also imply that there is a dependence of electron density (due to the changing electron

current) on compensation which will be investigated later in this section.

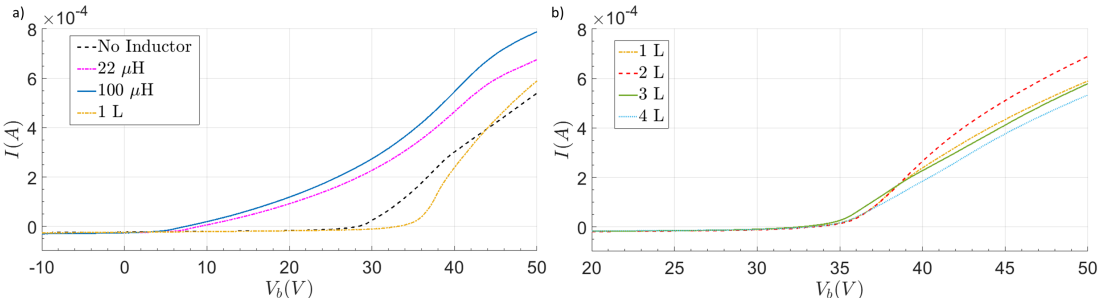


Figure 4.6: Langmuir probe (25 $\mu m$ diameter) IV curves with increasing inductance in the centre of a 10 W, 6 Pa Ar plasma. In (a) the inductance varies from 0 to 1 L $\mu$H and in (b) from to 1 - 4 L.

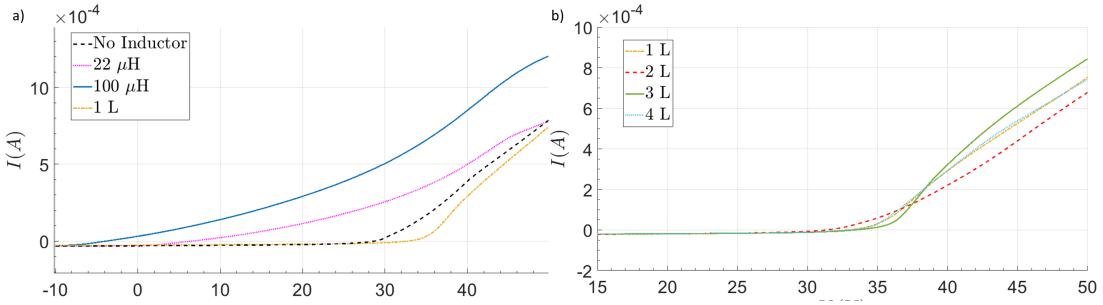


Figure 4.7: Langmuir probe (50 $\mu m$ diameter) IV curves (10 W RF, 6 Pa Ar). In (a) the inductance varies from 0 to 1 L and in (b) from to 1 - 4 L.

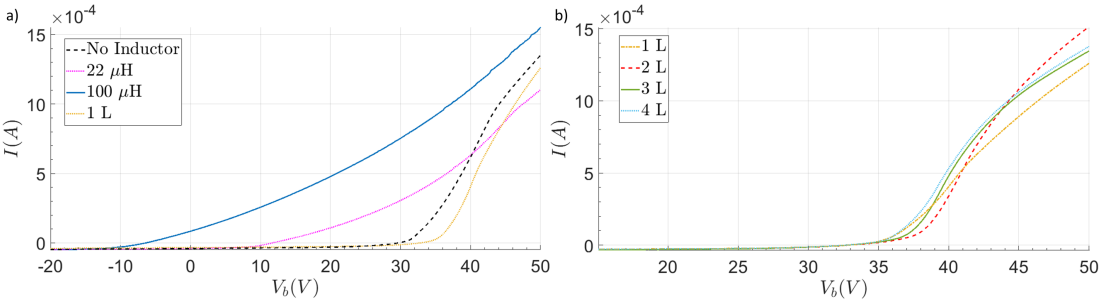


Figure 4.8: Langmuir probe (100 $\mu m$ diameter) IV curves with increasing inductance in the centre of a 10 W, 6 Pa Ar plasma. In (a) the inductance varies from 0 to 1 L and in (b) from 1 - 4 L.

The first derivatives of the IV curves are shown in figures 4.9, 4.10 and 4.11 for probe diameters of 25 $\mu$m, 50 $\mu$m, 100 $\mu$m respectively. A second order Savitsky - Golay smoothing function [110] is applied to the first derivatives in order to reduce noise but was checked to ensure it did not affect the shape of the curve. Taking the 25 $\mu$m probe as an example (see figure 4.9 (a)) with no inductor present the $dI/dV$ curve starts to increase at around 26 V and reaches a maximum at approximately 36 V. Between these two points there is a kink or "shoulder" at 32.2 V. It will be shown later, in the analysis of the second derivatives, that the voltage difference between this shoulder and the plasma potential is the RF voltage. When a

22 $\mu$H inductor is added the shoulder has moved further from the main peak which indicates an increase in the RF amplitude so compensation is worse than for no inductor. The voltage at the maximum of the first derivative also changes with inductance, but as the plasma is not changing $V_p$ should be constant. The difference in the peak maxima is likely due to the increase in RF voltage across the sheath. A similar curve is observed for the 100 $\mu$H inductor except the RF voltage has slightly increased. For the 1 L case $V_f$ has increased to 34 V and the RF voltage has significantly decreased. The shoulder is no longer observable because the RF voltage is too small to be distinguished from the main peak. In figure 4.9 (b) as L increases the peak height reaches a maximum at 2 L and then decreases. The position of the peak at 2 L is 38.7 V which varies by 5% over 1 - 3 L so over this range the position of the peak is relatively unaffected by RF voltage. There is no shoulder observed over the 1 - 4 L range which suggests that the RF voltage is small.

The same trends are observed for the 50 $\mu$m probe as shown in figure 4.10 (a) and (b) but there are some noticeable differences.There is no definable peak for the 2 L case and instead the maximum in $dI/dV$ is reached at 3 L. The RF voltage is higher for the 50 $\mu$m probe over the 0 to 100 $\mu$H inductances. For the 100 $\mu$m probe the trend is similar as shown in figure 4.11 (a) and (b), although the main peak at 100 $\mu$H is broad so becomes poorly defined. The RF voltages are approximately the same as for the 50 $\mu$m probe between the 0 to 100 $\mu$H inductances. Above 1 L, a maximum of $dI/dV$ is again seen at 2 L before decreasing to a minimum at 4 L. The position of the knee itself is relatively unaffected by increasing RF current as has commonly been reported in the literature [104, 82].

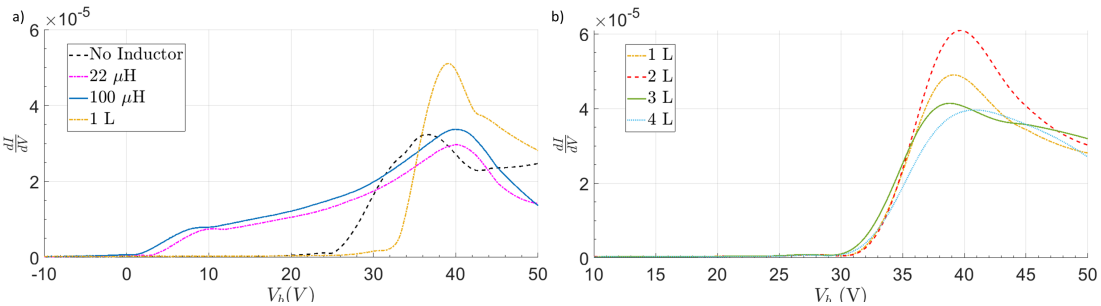


Figure 4.9: First derivative of IV curves (25 $\mu$m diameter probe) as shown in figure 4.6 (10 W RF, 6 Pa Ar). In (a) the inductance varies from 0 to 1 L and in (b) from 1 - 4 L.

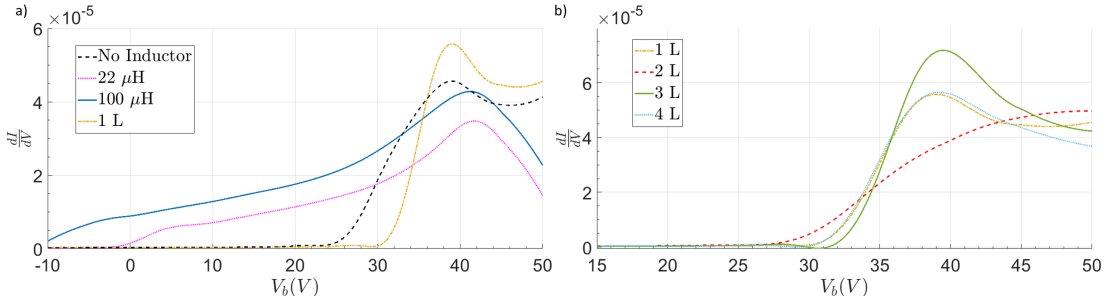


Figure 4.10: First derivative of IV curves (50 $\mu$m diameter probe) as shown in figure 4.7 (10 W RF, 6 Pa Ar). In (a) the inductance varies from 0 to 1 L and in (b) from 1 - 4 L.

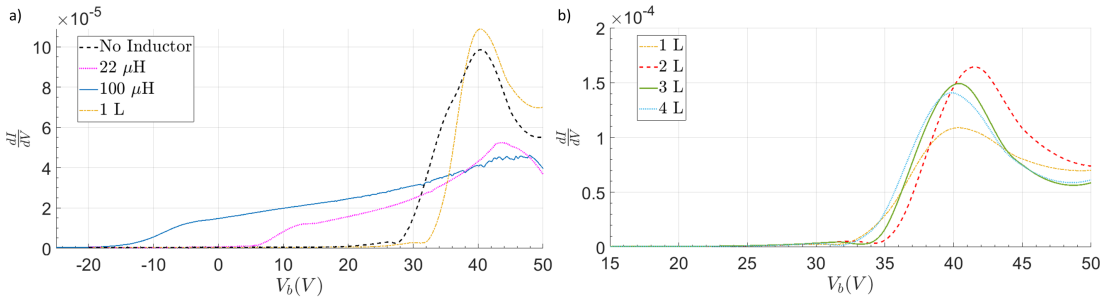


Figure 4.11: First derivative of IV curves (100 $\mu$m diameter probe) as shown in figure 4.8 (10 W RF, 6 Pa Ar). In (a) the inductance varies from 0 to 1 L and in (b) from 1 - 4 L.

The floating potentials are plotted in figure 4.12. All probe sizes show a similar value of $V_f$ with no inductor (about 28 V), before decreasing to a minimum at 100 $\mu$H and then reaching a plateau at around 34 V for all three probe sizes. At 100 $\mu$H the 25 $\mu$m probe has the highest floating potential which suggests the 25 $\mu$m probe has the lowest RF voltage. This is in agreement with the RF voltages as determined from figures 4.9 to 4.11. The trend in $V_f$ is very similar to that of impedance in the LT SPICE model at the fundamental frequency (see figure 4.5) as both reach a minimum at 100 $\mu$H and both reach a plateau over 1 - 4 L. The floating potential is inversely proportional to $V_{RF}$ as shown in equation 4.1 and $V_{RF}$ is inversely proportional to total circuit impedance, shown in equation 4.2. A small maximum in $V_f$ is observed for the 2 L case (25 & 100 $\mu$m) and the 3 L case (50 $\mu$m) which correspond to the maxima in the first derivatives for these probe sizes. The optimum compensation occurs when $V_f$ is greatest, when the peak value of $dI/dV$ is a maximum and when the RF voltage amplitude is smallest. For these experiments, optimum compensation occurs at 2 L for the 25 and 100 $\mu$m probes and 3 L for the 100 $\mu$m probe. The exact impedances and probe sizes will obviously change for different chambers, but an LT SPICE model based on a given system will provide an initial estimate for inductances needed for optimum compensation. By performing

experimental tests with a range of inductances around this estimate, the optimum compensation is found at the maximum value of $V_f$ and the maximum peak value of $dI/dV$. These results also show that, because of a difference in probe sheath impedance, changing the probe size can change the optimum compensation.

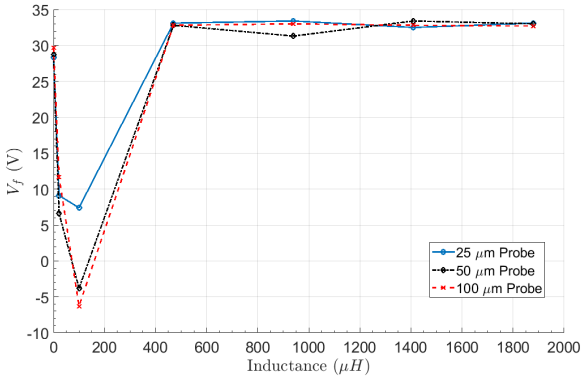


Figure 4.12: Floating potentials measured by the probe sizes used in experiments (25, 50 and 100 $\mu$m, 10 W RF, 6 Pa Ar).

In the literature it has been shown that an increase in RF compensation results in a decrease in the $V_f$ to $V_p$ voltage difference [104]. This steepens the gradient of the IV curves which results in an increase in the maximum of $dI/dV$. This was observed in these experiments implying the circuit impedance increases, although not linearly, with inductance up to 2 - 3 L after which it decreases again. The value of inductance where the $dI/dV$ peak and $V_f$ are greatest and the $V_f$ to $V_p$ difference is at a minimum correspond to the plateau in impedance around 2 - 3 L for 13.56 MHz in the LT SPICE model (figure 4.5). This also suggests that, as expected, the fundamental frequency dominates in experiments as the LT SPICE model predicts a minimum in impedance at 100 $\mu$H for the fundamental. This corresponds to the experimental results which show a maximum in RF voltage for the 100 $\mu$H inductance for all probe sizes.

The corresponding second derivatives are shown in figures 4.13 to 4.15 for each probe size used in experiments. The second derivative of a well compensated probe in a Maxwellian plasma should have a single positive peak followed by a zero crossing point and then a negative peak [88, 111, 107]. The zero crossing point of the second derivative gives the plasma potential if $V_{RF}$ is small. Ideally, the voltage difference from the maximum of the positive peak of the second derivative to the zero crossing point should be less than the electron temperature based on empirical results by Flender [111]. This is true provided there is no RF voltage drop across the sheath. Figure 4.13 (a) shows the second derivatives taken with a 25 $\mu$m probe over inductances ranging from 0 to 1 L. The curve for no inductor shows a broad positive peak and

a smaller negative peak around the zero crossing point (37 V). Hannemann [107] has shown that the voltage difference between the leftmost peak (the shoulder in the first derivative) and $V_p$ (the zero crossing point) is the RF voltage amplitude across the sheath (see figure 4.13). For the zero inductance curve the shoulder in the first derivative corresponds to the peak maximum in the second derivative. This voltage difference ($V_{RF}$) is 7.5 V which is greater than the electron temperature $T_e$ (around 3 eV for this type of discharge). Here $V_p$ is taken from the zero crossing point of the curve with the highest level of compensation (2 L). As a result of increasing the inductance to 22 $\mu$H $V_{RF}$ increases to 31 V due to the shoulder at 7 V. Increasing the inductance to 100 $\mu$H shows a small increase of 3 V in $V_{RF}$. When the inductance is increased to 1 L, there is no discernible shoulder so $V_{RF}$ cannot be measured which implies an increase in compensation.

The second derivative is related to the EEDF as described in section 2.3.1. It is clear from the changing shape of $d^2I/dV^2$ in figure 4.13 (a) that the measured electron temperatures will vary greatly between 0 - 1 L. Because of the flattening and broadening of the peak, the shoulders at lower inductances and the shift in the zero crossing point the entirety of the EEDF will be affected. By contrast, from figure 4.13 (b), the convergence of the curves at more than 8 V below $V_p$ and lack of shoulders means only the lower energy electron measurements would be affected. The actual EEDF should not be markedly changing, as evidenced by the convergence of the ion currents in the IV curves (see figure 4.6), so the changes in the second derivatives should be only because of the level of RF compensation. The trend in $T_e$ will be evident in passively compensated probe measurements taken in any given RF plasma. This means the level of RF compensation of a a passively compensated prove can be investigated by adjusting the inductance and measuring the effect on electron temperature (which will be described later in this section).

For the 50 $\mu$m probe the RF voltage with no inductor has increased to about 10 V. The 22 $\mu$H inductor gives $V_{RF}$ of 37.6 V, which is approximately the same as for the 25 $\mu$m probe. The most significant change is for the 100 $\mu$H inductor where the RF voltage has increased to 42.8 V, about 15 V more than for the 25 $\mu$m probe. In figure 4.14 (b), for the 50 $\mu$m probe, the peak at 2 L has become much broader with both a maximum and a shoulder present, implying two RF voltages of amplitudes 14 V and 4 V respectively. This is consistent with a minimum in $V_f$ (see figure 4.12) and no definable peak in the first derivative (figure 4.10). The 100 $\mu$m probe shows an even larger increase of $V_{RF}$ at this inductance, which increases to 50.1 V, although the

zero and 22 $\mu H$ inductances are similar to the previous probe sizes. The increase in RF voltage for both the 50 and 100 $\mu$m probes may be due to a change in the sheath impedance or a series resonance with the compensation circuit. Because the sheath impedance is in series with the compensation circuit, equation 4.2 implies the sheath impedance has increased with probe size. This in turn suggests there is an optimal probe size to be used with a given probe setup which depends on the probe compensation circuit, rather than simply adjusting the sheath capacitance to minimise the impedance for a given probe. The justification for using a certain probe size is often absent from probe compensation experiments in the literature.

The positive peaks at these inductances are flatter and broader than the curve with no inductor which give a $V_{RF}$ of about 4 V, comparably to $T_e$. A single positive peak is observed at 36 V with a zero crossing point of 39 V ($V_{RF} \leq T_e$). The positive peak amplitude is much greater than for the lower inductances. For 1 - 4 L (see figure 4.13 (b)) a clear maximum in $dI^2/dV^2$ is observed at 2 L before the peak maximum decreases with increasing inductance.

As is the case in the first derivatives, the 50 $\mu$m probe shows a similar trend but with some noticeable differences. The positive peak becomes broader for no inductor while $\Delta V$ increases. In figure 4.14 (b) the peak at 2 L is very broad and flat compared to the 25 $\mu$m which implies a worsening of compensation. For the 100 $\mu$m probe, shown in figure 4.15, the trend is very similar to the 25 $\mu$m probe although the positive peak for the 100 $\mu$H is broad and difficult to distinguish as is the case in the first derivative. All three probe sizes show the peak value of the curve reaching a maximum between 2 - 3 L and then decreasing with inductance which coincides with and increase in $\Delta V$.

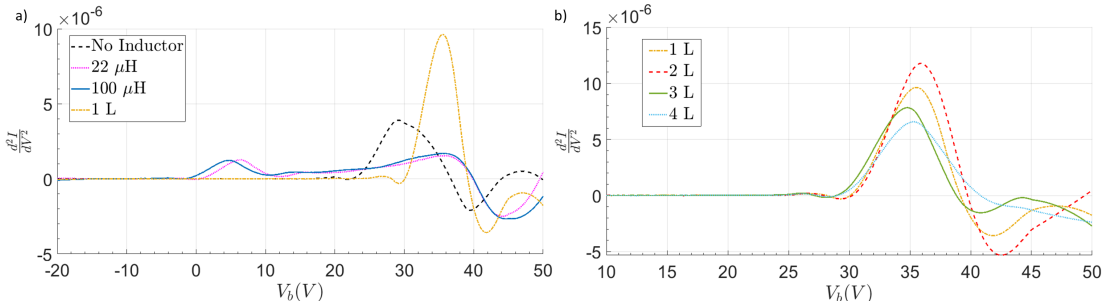


Figure 4.13: Langmuir probe (25 $\mu$m) 2nd derivatives of IV curves. In (a) the inductance varies from 0 to 1 L and in (b) from 1 - 4 L. (10 W RF, 6 Pa Ar)

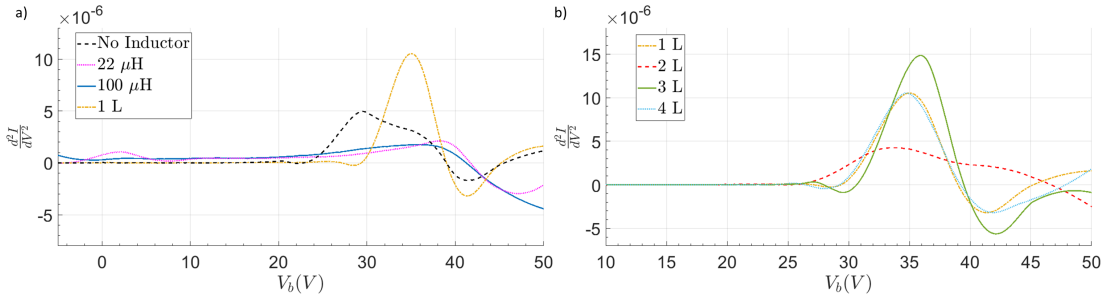


Figure 4.14: Langmuir probe (50 $\mu$m) 2nd derivatives of IV curves. In (a) the inductance varies from 0 to 1 L and in (b) from 1 - 4 L. (10 W RF, 6 Pa Ar)

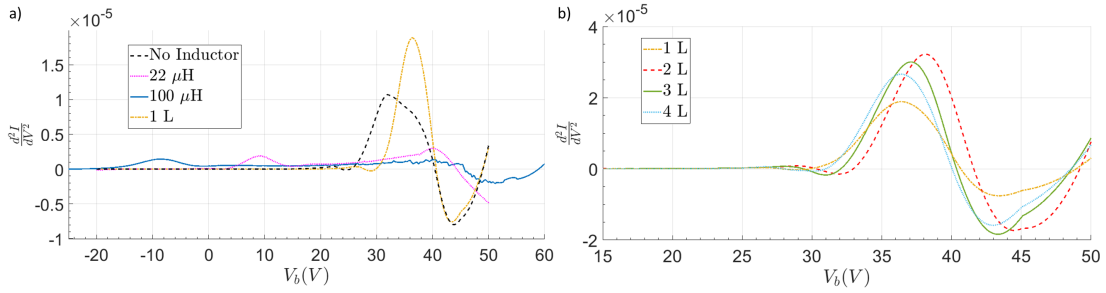


Figure 4.15: Langmuir probe (100 $\mu$m) 2nd derivatives of IV curves. In (a) the inductance varies from 0 to 1 L and in (b) from 1 - 4 L. (10 W RF, 6 Pa Ar)

Figure 4.16 shows $\Delta V$ normalised to the measured $T_e$ for each of the inductances used with the three probe sizes where $\Delta V$ is the difference between the maximum peak value of $d^2I/dV^2$ and the zero crossing point. According to Flender *et. al.* [111] optimum compensation is obtained when the condition $\Delta V \leq T_e$ is satisfied. This means that when $\Delta V$ / $T_e < 1$ for the criterion to be satisfied. It has been shown above that when $V_f$ is not constant (*i.e.* $<$ 1 L) the probe is not compensated (see figure 4.12). In the range 1 - 4 L, the 25 $\mu$m probe consistently increases with inductance up to 4 L. For both the 50 and 100 $\mu$m probe $\Delta V$ decreases over the same range to a minimum at 3 L, after which it increases. The two larger probes therefore reach a minimum in $\Delta V$ at a point which agrees with the maximum input impedance predicted by LT SPICE and by the previous analysis for optimum compensation for these probe sizes. The value of $\Delta V$ does not decrease below $T_e$ for any probe size which is not in agreement with the Flender criterion. The 50 $\mu$m probe shows a maximum in $\Delta V$ at 2 L due to the two RF voltages (14 and 4 V) obtained from the second derivative (figure 4.14). The LT SPICE circuit model does not show any minimum at this point and also does not include the sheath impedance. This could be caused by either a series resonance between the sheath impedance and the compensation circuit's impedance, or an increase in the sheath impedance [111]. In

either case this results in an increase in the RF voltage drop across the sheath. The minimum over the range (1 - 4 L) does not go below one for the any of the probe sizes used so it is possible that the criterion suggested by Flender *et. al.* cannot be used. However, it could also be the case that the inductance range where the criterion applies is more narrow than the inductances used in these experiments.

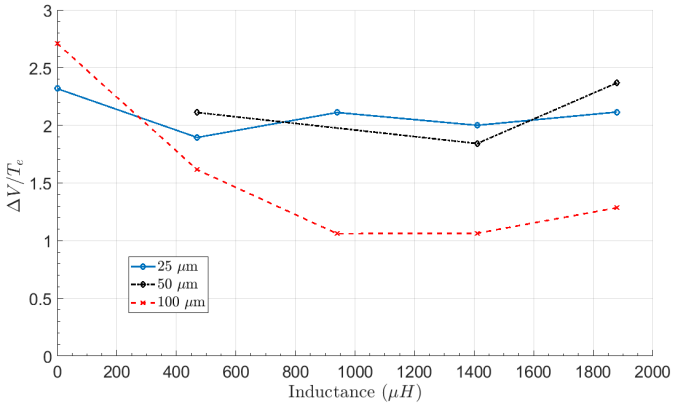


Figure 4.16: Peak to zero crossing point distance (ΔV) of the second derivatives normalised to the measured $T_e$ for each probe size used in experiments. (10 W RF, 6 Pa Ar)

As mentioned in section 2.3.1, the EEDF is related to the second derivative and it has been shown that it changes with inductance. Conventional analysis would therefore suggest the plasma is changing, which is not the case as evidenced from the constant ion currents and high repeatability of IV scans. The dependence of measured EEDF on the level of RF compensation supports observations in the literature [22]. The changes in the IV curves (and therefore the second derivatives) with increasing inductance are consequently due to the RF voltages across the sheath. As shown in figure 4.13 (b) for the 25 $\mu$m probe the differences in the EEDF with increasing inductance become smaller and limited to the low energy region around $V_p$. The same behaviour is observed for the 50 and 100 $\mu$m probes (except 2 L, 50 $\mu$m). This implies there is a correlation between the measured EEDF and RF voltage.

Figures 4.17 to 4.19 show the electron temperature as a function of voltage relative to $V_p$ calculated from the IV curves with the method described in section 2.3.1. The typical electron temperature is expected to be around 3 eV based on previous results in the plasma chamber and measurements from similar low pressure RF discharges [65, 99]. Using the 25 $\mu$m probe as an example (shown in figure 4.17 (a)) with no inductor, a measurement of $T_e$ can only be obtained between - 12 and - 7 V where temperature is nearly constant (3.3 eV). This is because of the RF voltage (4 V from the second derivative) being sufficient to create a gradient between - 7 and 0 V. When a 22 or 100 $\mu$H inductor is added, $T_e$ greatly increases to around 16 eV. As has

been shown in the second derivatives (figure 4.13) $V_{RF}$ is also approximately the same for both of these inductances (30 V). This means a similar level of RF distortion between two IV curves will result in a similar value of $T_e$. For the 1 L case $T_e$ reduces to 1.9 eV, which is lower than for no inductor. The region of near constant $T_e$ for 1 L has increased (relative to no inductor) from 5 V to 8 V. In figure 4.17 (b) there is no appreciable change of $T_e$ ($2.0 \pm 0.1$ eV) between 1 - 3 L so $T_e$ is steady over this range. In the 4 L case a gradient appears below $V_p$ which makes measuring the temperature difficult. This suggests a decrease in the level of RF compensation for the inductors used in these experiments.

The same general trends are observed for the 50 and 100 $\mu$m probes over the range 0 - 4 L as shown in figures 4.18 and 4.19 respectively. However, for the 50 $\mu$m probe with no inductor there is no region of constant $T_e$ to obtain an average value. In addition $T_e$ reaches a maximum of 16 eV (similar to the 25 $\mu$m probe) for the 22 $\mu$H inductor but decreases substantially to 11.1 eV when the 100 $\mu$H inductor is used. This is because the RF voltages are different (see figure 4.14) but there is no correlation between the value of $V_{RF}$ and that of $T_e$ due to the nature of the distortion. In figure 4.18 (b), for the the 50 $\mu$m probe, the 1 - 4 L curves give around 2 eV (similar to the 25 $\mu$m probe) but for the 100 $\mu$m probe (figure 4.19 (b)) this increases to approximately 3 eV. There is an exception for the 2 L case, shown in figure 4.18 (b) for the 50 $\mu$m probe, which does not have a flat region over the entire range of voltage. This is because of the RF distortion visible in the second derivative (see figure 4.14 (b)) which gives $V_{RF}$ values of 4 and 14 V. The temperatures for each probe size and inductance combination are shown in table 4.3. The region over which the electron temperature is measured (the flat region) changes in both position and voltage range with the level of RF distortion (the inductance). There is no relation for the 25 $\mu$m probe (figure 4.17) between the length of the flat region and the inductance but there is a correlation between this region and the inductance for the larger probe sizes. For Maxwellian plasmas, it is expected that the length of the flat region will increase with an increasing level of RF compensation. The 50 $\mu$m probe has the longest region for the 3 L case whereas this occurs at 2 L for the 100 $\mu$m probe. These have previously been shown to have the greatest peak maximum (in the first and second derivative) and minimum $\Delta V$. The RF distortion of the IV curves between 0 - 100 $\mu$H results in erroneous measurements of $T_e$. This is demonstrated by the 22 and 100 $\mu$H inductances giving electron temperatures a factor of 5 - 8 higher than the expected value.

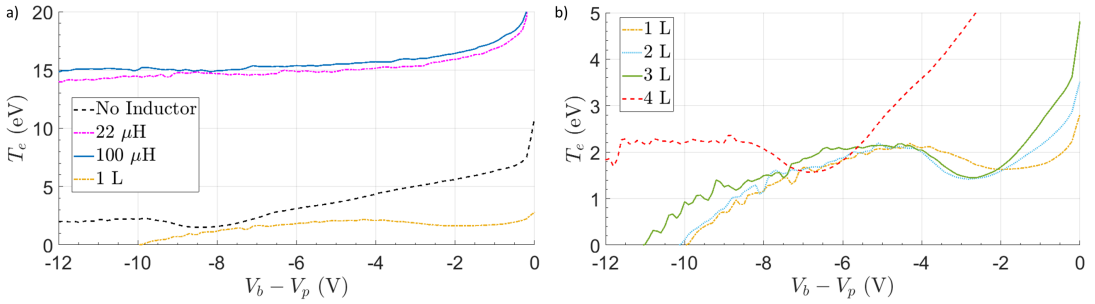


Figure 4.17: Langmuir probe (25 $\mu$m) electron temperatures for increasing inductances (10 W RF, 6 Pa Ar).

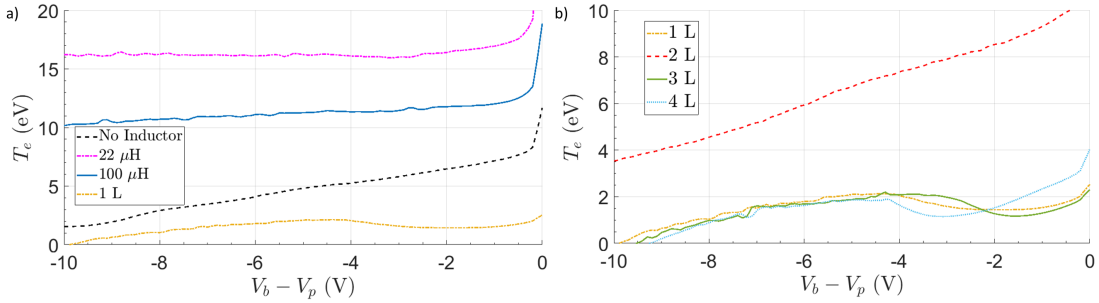


Figure 4.18: Langmuir probe (50 $\mu$m) electron temperatures for increasing inductances (10 W RF, 6 Pa Ar).

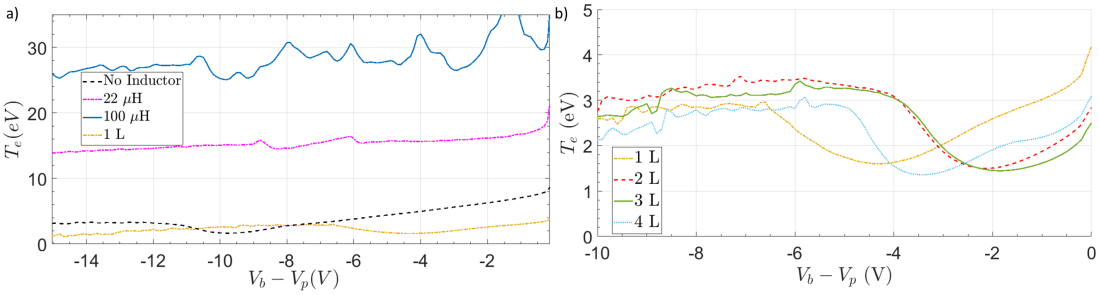


Figure 4.19: Langmuir probe (100 $\mu$m) electron temperatures for increasing inductances (10 W RF, 6 Pa Ar).

The values of $T_e$ and $n_e$ (described below) are shown in table 4.3. In the ideally compensated case, the slope of the semilog plot would be linear over the entire exponential region if the plasma is Maxwellian. The plasma is likely not Maxwellian so it cannot be said that the changes in the size of the linear region is solely related to the level of compensation. However, the value of effective temperature (the average over the linear region) is affected by the level of compensation as shown in figures 4.17 - 4.19 and table 4.3. The electron temperature for the 25 and 100 $\mu$m probes reaches a maximum with 100 $\mu$H before decreasing again to a minimum between 1 - 4 L which matches the trend in $V_{RF}$ measured from the second derivatives. This also

coincides with the inverse in $V_f$ shown in figure 4.12 and the maximum amplitude of $dI/dV$ shown in figures 4.9 to 4.11. The $T_e$ values both show that with no inductor the temperature is approximately a typical value for such a CCP plasma (3 eV) and there is a maximum after a 22 or 100 $\mu$H inductor is added. The trend is similar for the 50 $\mu$m, which is consistent with the trend in the impedance at the fundamental in the LT SPICE model (figure 4.5).

The trends shown in these experiments can be used to provide an extra measure of the level of RF compensation. When testing the compensation of a given system, the value of temperature (and, if the probe size can also be changed, potentially the length of the constant $T_e$ region) can be used as an additional check of sufficient compensation with increasing inductance. In general terms, optimum compensation can be found at the inductance that minimises the measured electron temperature and further increasing the inductance from this value will increase $T_e$. However, the influence of probe size (and thus probe sheath impedance) makes this compensation criterion less robust than those previously described especially when considering the length of the constant $T_e$ region.

Table 4.3: *Electron temperature ($T_e$) and knee electron density ($n_e$) obtained from IV curves for each probe size.*

| Inductance ($\mu$H) | 25 $\mu$m $T_e$ (eV) | 50 $\mu$m $T_e$ (eV) | 100 $\mu$m $T_e$ (eV) | 25 $\mu$m $n_e$ ($\times 10^{15} m^{-3}$) | 50 $\mu$m $n_e$ ($\times 10^{15} m^{-3}$) | 100 $\mu$m $n_e$ ($\times 10^{15} m^{-3}$) |
|---|---|---|---|---|---|---|
| 0 | 3.3 | N/A | 3.1 | 6.9 | 6.5 | 6.1 |
| 22 | 14.9 | 16.1 | 15.1 | 17.0 | 10.7 | 7.66 |
| 100 | 15.5 | 11.1 | 26.9 | 21.6 | 9.0 | 13.6 |
| 1 L | 1.9 | 1.8 | 2.6 | 7.2 | 4.9 | 4.3 |
| 2 L | 1.8 | N/A | 3.3 | 8.5 | 7.1 | 5.9 |
| 3 L | 2.0 | 1.9 | 3.1 | 6.1 | 5.5 | 5.2 |
| 4 L | 2.6 | 1.9 | 2.8 | 8.0 | 4.8 | 4.8 |

Another parameter commonly measured from IV curves is the electron density. The densities measured at the knee of the IV curve is calculated using equation 2.11 with the electron temperatures which are shown in table 4.3. Another common method to calculate the density is by using OML theory as discussed in section 2.3.2. The knee and OML densities at different levels of compensation are compared in figures 4.20 to 4.22.

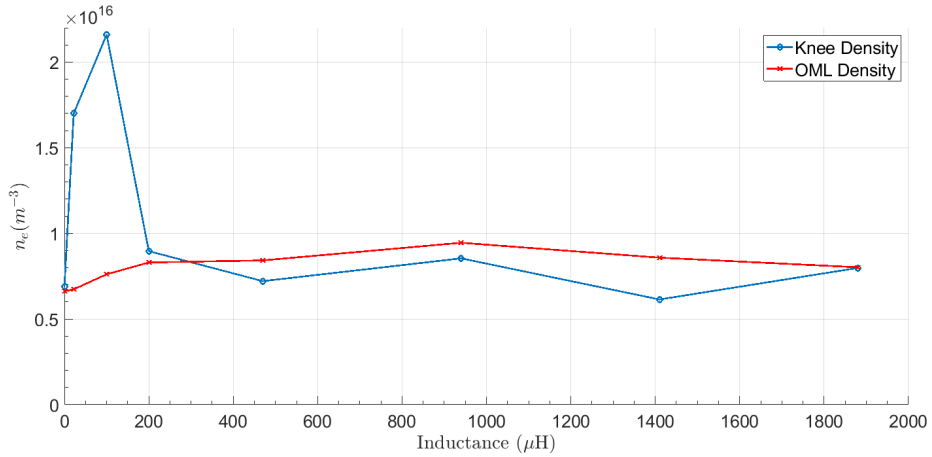


Figure 4.20: Langmuir probe (25 $\mu$m) OML electron density and the value at the knee. (10 W RF, 6 Pa Ar)

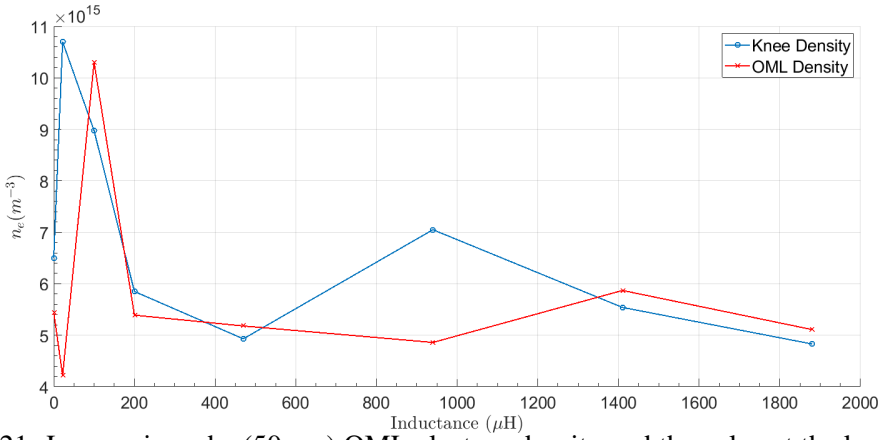


Figure 4.21: Langmuir probe (50 $\mu$m) OML electron density and the value at the knee. (10 W RF, 6 Pa Ar)

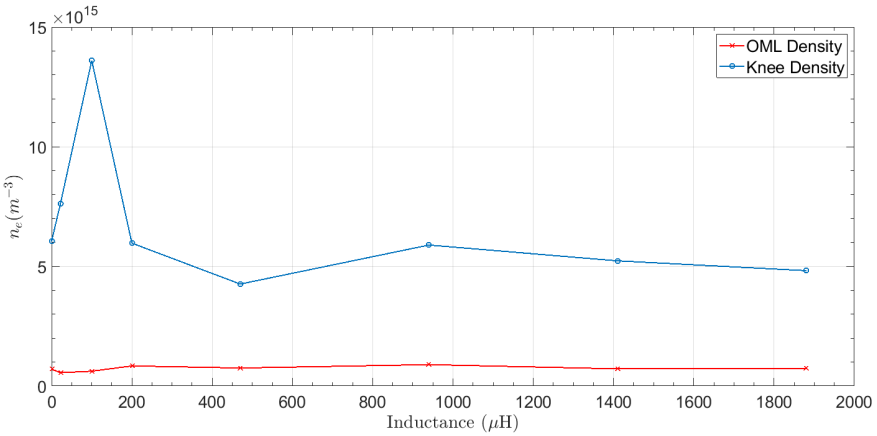


Figure 4.22: Langmuir probe (100 $\mu$m) OML electron density and the value at the knee. (10 W RF, 6 Pa Ar)

For all probe sizes, the knee density has a peak at 22 or 100 $\mu$H inductance before decreasing to approximately the same value as with no inductor ($\pm$ $1.5 \times 10^{15} m^{-3}$). This is caused by the decrease in input impedance for the 22 and 100 $\mu$H inductances (larger RF voltages across

the sheath) which leads to an increase in electron current at the knee as shown in figures 4.6 - 4.8. The density with no inductor, for all probe sizes, is close to the values given in the 1 - 4 L range because the IV curves give a similar electron current at the knee. This occurs as the RF voltage for 1 - 4 L becomes less than $T_e$, whereas for no inductance it is only slightly larger than $T_e$. There is a local maximum in the knee density between 2 - 3 L for all probe sizes. These local maxima (for the 25 and 100 $\mu$H probes) correspond to the maximum in $V_f$ and the peak amplitude of $dI/dV$ and the minimum in $T_e$ and $V_{RF}$ from the second derivatives shown previously. The 50 $\mu$m probe has a peak at 2 L which is caused by an increase in the RF voltage to 14 V and 4 V (see figure 4.14). This is possibly due to a series resonance between the probe sheath and compensation circuit or an increase in the probe sheath impedance. The OML density increases from 0 $\mu$H to a weak maximum at 2 L for the 25 and 100 $\mu$m probes which is in agreement with the knee density. For the 50 $\mu$m probe there is a peak at 100 $\mu$H (due to the large $V_{RF}$, see figure 4.7) and the density reaches a local maximum at 3 L which agrees with the conditions for optimum compensation (maximum $V_f$, $dI/dV$ and minimum $V_{RF}$) defined previously for this probe size. The agreement between the optimum compensation and the local maxima was repeatable for all probe sizes. Although the maxima in the OML are weak, if there were large random errors then the maxima would also be random and this would not be repeatable. Above 1 L, the knee and OML densities agree with each other to within 15 % for the 25 and 50 $\mu$m probes (except for the 2 L, 50 $\mu$m case) but the discrepancy is larger for the 100 $\mu$m probe. The general robustness of the OML density to RF may be due to the RF fluctuations being smoothed out by a least square fit over a voltage range. The knee method only uses a single point which is more sensitive to RF distortion as shown in figures 4.6 - 4.8. The local maxima for all probe sizes above 1 L coincides with the strongest peak in first derivative and the plateau in impedance from the LT SPICE simulations shown in figure 4.5.

The maxima of the measured OML density above a certain minimum inductance could potentially be used as an additional check of whether optimum compensation has been achieved in a given RF probe. To the author's knowledge, this has not been observed in the literature. It is possible that the maximum is stronger than observed here due to the range between the inductances being too large in these experiments. However, for these tests this maximum is both repeatable and coincides with the inductances where the previously described compensation criteria are observed.

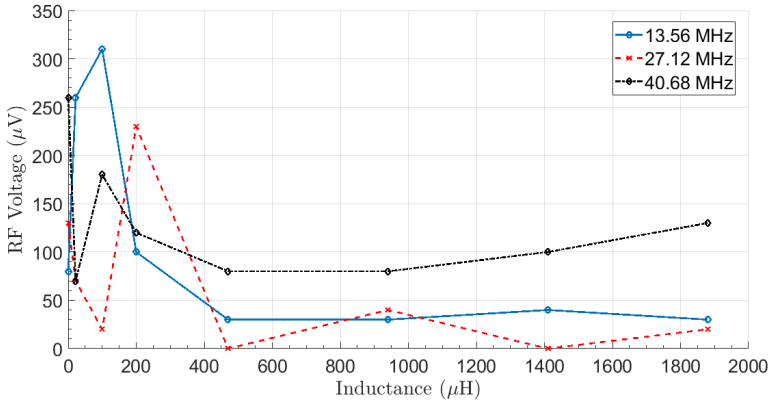


Figure 4.23: RF voltage amplitude of a Langmuir probe (25 $\mu$m diameter) measured with a spectrum analyser (10 W RF, 6 Pa Ar).

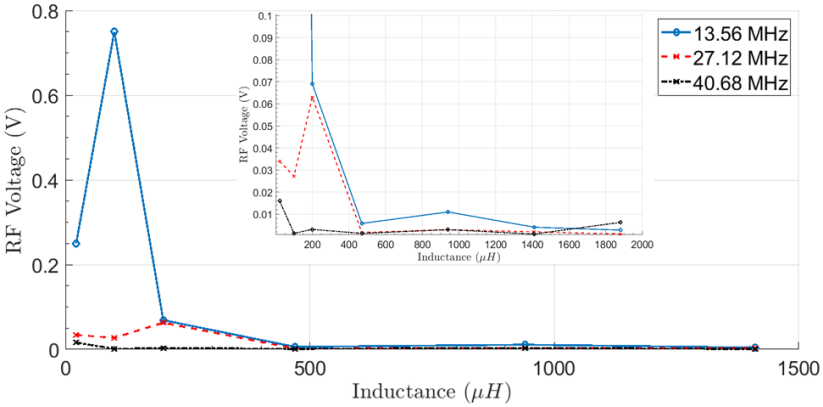


Figure 4.24: RF voltage amplitude of a Langmuir probe (50 $\mu$m diameter) measured with a spectrum analyser (10 W RF, 6 Pa Ar).

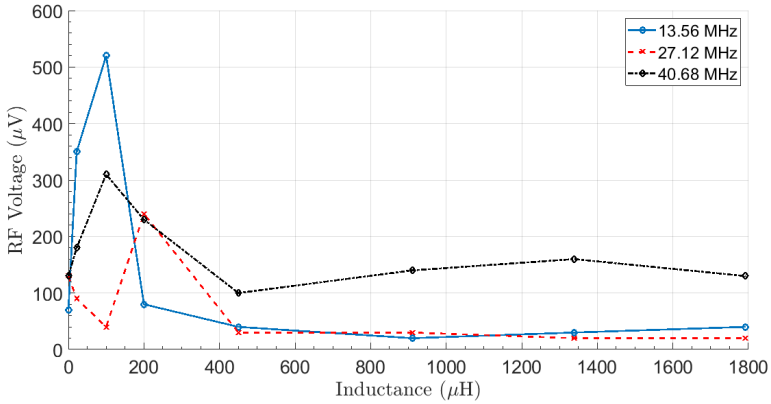


Figure 4.25: RF voltage amplitude of a Langmuir probe (100 $\mu$m diameter) measured with a spectrum analyser (10 W RF, 6 Pa Ar).

Figures 4.23 to 4.25 show the RF voltage measured at the output of the low pass filter (see figure 3.5) for each probe size and inductance combination. This was done by connecting a 1 m long, 50 Ω BNC cable (which was also used to connect the filter output to the Hiden unit) to a spectrum analyser (input impedance 50 Ω) integrated in the oscilloscope. The voltage

output, in dBm, was measured over a frequency range of 0 to 50 MHz and averaged over 128 scans. In the range 0 - 1 L and for 13.56 MHz the figures show that for all probe sizes, a maximum in voltage occurs at 100 $\mu$H. For 27.12 MHz there is a minimum at 100 $\mu$H and then a peak at 200 $\mu$H over the same range. The 40.68 MHz harmonic is less consistent, with maxima observed at 100 $\mu$H only for the 25 and 100 $\mu$m probes. The peak in voltage (and RF current) at 13.56 MHz agrees with the minimum in impedance predicted by the LT SPICE model (see figure 4.5). For 27.12 MHz, both the minimum and maximum in the voltage also agree with the LT SPICE model. The 40.68 MHz harmonic peaks do not coincide with the model. A minimum in impedance, not predicted by the model, occurs at 100 $\mu$H (for the 25 and 100 $\mu$m probes) although this harmonic should have a small effect on IV curves. In the range 1 - 4 L, the voltage for all probe sizes decrease and fluctuate around an average value. There are two exceptions to this: the second harmonic for the 25 $\mu$m probe, which reaches a minimum between 1 - 2 L and then continues to increase, and the fundamental for the 50 $\mu$m probe which reaches a local maximum between 1 - 4 L and then decreases. The latter case has been shown previously using values of $V_f$, $V_{RF}$ and $T_e$ to be poorly compensated which is caused by the increase in RF voltage measured here. For the other cases the peaks in voltage at low inductance coincide with the minimum in impedance for the fundamental predicted by the LT SPICE model (see figure 4.5). Similarly, the smaller and reasonably constant RF voltage between 1 - 4 L corresponds with the region of larger impedance in the model. The lower RF voltage between 1 - 4 L also agrees with the region of greatest $V_f$ (see figure 4.12) and minimum in $\Delta V$ measured from the second derivatives (figure 4.16). The minimum in $T_e$ and a reasonably consistent region in the density are also observed between 1 - 4 L. These comparisons provide experimental evidence to complement the conclusions made previously to determine when a Langmuir probe is optimally compensated. At higher inductances it is the third harmonic which has the largest voltage output for the 25 and 100 $\mu$m probes. This is not in agreement with the LT SPICE model, which predicted a much larger impedance for this harmonic over all inductances. However, the 40.68 MHz frequency is unlikely to have a large effect on RF distortion. For the 50 $\mu$m probe the fundamental is greatest for all inductances. The peak in RF voltage at the fundamental at 100 $\mu$H agrees with the minimum in impedance observed in the LT SPICE model (see figure 4.5) and the local minimum in RF voltage also agrees with the plateau in impedance which occurs in the model between 1 - 4 L. Similarly to the previously described criteria, the inductances and probe sizes used will vary between

experiments but this test provides a simple method to determine optimum compensation by finding the inductance where the impedance of the dominant harmonic is greatest (i.e. the RF voltage is lowest). The 50 $\mu$m probe is an exception to this in these experiments, showing a minimum in the RF voltage for 4 L rather than 3 L which would be expected from the previous results if it is assumed the fundamental is dominant.

### 4.5.2 Effect of Stray Capacitance on IV Characteristics

Due to the radius of the inductors and wire it is expected that stray capacitance will increase if the inductor chain is retracted into the tube as the distance from the inductors to the chamber bottom is around 1.5 cm in the chamber compared to 8 mm in the tube. The plasma also provides screening in the chamber which will further decrease the effect in the chamber. The length of the inductor chain has a direct relationship on the stray capacitance to ground via the stainless steel tube as described by the cylindrical capacitance equation (eqn. 4.6). This effect was tested by taking IV characteristics with the Langmuir probe tip (and the inductors) retracted from the chamber centre by 2 cm in the chamber towards Port B in figure 3.4 and then progressively inserted into the chamber until it is 1 cm displaced beyond the chamber centre. These limits were used because the probe must be moved manually by reaching between the Helmholtz coils, and it is difficult to accurately move the probe deep into the chamber. The plasma conditions are the same as for the inductor experiments (10 W, 6 Pa, Ar) with the 450, 460 and 429 $\mu$H inductors (as measured by the LCR meter, referred to as 3 L in section 4.5.1) and 50 $\mu$m diameter probe.

These characteristics are shown in figure 4.26. The curves clearly show an improvement in compensation when the probe is extended into the chamber based on the criteria previously mentioned, including strong peaks in the first derivative, an absence of shoulders, and a minimum in $T_e$ when the probe is extended. The plasma conditions are constant between scans as evidenced by the constant ion current region. The curves shown in figure 4.26 generally match the behaviour of improving RF compensation shown in figures 4.6 - 4.8. These include a generally decreasing current at $V_p$ for increasing probe extension, increasing $V_f$ with probe extension and a smaller gap between $V_f$ and $V_p$. Over the whole retraction distance the floating potential, $V_f$, increases from 29.0 V to 32.8 V with $V_p$ increasing by 1.5 V as shown in figure 4.27. The behaviour of the peak becoming narrower and larger with increasing compensation seen with the inductors is also observed here with increasing extension. The collected current

at plasma potential also decreases with increasing insertion, 0.23 mA compared to 0.28 mA when it is fully retracted.

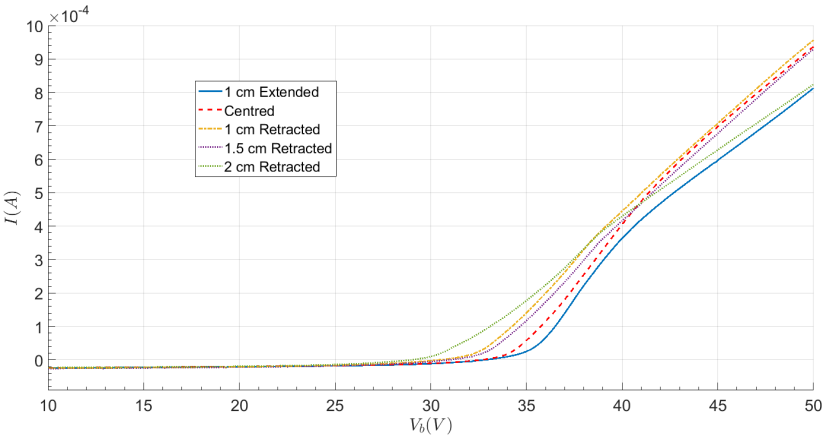


Figure 4.26: Langmuir probe (50 $\mu$m) IV curves with the probe retracted from the chamber centre (10 W RF, 6 Pa Ar)

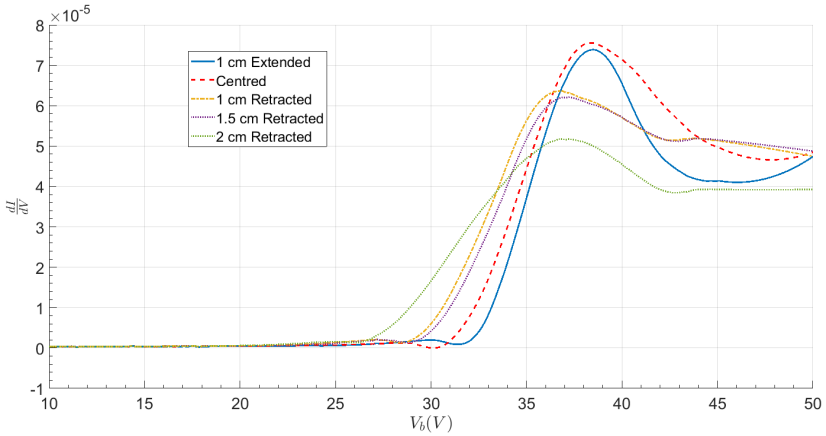


Figure 4.27: Langmuir probe (50 $\mu$m diameter) first derivatives with the probe retracted from the chamber centre (10 W RF, 6 Pa Ar)

As shown in figure 4.28, the narrowest/largest peak in the second derivative with the smallest gap between the maximum and zero crossing point is also coincident with the fully extended case. A similar trend in height/depth of the peaks and narrowness of the distance between the maximum and zero crossing point of the second derivative with retraction as compared to increasing inductance (figures 4.13 to 4.15) is observed. These relationships are similar to those described in section 4.5.1, showing a potential condition for optimum compensation.

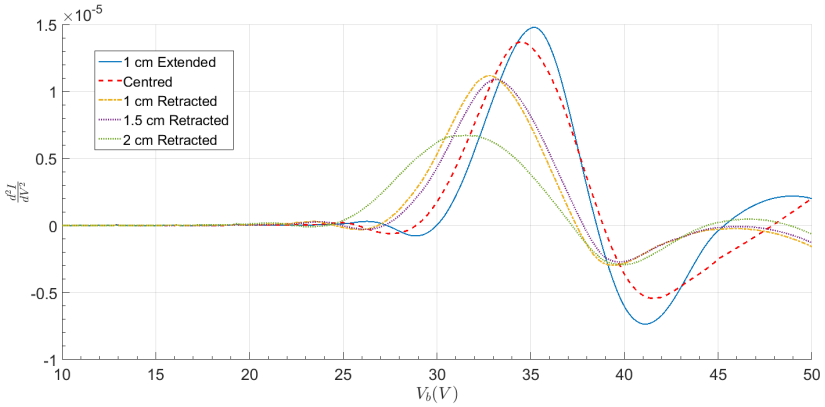


Figure 4.28: Langmuir probe (50 $\mu$m diameter) second derivatives with the probe retracted from the chamber centre (10 W RF, 6 Pa Ar)

The knee and OML densities are plotted against retraction distance in figure 4.29. Negative values indicate the probe retraced into the tube and positive numbers indicate the probe extended into the chamber. The knee densities are not sensitive enough to show any trend, however the OML density slowly decreases with extension into the plasma with the exception of the fully retracted case.

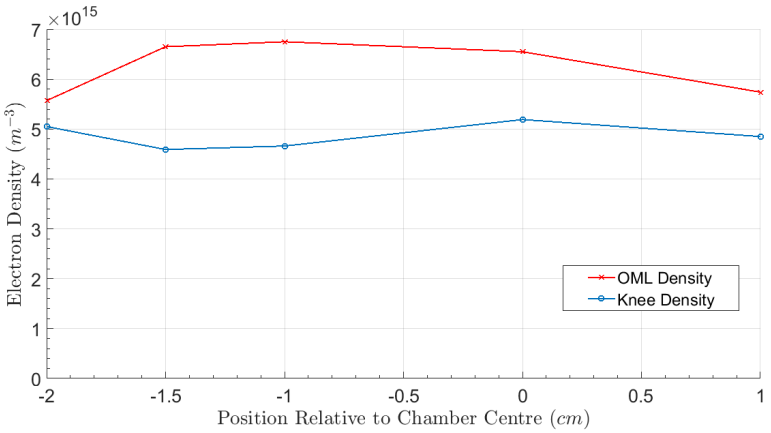


Figure 4.29: Densities measured by the Langmuir probe (50 $\mu$m diameter) with the probe retracted (negative values) and extended (positive values) from the chamber centre (10 W RF, 6 Pa Ar)

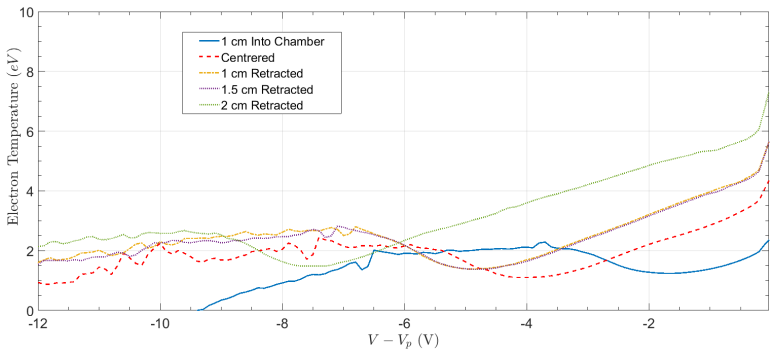


Figure 4.30: Temperatures measured by the Langmuir probe (50 $\mu$m diameter) with the probe retracted from the chamber centre (10 W RF, 6 Pa Ar)

The resulting electron temperature as a function of $V$ - $V_p$ is shown in figure 4.30. The linear region is relatively small, but it can be seen that the linear region denotes a higher temperature with increasing retraction, in a similar manner to a reduction in inductance in figures 4.17 - 4.19. To better demonstrate this a value of $T_e$, an average over the approximately 3 V linear region for each case, is shown in figure 4.31 for each retraction distance. A decrease in $T_e$ is observed with increasing extension of the probe into the plasma, similar to increasing inductance in the experiments in section 4.5.1. This therefore implies a possible connection between probe position in the plasma (and by association stray capacitance) and compensation. This is likely not due to differences in the local plasma because of the converging IV curves in figure 4.26. Additionally, an alternative Optical Imaging Spectroscopy (OIS) diagnostic has shown that the temperature throughout the plasma is reasonably constant (see section 5.5)

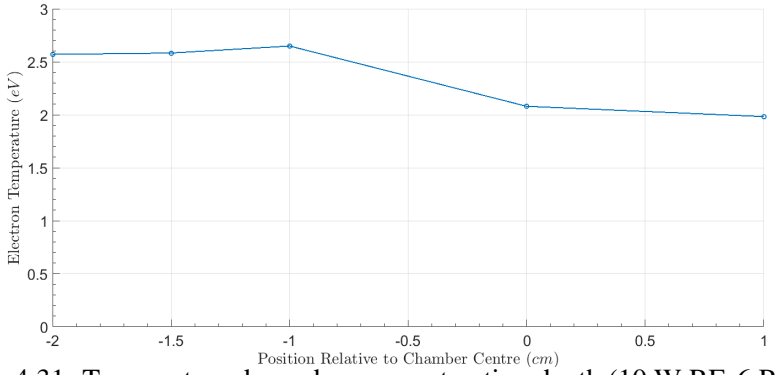


Figure 4.31: Temperature dependence on retraction depth (10 W RF, 6 Pa Ar).

Several conclusions can be drawn from this experiment as to when the probe is optimally compensated. Firstly, as RF oscillations widen the transition region, the floating potential will increase with compensation as reported in the literature. This gap is seen to narrow with extension into the chamber. Secondly, the peak of the first derivative will, for all wire sizes, reach a maximum at the greatest extension into the chamber. Furthermore, at this value of inductance, the difference between the peak and the zero crossing point of the second derivative is a minimum at maximum extension. Finally, electron temperature reaches a minimum at the maximum extension into the chamber. All of these conditions are consistent with the compensation behaviour observed with changing inductances.

Because of the dependence on radius in cylindrical capacitance (equation 4.6), an alternative method to investigate the effect of stray capacitance to ground is to vary the distance between the inductor/wire system and the chamber wall. This was done by replacing the KF 25 stainless steel tube with a KF 40 stainless steel tube on port B in figure 3.4 with a correspondingly larger

adaptor connecting the tube to the chamber. The probe setup is the same as that shown in figure 3.5 except with the KF - 25 and KF - 40 feedthroughs and stainless steel tube sizes being used. This adaptor filed down (to a dimension of 28 $\times$ 34 mm) to maximise the distance between the inductors/wire and the chamber ground. A comparison of IV curves taken in each case is shown in figure 4.32. There is a large reduction in floating potential with the KF 40 tube, and both characteristics were taken in identical conditions (6 Pa, 10 W Ar and with the 450 $\mu$H inductor only), but the ion currents do not converge implying a difference in the plasma.

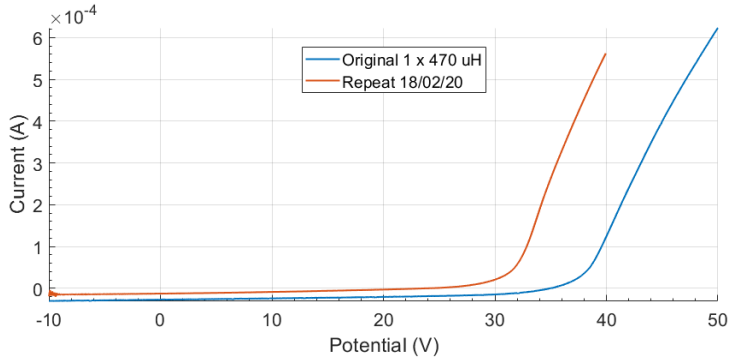


Figure 4.32: IV curves taken with KF-25 (blue) and KF-40 (red) feedthroughs (6 Pa 10 W Ar).

These tests demonstrate the influence of plasma size on the level of compensation. If the plasma is large enough that all inductors are shielded and stray capacitance effects are minimised then the effects shown here are likely to be small. However, in smaller plasmas such as used here, both the stray capacitance of the inductors to ground (the chamber wall) and the order of the inductors (as there will be a variance from the value given by the manufacturer and some inductors will be more shielded) begin to matter. It is therefore important to minimise stray capacitance between the probe and ground as much as possible and to ensure that inductors are shielded to the same extent by the plasma between experiments.

## 4.6 Effect of Compensation Electrode

As mentioned in section 4.2, inductors alone are not usually sufficient to compensate a probe. To further improve the level of RF compensation a compensation electrode (CE) is normally included, along with coupling capacitors, to provide capacitive coupling of the RF signal to the probe tip as shown in figure 4.2 [100, 82]. The CE has a low impedance to RF due to its large surface area. As shown in the figure, the sheath impedance ($Z_2$) is in parallel with the compensation electrode sheath impedance ($Z_3$). From equation 4.2, it can be seen that if

$Z_2 \gg Z_3$ and $Z_1 \gg Z_3$ then $V_0 = V_{RF}$. Consequently the RF voltage is coupled to the probe tip which reduces the voltage across the probe sheath. The coupling capacitor blocks the DC, or slowly varying signal, that is used to acquire the IV curve so the CE does not contribute to the IV curve.

In these experiments a CE was made of either a tungsten wire or a copper rod formed into a loop of various radii (to increase the surface area) centred on the probe tip as shown in figure 4.33 (a) which is commonly used in the literature [82]. Another method, also used in these experiments, consisted of wrapping a thin tungsten wire around the ceramic tube of the probe tip (see figure 4.33 (b)) along its length as used by Sudit and Chen [15].

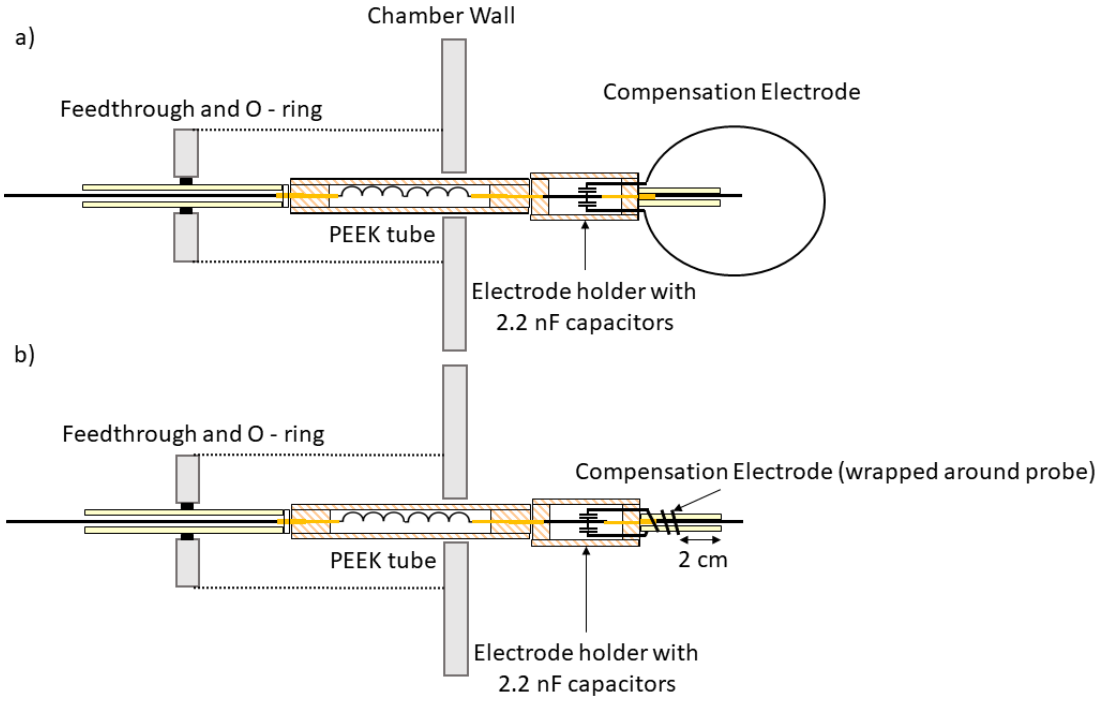


Figure 4.33: Schematic diagrams of the two compensation electrode (CE) geometries used with the modifications made to the Langmuir probe. In (a) the CE is shown as a loop and in (b) the CE wire is wrapped around the ceramic tube of the probe.

The CE in both geometries was soldered to two 2.2 nF ceramic capacitors, one at each end of the CE electrode and were contained in a separate PEEK electrode holder (see figure 4.33). This electrode holder has a diameter of 14 mm, slightly larger than the PEEK tube used to house the inductors, to accommodate the two capacitors. For the loop a 1.6 mm diameter rod (Cu) was used as the CE. In both geometries the CE was made of a 100 $\mu$m diameter wire (W). For the wrapped electrode, a gap of around 5 mm between the windings was used and the electrode stopped at a minimum distance of 2 cm short of the end of the probe. This was done to minimise the perturbation of the measured region around the probe tip. This is shown in (b)

in figure 4.33. The copper electrode could only be made into a loop because of the rigidity of the wire. The Langmuir probe is otherwise identical to that used in the previous section.

The total area of the CE was varied by changing the length of the electrode wire or rod. The electrode area was varied between 5 and 50 times the area of the probe tip (probe radius 25 $\mu$m, 1 cm length for probe area $A_p = 0.157\ cm^2$). Only the 50 $\mu m$ diameter probe was used with the compensation electrode. The CE loop electrode was placed at the same height as the probe tip, otherwise different parts of the electrode could pick up different RF signals. This is shown in figure 4.33 (a). The area of the loop CE was increased by increasing the radius of the tungsten wire or copper rod. For the wrapped CE, the area was increased by lengthening the wire.

IV curves were taken with the wrapped and looped CE electrodes and with 3 L inductors in a 10 W, 6 Pa argon plasma and are shown in figure 4.34. The 3 L case has previously been shown to be the most compensated configuration for this probe size in these experiments. As shown in figure 4.34 the floating potential shifts more negatively with compensation electrode area. The ion and electron currents also increase with area for the same probe bias. The copper CE (with no inductors) has the largest area and shows the most negative $V_f$, the largest ion and electron currents. Although the plasma conditions were the same as for the inductance chain experiments (see figures 4.6 - 4.8) the ion currents do not converge as was previously observed. The increase of ion and electron current with CE area implies the compensation electrode is perturbing the plasma even when a relatively small CE area is used. This was observed in all repeat experiments after checking the wiring of the CE was not causing a short circuit. This is not consistent with increasing compensation seen in previous experiments (figures 4.6 - 4.8).

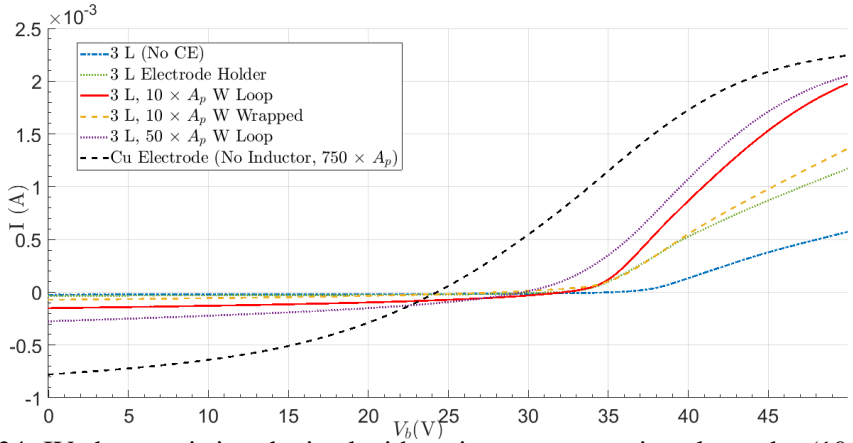


Figure 4.34: IV characteristics obtained with various compensation electrodes (10 W RF, 6 Pa Ar)

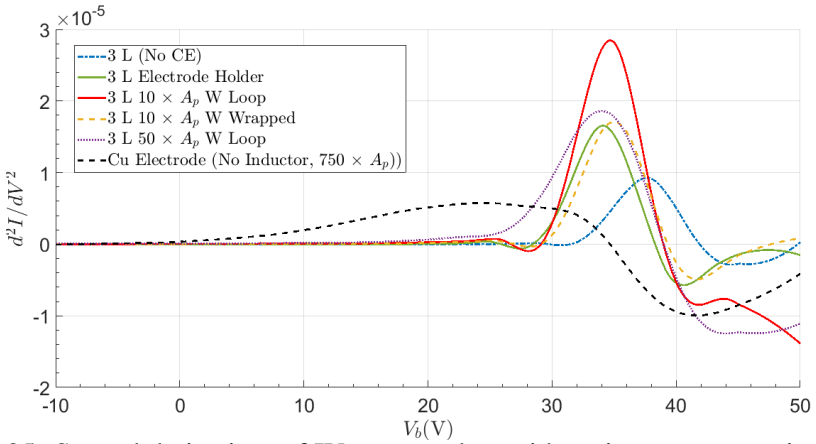


Figure 4.35: Second derivatives of IV curves taken with various compensation electrodes (10 W RF, 6 Pa Ar).

The second derivative curves are shown in figure 4.35. The wrapped and looped tungsten electrodes (with inductors) all agree on the zero crossing point but this point is 2.9 V ($\approx T_e$) below that of the 3 L inductors only. The zero crossing point with the copper electrode (no inductors) shifts most negatively. Based on previous measurements (figures 4.13 - 4.15), it would be expected that the best compensated curve is the one with the largest peak which is the 10 $A_p$ loop. However, the ion and electron current differences and the negative shift in $V_f$ show this is not the case. There is more RF across the probe sheath with the copper CE (no inductors) as shown by the broad peak which is similar to the 22 and 100 $\mu$H curves. No shoulders are seen on any curve for any CE (with inductors). The absence of the shoulders suggests the RF compensation is not significantly worsening as $V_s < T_e$. The results show that the introduction of even a small CE perturbs the plasma (i.e. changes the plasma potential and increases the ion current). This effect increases with CE area except that $V_p$ does not significantly change so the plasma is being perturbed in a different manner.

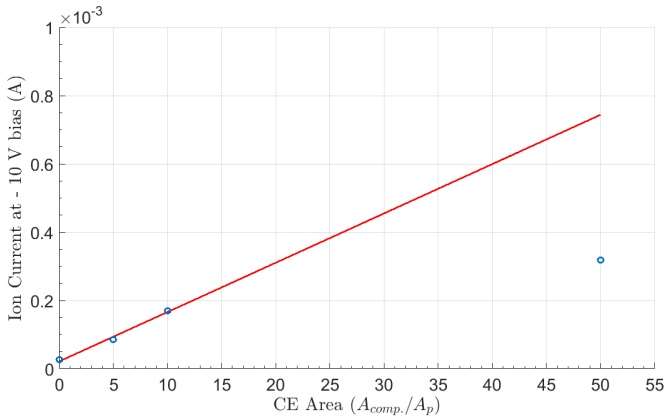


Figure 4.36: The effect of a compensation electrode on measured ion current at an applied bias -10 V (with ion current shown as positive). The relation is linear before a compensation electrode 50 times the probe area is added.

As shown in figure 4.34 the ion and electron currents both increase with larger CE area. In figure 4.36 the dependence of ion current against CE area is shown at -10 V. Initially this relationship is linear with an $R^2$ value of 0.96 between 0 - 10 $A_p$. However, with a larger tungsten compensation electrode of area 50 $A_p$ the ion current deviates from this relationship.

Since $I_i$ is proportional to $n_i$ and $I_i$ linearly increases with CE area then the density must also increase linearly with area. The increase in ion and electron currents is the likely cause of the observed shift in $V_f$ shown in figure 4.34. This is also responsible for the increase in the peak value and area of $d^2I/dV^2$ (i.e. the density from the EEDF). There are no shoulders in the second derivatives (with inductors) which suggests the RF compensation is not worsening ($V_{RF} < T_e$). The increase in electron and ion currents means there is an RF current flowing to ground. Ideally, the drawn RF current should be small compared to the RF discharge current to avoid plasma perturbation. However, in this case the drawn current is small (linear dependence on CE area) but large enough compared to the RF discharge current to cause a perturbation. This suggests the RF impedance of the compensation circuit is not sufficiently high enough for use in the small plasma chamber. When the same current is drawn from a small or large plasma, the perturbation will be greatest in a small plasma as the ratio of drawn to discharge current is greater. Even in a large plasma there is a requirement that the circuit impedance is large enough to not perturb the plasma, as although $V_{RF}$ may be less than $T_e$ (so no shoulders in second derivatives) there may still be distortion of IV curves.

These results are generally in contrast with Annaratone and Braithwaite [82] and Chatterton *et. al.* [100]. Both have reported an increase in floating potential when a compensation electrode was added (and an increase in $V_f$ with CE area up to a maximum value in [100]) while $V_p$ is approximately unchanged. This is not the case in these experiments, including in repeated measurements. However, those papers have an electrode gap either 12 % [100] or 75 % [82] larger than those used in these experiments and the driven and ground electrode diameters used are similarly both considerably larger. The corresponding differences in the plasma size mean that it is possible the CE in the present experiments perturb the plasma. This means that it is important to factor in plasma size when adding a compensation electrode to a passively compensated probe in an RF plasma rather than using a CE area a certain factor larger than the probe as is common in the literature.

## 4.7 Conclusion

Langmuir probe experiments were performed in an RF plasma with the objective of optimising the level of passive RF compensation. This work was motivated by the fact that the importance of compensating probes is well understood, but many papers present a compensation setup without proving the compensation is satisfactory. This was done by measuring the first and second derivatives of IV curves, $V_p$, $V_f$, $n_e$ and $T_e$ and using these values to determine the level of RF compensation. Langmuir probe IV curves where taken in experiments in which the probe input impedance (by means of an inductance chain) was changed and the resulting plasma parameters were measured using conventional analysis techniques. The level of compensation was investigated by increasing the number of inductors, and their inductance, in order to increase circuit input impedance. The parameters were used to determine the level of compensation and compared to the predicted impedance given by an LT SPICE model. This was done because a full description of RF compensation of Langmuir probes, including evidence of compensation, is missing from the literature. However, it has been shown in the literature that optimum compensation is obtained when $V_f$ is shifted most positively (in other words, the largest maximum value in the peak of $dI/dV$ for the same current at $V_p$) [23]. This was also observed in these experimental results in addition to other criteria not mentioned in the literature. The optimum level of compensation was determined using several other factors including the minimum in the measured $T_e$ (and the length of the linear region over which it is measured), the RF voltage output of the filter and the electron knee and OML densities. The optimally compensated probe was found to be the one with the narrowest and largest peak in the first derivative, the smallest gap between the floating and plasma potentials, the lowest measured $T_e$ and had at a local maximum in both the knee and OML density. Additionally there should be no shoulders present in the second derivative, although this alone is not sufficient for accurate results. The experimental data show that optimum compensation was achieved at 2 or 3 L which is in good agreement with the LT SPICE model. The model shows the degree of RF compensation (i.e. the input impedance) is limited by the stray capacitance added by each inductor and the subsequent series or parallel resonance effects. Experiments were performed for several probe sizes which would change the probe sheath impedance which was not taken into account in the model. For the case of a 50 $\mu$m wire in the 2 L case, a severe distortion effect is observed in the IV curves and the derivatives which is possibly due to a series LC series resonance effect between the sheath capacitance and stem inductance which was evidenced an

increase in the measured $T_e$ and $n_e$. This does not occur for the 25 or 100 $\mu$m wire. The inductors and probe sizes used in this thesis are specific to this chamber, but in any typical chamber the impedance will vary with inductance (see the moving peaks in figure 4.4). More generally, these trends will occur for different inductances and probe sizes in different RF chambers (due to changing levels of RF coupling, stray capacitance etc.). However, the patterns observed in this chapter can be used to determine when sufficient RF compensation has been achieved in a given RF plasma chamber by adjusting the level of probe compensation.

Secondly, the effect of stray capacitance to ground was investigated experimentally by both retracting the inductors in the chamber such that the level of shielding by the plasma was reduced and by increasing the inductor or wire to ground distance to increase cylindrical capacitance (see equation 4.6). Stray capacitance to ground in small chambers, where the inductors cannot all be shielded by surrounding plasma, is considered a key factor which is supported by LT SPICE simulations. Experimental evidence for this is provided by the worsening compensation with probe retraction into the tube and improving compensation when the inductors are extended into the plasma chamber. Accurately measuring inductance values and the physical positioning of inductors in passive compensation is therefore of great importance in taking profile measurements with compensated Langmuir probes to ensure stray capacitances are not introduced. In larger chambers than the one used here this may not be an issue if the probe inductors are sufficiently shielded. However, in most small chambers the importance of this effect in passively compensated probes can easily be measured by simply retracting or extending the probe stem into the chamber and taking IV curves.

With the addition of a compensation electrode, capacitively coupled to the probe tip, the level of compensation was expected to increase as has been reported in the literature [15, 100] and the area was increased to investigate the effect on the IV curves. Two different geometries of electrode were used, one made by wrapping the electrode wire around the probe stem and the other made by forming a loop centred on the probe tip. All of these compensation electrodes resulted in distorted IV curves, most prominently in the ion and electron current regions. This implies that for the small plasma used in the experiments any compensation electrode in any geometry would cause plasma loading or offer a low impedance path to ground for the RF signal so the use of a CE may contribute to distortion. This shows that CEs in passively compensated Langmuir probes in similar plasmas must also be carefully checked to ensure that the size and electrode geometry is suitable. Compensation electrodes are commonly used in

the literature, but relatively rarely are they proved to have their areas tuned to achieve sufficient compensation. This means that it is possible for a CE to appear to produce compensated IV curves but give inaccurate parameters when these curves are analysed.

In the literature maximum compensation is most commonly defined as the IV curve being shifted to the most positive voltages (i.e maximum $V_f$) [84, 82]. A general trend of increasing $V_f$ with decreasing RF has been observed in the present experiments. This has been reported in the literature, but the link between increasing inductance and increasing $V_f$ has not been reported in detail. Several other criteria for optimum compensation have been deduced from these experiments that have not been reported in the literature. The main peak of the first derivative reaches a maximum at optimum compensation and then decreases with increasing inductance due to the increased stray capacitance. The difference between the peak and the zero-crossing point of the second derivative is a minimum at optimum compensation. The impedance peak given by the LT SPICE model is generally in good agreement with the best probe compensation in experiments. The OML density may, for smaller probes, reach a local maximum at the level of compensation which agrees with the LT SPICE and the experimental criteria. For the 50 $\mu$m probe the strongest peak in the first derivative of the IV curve is obtained at 3 L. The 25 $\mu$m wire has a peak in the first derivative at 2 L, likely due to a difference in probe sheath impedance. Optimum compensation is achieved at different inductances for different probe wire diameters because of differences in probe sheath impedance (2 L for the 25 and 100 $\mu$m and 3 L for the 50 $\mu$m probe diameters). Compensation then generally decreases for increasing inductance after the optimum compensation due to additional stray capacitance introduced by adding unshielded inductors. Whilst probe sizes, inductors and plasma chambers (and the resulting parasitic capacitances) will change in different experiments, the trends identified here showing when optimum compensation is reached are generally applicable. Consequently, to ensure accurate measurements of plasma parameters it is necessary to prove that the level of RF compensation is sufficient (i.e. that the criteria presented here are satisfied).

# Chapter 5

# Optical Imaging Spectroscopy

## 5.1 Introduction

Optical imaging spectroscopy (OIS) is a non-invasive method of measuring bulk values of $n_e, T_e$ and, assuming quasineutrality holds, $n_i$. A non - invasive technique is needed for measuring the key plasma parameters in magnetised plasmas as emissive probes can only measure $V_p$ [14] and Langmuir probes are unreliable when magnetic fields are present [112] (see section 6.6). Because optical methods are unaffected by RF distortion and magnetic fields they are ideal for use in magnetised RF plasmas. A disadvantage of the OIS method compared to Langmuir probes is that a spectroscopic model is required to obtain plasma parameters. Several methods exist for optical analysis of plasmas including Thomson scattering and laser induced fluorescence (LIF). Thomson scattering is a technique in which the electric field of laser light elastically excites a free electron in a plasma. The scattered spectrum is proportional to the electron velocity distribution which gives a relatively simple, spatially resolved measure of $n_e$ and $T_e$ [113]. However, the scattering signal is generally weak and requires sensitive instruments to measure. The signal becomes even weaker in the sheath, where there are fewer electrons, making the method unsuitable for sheath measurements. LIF is a process by which a laser excites an atom and as the electron de - excites it emits a photon of a characteristic energy. This allows for a local measurement of density with high temporal resolution [114]. A principle disadvantage of this method is the requirement of complex instruments to measure the fluorescent emission.

Atoms, ions or molecules in plasmas become excited upon undergoing one of two main processes. Collisional excitation is caused by the transfer of kinetic energy from a colliding particle (electrons, ions, neutrals) to an orbiting electron. Radiative excitation occurs when a

photon is absorbed by an orbiting electron in the atom or ion. Excitation results in electrons moving to a higher energy level having acquired an energy equal to the difference between the initial ($E_i$) and final ($E_j$) levels. The gap between these levels is given by $\Delta E = E_j - E_i = hc/\lambda$ where $h$ is the Planck constant, $c$ is the speed of light and $\lambda$ is the photon wavelength. When this electron de-excites, which mainly occurs either by collisions (collisional de-excitation) or by spontaneous emission (where the probability is the Einstein coefficient, A) a photon is emitted with an energy corresponding to $\Delta E$. The three main features of a measured emission line that can be analysed are the wavelength (which provides information on the transition and species), the intensity (which is mainly proportional to the density) and the full width at half maximum. The last parameter gives information on particle velocities (Doppler shift), electric field (Stark broadening) and broadening mechanisms (instrument and pressure broadening). Spectroscopic methods (such as the line ratio method) rely on the measurement of emission lines at a number of wavelengths to determine the plasma parameters. Two of the most commonly used models are the Corona model and more complex collisional radiative model [115]. The Corona model describes a plasma which is far from thermodynamic equilibrium and is applicable to many low density laboratory plasmas. The collisional radiative model has a wider range of applicability, but requires solving a rate equation for each level. Due to the low densities used in the chamber in these experiments, the Corona model will be applied here as has been done on previous work with this chamber [65]. Although the theory can be involved, a relatively simple setup is needed which requires suitable diagnostic ports (windows) in the plasma chamber, a light collection system (e.g. optical fibre, lenses), filters or a spectrometer to isolate the desired emission lines, a detection system (e.g. iCCD, photomultiplier tube) and a system for calibration. One key disadvantage of conventional optical emission spectroscopy is that an optical probe or fibre must be scanned across the entire plasma to obtain a ”map” of plasma parameters.

Ion densities and electron temperatures measured by Langmuir probe have been verified by several optical methods including microwave interferometry, (Hopwood *et. al.* [37] and Tuszewski and Tobin [116]), absorption spectroscopy [117] and emission spectroscopy [118, 119]. Hope *et. al.* have used a ratio of line intensities (480.6 nm and 750.3 nm) to measure the temperature of an RF argon plasma with pressure increasing from 5 to 100 mTorr. The optical system was not absolutely calibrated, so the spectroscopy results were normalised to the value given by a Langmuir probe at 20 mTorr. The two techniques were found to give the same trend above 10 mTorr with the spectroscopic system giving a temperature consistently about 1 eV

higher than the Langmuir probe.

The work of Desai *et. al*, which is a development of the work of Hope *et. al.* [120], measured values of electron temperature using an absolutely calibrated optical emission spectroscopy and in both a DC hollow cathode glow discharge and an RF plasma. These values were compared to Langmuir probe parameters and good agreement was found, similar in value to the Hope paper (around 1 eV) but the Langmuir probe generally gave a higher value. This was done in an unmagnetised argon plasma at pressures between 0.005 and 0.1 mBar and RF power between 10 and 70 W. As in the paper by Hope *et. al.*, The ratio of emitted line intensities of ionic and atomic transitions was used to determine $T_e$. The temperature was found to decrease with an increase in pressure for DC plasmas because of the decreasing mean free path.

Optical fibres have been used to obtain spatial resolved measurements of $n_e$ and $T_e$ in low temperature plasmas [121, 65]. The optical probe method reduces the effect of line averaging which is prevalent in conventional emission spectroscopy. This technique requires a scan of a probe within a plasma, so the high spatial resolution comes at the cost of temporal resolution. Because of the drawbacks of these techniques, an optical imaging spectroscopy (OIS) system has been developed based on previous research which combines OES and multi-spectral methods (which involve taking photos of a plasma at different specific wavelengths).

In this chapter an optical imaging system will be described which is based on a method developed by a previous post doctorate researcher. The theoretical background of the OIS method including the corona model is described in section 5.2. The camera setup and calibration method are described in sections 5.4 & 5.3. Experimental results of electron density and temperature in unmagnetised and magnetised plasmas are presented in sections 5.5 and 5.6 respectively. A summary and conclusions are given in section 5.7.

## 5.2 Corona Model

The Corona model has commonly been used in both DC [120] and RF plasmas [118] with similar electron densities and temperatures to those in these experiments. A review of the Corona model is given by Fantz [122]. The most important population processes are electron impact excitation (and de-excitation), spontaneous emission, radiative recombination and three body recombination. It is assumed in the Corona model that the density is low enough that

electron impact de-excitation is negligible compared to spontaneous emission [122]. As a free electron or photon collides with a bound electron in the ground state, there is a probability that the bound electron will absorb energy and be excited into a higher level, j. As this occurs throughout the plasma volume, there will be a population of electrons per unit volume in level j. These electrons will then be spontaneously de-excited into a lower level i and release a photon of a characteristic wavelength. Similarly, electrons may become excited by absorbing a photon of that characteristic wavelength. The intensity (power per unit area), $\phi_{ij}^n$ of a transition is given by:

$$\phi_{ij}^n = \frac{C(\lambda^n)\Omega(d)}{4\pi} \int_0^B n_j^n A_{ij}^n \Delta E_{ij}^n dx \tag{5.1}$$

Here, $A_{ij}^n$ is the Einstein transition probability which gives the probability of spontaneous de-excitation from $j$ into a lower level $i$. The photon energy is given by $\Delta E^n$, $C(\lambda^n)$ is the wavelength correction factor, $\Omega(d)$ is the distance correction factor and $n_j^n$ is the density of particles in the excited state. The $1/4\pi$ factor converts emission over a sphere into a solid angle. The superscript $n$ refers to neutral species. In equation 5.1 the energy emitted per unit volume ($n_j^n A_{ij}^n \Delta E^n$) is integrated over a length of plasma, B (which is assumed to be $\ll$ d). This equation assumes an optically thin plasma (i.e. emitted photons are not reabsorbed) so the radiation density is negligible [122].

The steady state Corona model assumes a constant population of electrons in level $j$ as well as no population contributions due to cascading into level $j$. This occurs when there is a balance of excitation rate and decay rate into and out of level $j$. The direct cross section is therefore equal to the apparent cross section. This equilibrium is given by equation 5.2.

$$n_j^n A_{i<j} = n_0 n_e(x) X_{exc}(T_e) \tag{5.2}$$

where

$$A_{i<j} = \Sigma_i A_{ij}^n \tag{5.3}$$

Here, $A_{i<j}$ is the sum of Einstein transition probabilities ($A_{ij}^n$) which gives the total probability of spontaneous de-excitation from j into all lower levels i $<$ j. The density of atoms in the ground state is given by $n_0$ and the excitation function, $X_{exc}$, is defined as:

$$X_{exc}(T_e) = \int_{E_{th}}^{\inf} \sigma(E)(2E/m_e)^{1/2} f(E) dE \tag{5.4}$$

Here, $\sigma(E)$ is the direct cross section of the electron transition, $E$ is the electron energy, $f(E)$ is the electron energy distribution function and the other symbols have their usual meanings. The lower integration limit, $E_{th}$, is the threshold energy of the transition. Equation 5.2 assumes no other contributions to the electron transitions into level $j$. These can be due to cascades from energy levels above $j$, collisional excitations from lower levels (other than the ground state) or radiative absorption of photons. By substituting equation 5.1, equation 5.2 can be rewritten as:

$$\phi_{ij}^{n} = \frac{C(\lambda^{n})\Omega(d)}{4\pi} \int_{0}^{B} \frac{n_0 n_e(x) X_{exc}(T_e) A_{ij}^{n} \Delta E_{ij}^{n}}{A_{i<j}^{n}} dx \tag{5.5}$$

Here $R_A = A_{ij} \,/\, A_{i<j}$ is known as the branching ratio and describes the probability of one transition occurring relative to all possible transitions. By assuming the EEDF and the electron density are constant over the plasma volume, equation 5.5 simplifies to:

$$\phi_{ij}^{n} = \frac{C(\lambda^{n})\Omega(d) n_0 n_e X_{exc}(T_e) R_A \Delta E_{ij}^{n} B}{4\pi} \tag{5.6}$$

Equation 5.6 allows the density to be calculated if a calibration is performed to measure $C(\lambda)$ and $\Omega(d)$. The neutral density can be obtained from pressure measurements (and using the ideal gas law, equation 2.2), $\Delta E_{ij}$ and $\sigma(E)$ can be obtained from a spectroscopic database (e.g. NIST) or from cross section data. It is assumed that B is the diameter of the powered electrode since most of the emission (plasma bulk) is located above the powered electrode. It is also assumed the EEDF is Maxwellian. Although the EEDF is likely to be non-Maxwellian in magnetised plasmas it could not be easily and reliably measured in these experiments.

The intensity of a single emitted wavelength (that is, the intensity of one transition) cannot be used to give the electron temperature or density (unless $T_e$ is already known) as the intensity depends on both of these parameters. This can be overcome by taking the ratio of two emission lines (line ratio method) from different excited states. This method typically uses emission lines from a neutral and ion species as $\Delta E$ between these is usually on the order of $T_e$ [123]. The above equations can also be used to determine excitation in an ion by replacing $n_0$ with $n_i$. This is important as the intensity from the neutral line, initially in the ground state and excited to level $j$, is a one - step process (equation 5.6). However, there are two possible processes which can occur with ion excitation. The first process is an electron in the ground state of a neutral

atom which ionises and excites to level $j$ in one collision (single step process). The second process involves the atom ionising first (into the ion ground state) and separately exciting into level $j$ (the two step process). The intensity of the single step process from level $j$ is given by:

$$\phi^i_{ij,1} = \frac{C(\lambda^i)\Omega(d)n_0 n_e X^i_{1,exc}(T_e)R^i_A \Delta E^i B}{4\pi} \tag{5.7}$$

The two step process is given by:

$$\phi^i_{ij,2} = \frac{C(\lambda^i)\Omega(d)n_i n_e X^i_{2,exc}(T_e)R^i_A \Delta E^i B}{4\pi} \tag{5.8}$$

Where $n_i$ is the ion density. By taking the sum of equations 5.7 and 5.8:

$$\phi^i_{ij,1} + \phi^i_{ij,2} = \frac{C(\lambda^i)\Omega(d)n_0 n_e R^i_A \Delta E^i B}{4\pi}(X^i_{1,exc}(T_e) + \frac{n_i}{n_0}X^i_{2,exc}(T_e)) \tag{5.9}$$

And divide the intensities of the neutral line by the ion line:

$$\frac{\phi_{ij}}{\phi^i_{ij,1} + \phi^i_{ij,2}} = \frac{C(\lambda^n)R_A \Delta E}{C(\lambda^i)R^i_A \Delta E^i}\frac{X_{exc}(T_e)}{(X^i_{1,exc}(T_e) + \frac{n_i}{n_0}X^i_{2,exc}(T_e))} \tag{5.10}$$

Here $n_i$ / $n_0$ is the ionisation fraction. The resulting ratio of these intensities (equation 5.10), depends on the temperature and the ionisation fraction. It is assumed that $n_e = n_i$ by quasineutrality which leaves $T_e$ and $n_i$ / $n_0$ as the only unknown variables in the equation. There are several possible methods to obtain $n_i$ / $n_0$, the simplest of which is to use the ideal gas law if the pressure is known accurately and if $n_i \ll n_0$ as is expected in these experiments.

A test was performed to investigate the importance of single and two step processes by varying the ionisation fraction in equation 5.10. The equation was then solved for $T_e$, at several ionisation fractions, with the (theoretical) 750 nm / 488 nm line ratios varying between 0 - 10,000. The results are shown in figure 5.1 with increasing ionisation fraction and shows that for all ionisation fractions the line ratio decreases with increasing temperature. The figure shows that when $n_i$ / $n_0 < 10^{-5}$ the curves begin to converge and the single step process dominates. When the ionisation fraction is increased above $10^{-5}$ the curve shifts to the left. Depending on the pressure and power, the typical experimental line ratios are on the order of 7000 with $T_e \approx 2$ eV (from Langmuir probe measurements). The figure shows that for these conditions, the ionisation fraction is expected to be about $10^{-4}$. Using Langmuir probe measurements for the plasma density ($n_i \approx 1 \times 10^{15}\ m^{-3}$) and the ideal gas law (equation 2.2)

for the neutral density (6 Pa, 293 K, $n_0 \approx 1 \times 10^{19}\ m^{-3}$) the ionisation fraction is around $10^{-4}$. This shows that both the single and two step excitation processes are important. However, it is important that the ionisation fraction is estimated accurately for each given experimental condition as there is an uncertainty in obtaining $T_e$ from the line ratio using this estimation.

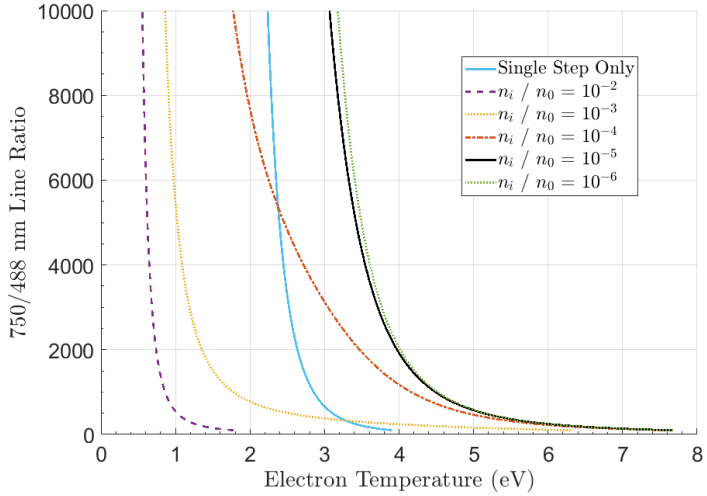


Figure 5.1: Dependence of line ratios from equation 5.10 on electron temperature at several ionisation fractions.

## 5.3 Practical Considerations of Emission Lines

The choice of emission lines depends on several factors such as intensity of emission, the contribution of long lived metastables or cascades to the state, and the process of excitation for certain states [123]. In addition, the emission lines must have a sufficiently large wavelength gap between them. The visible range is commonly used for emission spectroscopy because of the prevalence of transition wavelengths in argon, the transparency of air to the spectrum and the prevalence of detectors available [122]. For experiments in this chapter, the 488 nm ($3s^2 3p^4 (^3P) 4p - 3s^2 3p^4 (^3P) 4s$) ion and 750 nm ($3s^2 3p^5 (^2P^0_{1/2}) 4p - 3s^2 3p^5 (^2P^0_{1/2}) 4s$) neutral transitions [123, 124] were used. These were chosen because of the high intensity of these lines, small contribution due to metastable states and small cascade cross sections. The 750 nm line in particular has a relatively large cross section excitation cross section for transitions from the ground state ($\approx 10^{-17} cm^{-2}$) [123] so the Corona model can be used. The energies of transitions of noble gases commonly used in plasmas are given in the NIST database [124].

The Corona model is commonly used for low temperature plasmas where the McWhirter criterion is satisfied. The criterion is used to determine whether collisional or radiative pro-

cesses dominate in a plasma [125]. The McWhirter criterion was derived for homogeneous and stationary plasmas [126] which is a reasonable approximation in unmagnetised experiments in this work. The criterion assumes hydrogen - like species which is not the case in the argon plasma used in these experiments but is nevertheless a reasonable approximation. The criterion is given by $n_e(m^{-3}) < 1.6 \times 10^{18}\sqrt{T_e}(E_j - E_i)^3$ where $(E_j - E_i)$ is the energy gap between the levels [126]. This energy gap for the 750 nm transition is 1.65 eV [127] and with electron temperatures of around 2.5 eV (as measured by the RF compensated Langmuir probe, see chapter 4) means density must not exceed $1.14 \times 10^{18} m^{-3}$. The density measured by the Langmuir probe is $\approx 10^{15} m^{-3}$ so the criterion is easily satisfied.

The various types of cross section are discussed by Boffard [123]. The relevant cross sections are the direct cross section, the optical emission cross section, the cascade cross section and the apparent cross section. The direct cross section relates to electron excitation populating a a specific (higher) state. The optical emission cross section describes the number of photons emitted by a specific decay from a level (e.g. j to i). The apparent cross section is the sum of all optical emission cross sections decaying out of a level. The cascade cross section is related to the probability of electrons decaying into a level from all higher energy levels.

The measurement of electron density and temperature by optical methods requires the cross sections of the relevant optical transitions to be known precisely. The cross sections of the chosen transitions can be obtained by measuring the florescence from the decay between energy levels [128]. Alternatively, the energy loss of an electron incident on the atom or ion can be measured and the energy difference corresponds to the difference in energy levels. This is because the electron excites the target by collisional excitation [129]. The exact transitions used for argon can be selected from a number of lines in the range of 350 - 1100 nm. The electron temperature can be measured from the ratio of two emission lines given by equation 5.10 if the ionisation fraction is known. Determination of the electron density is more difficult, and requires absolute calibration of the diagnostic system which is described in section 5.4.1. The optical emission cross sections of the 488 (both single and two step) and 750 nm transitions as a function of energy have been measured by several authors and their results are used here, shown in figures 5.2 [130, 131] and 5.3 [132]. One issue that is clear from the figures is that the range of energies is different. The two step process is limited to 35 eV, but this will not be a significant problem as the single step process dominates above 35 eV.

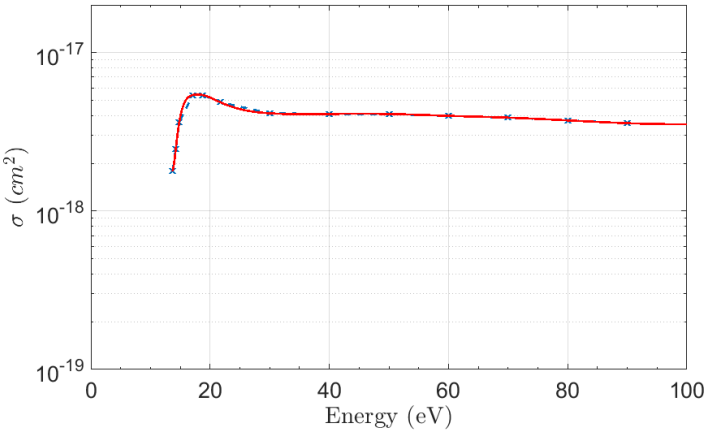


Figure 5.2: Cross section of single step 750 nm transition and fit used in calculations [123].

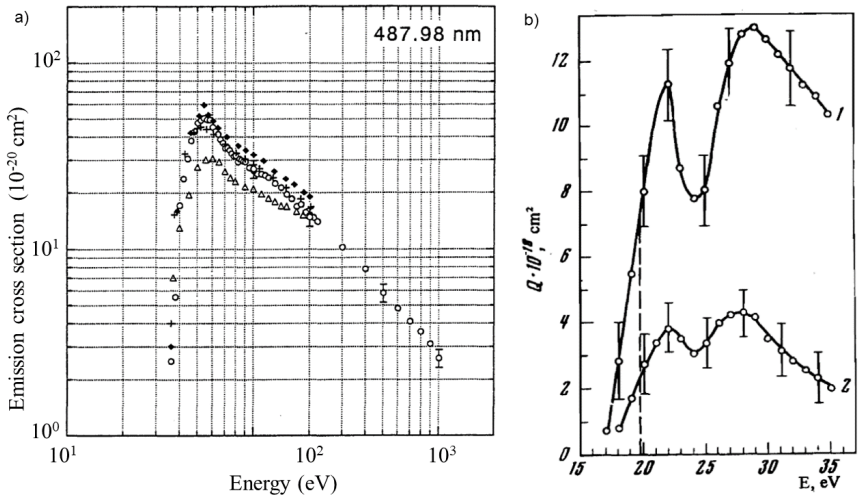


Figure 5.3: Cross section of single step (a) and two step (b) 488 nm transitions measured by Tsurubuchi and an average (open circles) [131] of measurements with previous authors. The two step cross sections are shown in (b) from Zapesochnyi *et. al.* [132]

## 5.4 Optical Imaging Setup

### 5.4.1 Absolute OIS calibration

The calibration of the system can be done in one of two ways. A relative intensity calibration only provides information about the relative spectroscopic sensitivity with wavelength. This allows a measurement of the electron temperature. However, an absolute calibration provides a conversion between the measured signal in counts to power which is necessary to measure density (and temperature). Absolute calibration requires a light source with a known radiance which was provided by a 1 kW NIST - traceable tungsten lamp (Newport traceable quartz tungsten halogen QTH ribbon lamp model 63350).

To calibrate the system, and measure $C(\lambda^i)$ in equation 5.6, a camera (with macro lens and 488 nm or 750 nm filter) and the lamp were placed on an optical rail secured to an optical table. The front of the filter was positioned 50 cm from the centre of the tungsten lamp filament. A black acrylic baffle with a square 1 $cm^2$ hole in the centre is push - fitted into the filter holder. The camera and lamp were both mounted on aluminium plates (secured to carriers) to ensure that the camera image is centred on the lamp filament. The camera was focussed manually onto the lamp while it was off. In order to minimise reflections black card was used to cover all surrounding surfaces including the optical table and nearby walls. A 1 $m^2$ screen placed 50 cm behind the lamp was also covered in black card. The camera was cooled to -30 °C using the Andor software and camera fan. In a darkened environment the power to the filament is slowly increased to 1 kW using the filament power supply. The exposure time is then adjusted using the Andor software to the minimum (1 ns) with no gain to the signal and images are recorded with increasing exposure time ($\tau_c$) until a signal of approximately 20,000 counts was obtained for each filter. This was achieved at around 1 $\mu$s for the 488 nm filter and 50 $\mu$s for the 750 nm filter. A background image was also taken with the lamp off for each filter which was subtracted from the calibration image. The total counts over an area encompassing the filament is found using the Andor software. The irradiance at the two filter wavelengths (at 1 kW and 50 cm distance) is given by:

$$L(mW/m^2nm) = \lambda^{-5} exp(A + B/\lambda)(C + D/\lambda + E/\lambda^2 + F/\lambda^3 + G/\lambda^4) \qquad (5.11)$$

Where A = 44.535, B = -4638.355, C = 0.833, D = 382.083, E = -264257.843, F = 66537590.739, G = -6646282298.334. These numbers are taken from the calibration data provided by NIST. To take the bandwidth of the filters into account, equation 5.11 was plotted over the transmission range of the filter. This was found to be linear (750 nm: $R^2 = 0.9996$, 488 nm: $R^2 = 0.9998$) with relatively small uncertainties over the transmission range for both filters. A simple integration over the FWHM was used to obtain the intensity (power per unit area). This method was found to give almost exactly the same intensity as multiplying the centre wavelength by the FWHM. This intensity was multiplied by the area of the baffle (1 $cm^2$) to obtain the total radiated power. This was then divided by the total counts (in the area surrounding the filament) to calculate the total radiated power per count, C($\lambda$). This gives values of C($\lambda$) = 5.6819 $\times$ $10^{-3}$ mW / count for the 488 nm filter and 1.9245 $\times$ $10^{-2}$ mW / count for the 750 nm filters.

In order to convert a plasma image to a form that can be used in equation 5.10, a number of other correction factors must be applied to it as well. One of these is the transmission factor of the quartz window ($\gamma$). This has been determined to be $\gamma = 0.935$ by a previous post - doctorate researcher using data provided by the manufacturer. Plasma images were taken at different exposure times so an additional calibration factor is introduced in the form of $\tau_c / \tau_m$ where $\tau_m$ is the plasma exposure time and $\tau_c$ is the camera calibration exposure time.

The filter correction factor has, prior to the author's work, been measured for each filter at several plasma pressures and powers by the same post - doctorate researcher. This factor accounts for the presence of intensity peaks at wavelengths other than the desired one which are transmitted by the filters. A Gaussian fit to the desired peak was made to obtain the total number of counts under the curve. This was then divided by the total number of counts over the FWHM range of the filter to obtain the correction factor, F. The filter correction factors used here were 0.5 (750 nm) and 0.2 (488 nm). These are reasonably constant over the range of pressures and powers used in experiments. These correction factors are combined to obtain a corrected intensity using equation 5.12. This equation is performed for each pixel in the image.

$$\phi = I' C'(\lambda) \gamma F \frac{\tau_c}{\tau_m} \tag{5.12}$$

Where $I'$ is the measured pixel intensity of the image. The factor $\Omega(d)$ in equation 5.10 accounts for the effective solid angle, subtended by the area of the macro lens, of the extended plasma source. The solid angle factor is not important when measuring temperature as the factors cancel (see equation 5.10). However, the factor is important when measuring density (see equation 5.9). This is difficult to calculate for two main reasons. Firstly, the diffuse plasma edges (sheaths) means the edges of the emission volume are not well defined. Secondly, the emissivity as a function of position within the plasma is not known and may also change with magnetic field, pressure and power. In order to estimate $\Omega(d)$, Langmuir probe measurements were used to obtain density and temperature along with intensity images (750 nm line) at various pressures and powers. Further details will be given in section 5.5.2.

### 5.4.2 Plasma Setup

Images of the plasma were taken with an Andor iStar 334 T iCCD camera with a sigma EX 105 mm DG macro lens attached to it using a C - mount adaptor plate. Two 50 mm diameter

Edmund Optics filters of 488 nm (3 nm full width half maximum) and 750 nm (10 nm full width half maximum) were used. Each filter was mounted separately into a 70 mm outer diameter aluminium holder with grub screws securing the filters into position. The holder was then screwed into the macro lens. The camera was then mounted on an aluminium stand to ensure the camera was at the same height as the chamber window (see figures 3.4 & 3.2). The stand was then mounted onto an optical rail on an optical table adjacent to the plasma chamber. All measurements were taken at a fixed position with the filter 50 cm away from the chamber window, adjusted using the optical rail. The ambient light was minimised by turning off the laboratory lights and placing the camera in the laser enclosure. The camera was cooled to -30 $^{\circ}$C with the internal fan and controlled by the Andor software (as for the calibration). The gain of the camera was set to 1 using the Andor software. The spatial resolution of the pixel array (1024 $\times$ 1024) is determined by the pixel size of 1.6 $\mu m^2$ on the array but this is not the same as the effective size on the image. To determine the spatial resolution on the focal plane the camera was focussed manually onto an object of known size at the measurement distance (the Langmuir probe ceramic tube, O.D. 2.5 mm). The full camera image at 50 cm distance from the chamber was divided into 1024 $\times$ 1024 equally sized squares. The number of pixels corresponding to the diameter of the ceramic tube was determined (31 pixels) giving a conversion factor of 0.081 mm / pixel and a spatial resolution on the focal plane of 81 $\mu m^2$ at the focal plane. To obtain a signal with a sufficient intensity an exposure time of at least 0.05 seconds for the 488 nm line and 0.1 seconds for the 750 nm line is needed.

Separate plasma images were taken with each filter with the plasma off to obtain a background image which was taken at the same exposure time. This was then subtracted from the plasma image for the respective filter using the Andor software. The ratio of the 750 / 488 images were then obtained using the Andor arithmetic software. This software was then used to multiply the line ratio image by the ratio of absolute calibration factors (measured as 157.9062025 prior to the author's work). For the single 750 nm line, the image was multiplied by its absolute calibration factor. The images were then cropped to only encompass the window area. Finally, the images were exported as a .csv file which could be read by a MATLAB code.

The code uses the binary search method (tolerance 0.01 eV) to solve equation 5.10 for $T_e$ (pixel by pixel) and generates a temperature map. Using the temperature map equation 5.6 was solved for $n_e$ (tolerance $1 \times 10^{-11}$ $m^3$) to create a density map using the binary search method.

The code was checked to ensure the equations gave only one root. Solving equation 5.10 for the single and two step processes takes around 9 hours for the whole image. To reduce the computation time, the analysis region was restricted to only the area around the probe tip (250 $\times$ 250 pixels, corresponding to $1.6 \times 10^3\ \mu m^2$). This restricted area (referred to as the analysis region) takes around 4 hours to complete.

## 5.5 OIS Experimental Results

### 5.5.1 Preliminary Tests

Typical temperature and density maps given by this method are shown in figures 5.4 and 5.5 respectively (10 W, 5 Pa). The Langmuir probe is not present (therefore not used) in the first two images (figures 5.4 and 5.5) but is present in all the other images. For these images $T_e$ and $n_e$ were calculated over the whole image and a value of $T_e$ or $n_e$ was obtained from taking the mean value of the pixels over the plasma region. Within the plasma region the ground electrode is located at the top of the image and the driven electrode is at the bottom. The dotted white lines indicate the spatial extent of the driven electrode. The dust dropper, indicated in figure 5.5 was rotated to the far wall to avoid perturbing the plasma. The dust dropper is not present in any other experiments in this chapter, but is only present here to ensure the image is in focus.

The temperature is shown to be almost constant throughout the entirety of the plasma at around 2.85 eV. The temperature varies by less than 0.2 eV throughout the plasma region. This uniformity was observed for all pressures and powers used. There are also only small variations (less than 0.4 eV) in the average temperature with pressure and power, as shown in figures 5.6 and 5.7. The electrons, which have a much higher velocity ($\approx 1 \times 10^6\ m/s$) than the ions ($\approx 4 \times 10^2\ m/s$), move relatively unimpeded throughout the plasma bulk (as electric fields are small) so they do not encounter potential barriers. This means the electron velocities, and hence temperature, will be uniform throughout the plasma. The density map, by contrast, has a region of high density near the driven electrode (seen in the vertical intensity profiles, figure 5.14) at just over $2 \times 10^{15}\ m^{-3}$. This region extends approximately 1 cm vertically and horizontally over the entire electrode. Below this region the density abruptly decreases in the sheath and also decreases less rapidly towards the ground electrode. The dust confinement ring, used to set the focal distance, is clearly visible in the sheath. The main mechanism

for sustaining the plasma is the emission of secondary electrons (sometimes called primary electrons) from the driven electrode. Ions are accelerated by the sheath electric field towards the driven electrode. The resulting energetic impact releases electrons (secondary electron emission) which are accelerated by the sheath electric field into the plasma where additional (secondary) electrons are generated by ionisation. This causes the high density region shown in the figure.

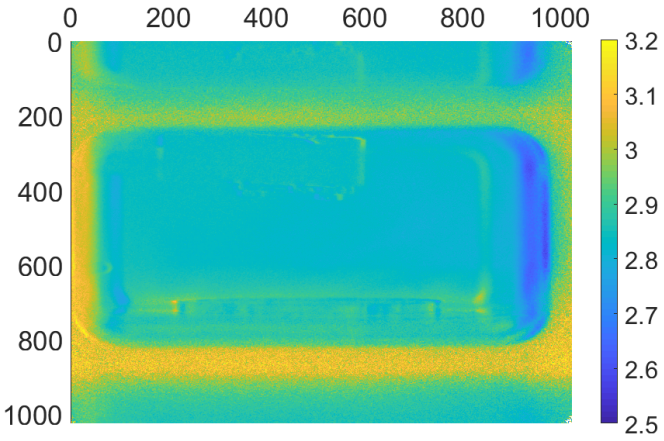


Figure 5.4: Electron temperatures calculated for each pixel over the entire image (10 W 5 Pa Ar)

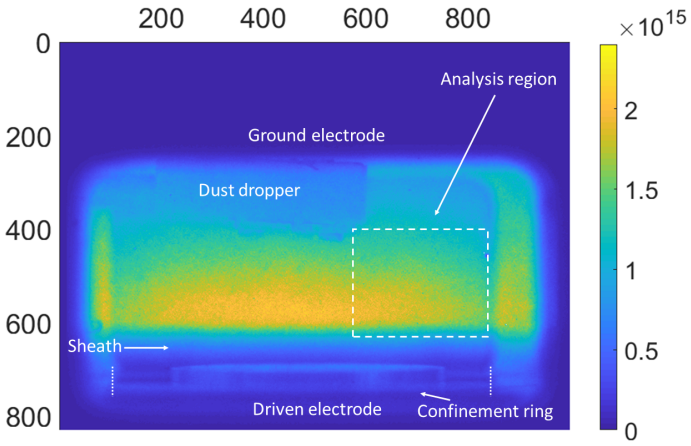


Figure 5.5: Electron densities calculated for each pixel over the entire image. The dotted lines indicate the spatial extent of the electrode (10 W 5 Pa Ar)

As mentioned in section 5.4.2, solving the equations for $T_e$ with both the single and two step excitation processes simultaneously significantly increases computation time. To reduce this the analysis region was restricted to only the area where the Langmuir probe tip is in experiments (although it is absent in these preliminary example images). The analysis region has dimensions of 40 $\times$ 40 mm and is indicated in figure 5.5.

Comparisons between the OIS method and Langmuir probe, at several pressures and powers, were made to determine the validity of the OIS method. For these tests the solid angle factor $\Omega(d)$ was set to 1 and the plasma was unmagnetised. The electron temperatures and densities were averaged over the restricted area to provide a single value of the plasma parameters which are compared to the Langmuir probe. As shown in figure 5.6, for increasing power, the OIS consistently overestimates the temperature obtained by the Langmuir probe by around 0.6 eV with both methods following the same trend. The average temperature from both methods is between 2 and 3 eV. For the pressure dependence, shown in figure 5.7, the OIS gives a constant temperature of around 2.9 eV over the pressure range. This is around 0.4 eV higher than the Langmuir probe up to 4 Pa. Between 4 - 5 Pa the Langmuir probe temperature decreases but remains constant between 5 - 7 Pa. This causes the temperature difference to increase to 0.8 eV. The Langmuir probe - OIS difference factor, $K$, can be used to correct the OIS temperature to take this into account. The value for $K = 0.7009$ was taken from the ratio of Langmuir probe to OIS temperatures at 6 Pa, 10 W as these were the conditions used in magnetic field experiments. The corrected temperature can then be obtained from $T_e^{corr} = T_e^{OIS}K$. The difference between the OIS and the probe is much smaller for $T_e$ than $n_e$ which is expected as the solid angle factor cancels out in equation 5.10 but is present in equation 5.6.

For increasing pressure (shown in figure 5.8) both methods follow the same trend of increasing density with pressure. Between 2 - 5 Pa the knee density increases more rapidly than the OIS with a maximum difference of $3.1 \times 10^{15}\ m^{-3}$ at 5 Pa (factor of 2.1). There is then a rapid increase in the OIS density between 5 - 6 Pa whereas the Langmuir probe density becomes constant for pressures greater than 5 Pa. Above 6 Pa the discrepancy between the two methods decreases to around $1 \times 10^{15}\ m^{-3}$ (factor 1.2). With increasing RF power (shown in figure 5.9) the OIS and Langmuir probe density agree to within $1.5 \times 10^{15}\ m^{-3}$ (factor 1.1) up to 10 W. Above 10 W the OIS density rapidly increases.

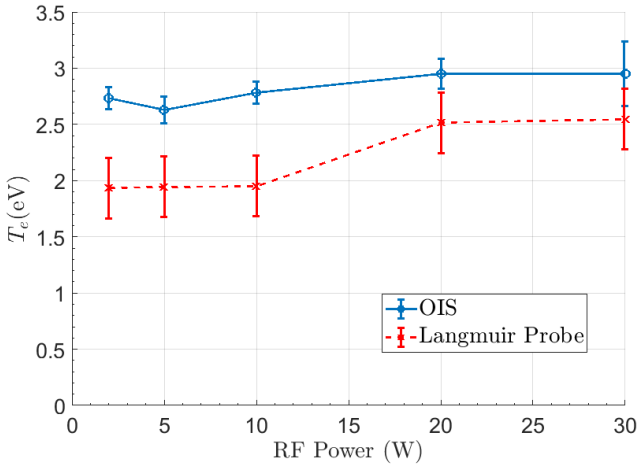


Figure 5.6: Electron temperatures obtained from OIS and Langmuir probe data for increasing power (6 Pa Ar)

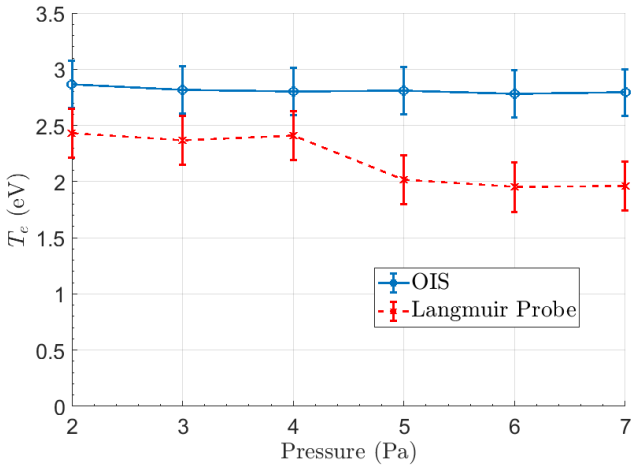


Figure 5.7: Electron temperatures obtained from OIS and Langmuir probe data for increasing pressure (10 W Ar)

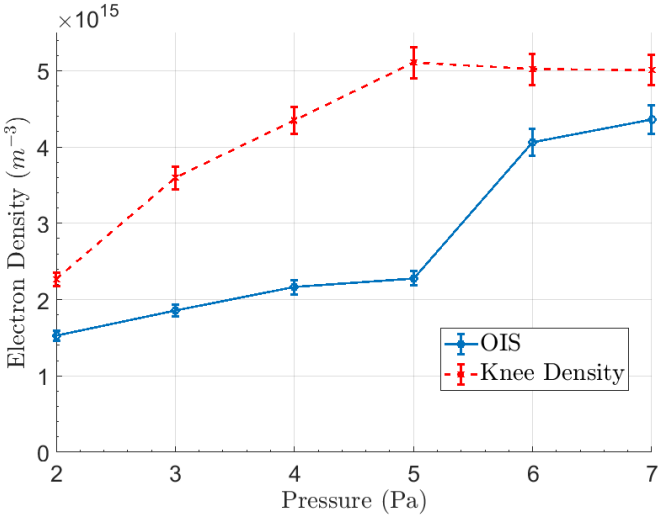


Figure 5.8: Electron densities obtained from OIS and Langmuir probe data with increasing pressure (10 W Ar).

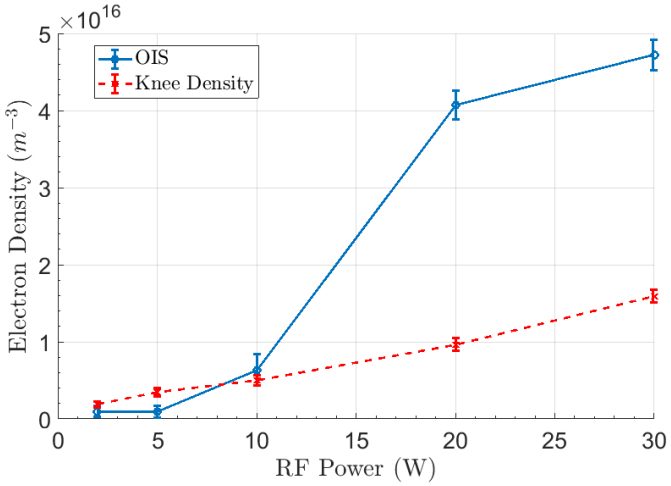


Figure 5.9: Electron densities obtained from OIS and Langmuir probe data with (6 Pa Ar).

Figure 5.9 shows the OIS and Langmuir probe agree within 18 % at 10 W, above which a large difference in densities between the methods is observed. Note that the 6 Pa, 10 W cases in figures 5.8 and 5.9 are not the same as this point was repeated separately for both experiments in order to provide an estimate of repeatability. The Langmuir probe shows a small monotonic increase in density with power, while the OIS density rapidly increases to over four times the Langmuir probe value. Variations in $\Omega(d)$ may be due to the increase in width of the high intensity region near the driven electrode sheath (see figure 5.5) which will lead to changes in emissivity over this region. This will change the solid angle factor, which is not only a function of distance but also of spatial variation in emissivity. Since $d$ is constant, any change in emissivity will result in a change in $\Omega(d)$. The discrepancy between the two methods in figure 5.9 mean that $\Omega(d)$ must increase to decrease the OIS density to that of the Langmuir probe. An increase in $\Omega(d)$ must occur for the same intensity because of equation 5.6.

These results of monotonically increasing density with power and pressure are in agreement with multiple results in the literature. Voloshin *et. al.*[133] have found a similar monotonic increase in density (using a 50 $\mu$m diameter Langmuir probe) with both pressure and power in a capacitively coupled RF plasma. The authors of that paper measured density with several probe analysis theories, including OML, at input RF powers of 5 to 20 W at pressures of 30, 100 and 200 mTorr (4, 13.3, 26.6 Pa respectively). All probe analysis theories used gave an increase in density with power and, to a lesser extent, pressure as has been observed here with OML only. Similarly, an approximately constant electron temperature with pressure is in agreement with Hope *et. al.* (above a certain threshold). This was done in an RF RIE system with an electrode gap of 6 cm where the DC bias could be varied between 0 and - 250 V (although not

specified for this result) and pressure was varied between 5 and 100 mTorr (0.67 - 13.3 Pa).

It is useful to demonstrate the distance dependence of $\Omega(d)$. This was done by taking background corrected images with the 750 nm filter from 50 to 138 cm from the chamber window with the method described in section 5.4. The number of counts as a function of distance is shown in figure 5.10. Measurements could not be taken closer than 50 cm due to the magnetic stacks obstructing the camera. It is shown that $\Omega(d)$ is a strong function of distance as the gradient increases rapidly approaching the window. It is not possible to reliably extrapolate back to the chamber window because the curve is rapidly varying and the extrapolation distance is large. This means $\Omega(d)$ cannot be reliably obtained from the figure. This also means that distance must be kept constant for all experiments otherwise recalibration must be done for each distance used. In these experiments, $d$ was chosen to be 50 cm (as close as possible to the chamber window).

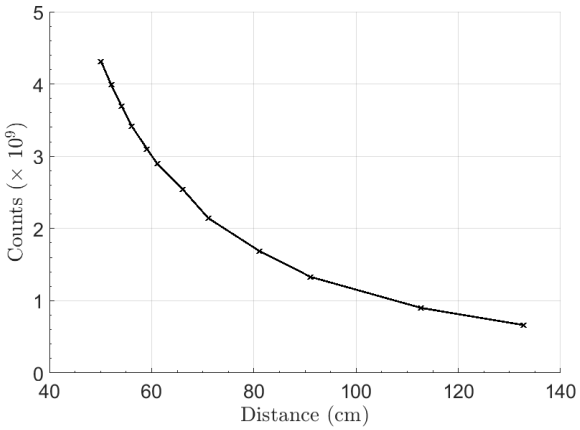


Figure 5.10: Variation of intensity (counts) with distance from the chamber window. (10 W, 6 Pa Ar).

### 5.5.2 Calibration Results

The image was first corrected using equation 5.12 and the total intensity of the corrected image was obtained by adding all the pixel intensities together. This total was then divided by the area of the window ($2.4 \times 10^{-3}$ $m^2$) giving the intensity in mW / $m^2$. Equation 5.10 was then solved for $\Omega(d)$ using the Langmuir probe density and temperature. Since the plasma emission fills most of the chamber window (apart from the small driven sheath area) dividing the total intensity by the window area is justified. This essentially smooths out any non - uniformity in emissivity throughout the plasma (i.e. constant emissivity). This is justified as the emission (and density) is relatively uniform over the window area. In using the Langmuir probe for $n_e$

and $T_e$, it is assumed that the plasma is uniform everywhere which is usually a good assumption. Because of the use of the Langmuir probe, the measured $\Omega(d)$ will include other calibration factors. Nevertheless, the value of $\Omega(d)$ will be an approximation of the solid angle factor.

The solid angle factor was calculated for a range of pressures at 10 W (2 - 7 Pa) and powers at 6 Pa (2 - 50 W) using the method described in section 5.4.1. These are plotted in figures 5.11 and 5.12 respectively. The solid angle factor varies between 0.24 sr and 0.82 sr, with several maxima and minima, over the pressure range with an average of 0.46 (-0.22, +0.36). These fluctuations are most likely due to a variation of emissivity as the plasma fills most of the area of the window (except for the driven electrode sheath). The variation of solid angle factors is greater with power, increasing from around 0.5 to a maximum of 2.3 at 30 W before decreasing to around 0.3 above 40 W. A single peak in power is observed whereas in pressure multiple maxima and minima occur around an average value. The camera images show the intensity increases up to 30 W, after which it remains fairly constant. The decrease in solid angle factor above 30 W may be explained by the increase of density (with power) in equation 5.6. In order to achieve this in the equation $\Omega(d)$ must decrease.

Using these results a solid angle factor of 0.7 at 6 Pa, 10 W was used as these conditions were chosen for all magnetic field experiments. However, as there was no way to reliably measure density or temperature in magnetised plasmas that did not have a solid angle dependence, this value may not be accurate in magnetised plasmas. When the magnetic field is applied the plasma collimates along the field lines over the entire driven electrode area. This will change the shape (as the plasma becomes collimated when magnetised) and emissivity of the plasma which in turn changes $\Omega(d)$. The plasma still occupies approximately 90 % of the window, so the changes in $\Omega(d)$ are expected to be relatively small.

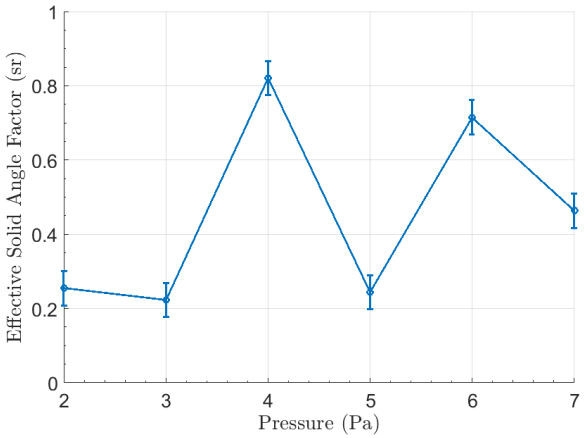


Figure 5.11: Variation of solid angle factor ($\Omega$ (d)) with increasing pressure (10 W Ar).

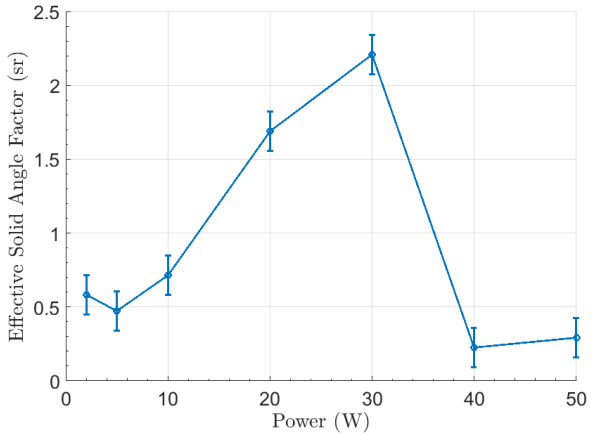


Figure 5.12: Variation of solid angle factor (Ω (d)) with increasing pressure (10 W Ar).

By incorporating this solid angle factor into the average temperature and density results from the previous section the OIS measurements can be forced to agree with the Langmuir probe. The agreement is therefore generally improved compared to figures 5.6 - 5.9, especially at 20 - 30 W.

### 5.5.3 OIS Parameter Maps in Unmagnetised Plasmas

With the solid angle factor accounted for, images were taken using the 488 nm and 750 nm filters in an argon plasma where the pressure at 10 W was increased from 2 to 7 Pa. In a separate experiment, the power supplied to a 6 Pa argon plasma was increased from 2 to 30 W. No dust was used in these experiments, although the dust dropper was sometimes present in the chamber as an object to focus the camera on and then moved to the chamber wall to avoid plasma perturbations. Figure 5.13 shows horizontal profiles of the raw intensity using the 750 nm filter (which is proportional to $n_i \approx n_e$) averaged over 100 pixels ($\approx$ 8.6 mm) immediately above the driven electrode sheath. Both of these figures are plotted from between ends of the window (either top and bottom or the sides) including the sheaths. In the figures the edges of the electrode are located at 20 and 60 mm. Over the electrode the horizontal profiles for all pressures and powers are relatively uniform across the bulk. Outside of the electrode, the intensity decreases. The two peaks at 16 mm and 65 mm in both figures are likely due to reflections from the corner of the chamber. The intensity, and therefore the density, increases with both pressure and power. Figure 5.14 shows vertical profiles of the centre of the image, averaged over 50 pixels on each side, for each pressure and power. In the vertical profiles a high intensity peak is observed above the driven sheath. This peak increases with both pressure

and power although the peak is more distinct with increasing pressure. The driven sheath is expected to be wider than the ground sheath due to the greater voltage drop across the driven sheath.

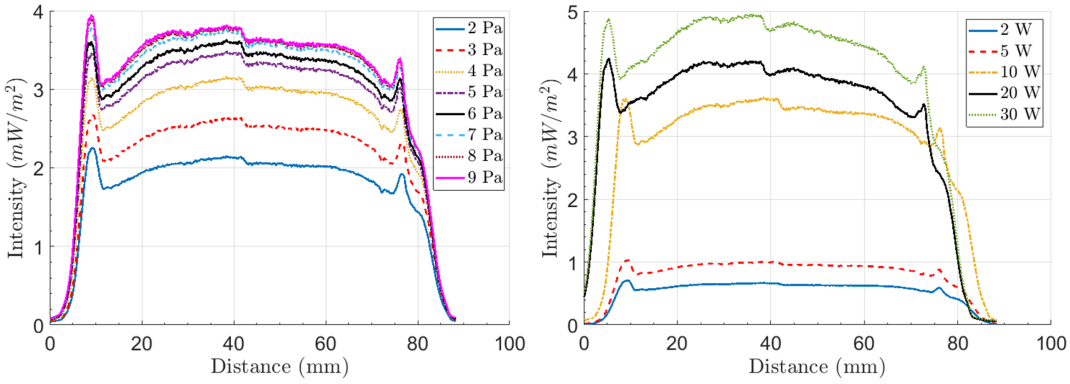


Figure 5.13: Horizontal intensity scans (750 nm filter): (a) with increasing pressure at 10 W and (b) with increasing power at 6 Pa. The scans are averaged vertically over 8.6 mm (100 pixels) above the top of the driven electrode sheath (which changes with pressure and power). The left of the chamber window (inside) is located at 12 mm.

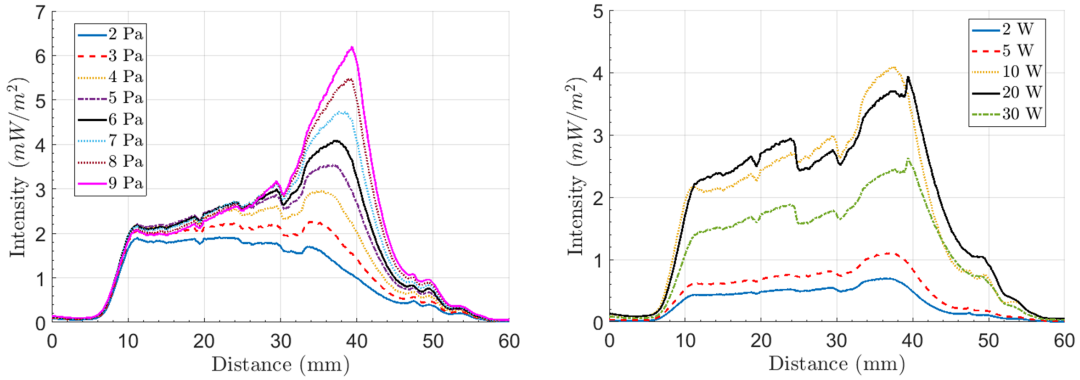


Figure 5.14: Vertical intensity scans (750 nm filter): (a) with increasing pressure at 10 W and (b) with increasing power at 6 Pa. The scans are averaged horizontally over 8.6 mm (100 pixels) at the centre of the electrode. The top of the window (inside) is located at 5 mm.

Some typical images of the analysis region around the probe are shown in figure 5.15. This region includes both the high density region and a small section of the upper sheath transition area (seen most obviously in the density maps). This sheath region was excluded from the analysis region. The temperatures are line averaged through the plasma and the probe ceramic stem is in the line of sight of the camera (indicated in figure 5.5.3). To investigate whether the probe stem affected the average $T_e$ and $n_e$ the averaging was done over the analysis region both with and without the probe stem. The probe stem was excluded by applying an image mask which set the image intensity to zero over the probe stem. The averaging was applied over the rest of the area. This resulted in a temperature difference of less than 2% (0.03 eV)

and a density difference of 3% ($1 \times 10^{13}\ m^3$) so the effect of the probe region is negligible. Consequently the mask was not applied to the data.

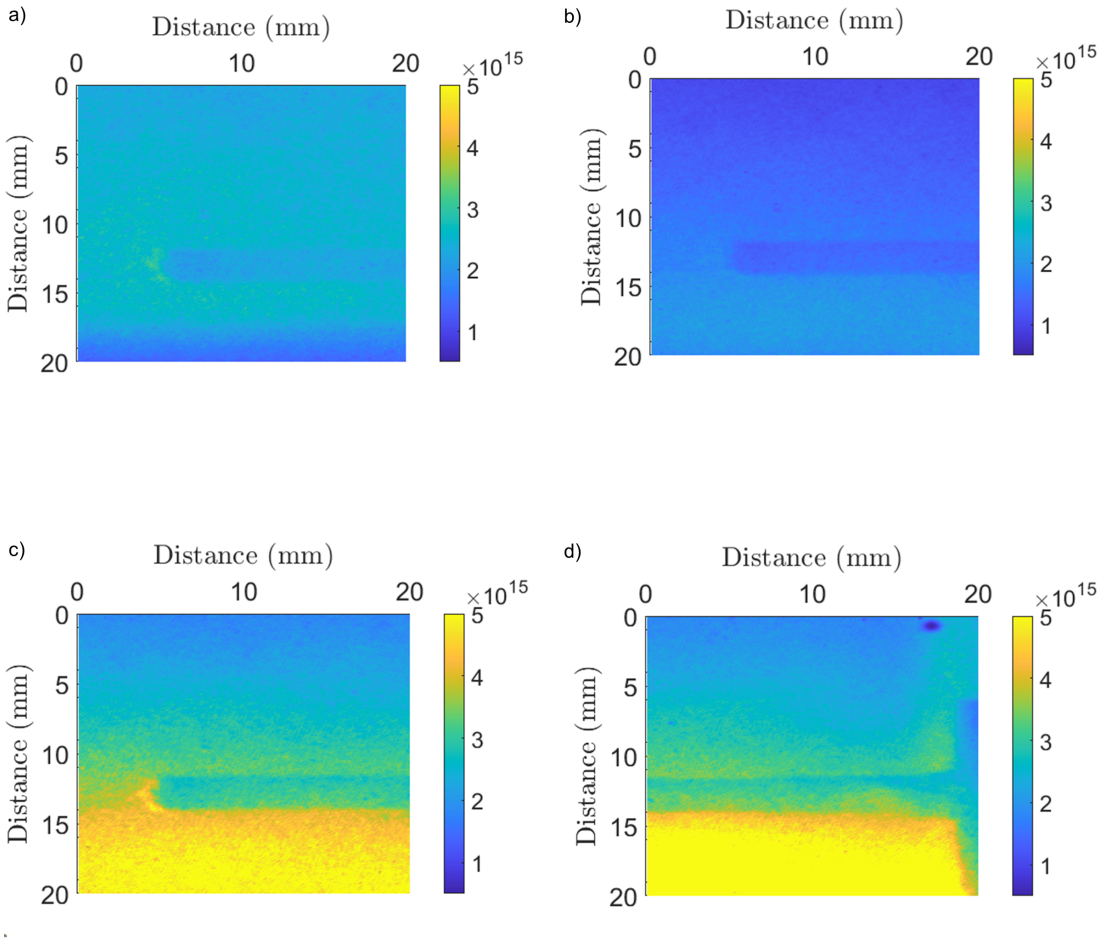


Figure 5.15: Electron density maps obtained with the OIS method over the analysis region with increasing pressure. (2 Pa in (a), 5 Pa in (b), 7 Pa in (c), 9 Pa in (d) 10 W Ar).

Figure 5.15 (a - d) shows the spatial variation of the plasma density throughout the analysis region with increasing pressure. It is shown in the figures that the sheath width decreases with increasing pressure, indicated by the increase in density at the bottom of the image. Since $\lambda_D \propto 1 / \sqrt{n_e}$ and the average density increases with pressure (as shown in figure 5.8) $\lambda_D$ decreases with pressure which causes the observed decrease in sheath width. There is a rapid increase in density in the lower part of the image between 5 Pa and 7 Pa (b and c in the figure). This region, present at lower pressures (a and b) but is less visible at this scale, moves towards the driven electrode with increasing pressure. The temperature images show a relatively uniform value of $T_e$ (within about 0.5 eV) for each pressure and power (as expected from figure 5.4) so they are not shown here.

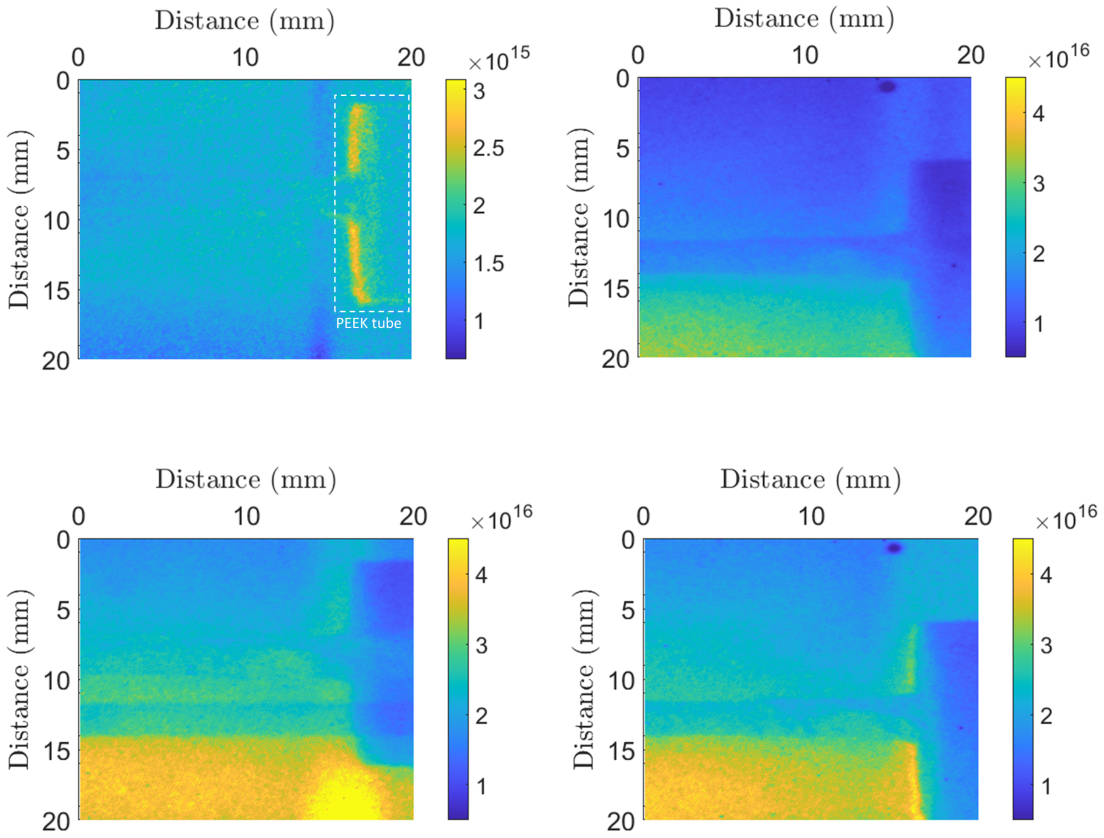


Figure 5.16: Electron density maps obtained with the OIS method over the analysis region with increasing power. Note the lower scale in the 2 W case (a) (2 W in (a), 10 W in (b), 20 W in (c), 30 W in (d) 6 Pa Ar).

Temperature and density maps of the analysis region were also taken with increasing power. The density maps are shown in figure 5.16 (a) - (d). The vertical high - density bands on the right of the image is the edge of the PEEK holder for the Langmuir probe. Note that figure 5.16 (a) shows a lower scale than the other images. There is an increase in the average density with power (also shown in figure 5.9), which is a result of an increase in energy transferred to the electrons which causes an increase in the ionisation rate. A high density region is visible at 20 W (c in the figure) which moves towards the driven electrode with increasing power (although this is less visible at lower powers). The sheath width does decrease (due to the increase in $n_e$ in $\lambda_D$) although this is less obvious above 20 W (figure (c)). These trends in the sheath width and the behaviour of the high density region are also observed with increasing pressure. Just as with pressure, the temperature maps (not shown) are relatively uniform and show only small variations with increasing power.

## 5.6 OIS Parameter Maps in Magnetised Plasmas

The electrons and, at much stronger magnetic fields, the ions become magnetised and as a result are constrained to follow and gyrate around the field lines. The field lines in the chamber are vertical and this is seen by visual observation (and in the plasma images obtained by OIS) as the plasma forms a central column over the driven electrode. This is shown in the horizontal profiles of the 750 nm images (see figure 5.17 (a)) where the dashed vertical lines indicate the edge of the electrode. As is shown figure 5.17 (a), the plasma fills almost the entire window horizontally with no magnetic field. The width of the high intensity band above the driven electrode decreases by around 7 mm when the magnetic field is applied and the intensity, which is proportional to density, increases when the magnetic field is applied. As the magnetic field is increased, the profile shape remains the same but the intensity increases up to 15 mT, after which the intensity decreases to a minimum at 25 mT. The intensity then rapidly increases to a second and greater maximum at 30 mT above which the intensity decreases again. The vertical profiles (see figure 5.17 (b)) show a similar trend in that the shape changes when the magnetic field is applied. The maximum and minimum intensities occur at the same magnetic fields as for the horizontal profiles. The minimum in intensity for both the horizontal and vertical profiles is approximately equal to the unmagnetised case, so it can be expected that the densities at 0 and 25 mT will be similar. The profile with no field is flat from the top of the window to the high intensity band above the driven electrode (shown at around 35 mm). With a magnetic field applied a step in the intensity profile appears in the centre of the window which is observed at all field strengths used (except for 0 mT). This is not caused by an object present in the plasma, such as the dust dropper, as the dropper extends 21 mm vertically (from 0 mm) on the image whereas the edge of the step occurs at around 25 mm. Additionally, the step is not present with no magnetic field but the dust dropper is located in the same region of the image. The step is the result of an electric field in the centre of the chamber which acts to repel electrons. This reduces the density and therefore the intensity of the 750 nm image in this region. It is not clear what causes this, although it is related to the magnetic field as the step is not present in the no field case and is observed even at the weakest magnetic field used (6 mT).

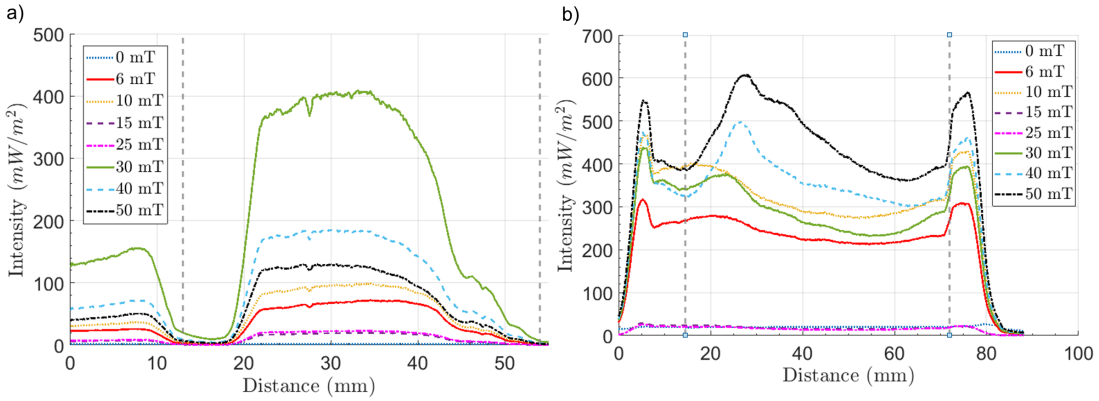


Figure 5.17: Horizontal profile (a) and vertical profile (b) of the intensity with the 750 nm filter averaged over 100 pixels of the high intensity band near the powered electrode (horizontally) and 50 pixels either side of the image centre (vertically) (6 Pa, 10 W Ar).

With the OIS system calibrated in unmagnetised plasmas, temperature and density maps were then obtained in magnetised plasmas with the field strength increasing from 0 to 50 mT. The power and pressure were kept constant at 10 W and 6 Pa respectively. The image was analysed over an identical analysis region to that used in the unmagnetised images. The use (and the size) of the analysis region may be justified by comparing key length scales in the plasma. Table 5.1 shows these key magnetised plasma parameters (determined with the OIS results of temperature and density when necessary) with increasing magnetic field. For all the magnetic fields used, the electron Larmor radius is much less than the length scale of the analysis region (20 *mm*). Consequently the plasma in the analysis region is sufficiently magnetised. Here, the Hall parameter describes the number of gyro orbits completed by a particle between collisions and is given by $\omega_{i,e}$ / $2\pi\nu_{thi,e}$.The bold text indicates approximately the 10 $\times$ limit of $r_{Le}$ / $R_p$ which Lange [19] suggests is the limit of the applicability of OML. The accuracy of OML in magnetised plasma sheaths will be investigated in Chapter 7.

Table 5.1: *Key plasma parameters in the magnetic fields used in these experiments from densities and temperatures measured with the OIS system*

| | |
|---|---|
| Ion mean free path ($\mu$m) | 94.8 |
| Electron mean free path (cm) | 1.53 |

| Magnetic Field (mT) | 0 | 6 | 10 | 25 | 30 | 40 | 50 |
|---|---|---|---|---|---|---|---|
| Electron Debye length ($\mu$m) | 147 | 60.5 | 47.1 | 194 | 30.4 | 80.3 | 238 |
| Ion Larmor radius (cm) | - | 2.7 | 1.6 | 0.65 | 0.54 | 0.41 | 0.33 |
| Electron Larmor radius ($\mu$m) | - | 890 | **530** | 210 | 160 | 140 | 100 |
| Ion Hall parameter | - | 5.86 | 9.77 | 24.4 | 29.3 | 39.1 | 48.9 |
| Electron Hall parameter | - | 178 | 299 | 769 | 973 | 1070 | 1603 |

A typical density map of the analysis region is shown in figure 5.18 (a) for a 10 mT argon plasma. The figure shows that the density is relatively uniform over the analysis region except for a horizontal band near the bottom of the image. This band, which corresponds to the high density region as shown in figures 5.15 and 5.16, shows a temperature (not shown) approximately 0.2 eV higher than its surroundings. Figure 5.18 (b) shows the vertical line profiles of $T_e$ with increasing magnetic field strength averaged over 4.3 mm (50 pixels) from 0 mm (figure 5.18 (a)). The figure shows that with increasing field strength the temperature profile remains spatially constant and varies little with magnetic field (0.7 eV). Whilst there is an effect of the plasma becoming magnetised, as shown in figure 5.17, the temperature remains approximately constant both spatially and with magnetic field up to 50 mT. Similarly, the density was calculated at each of the magnetic fields for the temperatures shown in figure 5.19. The diffusion coefficient is a measure of mobility [134] and in magnetised plasmas is given by a well - studied relation of $D \propto B^{-2}$ [135] which is in agreement with these results.

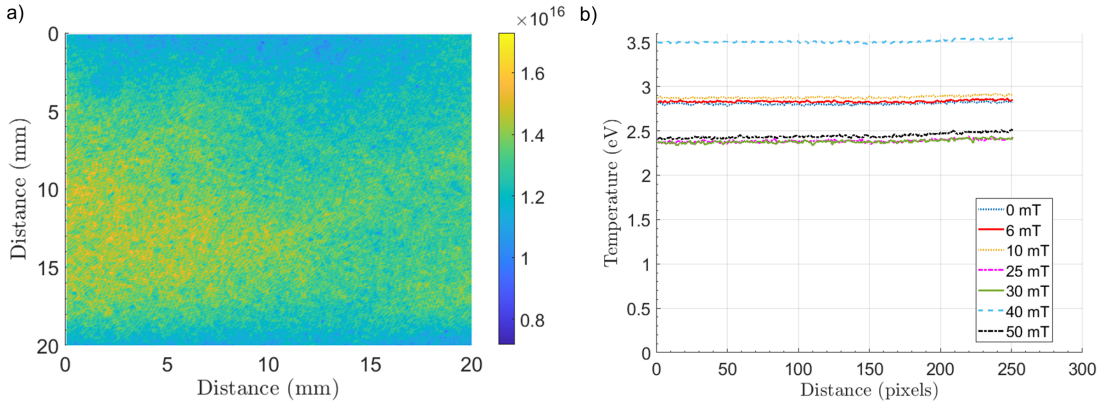


Figure 5.18: (a) Electron density map and (b) temperature vertical profiles with increasing magnetic field over the analysis region (10 W, 6 Pa Ar)

This means the average energy per particle is also unchanged which suggests the number of collisions and heating mechanisms (principally ohmic and stochastic heating) are not affected by the magnetic field. The unchanged collision frequency is supported by calculations of the Hall parameter with each field (shown in table 5.1). The table shows the Hall parameter increases from a minimum of 178 at 6 mT, indicating the plasma is relatively collisionless. However, there are plasma oscillations which become visible (as a frequent pulsating effect) at around 80 mT but may affect the plasma at the magnetic fields used in these experiments. These oscillations may be caused by drifts introduced by the magnetic field. As the magnetic field is uniform to within 0.3 % horizontally and 0.6 % vertically in the chamber [65] these drifts are not likely to be due to curvature or grad - B drifts. E $\times$ B drifts are also unlikely in

the plasma bulk, as the electric field is weak. However, as the powered electrode is isolated from the grounded chamber by a small ($\approx$ 10 mm) insulating ring, there is an electric field in the sheath between the electrode and adjacent grounded chamber which can be perpendicular to the magnetic field. This sets up an E $\times$ B drift which is proportional to the strength of both the electric and magnetic field (drift velocity, $v = (E \times B)/(ZeB^2)$ [5]) so will be stronger nearer the powered electrode and with increasing magnetic field strength.

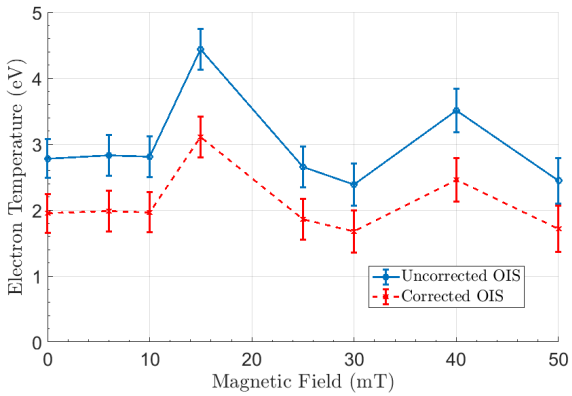


Figure 5.19: Electron temperatures calculated from OIS for increasing magnetic field (10 W, 6 Pa Ar)

A vertical density profile in the centre of the image (10 mm to the left of 0 mm in figure 5.15) is shown in figure 5.18. The densities obtained from both the OIS values corrected to the Langmuir probe and the unmodified values are shown in figure 5.21. The horizontal density profile in magnetised plasmas is shown in figure 5.20. The averaging and analysis region size and position is the same as for the unmagnetised case. The collimation of the plasma can clearly be seen as at no field the profile is flat over the analysis region. When the magnetic field is applied, the density increases and the shape of the profile changes to having a peak near the edge of the region. The density then decreases again towards the edge of the chamber. This shape is observed for all magnetic fields used, with a maximum density observed at 40 mT. This shape may be explained by the formation of a hollow column within the plasma. This has been observed by eye in this chamber and as the density is line integrated, the hollow central column will give a smaller density than the edges. The abrupt decrease in density towards the edge of the chamber may be explained by the electrons becoming constrained to gyrate along the field lines above the electrode.

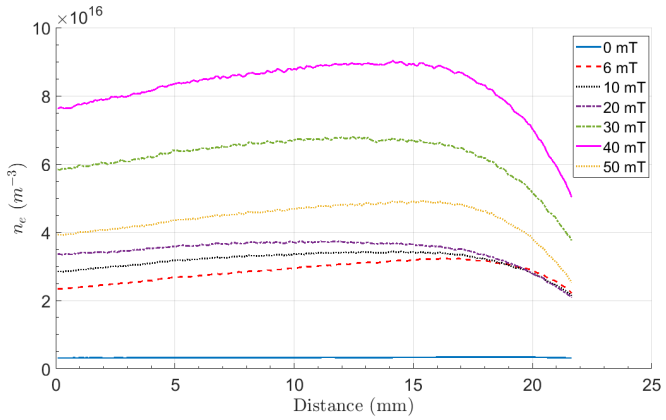


Figure 5.20: Electron density horizontal profiles with increasing magnetic field over the analysis region (10 W, 6 Pa Ar)

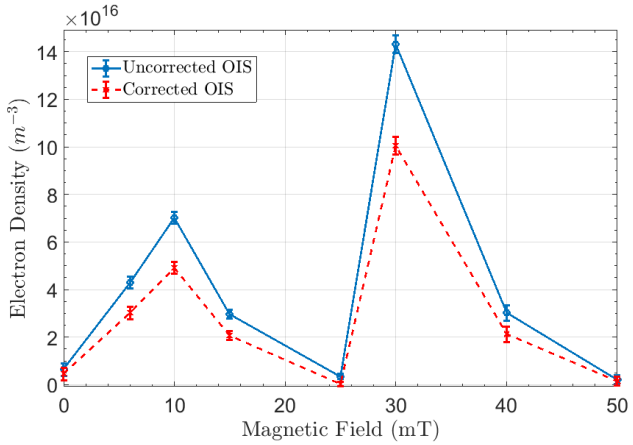


Figure 5.21: Electron densities calculated from OIS and averaged over the entire analysis region for increasing magnetic field (10 W, 6 Pa Ar)

Two peaks are observed in both density and temperature for increasing magnetic field but these peaks do not occur at the same magnetic field but are offset from each other by 10 mT. This may be explained by the raw data showing peaks in the 750 nm intensity but not the 488 nm intensity as temperature is proportional to the ratio of these but the density is proportional to the 750 nm intensity. It should be noted that the uncertainties from the Langmuir probe will contribute to both uncertainties in the OIS temperature and density as the OIS is corrected to the Langmuir probe value. The errors in the Langmuir probe measurements mainly arise from the determination of the $T_e$ range and the fact the knee density is obtained from a single point of the IV curve. The Langmuir probe values are thus one of the main sources of error in the OIS measurements, and errors will likely be even higher in magnetised plasmas but this could not be directly determined. The errors in figure 5.21 appear to be small due to the scale and the large peaks at 10 and 30 mT.

## 5.7 Conclusion

An optical emission spectroscopy diagnostic based on the corona model has been used in magnetised and unmagnetised plasmas which incorporates both single step and two step excitation processes. The system was absolutely calibrated with a 1 kW NIST - traceable tungsten lamp to allow electron density to be measured as well as electron temperature. The OIS diagnostic was then used in an RF argon plasma where the measured parameters of $T_e$ and $n_e$ were compared to those measured obtained with a Langmuir probe. The probe provides a direct local measurement, whereas the OIS provides line - averaged data over the area of the plasma window. A correction factor was applied to the OIS image in the region of the Langmuir probe to ensure the two methods agreed in an unmagnetised RF plasma. Two step excitation processes were also included in the model as these have been predicted to be important both in the literature [123] and theoretically in figure 5.1. A small reduction in $T_e$ was recorded for the same plasma conditions with this inclusion, bringing the OIS into closer agreement with the Langmuir probe at the cost of computation time. The electron temperature given by the OIS method generally follows the trend given by the Langmuir probe as shown in figures 5.6 and 5.7. The densities, shown in figures 5.8 and 5.9 show a similar correlation. The limits on the computation time mean the OIS analysis was restricted to a region of the plasma around the probe tip to ensure a similar region of the plasma was measured. The OIS system was then used in magnetised plasmas in which Langmuir probe IV curves are unreliable so were not used. The OIS system gave temperature values which were constant over the area of the analysis region for each magnetic field and varied by a maximum of 1.3 eV between all magnetic fields used but generally remained at an average of 1.9 eV. This suggests that, up to the maximum field used of 50 mT, the electron heating mechanisms are largely unaffected by the magnetic field. This OIS system will be used in Chapter 7 to determine $n_e$ and $T_e$ in magnetised dusty plasmas in order to investigate dust charging mechanisms.

# Chapter 6

# Emissive Probes

## 6.1 Introduction

Emissive probes have been used as an invasive probe diagnostic to measure local potential in the plasma bulk [72], sheath [136] and in vacuum conditions [137]. They have seen extensive use in both DC and RF plasmas [138, 139] and have been used in the literature to measure $V_p$ in magnetised [140, 141] and unmagnetised [142, 143] plasmas. Langmuir probes can also measure $V_p$, but can be unreliable in magnetised plasmas and in sheaths. Emissive probes, with correct construction and heating methods, are robust in extreme plasma conditions so they have also been used in tokamaks [71]. Unlike Langmuir probes, emissive probes cannot be used to measure density and require a more complex technique to measure electron temperature [74]. Despite these drawbacks, emissive probes can be used reliably to obtain sheath potential profiles [76, 144]. One of several techniques is necessary to extract $V_p$ from emissive probe data which generally involve either taking IV curves at increasing levels of emission, such as the separation point and inflection point in the limit of zero emission (I.P.) methods, or measuring the floating potential at increasing electron emission (the floating method). The two most commonly used techniques using this principle are the floating point method and the I.P. method as the separation point method has been shown to be unreliable [73].

In the literature the most commonly used setup to take emissive probe measurements employs a 50 or 60 Hz mains signal with a varying amplitude to control heating current to the probe tip [14]. If the probe is biased more positively than the plasma potential, most electrons cannot be emitted from the probe (except for higher energy electrons which can overcome the potential barrier). When the probe is biased more negatively than the surrounding region, elec-

trons can be emitted from the probe which provides a measure of the local potential. The use of a mains signal (and unshielded components) results in mains noise in the resulting current - voltage plots. There are two aims of this section, firstly to describe a novel method of obtaining $V_p$ from emissive probes, in both the sheath and the bulk, which drastically reduces the effect of mains noise. This will be investigated experimentally in both magnetised and unmagnetised plasmas. The second aim is to take local potential measurements taken at several heights above the powered electrode in the sheath (both magnetised and unmagnetised) which will be used to calculate a potential profile. The potential profile will be used to calculate the electric field in the sheath which will then be used in the calculation of the charge on a dust particle with equation 2.27 (see chapter 7).

The plasma chamber that measurements are taken in is described in Chapter 3. Emissive probe construction and general theory is described in section 6.2. The floating method and initial experiments performed using it are detailed in section 6.3. The novel setup, the inflection point method and the associated experiments are outlined in section 6.4 and potential profile measurements performed with the I.P. method in unmagnetised and magnetised plasmas are presented in section 6.5. A summary and conclusions are given in section 6.7.

## 6.2 Emissive Probe Operation

### 6.2.1 Emissive Probe Theory

The principle of operation of an emissive probe is based on thermionic emission of electrons from a filament immersed in a plasma. When a filament is heated electrons can gain enough energy to be emitted from the filament. This occurs when the electron thermal energy, provided by the electric current, is enough to overcome the work function of the material. If the filament is biased more negatively than the local plasma potential, the electrons emitted from the filament will be accelerated into the plasma [14]. If the filament is biased more positively than the local potential the electrons will return to the wire except for those in the high energy region of the distribution. When it is biased more than $T_e$ above the plasma potential, the probe acts as a conventional collecting probe as no electrons are repelled by the probe. By this principle emissive probes are mainly used to measure $V_p$ but can be used to measure $T_e$ as well [74]. A current (usually 50 or 60 Hz mains) on the order of 0.5 A is passed through the filament, although the current needed for emission strongly depends on the ratio of $R_p$ / $\lambda_D$. A variable

AC transformer is commonly used in the literature [145] to control the heating current. Diodes are used to half-wave rectify the mains signal so that measurements can be taken in the heating off period. This was done to minimise the potential drop across the filament. An alternative heating method uses a laser heated probe which is commonly done in tokamaks [146].

The current - voltage curve for an emissive probe consists of the combination of both collected and emitted current [14]. The collected current is identical to that of a Langmuir probe. The emitted electron current ($I_{em}$) depends strongly on wire temperature, $T_w$ (and indirectly by heating current), and is given by the Richardson-Dushman equation if the probe bias is less than the plasma potential [14]:

$$I_{em} = RT_w^2 A_p exp(e\phi_w / k_b T_w) \tag{6.1}$$

When the probe bias is greater than the plasma potential, the emitted current is instead given by:

$$I_{em} = RT_w^2 A_p exp(e\phi_w / T_w) exp\left(\frac{-e(V_b - V_p)}{T_w}\right) g(V_b - V_p) \tag{6.2}$$

Here $g(V_b - V_p)$ is a function relating to the angular momentum of emitted electrons, $A_p$ is the probe surface area, $R$ is the Richardson constant and $\phi_w$ is the work function of the material. From equation 6.1 it can be seen that the emitted current has an exponential region dependent on the wire temperature rather than the electron temperature as is the case in collecting probes. Since in most plasmas $T_w \approx 0.1T_e$ emissive probes can determine $V_p$ more accurately than collecting probes [72]. Equation 6.1 provides the temperature limited emission for an emissive probe. As emission increases further, it will then be limited by the build up of electrons around the emitting surface (space-charge limited emission) which act to repel more electrons entering the plasma [147]. The emission of electrons results in a reduction of potential until the electric field surrounding the probe becomes zero at strong emission. At even stronger emission, a potential "dip" around the probe which acts to repel emitted electrons back to the probe appears. This is demonstrated in figure 6.1. Ye and Takamura [142] have performed a theoretical derivation for the emitted current in both the temperature and space charge limited regimes. If $V_b < V_p$ then the emitted current is temperature limited and given by equation 6.1. The space charge limited equation is instead given by:

$$I_{ems} = 0.5AG(1+G)^{-1}en\sqrt{\frac{8T_e}{\pi m_e}}\sqrt{-\pi\Phi} \tag{6.3}$$

Where

$$G = [-\beta_1 + (\beta_1^2 - 4\beta_0\beta_2)^{1/2}]/(2\beta_2) \tag{6.4}$$

$$\beta_0 = -4\Phi^2 - 2\Phi([exp(\Phi)-1]^2 - 2(exp(\Phi)-1)) \tag{6.5}$$

$$\beta_1 = 4(-2(exp(\Phi)+1)\Phi^2 + 8(exp(\Phi)-1)(\Phi) - (exp(\Phi)-1)^2 \tag{6.6}$$

$$\beta_2 = 4\Phi^2 - 8\Phi^3 \tag{6.7}$$

$$\Phi = e(V_b - V_p)/T_e \tag{6.8}$$

Ion current is neglected as it is typically several orders of magnitude smaller than electron current. The collected current is the same as a Langmuir probe in the absence of space charge effects [14].

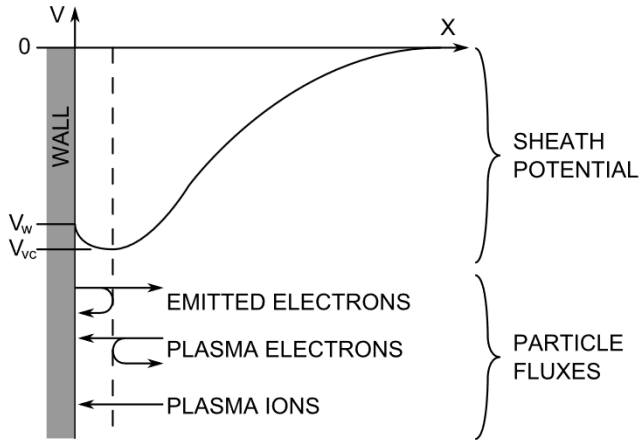


Figure 6.1: Potential profile surrounding an emitting surface in a plasma from Sheehan [14]. $V_w$ is the wall potential and $V_{VC}$ is the potential of the virtual cathode created by electron emission.

The effect of limiting emission due of space charge is shown in figure 6.1. A virtual cathode forms when emission reaches a critical point [148] whose potential is indicated by $V_{VC}$ in the figure. This is due to the negative charge of the electrons which, present in sufficient numbers, will modify the sheath potential by making it more negative which prevents further emission of electrons at high emission. The sheath potential is given by the difference between the wire potential, $V_w$, and ground. The direction of flow of plasma particles are also shown in the figure, and several electrons are repelled by this virtual cathode which demonstrates space charge limited emission.

Increasing the wire temperature leads to increased electron emission current, which is analogous to increased ion current. Because of this it is not possible to derive plasma parameters such as ion or electron density from an emissive probe IV curve. Figure 6.2 shows the effect of changing the level of emission of a probe. These curves were taken in the centre of a 6 Pa, 10 W argon plasma with a 50 $\mu$m diameter V - shaped emissive probe. The measured current through the probe tip (the heating current) is shown in the legend. Due to the distortion of the IV curve (as shown in figure 6.2) $n_e$, $T_e$ and the EEDF cannot be determined using standard cold probe (0 mA) methods.

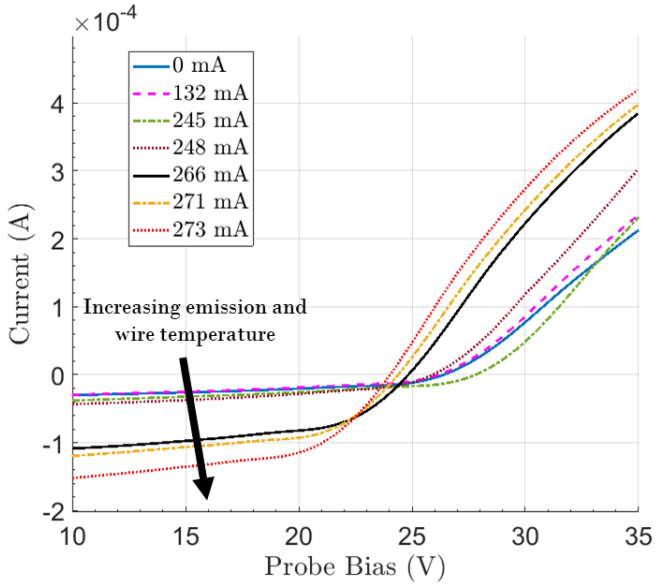


Figure 6.2: Example emissive probe current-voltage curves demonstrating the effect of increased emission. (6 Pa, 10 W Ar)

Several methods exist in the literature to obtain the plasma potential from emissive probes, the oldest of which is the separation point technique originally developed by Langmuir [34]. This involves superimposing the IV curves of an emitting and warm but non - emitting probe and taking the point where the two curves separate to be the plasma potential. However, this theory does not take into account the space-charge build up of electrons around an emitting probe and also assumes the electrons cannot be emitted below the local plasma potential (i.e. there is no distribution of emitted electron energies). However, the emitting probe contributes electrons to the region surrounding it which changes the potential difference between the probe and the plasma bulk which makes the separation point method unreliable [73]. Secondary electron emission is also ignored, which may be important under certain plasma conditions. For this reason the separation point technique was not used in these experiments. The other methods are the floating point and inflection point in the limit of zero emission (I.P.) techniques

which are described in section 6.3 and 6.4 respectively.

There are few papers regarding sheath potential profiles in magnetised plasmas. However, Sheehan *et. al.* [73] have investigated three different emissive probe methods (the floating, separation point and I.P. methods) in a 2 kW cylindrical Hall thruster (xenon) plasma with a magnetic field of up to 10 mT although the measurement locations used in those experiments only had a 5 mT field. The methods agreed to the same degree as in unmagnetised plasmas, indicating the magnetic field did not have a significant effect at that magnetic field and probe wire size. Emissive probes have also been used in other 13.56 MHz RF CCP discharges [149]. Other magnetised plasma environments where emissive probes have been used are tokamaks [150] and magnetrons[141].

### 6.2.2 Probe Construction

The most commonly used technique in the literature to construct emissive probes is to create a hairpin loop between two conducting electrodes contained within parallel alumina tubes [72, 151] shown in figure 6.3 (a). Due to its larger size the sheath around the alumina tube will be much larger than the sheath around the wire. This can distort the local space potential in the region near to the end of the ceramic tube. The sheath around each of these ceramic tubes (and the looped wire) in low density regions (i.e. the plasma sheath) can overlap at the end of the tubes leading to distorted IV curves [14]. The part of the wire exposed to the plasma must be long enough to minimise the perturbation from the tubes. Another design of probe tip uses a V - shaped arrangement of the ceramic tubes (also known as a linear probe in the literature [14]) and is shown in figure 6.3 (b). The V - shaped arrangement allows the ends of the ceramic tube to become further apart which will minimise the effect of overlapping sheaths present in the loop design [14, 72]. This also improves spatial resolution as a taut wire is less likely to sag under its own weight. The drawback of the V - shaped probe is that the increased tautness of the tungsten wire means the heating current may drastically reduce the life time of the probe [14]. Another limitation is that too much current through the tungsten wire (which is in contact with the ceramic tube as shown in figure 6.3 (b)) will create a hotspot which will cause the wire to break. This limitation on heating current means the V - shaped probe cannot be used with the floating method as large heating currents are required. The loop is made of thoriated tungsten because of its high melting point which prolongs the lifetime of the probe at high emission. Thorium doping was used as thorium oxide reduces the work function of the wire compared

to oxides of tungsten to increase electron emission [14]. In order to measure the potential in the plasma sheath, it is important to minimise the effect of overlapping tube sheaths so the V - shaped probe is most suited for this. Because of the limitations on heating current the loop probe was used with the floating method in the bulk.

For early emissive probe measurements, a separate probe was used which was designed by a previous PhD student (see section 6.3). In later measurements new designs for the emissive probes were used which are presented here. For both probes (loop and V - shaped) the flexible copper electrodes are soldered to female gold plated pins. Two holes are drilled in a 10 mm diameter, 50 mm long PEEK tube through which these electrodes and pins are then pulled through. The pins are then push fitted into two smaller holes in the top end of the PEEK tube. The two 60 mm long alumina tubes (I. D. 1.5 mm, O.D. 2.0 mm) are glued to the PEEK around the bottom holes. A cap is placed over the lower end to encase the wires. For these probes (both the loop and V - shape), a 1 cm long, 50 $\mu$m diameter thoriated (0.6 %) tungsten wire was used (Goodfellows). The diameter was chosen as the wire must not be so large to perturb the plasma, but must also be large enough to be resistant to melting at high temperatures [72]. The thoriated tungsten wire was crimped to the electrodes as tungsten cannot be spot welded.

For the loop probe design, there may be errors if the Debye length is on the order of the radius of the loop because the sheaths of different parts of the wire can overlap [72]. A typical Debye length in the plasma used in these experiments is approximately 0.18 mm (3 eV, $1 \times 10^{15}$ $m^{-3}$) whereas the probe loop radius is about 2 mm so this is not likely to be an issue in the plasma bulk.

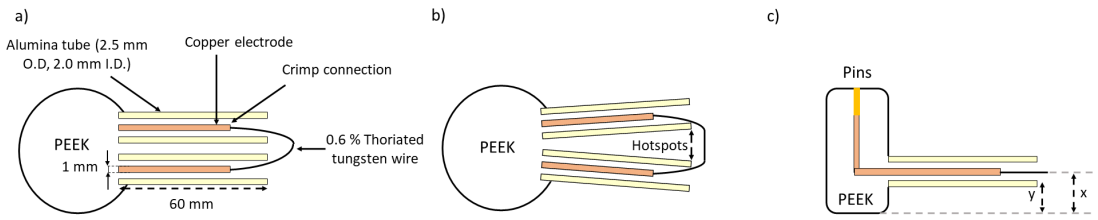


Figure 6.3: The two arrangements of emissive probe tips used in experiments. The loop probe shown in (a) is the most commonly used design in the literature and has a smaller wire so is less perturbing to the plasma. The V - shape, shown in (b) was used to prevent overlapping sheaths between the wire and tubes. The side profile is shown in (c).

When the probe tip is lowered to its maximum extent (when the PEEK is touching the powered electrode) the filament is offset from the surface of the electrode by a distance, $x$, shown in figure 6.3 (c). The midpoint of the filament is used to measure $x$. This distance had to

be measured for each new probe tip used as the ceramic tubes could become slightly offset from each other during the construction process, changing $x$ between probe tips. The probe stem is secured in the positioning system which can be used to adjust the height and horizontal position of the probe tip in the chamber using a digital micrometer and a protractor and is described in section 3.2.2. This system was always used for adjusting the position of the emissive probe, but in magnetised plasma sheath scans the position of the probe was measured using a camera.

The two female pins in the probe are connected to corresponding male pins in a probe stem (shown in figure 6.4) which is similar in construction to the Langmuir probe, but with two 0.9 mm diameter copper rods running through the stem and two male pins. These pins are secured in the end of the stem by epoxy resin. The two copper rods are each contained within a 2 mm O.D. ceramic tube inside the outer tube to electrically isolate them. The copper rods are then soldered to two wires which connect to two banana connectors (female) on the probe box. These are used to connect the probe to the heating and data acquisition circuits.

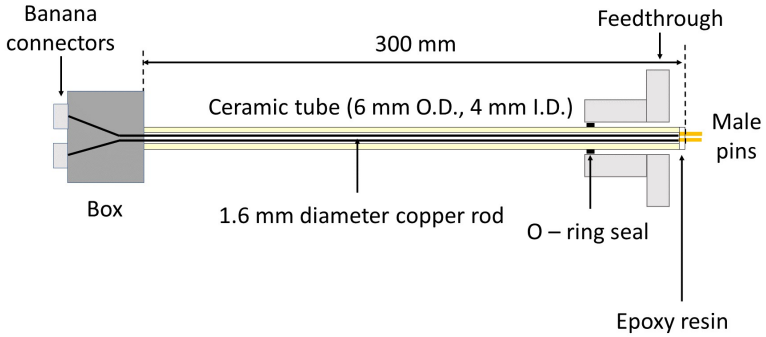


Figure 6.4: Emissive probe stem used in all experiments. The two copper rods are isolated from each other by a small internal ceramic tube.

## 6.3 Measuring Plasma Potential With The Floating Method

The floating method relies on the principle that as emission increases with a higher AC current the floating potential of the probe approaches the plasma potential [72]. Increasing emission from zero will eventually cause the measured DC floating potential to reach a plateau (in theory) at the plasma potential on a plot of current against potential. In practice, further increasing the emission will continue to cause the measured potential to rise due to space charge effects such as sheath expansion at high potentials [73]. This can be negated with a linear fit in the regions above and below the knee, and the point of intersection is taken to be the plasma potential. In the literature emissive probes have been found to typically float at 1.5 to 2 $T_e$ below the true plasma potential [152, 153].

The experimental setup used in these experiments for the floating emissive probe is based on one that is common in the literature [14, 77]. The circuit used for acquiring $V_p$ with the floating method is shown in figure 6.5. The mains (50 Hz) source is connected to a variable transformer (Zenith Variac) which steps down the voltage and steps up the current. This is connected to a fixed transformer with a turns ratio of 26 whose purpose is twofold. Firstly, this steps up the voltage and decreases the current so the probe will not melt. Secondly, the transformer acts to isolate the emissive probe from ground as the two transformer windings are not in direct contact. The centre tap of the transformer is connected to one end of a measurement resistor (100 MΩ). The other end is connected to a voltage probe, with an input impedance of 10 MΩ, which is connected to a Tektronix MDO 3054 oscilloscope. The setup forms a potential divider circuit so the reading on the oscilloscope is multiplied by 11. This provides a simple and direct method of measuring the floating potential. The other terminals of the isolation transformer are connected to the emissive probe via the banana sockets on the stem box (see figure 6.4). A Fluke 87 III multimeter to measure the heating current. The heating current is then increased by adjusting the Variac, in increments of around 10 mA and the corresponding potential is measured. This process is repeated until the gradient of the measured potential changes (i.e. where it begins to saturate at strong emission). One potential problem of the floating point method is that, in order to take an accurate measure of $V_p$, the measuring resistance must be large. However, the large resistance increases the circuit's time constant which reduces the temporal resolution of measurements [144].

All measurements in this section were taken with a 50 $\mu$m diameter probe designed by a previous PhD student (see [154] for details). The tungsten wire was not crimped to the electrodes and the connection was secured mechanically by pushing the wire into the ceramic tubes and shaping it into a hairpin loop. In experiments with a magnetic field, the field must be slowly changed or the filament can be forced out of the tubes.

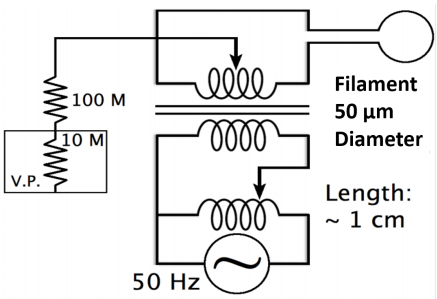


Figure 6.5: The emissive probe heating and acquisition circuit for the floating method. The 50 $\mu$m wire was replaced by a 25 $\mu$m wire for some experiments.

### 6.3.1 Floating Method Results

An example plot of the measured potential at several heating currents is shown in figure 6.6 in the central bulk of a 10 W 3 Pa argon plasma. A linear region is observed below the plateau which begins at around 390 mA. The plateau does not completely flatten due to space charge effects and the resulting sheath expansion which increases the probe's effective collection area. The intersection of the linear region with the plateau is taken to be the plasma potential which for this example is 26.18 V.

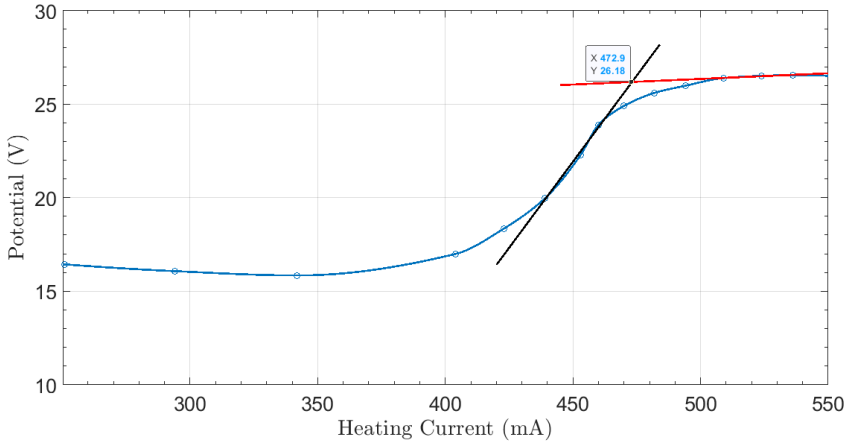


Figure 6.6: Example data to measure plasma potential (26.18 V) with the floating method (3 Pa 10 W Ar).

In the rest of this section all horizontal potential profiles of the plasma are measured in a 10 W, 6.3 Pa Ar plasma. These are shown in an unmagnetised plasma at several heights above the powered electrode in figure 6.7. All angles have been corrected with the method described in section 3.2.2. Note that as this was performed by rotating the emissive probe in port A in figure 3.4, the profile is an arc travelling from wall to wall through the centre of the plasma. The horizontal profile is approximately constant for each height, varying by less than 1 V across the profile and by less than $T_e$ (3 eV) between all heights used. This indicates that the plasma bulk region is reasonably homogeneous which is the expected result. The emission profile was judged visually to determine the plasma bulk region. At all heights except the lowest (5 mm) there is a weak minimum in the middle of the plasma.

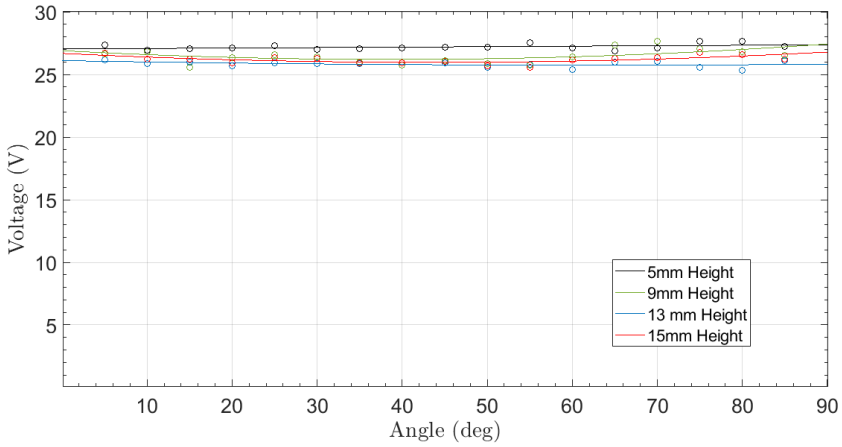


Figure 6.7: Horizontal profile measured by a 50 micron emissive probe in unmagnetised plasmas with the floating method (6 Pa 10 W).

Figure 6.8 shows a similar experiment to measure the horizontal potential profile with increasing magnetic field. These results were taken at a height of 7 mm above the powered electrode. The profile changes shape even for a relatively small magnetic field (17 mT) with a peak observed in the centre of the chamber which decreases towards the walls. This is expected given that the magnetic field will constrain electrons to field lines in the centre of the chamber, which will increase electron density in that region. This is in agreement both with visual observations, as the central column becomes brighter, and with OIS measurements of density (see chapter 5).

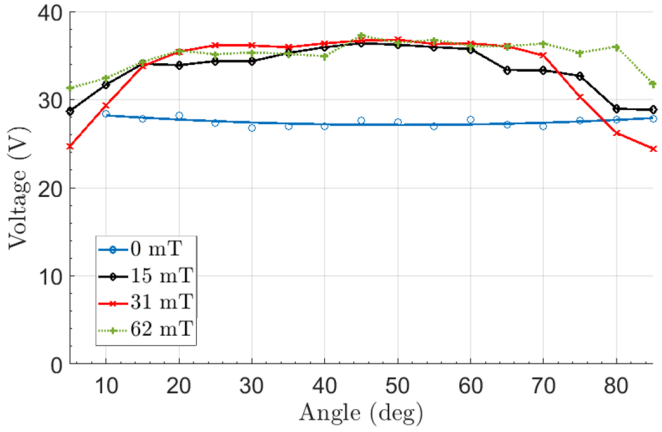


Figure 6.8: Horizontal profile measured by 50 micron emissive probe in magnetised plasmas with the floating method (6 Pa 10 W).

The floating point method, with a setup similar to that described above, has been used to measure the potential profile of the sheath in DC plasmas [76, 144]. Fujita and Yagura have developed a method which uses a lower resistance to improve the time response of the circuit which was used to obtain temporally-resolved potential measurements in a low density ($10^{12}$

$m^{-3}$) double plasma device. The authors of that paper also found that the floating method would fail in this region if the measurement resistance (with the conventional method) is too small. Measurements of potential in the sheath require high impedance so a balance must be found between time response and measurement accuracy.

The floating method has also been used in magnetised plasmas, including magnetrons [78] where the floating potential was found to be accurate to within 2 V (less than $T_e$). In a DC plasma with increasing magnetic field, the three methods have been compared and found to agree to within 1.5 $T_e$ in a magnetised plasma up to 30 mT [78].

The three most common methods have been compared in the literature by Sheehan *et. al.* [73] and Bradley *et. al.* [78, 155]. In general, it has been found that the separation point technique gives the highest measure of $V_p$ and the inflection point method gives the lowest but within approximately 3 V. Bradley *et. al.* have found they all agree to within 0.5 V in measurements taken in the unmagnetised region of DC magnetron with a pressure range of 0.26 to 0.78 Pa and cathode voltages between - 236 and - 338 V. For the same conditions in a magnetised (0.03 T) region of an identical discharge, the methods agreed to within 2 V. Sheehan *et. al.* have found that the floating point gives a value of around 2 V below the IP method, the latter of which gave the most accurate measure of $V_p$ [73]. This experiment was performed in a 2 kW, non - Maxwellian Hall thruster xenon plasma with $T_e = 10 - 50\ eV$, $n_e = 10^9 - 10^{10}$ $cm^{-3}$ and 0.005 T magnetic field.

## 6.4 Plasma Potential - Inflection Point In The Limit of Zero Emission Method

The main alternative to the floating method is the inflection point (I.P.) in the limit of zero emission technique. The I.P. method was developed by Smith *et. al.* [77] to mitigate space charge effects common at high emission in the floating point method. This method involves taking IV traces with increasing heating currents where the probe is warm but not strongly emitting. The space potential is found by plotting the potential at the peaks of first derivatives at different levels of emission against heating current. The potential is then extrapolated back to zero emission which allows $V_p$ to be found with a minimum of space charge effects. Some authors have found that a linear relationship is observed by plotting against heating current rather than emitted electron current [156].

An example of measuring $V_p$ with the I.P. method is shown in figures 6.9 using bulk plasma data. This was taken by a 50 $\mu$m V - shaped emissive probe 12 mm above the powered electrode in an unmagnetised 6 Pa 3 W argon plasma. Figure 6.9 shows the first derivatives of typical IV curves. A linear fit to the potential peaks of the first derivative (a separate example is shown in figure 6.10) can be extrapolated to the point of zero emission, giving the plasma potential. Although this is a more convoluted method than simply taking the peak of the first derivative of a Langmuir probe trace, there are multiple advantages to the emissive probe method. By taking the average fit of multiple measurements at low emission, a more accurate value of $V_p$ can be obtained which will reduce the effect of any noise in the measurements. It is important to note that the extrapolation to zero emission current is not necessarily the same as extrapolation to zero heating current.

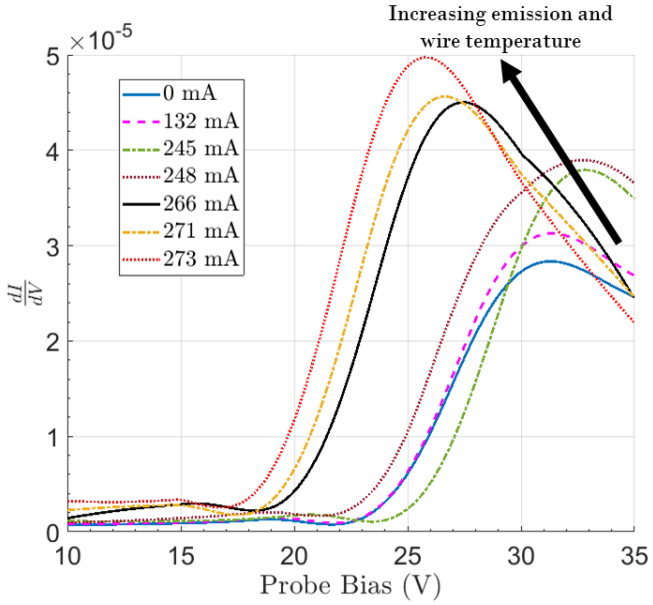


Figure 6.9: Example emissive probe first derivatives of typical IV curves demonstrating the effect of increased emission (unmagnetised 6 Pa, 10 W Ar).

For all experiments performed with the I.P. method in this thesis the fit to the inflection points was extrapolated to the potential at the heating current where the IV curves do not change shape with heating current (see figure 6.2). In the bulk, this is generally very close to zero heating current. The error in this method is, in theory, approximately the wire temperature but has been predicted by numerical simulations to be on the order of 1.5 $T_e$ [152]. Moving into the sheath, where the electric field is stronger, emitted electrons are quickly accelerated away from the probe so stronger emission is required to detect an inflection point. This means that, as the inflection point is only discernible above a certain heating current, extrapolating to

0 mA will give greatly erroneous results.

In figure 6.9 some peaks at lower heating currents shift to more positive biases. This was commonly observed in these experiments but the shift was always within $T_e$ (around 3 eV) so is likely not caused by the plasma changing so these points were ignored for fitting. Although a full passive RF compensation system could not be used due to space constraints, some external inductors were added to the circuit (on both terminals of the transformer) to investigate if RF could be the cause of this shift. Only small changes in the shape of the IV curves were observed while the trend remained, but as these inductors could not be placed in the probe itself RF cannot be definitively eliminated as the cause.

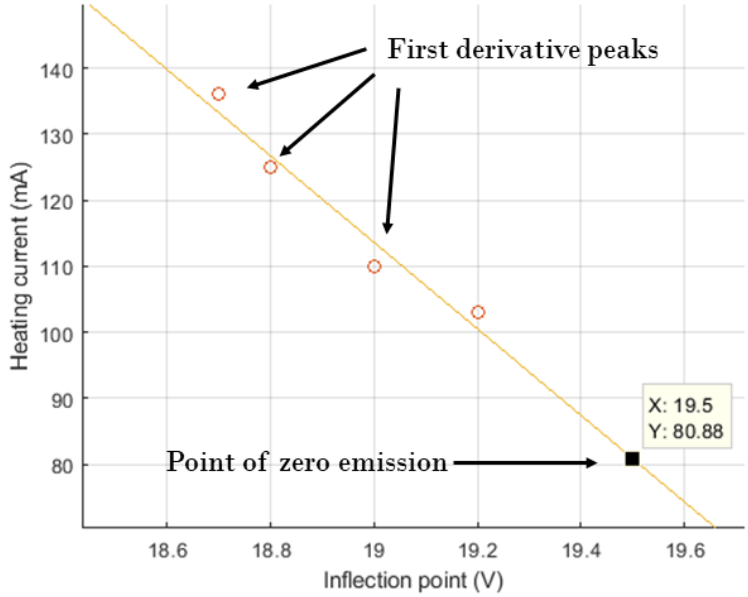


Figure 6.10: Inflection points taken by a 50 $\mu$m V - shaped emissive probe 12 mm above the powered electrode. The point of zero emission is taken at the heating current at which the inflection point no longer shifts. (unmagnetised, 6 Pa 3 W Ar).

Figure 6.11 shows a preliminary vertical sheath profile measured with the floating and the inflection point method in a 6 Pa, 10 W Ar plasma. The sheath boundary, approximated visually using the boundary between the bulk and dark space, is shown by the dashed line. In the plasma bulk (to the right of the dashed line) the I.P. method measures a value of $V_p$ about 2 $T_e$ above the floating method which is consistent with the literature [14]. In the sheath only the I.P. method tends towards the DC bias on the electrode (- 120 V). A functional fit of the Child - Langmuir law (not including density or temperature) is in good agreement with the I.P. data in the sheath. The floating method does not agree with the I.P. method in the sheath which may be due to the

sheath overlap effect described in section 6.2.2 or the resistance being too low. Consequently the I.P. method must be used for all experiments performed in the sheath.

When a vertical potential profile was performed moving into the sheath, the floating method failed to respond as expected. This response was observed even when a high impedance operational amplifier was used instead of the 100 MΩ measurement resistor. This is consistent with observations by Fujita *et. al.* at low resistance who observed that the potential drop moving into the sheath did not follow the expected potential for any resistance close to the powered electrode, and further away from it became more accurate with increasing resistance [144]. However, the present results differ from those of Diebold *et. al.* who found that a high impedance operational amplifier was sufficient to observe the expected trend in sheath potential with the floating method. A crucial difference between the present experiments and those papers is the DC plasma used in both papers and the RF plasma used here, as a low impedance path to ground at high frequency is present with the measurement resistance or operational amplifier.

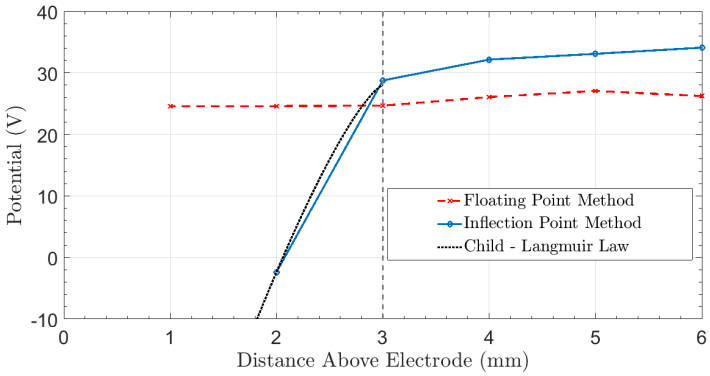


Figure 6.11: Sheath profile measurements with 50 micron emissive probes using floating and IP methods (6 Pa 10 W Ar).

### 6.4.1 DC Electric Field Scans

As the I.P. technique is the only method that can be used in these experiments to measure the potential in both the bulk and the sheath, it must be demonstrated that it is accurate and reliable. In order to do this, vertical profile scans in vacuum with only a DC bias on the powered electrode have been performed. This was done by removing the N-type connector, located below the plasma chamber (see figure 3.2), and replacing it with a BNC to N - type adaptor. This was then connected to a DC power supply (EA ELEKTRO AUTOMATIK 3050A). The chamber was pumped down to its base pressure of $5 \times 10^{-5}$ Pa. Several scans were taken by

the probe at different biases and increasing height above the powered electrode. The height was measured using the positioning system shown in figure 3.6.

Figure 6.12 shows some example IV curves taken with a DC bias of - 50 V with smoothing applied. When the probe is biased below the local potential and is heated electrons are emitted resulting in an emission current ($\approx$ -1.5 $\times$ $10^{-8}$ A). When the probe is biased above the local potential the emitted electrons are returned to the probe with approximately zero emission current. In the intermediate range, around the local potential, those electrons with enough energy can overcome the potential barrier and are not returned. Those with lower energies are returned to the probe. This creates two flat regions with and without emission resulting in an S - shaped curve. Emission above a certain level is necessary to observe an I.P. (164 mA in this example). It was found that when the local potential was measured in the same way as for plasma conditions (i.e. the limit of zero emission method) the local potential was in severe disagreement with the expected value (by up to 40 V). The expected value was calculated from $V = E / d$ where $V$ is the local potential, $d$ is the height above the powered electrode and $E$ is the electric field (- 50 V / 40 mm in this example). The local potential was instead measured from the peak of the first derivative of the curve with the smallest emission current where the S - shape starts to develop. This was found to give closer agreement.

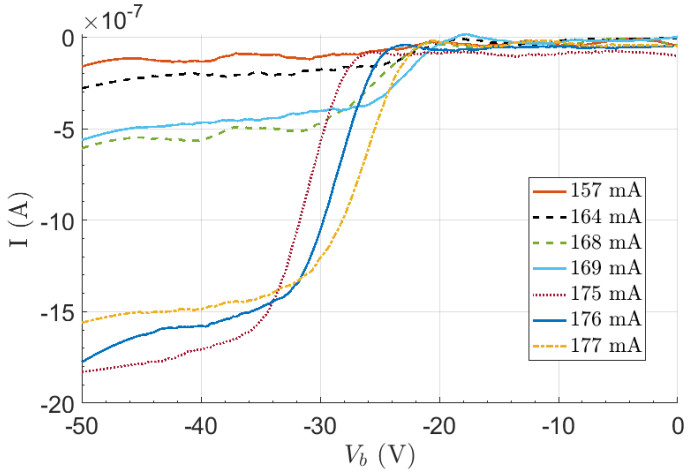


Figure 6.12: *Example IV curves taken at 10 mm above the powered electrode (biased at - 50 V) in vacuum.*

Figure 6.13 shows an example vertical potential profile, measured with the minimum emission method and a V - shaped probe, along with the predicted field for a DC electrode bias of - 28 V. The probe was moved vertically upwards in the centre of the chamber over the course of the scan. The measured field does not agree with the predicted field. One possible reason for this disparity is the potential not being linear between the electrodes (i.e. $E = V / d$

fails). The walls are also grounded and the chamber is relatively small. This could distort the field above a certain height leading to a change from the expected potential. Close to the electrode, however, the profile should still be linear and tend towards the DC bias but this was not observed in experiments. This could also be due to the surface condition of the electrode which could be contaminated with insulating impurities [137]. This will induce charge on the vacuum side of the insulating layer and cause a voltage drop across it so extrapolation of the local potentials will be erroneous. A further possible explanation for the disparity is that the ITO coated ground electrode could be floating (i.e. the conductive coating had been removed by the plasma) which would change the shape of the field. This was later investigated using an ohmmeter with probes to test the conductivity of the ITO coated electrode at several points across the surface. No conductivity was measured in the plasma facing area so the electrode was floating. It is not known whether the ITO coating was present in the DC tests.

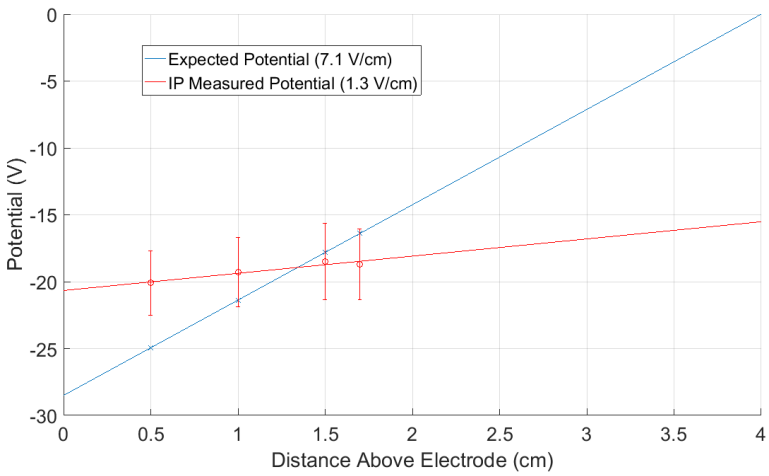


Figure 6.13: *Inflection point potential scan in DC electric field using the minimum emission I.P. method with predicted values (-28 V DC bias). The error bars were calculated from the potential between the two turning points in the IV curves.*

Another possible explanation is that of noise. Although the IV curves shown in figure 6.12 are smoothed, it is clear from the unsmoothed curves (see figure 6.14 for an example) that there is an oscillating ”ripple” effect in the IV curve which may cause the disagreement between theoretical and experimental potential profiles. By using the time between voltage steps on the Hiden (0.002 s per voltage step of 0.1 V) and the period of the oscillations in the IV curves (1.2 V), the frequency of these oscillations was calculated to be approximately 50 Hz. This shows there is mains noise in the system. Note that in figure 6.14 the frequency of the noise is constant but the amplitude scales with the applied potential. This could be an issue in sheath measurements because the lower density in the sheath results in a lower current measured by

the probe and therefore a lower signal to noise ratio. The mains supply is used in the Variac and the isolation transformer which gives rise to this noise. In order to see whether this effect is present during plasma measurements, IV curves (unsmoothed and without averaging) were taken using a cold Langmuir probe in the bulk of a 2 Pa 10 W argon plasma. As shown in figure 6.15 noise can clearly be seen throughout the entire IV curve. A mains filter was then added to the circuit (between the mains source and the variable transformer) in order to reduce this noise. The mains filter clearly improves the signal to noise ratio throughout the IV curve, but it can be seen in the ion current region that some 50 Hz oscillations remain. The frequency of oscillations was calculated using the same method as for the DC curves. During a sheath scan the inflection point will occur in the ion current region so the effect must be minimised.

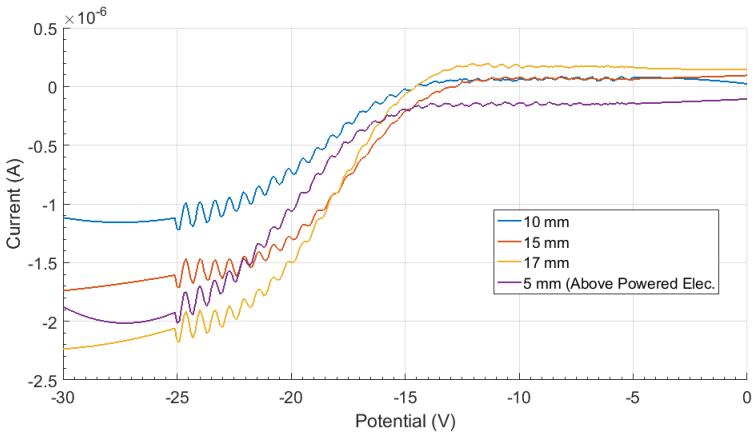


Figure 6.14: IV curves taken in DC conditions without smoothing (-30 V DC bias).

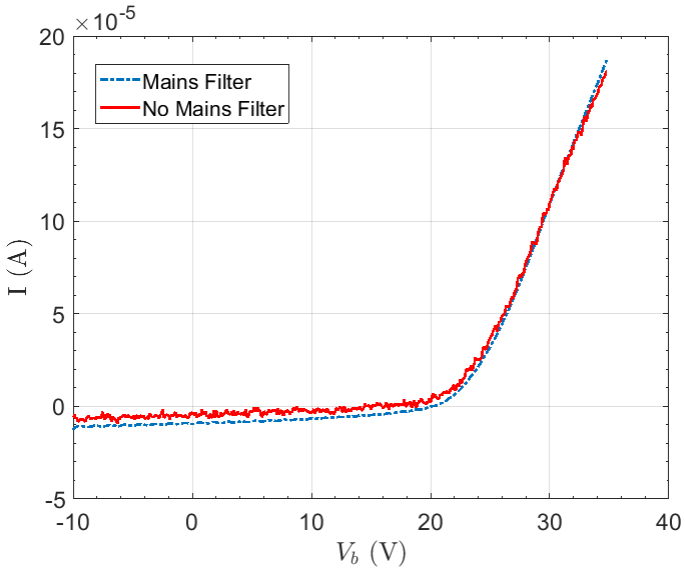


Figure 6.15: IV characteristic taken in plasma with and without a mains filter (10 W, 2 Pa Ar).

In order to remove the possible non - linearity of the electric field a moveable ground elec-

trode was designed and is described in section 3.1.2. By moving the rod into the chamber, the gap between the electrodes can be adjusted from 0 - 40 mm. The electrodes were cleaned to remove insulating impurities which was initially done by using a coarse emery cloth (sprayed with isopropanol) mounted on a spinning machine along with the electrode. The electrodes were cleaned until the cloth showed very little discolouration at which point a finer grade emery cloth was used. This process was repeated a total of 11 times until the finest grade emery cloth available had been used. As well as removing impurities from the electrode, this would also reduce the surface roughness. The electrodes were removed from the spinning machine and installed in the chamber whilst wearing latex gloves to avoid contamination of the electrode surface. The electrodes were also cleaned with the plasma (by ion bombardment) for one hour in a 40 W, 6 Pa Ar plasma. This was repeated weekly over the course of the experiments.

Figure 6.16 shows several potential profiles taken at different electrode gaps ($<$ 20 mm) and biases along with the expected profiles. The mains filter was used in these tests. Significant improvement in the measured profiles were observed compared to the larger electrode gap (40 mm) prior to the cleaning. The profiles are generally in agreement with the expected values. It was found that for an electrode gap $>$ 20 mm the measured profile diverged from the prediction which supports the hypothesis that the electric field is non - linear. As the mains filter did not sufficiently remove the 50 Hz oscillations in the IV curves a new setup was developed.

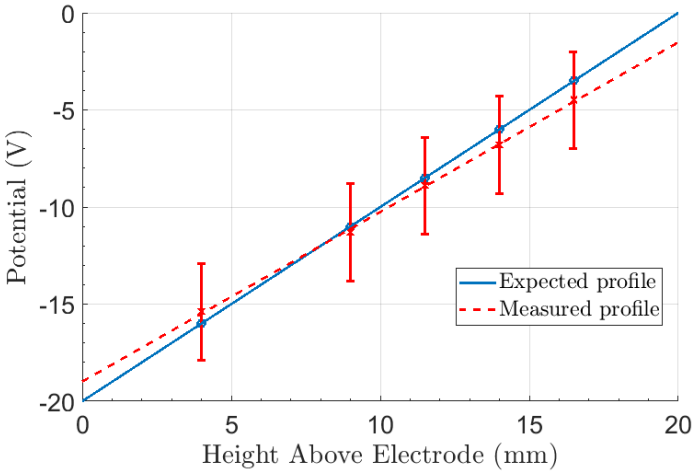


Figure 6.16: *Inflection point potential scan in DC electric field using the adjustable ground electrode (positioned 20 mm above the powered electrode) with predicted values (-20 V DC bias).*

An experimental method was still needed that could minimise the 50 Hz noise in low density sheaths. This was achieved using a novel setup which is shown in figure 6.17. This setup involved removing the variable transformer and instead using a signal generator (Aim

TTi TG135) connected to an audio power amplifier (Citronic PPX900) which was operated in bridge mode (which allowed the largest power output). The use of an audio power amplifier significantly reduces the amount of mains noise, as this is necessary to eliminate electrical humming in audio systems. A new fixed transformer (also of a turns ratio of 26) was constructed with two diodes added in order to provide half-wave or full-wave rectification of the signal which could be switched in individually. A TTL triggering signal was used to take scans in the off-cycle period of the heating cycle. The position of the triggering signal was checked on the oscilloscope. The system was tested by using the inflection point method to determine the linear electric field between the electrodes in a vacuum with only a DC bias (no RF) applied to the lower electrode as for the previous tests (including the adjustable ground electrode). The signal generator sets the frequency and amplitude, and the amplifier is used to increase the power supplied to the filament. The heating current could be measured either externally using a multimeter or using the current probe built into the transformer. For these experiments the average heating current was recorded with a multimeter. The TTL trigger output of the signal generator was connected to a pulse generator (Thurlby-Thandar TGP 110) which provided a delayed TTL pulse to the Hiden triggering input. The current is half - wave rectified with the switched - in diodes located between the transformer and the probe tip. This allows for a half - cycle off period for triggering. The novel setup offers several advantages, including a reduction of mains noise and, as a 50 Hz mains signal is not needed, the frequency can be increased over a certain range. This allows for a faster measurement time if a frequency higher than 50 Hz is used.

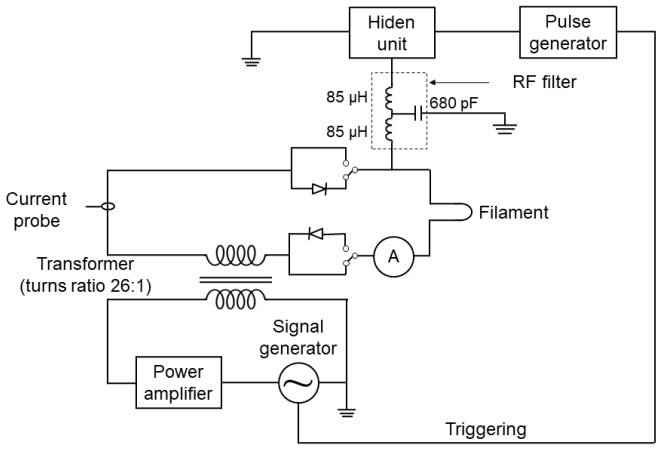


Figure 6.17: The emissive probe heating and acquisition circuit including a low - noise audio power amplifier and signal generator typically used at 600 Hz.

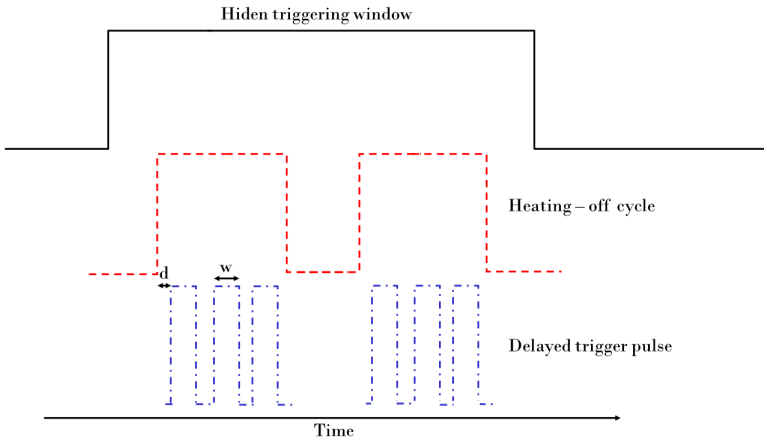


Figure 6.18: Triggering signals used in the acquisition of IV curves with the audio power amplifier and signal generator setup.

The triggering sequence, shown in figure 6.18, worked as follows: The auxiliary output of the signal generator (figure 6.18 (a)) was connected to the pulse generator input. The rising edge of this auxiliary output is simultaneous with the start of the heating off cycle. The pulse generator was used to make a second TTL pulse train (figure 6.18 (b)). This was delayed by a time ($d$) and of a much shorter duration compared to the input pulse. The delay was adjusted to position the output pulses in the centre of the heating - off period which was measured on an oscilloscope. The output of the pulse generator was connected to the TTL triggering input of the Hiden unit. The Hiden unit, operating in level triggering mode, provided a long duration measurement window (figure 6.18 (c)). Pulses outside of this window are ignored whereas those inside the window were used to acquire measurements. The pulse width ($w$) and frequency were adjusted using the pulse generator to determine the number of measurement points taken by the Hiden within the same half cycle. The pulse width must be larger than the time taken by the Hiden unit to measure a point (2.12 $\mu$s) or the unit will stall. Measurements were taken at several positions in the heating - off period (see figure 6.19) since there would be no current flowing through the probe that would create a potential drop (across the wire) which would affect measurements. Triggering was done to ensure the wire was at the same temperature at each measurement point. Since the number of measurement points can be adjusted, increasing this can be used to acquire measurements faster with the possible drawback of changing wire temperature.

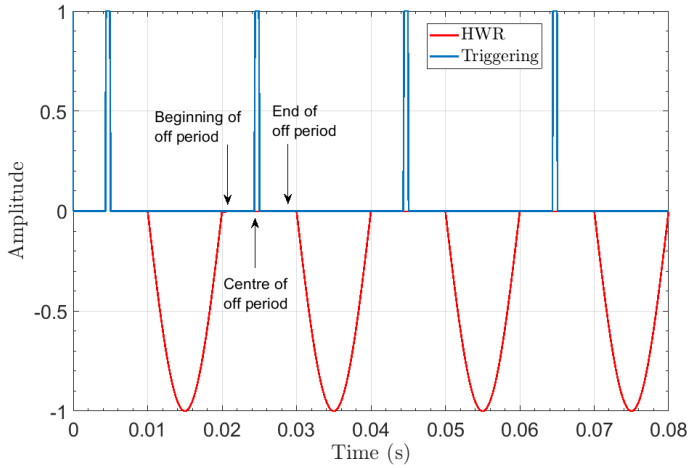


Figure 6.19: Schematic triggering waveform and half wave rectified signal.

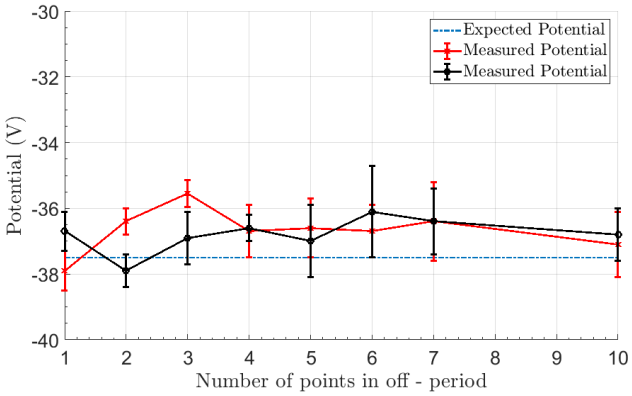


Figure 6.20: Local potentials measured 10 mm above the powered electrode in vacuum (DC bias -50 V) with increasing number of measurement points in the heating - off period (50 Hz driving frequency).

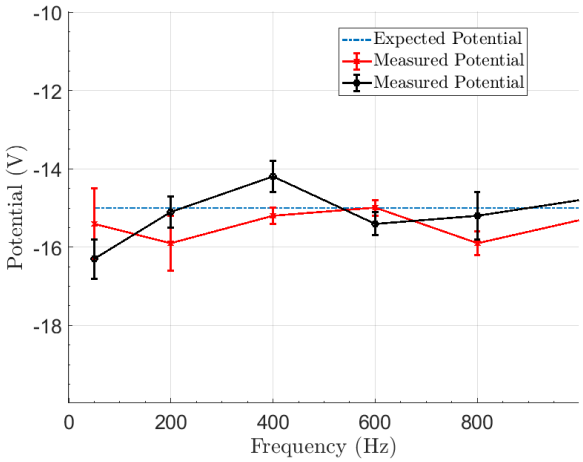


Figure 6.21: Local potentials measured 10 mm above the powered electrode in vacuum (DC bias - 20 V) with increasing signal frequency.

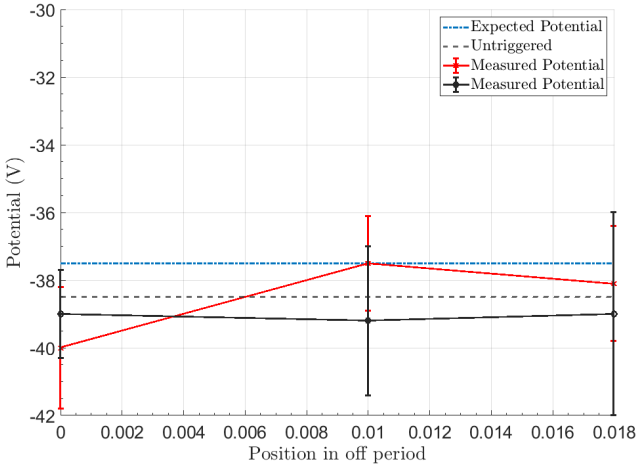


Figure 6.22: Local potentials measured at different triggering signal position in the heating period measured 20 mm above the powered electrode in vacuum (DC bias - 50 V, 50 Hz). Zero indicates an untriggered signal.

Experiments were carried out to optimise the new setup by adjusting the number of data points measured by the Hiden in the heating off - period. The system was tested by measuring between 1 and 10 points in the heating - off period with the position of the pulse in the off-cycle kept constant in the centre of the heating - off period. The frequency was also kept constant at 50 Hz. As shown in figure 6.20, the results generally indicate an approximately constant potential with an increase in the number of data points in the off cycle. The average difference between the measured and expected values was 1.1 V. The measured and expected values generally agree within error, with the exception of some points between 2 - 4 points in the off - period.

The disparity between the measured and expected values may be explained by a number of factors: (i) an offset in the height of the probe, which is described in section 6.2.2. The two ceramic tubes are at a slight angle relative to each other which will give a 2 - 3 mm difference in height of the ends of the tubes. This results in a potential difference of 3 V (number of point scans) or 1 V (frequency and position in off cycle scans) which would account for the disagreement observed.

In a separate experiment, the signal frequency was varied between 50 and 1000 Hz with the TTL triggering signal kept at the centre of the off heating period. The probe was positioned 10 mm above the powered electrode (halfway between the electrodes). A DC bias of - 20 V was applied to the powered electrode leading to an expected potential at the measurement point of - 15 V. These were performed at the base pressure of 2 $\times 10^{-3}$ Pa. The effect of increasing the

frequency of the applied signal on the measured local potential is shown in figure 6.21. The largest disparity between prediction and measurement (2.2 V) is observed at 50 Hz, which is the mains frequency used with the previous setup and by other researchers [14, 81, 136]. As the frequency increases, the discrepancy decreases to an approximately constant value of 0.15 V above 400 Hz. The reason for the disparity at 50 Hz is not clear, but may be caused by the cooling of the filament between heating cycles. A longer heating off period (i.e. a lower frequency) results in more cooling of the filament over the off - period so the temperature drops further from the average value. This results in larger temperature fluctuations. At higher frequencies, the cooling time and temperature fluctuations are reduced so the temperature tends towards its average value and becomes more stable. The shape of the IV curves changes with wire temperature (see figure 6.12), so ideally this temperature should be constant over the measurement time ($\tau_m$ = 2 ms on the Hiden) giving a measurement frequency of $f_m$ = 500 Hz which is near to the region of closest agreement in figure 6.21. This suggests that if the driving frequency, $f_d = 1/\tau_d$, satisfies $f_d > f_m$ then the temperature fluctuations will be minimised. However, if $f_d$ is too large, then $\tau_m$ will become greater than $\tau_d$ / 2 (i.e. the measurement half period) so the measurement time will include part of the heating cycle. This will result in a temperature change during the measurement time which will in turn change the measured potential. Consequently there is a requirement that $f_m < f_d < 2f_m$ in order to achieve an accurate potential measurement (within 0.15 V). This criterion is not strict and depends on several factors. This assumes that the measurements are taken at the start of the heating - off period which is generally not the case. Furthermore, the lower limit of the criterion is approximate and depends on the cooling frequency which is more rapid at high pressure so this criterion also has a pressure dependence.

The position of the delayed pulse was changed to different points in the heating - off cycle shown in figure 6.22 (50 Hz driving frequency). The pulse was delayed such that the measurements (dots) were taken at the start, centre and close to the end of the half - period. In a separate test, no triggering was applied which is indicated by the horizontal dashed line. As for the previous parameter scans, the error bars are calculated from the noise in the IV curves and the measured potentials only agree within the error for one scan at the centre and end of the off - period. The measured potentials are generally lower than the expected potentials which may be explained either by the height offset of the probe described previously or an overestimate of the emitted current (which will shift the potential more negatively).

The error bars for all of these parameter scans are given by the differences between the lower turning potential in the IV curve at the same emission (see figure 6.12) between repeat measurements. Initially the error was also calculated from $2\sigma$ (standard deviations) from the noise in the raw IV curves. Not only was the error in turning potential on average 0.4 V larger than the noise, but there was no consistent trend in the noise errors. The error in the turning points are both larger and, in general, more consistent.

Although most of the measured points on these plots agree with the expected value within error, some may have a disparity of more than 1 V. This is most likely due to the degradation of the probe with time. As the heating current is passed through the probe, the thorium doping begins to boil off and the structure of the wire is weakened. After a certain amount of time (depending mostly on wire size and current), the probe will break and must be replaced. This occurred several times during these experiments, but does not systematically affect the results.

A further test involved switching between using one, both or no diodes on the fixed transformer. When both diodes were switched in, the impedance was too great to achieve a sufficient level of emission. With no diodes, there was not a period of zero current to take measurements. All experiments were therefore taken with the same (single) diode switched in each time for half wave rectification.

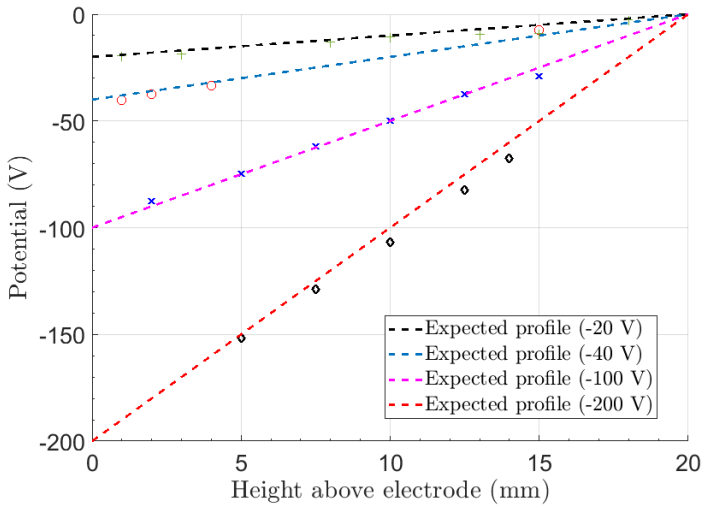


Figure 6.23: Measured vacuum potential profile with the signal generator and audio power amplifier (600 Hz, 1 point in centre of off period) .

In order to verify the new setup, it was used to acquire vacuum DC potential profile scans at two DC biases of -20 V and -40 V. This was done with a 600 Hz driving signal and one measurement point in the centre of the off period. As shown in figure 6.23 the measured (solid

line) and expected (dashed line) profiles agree to within 5 %. This key result shows that the novel setup is effective in removing mains noise and allows accurate measurements of potential in vacuum DC systems. It is therefore possible that the method will also work in low density plasma sheaths which will be investigated in the following section.

## 6.5 Potential Profile Measurements

With the novel setup shown to work in vacuum DC conditions, with good accuracy to within 0.2 V, it was then used to measure the potential profile in RF plasma sheaths. Note the emissive probes used in RF conditions in this section are not RF compensated. This is partly due to a lack of space inside the probe stem for inductors and partly due to findings in the literature that RF compensation of emissive probes is generally unnecessary (see [14] and the references therein). The driving frequency used was chosen to be 600 Hz to provide a reasonably fast measurement time. With 1000 averaging and 50 V voltage range at one data point per cycle the measurement time is 14 minutes. This is considerably shorter than the same conditions at 50 Hz, which lasts 3 hours. Measurements were taken in the middle of the half-wave rectified off - cycle. The V - shaped emissive probe was used to measure the sheath potential profile from which the electric field was calculated. This was done by fitting a second order polynomial fit to the data and taking the derivative. This has been shown by Tomme *et. al.* [157] to agree with a number of sheath models, including RF models, to within 1%. Emissive probes have also been used in magnetised plasmas in the literature [158], including in tokamaks [159, 150], Hall thrusters [73] and magnetrons [78].

An important observation from the literature is that of Wang and Hershkowitz [136] who observed that as the probe moves into the sheath, the gradient of the fit to peaks of first derivatives changes sign. In other words, the inflection point potential shifts from increasing with decreasing emission current in the bulk to increasing with increasing current in the sheath. This was done in a multidipole DC plasma with a base pressure of $1.3 \times 10^{-4}$ Pa. The authors show that this change occurs in the transition region (sheath edge). They state that this occurs because the electrons are accelerated into the plasma due to the strong electric field and they reduce $n_i$ - $n_e$ in Poisson's equation (equation 1.1). A stronger emission current is needed to perturb the local potential and therefore change the shape of the IV curve. This will reduce the local dV / dx in the vicinity of the probe which makes the measured potential higher than

the undisturbed potential. This effect increases as emission increases, and moves the inflection point more positively with emission [136]. In the bulk, where there is no electric field, the emitted local electrons are not accelerated away and decrease the local potential around the probe.

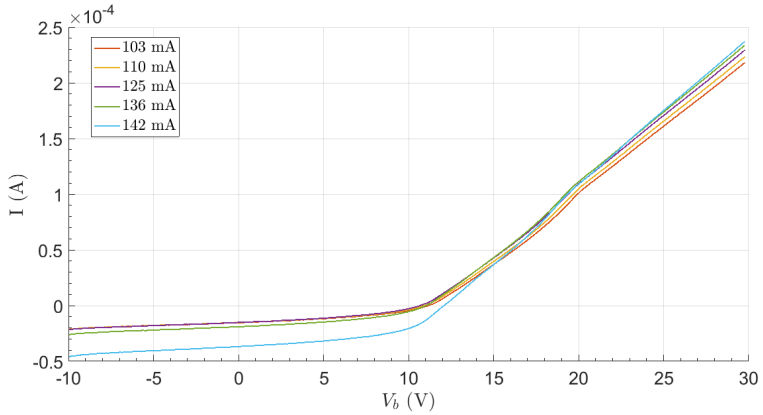


Figure 6.24: Example IV curves taken in the bulk with the V - shaped emissive probe (11 mm above powered electrode in a 6 Pa 3 W, Ar plasma).

Using the emissive probe positioning system (see section 3.6) a vertical potential profile scan was performed in an unmagnetised, 6 Pa argon plasma by taking scans at 0.5 mm increments into the sheath. The RF power on the electrode was varied from 2 - 10 W in order to vary the DC bias on the powered electrode from approximately - 80 V to - 120 V. This range was chosen as the Hiden unit cannot measure potentials below - 200 V. Figures 6.24 and 6.25 show typical IV curves taken in the plasma bulk and sheath respectively with increasing emission. The shape of the IV curves in the sheath mean they cannot be analysed with cold probe theory, but the first derivatives (shown in figure 6.27) do show an inflection point which changes with emission. This means that the local potential can be measured in the sheath with the IP method.

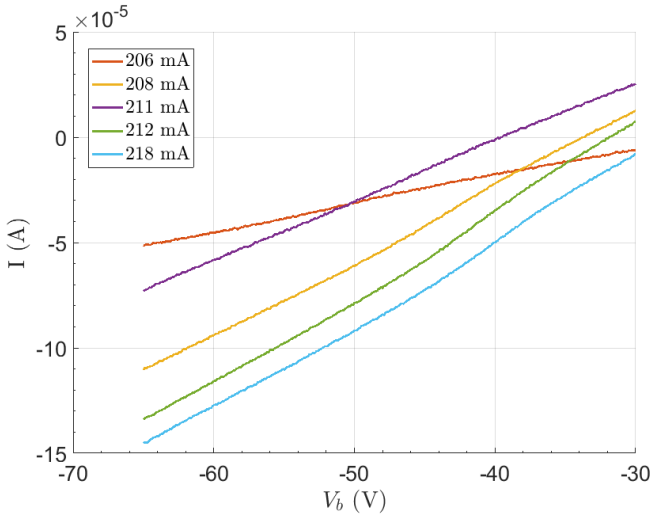


Figure 6.25: Example IV curves taken in the sheath with the V - shaped emissive probe (2.5 mm above powered electrode in a 6 Pa 3 W, Ar plasma).

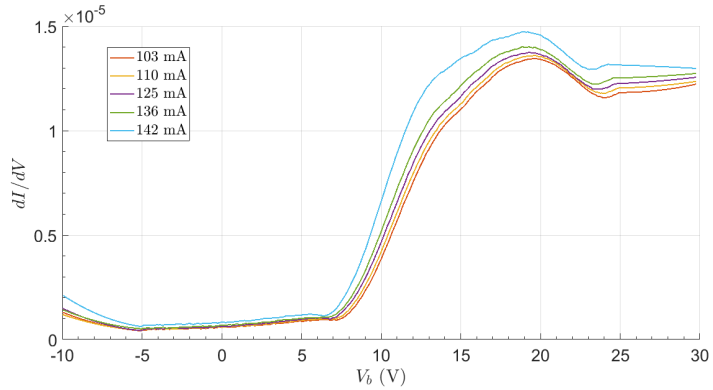


Figure 6.26: Example IV curves taken in the bulk with the V - shaped emissive probe (11 mm above powered electrode in a 6 Pa 3 W, Ar plasma).

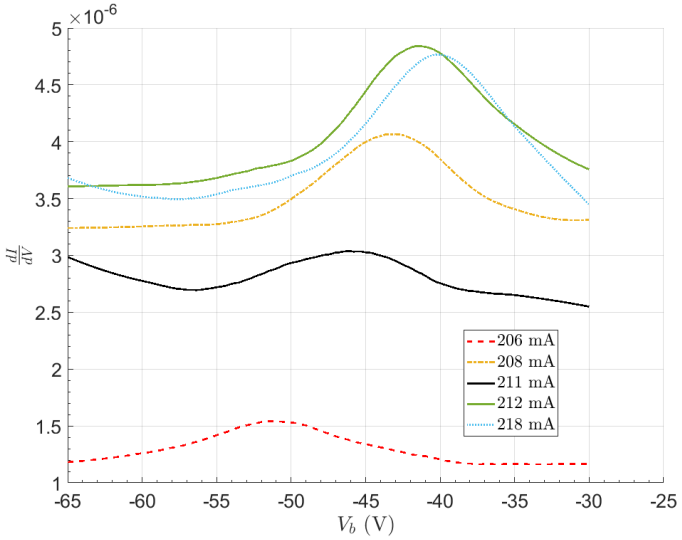


Figure 6.27: Example first derivatives of the IV curves (shown in figure 6.25) taken in the sheath with the V - shaped emissive probe (2.5 mm above powered electrode in a 6 Pa 3 W, Ar plasma).

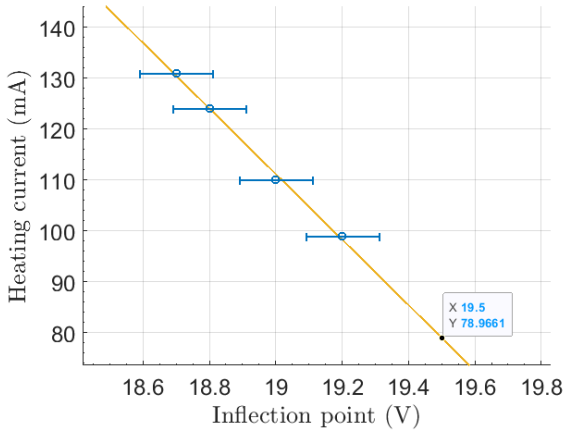


Figure 6.28: Extrapolation of peak potentials to zero emission in the bulk (11 mm above powered electrode in a 6 Pa 3 W, Ar plasma). The local potential is indicated by the square.

Figures 6.28 and 6.29 show examples of the extrapolated fits to the first derivative peaks in the plasma bulk (11 mm above the electrode) and sheath (2 mm above the electrode) respectively. These were both taken in a 6 Pa, 3 W argon plasma with a DC bias of - 80 V on the electrode. The local potential is indicated by the black square on the figures. The scans are not extrapolated to zero heating current as these will give highly erroneous measurements which is particularly true of the sheath scan. Measurements were taken with decreasing heating current until the peak of the derivative can no longer be discerned as indicated by the square on the figures. This is taken to be the limit of zero emission and all the points are extrapolated to this heating current (see section 6.4). The figures show that the gradient changes sign upon moving into the sheath which is in agreement with Wang and Hershkowitz [136]. This effect has been consistently observed in these experiments and has been used as a measure of the sheath edge.

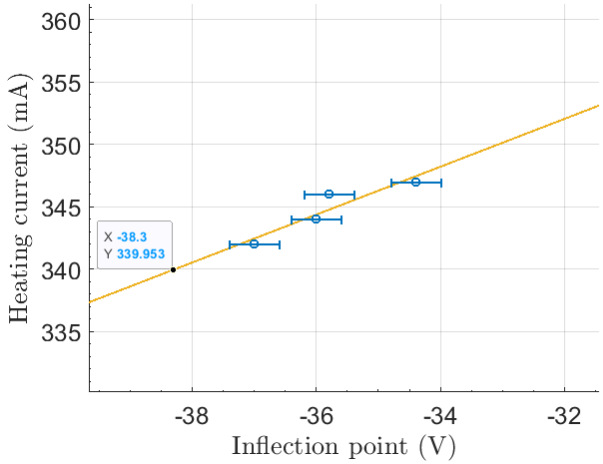


Figure 6.29: Extrapolation of fit to peak potentials to zero emission (2 mm above powered electrode in a 6 Pa 3 W, Ar plasma).

By taking a series of these measurements at several heights above the electrode, a potential profile of the sheath can be plotted. Some examples of these, taken in a 6 Pa argon plasma, are shown in figure 6.30. The RF powers used were 2, 3 and 5 W to vary the DC bias on the electrode from -70.2 V to -99.2 V. A simple second order polynomial (from Tomme *et. al.*) is a good fit to all of the profiles, with $R^2$ values of greater than 0.91. The peak of the polynomial agrees with the average bulk plasma potential to within 1 V.

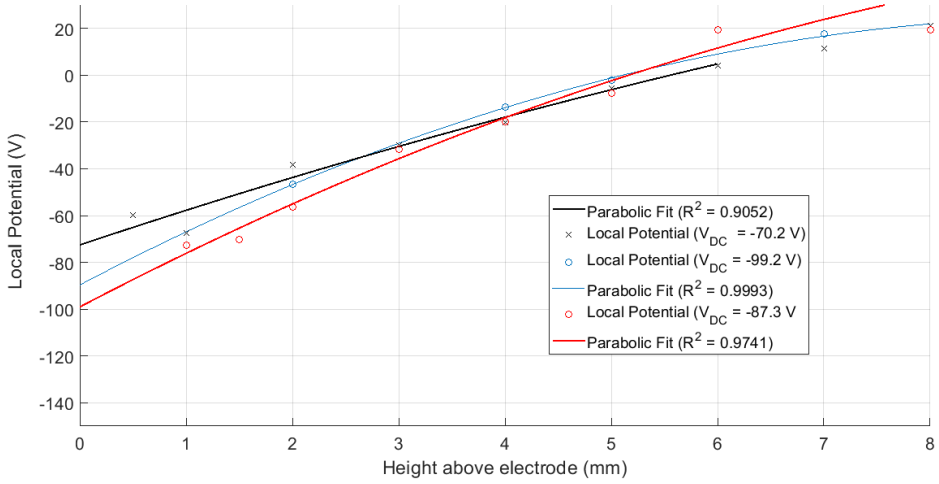


Figure 6.30: Plasma sheath profiles taken at varying DC biases on the electrode (6 Pa, 2, 3 and 5 W RF ).

The fit was extrapolated to the potential at zero height (the powered electrode) to predict the DC bias which was compared to the measured value and was found to agree to within 12 %. This has been measured at DC biases of -70.2 V (extrapolated to -71.4 V), -99.2 V (extrapolated to -89.9 V) and -87.3 V (extrapolated to -99.1 V). This novel method therefore provides an accurate measure of potential over the bulk and sheath regions in unmagnetised RF plasmas, minimising the issues of mains noise described previously. This can be used to determine the electric field in a sheath by taking the derivative of the polynomial fit. This key result demonstrates the novel method can measure the potential profile in unmagnetised RF sheaths and will be extended to determining that of magnetised plasmas.

## 6.6 Emissive Probes in Magnetised Plasmas

Emissive probes have been used in the bulk of magnetised plasmas in the literature including in Hall thrusters [141], anode-type double layers [160], tokamaks, [150], magnetrons [78] and magnetised RF plasmas [65]. Smith *et. al.* [77] have shown that in a magnetised multidipole

DC argon plasma at $7 \times 10^{-5}$ Torr ($9.33 \times 10^{-3}$ Pa) the inflection point shifts more negatively with increasing magnetic field for the same emission current. The shift in inflection points results in a decrease in the gradient of the extrapolated fit when the magnetic field is increased. The authors did not explain whether this shift is a change in the plasma itself or whether the method is affected by the magnetic field [161]. This was done with a "picket fence" cusped magnetic field between 16 - 30 mT and with the emissive probe oriented perpendicular to the field.

Recently, an experimental comparison of ball pen and emissive probes in strongly magnetised plasmas up to 500 mT has been performed by Harris *et. al.* [65]. In that experiment, performed in the same RF plasma chamber used in this thesis, an argon plasma of $\approx 0.5$ Pa was used with increasing magnetic field. Emissive probes, using the floating method, were compared to ball pen probes of both conical and flat geometries. At a field strength of 81 mT (i.e. within the ball pen probe's operational range) the ball pen probe underestimated the potential of the floating emissive probe by at least 2.7 $T_e$ where $T_e$ was taken to be 3 eV. Above 81 mT the two methods diverge with the emissive probe giving a higher $V_p$ of up to 10 V at 500 mT. The emissive probe was found to track changes in the plasma potential but not necessarily accurately. The authors suggest that this may be due to more ions becoming magnetised which is assumed not to be the case in ball pen probe operations. In unmagnetised plasmas it has been shown experimentally and theoretically that a floating probe floats approximately 1.5 - 2 $T_e$ below $V_p$ [14]. To the present author's knowledge there is currently no general theoretical description of emissive probes in magnetised plasmas.

### 6.6.1 Results

### 6.6.2 Comparison of probe methods in magnetised plasmas

Having established that the I.P. method is reliable in both the bulk and the sheath, in unmagnetised plasmas, experiments were performed to determine its range of applicability in magnetised plasmas. In these experiments bulk measurements were taken with the floating and inflection point methods and compared with the RF compensated Langmuir probe (0.9 cm long, 50 $\mu$m diameter, 3 L ) with the earlier setup described in section 6.3. Experiments were performed in a 10 W RF, 6.3 Pa argon plasma with all the probes arranged perpendicular to the magnetic field. The loop (loop diameter 1 cm, floating method) and the V - shaped (1 cm

long, I.P. method) probes were both used but only one could be used at a time due to space constraints. The emissive and Langmuir probes were both in the chamber at the same time but the emissive was rotated away to the wall when the Langmuir was used to avoid perturbation. Similarly, when the emissive probe was used the Langmuir probe was retracted by about 2 cm. It could not be fully retracted because of the risk of disconnecting the PEEK holder. The emissive probe was positioned to be approximately the same position as the Langmuir probe. The Langmuir probe was common to both experiments to ensure repeatability of the plasma parameters.

The local plasma potential for these probes with increasing magnetic fields are shown in figure 6.31. For the Langmuir probe $V_p$ was taken from the peak of the first derivative. All of the methods agree to within $T_e$ at low magnetic fields below 15 mT where the potential decreases. For fields greater than 15 mT, the plasma potential (of the I.P. and Langmuir methods) continues to decrease, reaches a minimum at 30 mT, and then increases until 60 mT. It was also observed by Smith *et. al.*, in a DC multidipole plasma using the I.P. method, that $V_p$ decreases with increasing magnetic field between 16 to 30 mT [77]. Over this range both methods agree to within 3 V. Above 60 mT, the Langmuir and I.P. methods diverge. For the emissive probe $V_p$ increases, after the minimum at 15 mT, to 50 V at 60 mT and then stays approximately constant with increasing field up to 120 mT.

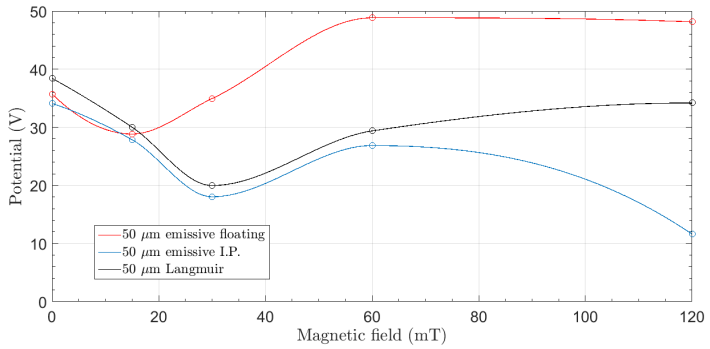


Figure 6.31: Bulk comparisons of loop emissive and Langmuir probes in a magnetised plasma (6.3 Pa 10 W).

It has been recently shown in simulations that for a spherical dust particle (radius $r_d$) $V_f$ is given by OML theory until $r_{Le}$ is approximately 10 times the dust radius [19]. If $r_{Le} < 10$ $r_d$ then the trajectories of the electrons are more influenced by gyration. This suggests that conventional cold probe theory (cylindrical geometry) should become increasingly valid as $r_{Le}$ increases above 10 $R_p$ as gyration effects become less significant. For a 50 $\mu$m the ratio $r_{Le}$ /

$R_p$ = 10 at a magnetic field of 20 mT with $T_e$ = 2.1 eV taken from the OIS measurements (see section 5.6). This is in agreement with the trend shown in figure 6.31 as the calculated value is between 16 and 30 mT.

For the cold probe electron collection is significantly influenced by electron gyration around the probe. This is shown in figure 6.32 where the electron current decreases with increasing field. This well - known effect [14] means collecting probes cannot be used to measure $T_e$ or $n_e$ which depend on the electron current. However, a peak in the first derivative is still observed (shown in the insert) which gets broader and flatter with increasing field. The good agreement between the floating and Langmuir probe up to 16 mT means that the plasma potential can be reliably determined up to $R_p \approx 10\ r_{Le}$. At stronger magnetic fields the peak in the first derivative becomes broader and flatter to the extent that the plasma potential can no longer be accurately determined (120 mT in figure 6.32). This also occurs for the I.P. method which uses IV curves and their first derivatives to obtain $V_p$. Consequently, it is expected that the Langmuir and I.P. methods will track each other. The floating emissive probe is less sensitive to magnetic fields than the collecting probe because the principle of operation relies on the emitted electrons partially cancelling the collected electrons. This principle is insensitive to magnetic fields because even though collected current decreases, as shown in figure 6.32, as long as the emitted current partially cancels the collected current $V_f$ can approach $V_p$. This is possible up to the point where the emitted electrons, under the effect of gyro motion, are returned to the probe (i.e. $r_{Le} \approx R_p$). Above this limit, it becomes increasingly difficult to partially cancel the collected current so $V_p$ cannot be reliably measured. For the 50 $\mu$m probe used here the floating method should be reliable up to approximately 240 mT assuming $T_e$ = 3 eV (see section 2.1). In these experiments the maximum field used was 120 mT which is significantly below this limit.

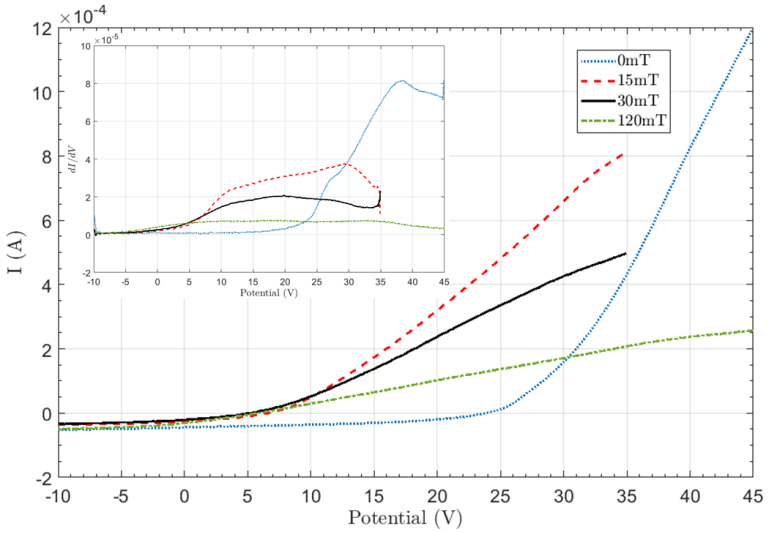


Figure 6.32: IV curves taken in the bulk of a magnetised plasma with increasing magnetic fields. Inset: The first derivatives of these IV curves (6.3 Pa 10 W).

### 6.6.3 I.P. measurements in magnetised plasmas

Figure 6.33 shows the inflection point fits extrapolated to zero emission in the bulk of a 6 - 91 mT magnetised plasma (6 Pa, 10 W). As the field is increased the gradient of the fit initially increases, then decreases before increasing again. This has been consistently observed in these experiments which is not in agreement with the findings of Smith *et. al.* in a DC multidipole plasma [77]. However, in that paper, the field was varied from 16 to 30 mT and over approximately this range (10 mT - 20 mT) the current findings are in agreement. This suggests that the novel setup used here provides a fast, reliable and robust method of measuring plasma potential even in magnetised plasmas.

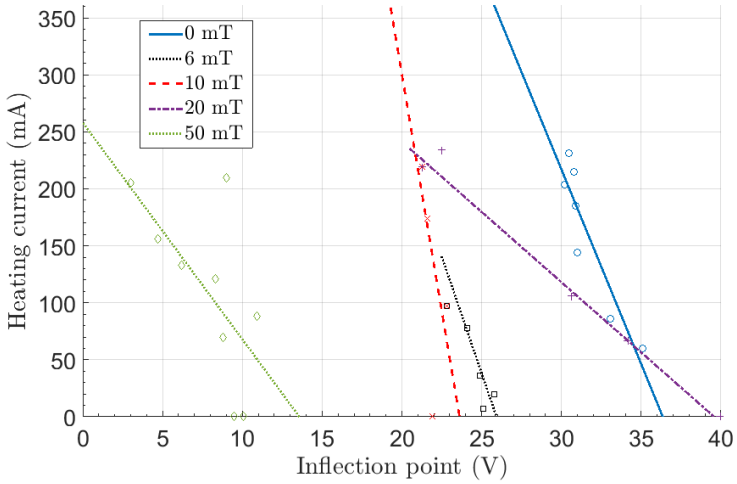


Figure 6.33: Inflection points of IV curves taken with increasing magnetic field in the bulk of a magnetised plasma (6 Pa 10 W Ar).

Having established the feasibility of using the novel method in unmagnetised sheaths and bulk magnetised plasmas, the final step is to measure sheath potential profiles in magnetised plasmas. This was done in an identical manner to the non-magnetised sheath experiments in magnetic fields between 0 - 30 mT. The resulting sheath scans are shown in figure 6.34 where the error bars are calculated from taking the range of fits within the uncertainty of the plot of peak potentials (see section 6.5). Also shown are the second order polynomial fits for each curve. These were constrained to the measured DC bias as an unconstrained fit to the data gave poor agreement ($\approx$ 20 V offset). The plasma conditions were a 6 Pa, 10 W argon plasma and a 50 $\mu$m diameter V - shaped probe was used at increments of 0.5 mm above the powered electrode. A 600 Hz driving signal was applied by the signal generator with a single point measured at the centre of the heating off half - cycle to minimise probe cooling over the measuring period.

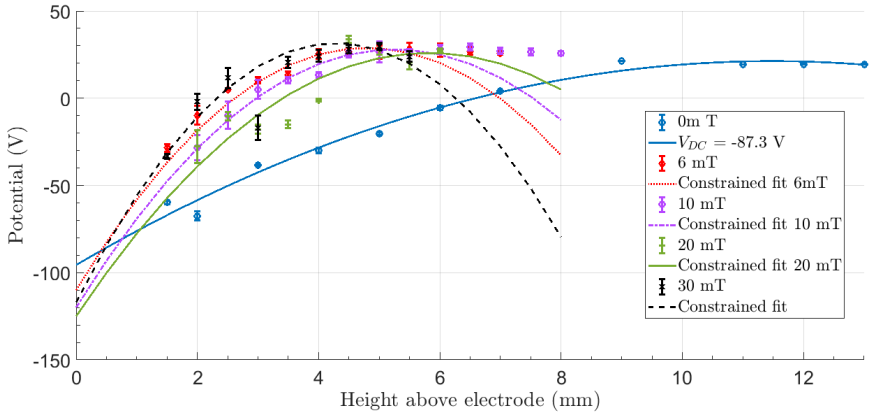


Figure 6.34: Local potentials measured by emissive probes with polynomial fits in magnetised plasma sheaths (10 W, 6 Pa Ar).

As shown in the figure, the approximate size of the sheath (indicated by the distance between 0 mm and the maximum of the parabola) initially decreases with magnetic field from 7 mm to 4.8 mm. Because the density increases with field in this range (see OIS data in chapter 5) while $T_e$ remains approximately constant, the Debye length decreases with field which causes the sheath size to decrease. The sheath then increases in size again up to 5 mm at 20 mT before decreasing to 4 mm at 30 mT. From 6 mT to 30 mT the extrapolated DC bias follows the same trend as the sheath width. A minimum in $V_p$ is observed at 20 mT which is consistent with the bulk data shown in figure 6.31. The results shown in figure 6.34 will be used to determine the charge on a dust particle in a magnetised plasma (see chapter 7).

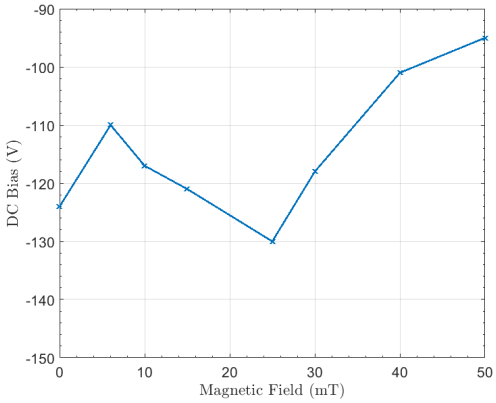


Figure 6.35: Measured DC bias on the powered electrode with increasing B field (6 Pa 10 W Ar).

## 6.7 Conclusion

Experiments were performed in the bulk and sheath of magnetised and unmagnetised RF plasmas in order to measure the potential profiles of those regions. These were done with two emissive probe methods, the floating point and inflection point in the limit of zero emission techniques. The floating point method was found to give reasonable estimates of bulk plasma potential (floating around $T_e$ / $e$ V below the plasma potential) as has been observed in the literature [14, 152]. This was the case in both magnetised and unmagnetised plasmas (e.g. figures 6.8 and 6.7). In the sheath, with no applied magnetic field, the floating potential method was found to fail as shown in figure 6.11. This is thought to be because of the decreasing density in the sheath. A similar effect has been observed by Fujita and Yagura [144] in a DC plasma when the measurement resistance was not sufficiently large. The floating method in the present experiments still failed even when the 10 MΩ resistor was replaced by a high impedance operational amplifier. This may be because the Op Amp only has a high impedance to DC and not to higher frequency signals. Consequently it was necessary to use the I.P. method for measuring the sheath potential profile.

The fact that density decreases moving into the sheath is known from the literature [144] and has been shown in these experiments using the inflection point method. The decreasing density is observed as decreased current, which worsens the signal to noise ratio and can make IV curves in the sheath inaccurate. The decreasing density makes the floating point method for determining plasma potential unreliable in sheaths given the criterion of Kemp and Sellen [72] (density from $10^5$ - $10^{12}$ $cm^{-3}$) and has been described previously (figure 6.11). Some

distortion of the IV curve will also occur as a result of the low impedance path to ground for 13.56 MHz signals (and harmonics) through the measurement resistor. A novel emissive probe setup was designed to improve the signal to noise ratio using a signal generator and an audio power amplifier to reduce mains noise. The signal generator also allows frequencies other than the mains frequency to be used which makes measurements (taken in the heating off period) faster by increasing the heating signal frequency. This technique and setup has not been reported in the literature to the author's knowledge. This method was used in the plasma bulk and to measure potential profiles in unmagnetised and magnetised plasma sheaths shown in figures 6.30 and 6.34 respectively. A simple parabolic fit, which approximates several sheath models according to the literature [157], was plotted for each of these results and extrapolated to the DC bias on the powered electrode which was accurate to within 12 %. These fits had an $R^2$ of 0.9 or greater. To the author's knowledge, such an experiment has not been performed in a magnetised sheath in the literature, nor has an audio power amplifier and signal generator been used in combination to generate a low - noise signal. This method will be potentially extremely important when measuring the sheath potential of any low - density region of a plasma (usually a sheath). This is likely to not be dependent on whether the plasma is RF or DC, as evidenced by the improved relationship in a DC field shown in figure 6.23, but all plasma experiments performed here were with RF plasmas. In magnetised or unmagnetised plasma sheaths, where mains noise is likely to be large, the present method is likely to be superior to the conventional setup used in the literature and is also faster if a frequency greater than 50 or 60 Hz is used. When using the IP method, the peak of the first derivative of IV curves was found to shift negatively instead of positively when moving into the sheath which is in agreement with observations in the literature [136].

Several opportunities for further work exist in this field. Most simply, the range of magnetic fields used could be expanded. This is possible as long as the plasma oscillations observed in magnetised plasmas are avoided and will allow for measurements of dust charging in tokamak relevant conditions. This could be achieved by using an alternative heating method, such as laser heating which has been used in the literature [162] including in RF plasmas [163]. The current and laser heated emissive probe methods were compared by Kella *et. al.* [164] in an unmagnetised RF plasma sheath. The laser heated probe allows for higher wire temperature without melting, no deformation in a magnetic field and no potential drop across the probe wire.

# Chapter 7

# Dust Charging in Magnetised Plasmas

## 7.1 Introduction

This chapter combines the results and methods used in the two previous chapters. The levitation condition of dust in an Earth - based lab is described using the force balance equation (equation 2.27). In general, the force balance equation should include the thermophoretic force [52] and neutral drag force as is the case in equation 2.27. It is assumed that $T_n = T_i$ is approximately constant in the plasmas used in these experiments. When the thermophoretic force is investigated in the literature, the electrode generally has to be heated (350 - 500 K) [52]. This is done to create a temperature gradient in the direction of the bulk which can counteract gravity and moves dust particles into the bulk. This is often desirable as if dust particles are in the bulk, then the charging dynamics become much simpler than the sheath (i.e. OML is applicable). Since the driven electrode was not heated in these experiments then $F_{th}$ can be assumed to be negligible. However, as the system is asymmetrical it is possible that a small temperature gradient exists and accurate measurements of the electrode temperature are required to know for certain. The neutral drag force is proportional to $v_d$ - $v_n$ [165, 166] (see equation 2.29) where $v_d$ is the dust velocity and $v_n$ is the neutral velocity. Typical argon neutral velocities, assuming room temperature neutrals (0.025 eV), are 390 $ms^{-1}$ far from the gas injection and extraction ports. It has been observed in these experiments that the levitated dust particles are stationary so it is reasonable to assume $v_d$ is much less than $v_n$ so $v_d \approx 0$. This approximation is commonly used in the literature for similar sized dust [50, 167]. In these experiments spherical Melamine Formaldehyde (MF) dust particles were used. These have a mean radius $r_d$ = 4.74 $\mu$m and a mass density $\rho_d$ = 1570 $kg/m^3$. The dust mass can then be calculated from $\rho_d V_d$ where the volume $V_d$ = (4 / 3) $\pi$ ${r_d}^3$. Using equation 2.29 the neutral drag force is 5 $\times$ $10^{-16}$

N assuming the neutral density is given by the ideal gas law (P = 6 Pa, $T_n$ = 0.025 eV). The neutral drag force is four orders of magnitude below the gravitational force on the grain (g = 9.81 $ms^{-1}$) giving $m_d g = 10^{-12}$ N so $F_n$ can be ignored. This reduces equation 2.27 to:

$$q_d E = m_d g + m_d \mu_{di}(E, q_d) u_i(E, q_d) \tag{7.1}$$

When only the electrons are magnetised in a weak field ($r_d \ll r_{L,e} <$ chamber size) the plasma will be modified as the electrons gyrate around the field lines and their motion becomes anisotropic. The confined electrons cause ionisation to become more localised resulting in an increase in the local plasma density. Both of these effects will change the values of $E$ and $q_d$ in equation 7.1 as well as the ion drag force (the second term on the right hand side). Because the charging dynamics to the dust remain unchanged conventional unmagnetised theory still applies. When the magnetic field becomes stronger ($r_{L,e} \leq 10\ r_d$) the charging currents to the dust become affected by the gyration [19, 168, 24]. Here there is the assumption that the particles remain in the bulk (which may not be the case). This will cause $q_d$ in equation 7.1 to deviate from the OML value as gyration is not taken into account in the theory. This also means the ion drag force becomes a function of $B$ which will also invalidate the conventional expression for the ion drag force [1] in equation 7.1. To the author's knowledge there is no general theory describing dust charging and ion drag force for any magnetic field, although some theory for a range of magnetic fields is provided by Tsytovich *et. al.* [57]. When the ions also become magnetised in a strong field the gyration around the field lines and anisotropic motion will also affect $q_d$ [19] as well as the ion drag force.

This chapter will use magnetised sheath potential profiles, obtained using the emissive probe (Chapter 6), and plasma parameters, measured using the OIS diagnostic (Chapter 5), to experimentally verify that conventional theory can be used in weak magnetic fields ($r_{L,e} < 10\ r_d$) [19, 24]. This was done by comparing the levitation heights obtained from conventional theory to those measured using a camera in magnetised plasmas. The magnetic fields used in these experiments give a maximum electron Larmor radius of $\approx 0.1$ mm which is approximately equal to the $10 r_d$ limit, so if the theoretical limit holds experimentally OML should be applicable. It is assumed in these experiments that there are no forces acting on the dust perpendicular to the magnetic field (i.e. drifts). Any curvature or grad - B drift is considered negligible as the magnetic field is uniform to within 0.3 % horizontally and 0.6 % vertically (see Chapter 3). The E $\times$ B drift in the sheath above the centre of the driven electrode is assumed to be negligi-

ble as the electric and magnetic fields in the sheath are parallel and quasi-neutrality means the electric field is weak in the bulk. The setup can be tuned to observe horizontal motion effects (e.g. plasma crystal rotation) but this was not done in these experiments and the conditions were chosen such that visible horizontal motion was minimised. The dust levitates above a 2 cm diameter confinement ring (2 cm smaller than the electrode diameter) which is placed in the centre of the powered electrode.

The mechanisms and theory regarding dust charging in plasmas has been described in section 2.4. This includes the applicability of OML theory in complex plasmas and modifications to OML theory to include ion flow (shifted OML). The ion drag force, needed to satisfy the force balance condition, is described in section 7.2. The solution of the force balance equation using the ion drag force and potential profile is described in section 7.3. Experimental results of the charging of MF dust grains in magnetised plasmas is presented in section 7.4. The conclusions are presented in section 7.5.

## 7.2 OML Charging Theory: Limiting Case of Zero Flow Velocity

Allen *et. al.* [169] have calculated dust surface potential in hydrogen and argon plasmas for increasing ion to electron temperature ratio ($\beta$). This was done using the floating condition and the standard OML expressions for the particle currents to an object:

$$I_i - I_e = An_i Ze\sqrt{\frac{k_B T_i}{2\pi m_i}}(1 - \frac{ZeV_p}{k_B T_i}) - An_e e\sqrt{\frac{kT_e}{2\pi m_e}}exp(\frac{eV_p}{k_B T_e}) = 0 \tag{7.2}$$

Note that in this equation the temperatures (and all other parameters) are in SI. A code was written by the author of this thesis to solve this equation for $V_p$ for increasing $\beta$ (in $log_{10}$ scale). The solutions for hydrogen and argon ions are shown in figure 7.1. The results shown are the same ions as used by Allen *et. al.* and agree well with the authors of [169] as expected. For the expected $\beta$ in the present experiments ($\beta \approx 0.01$, Ar+) the OML floating potential is 1.7 $T_e$.

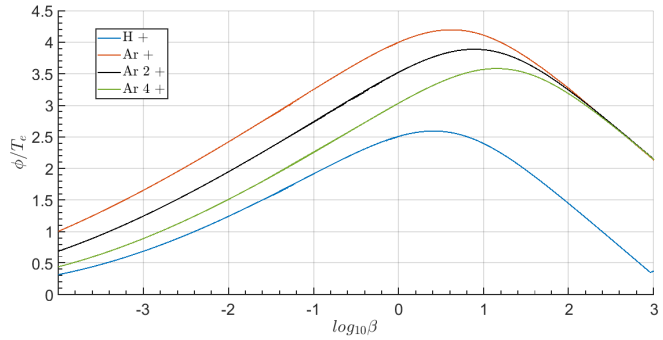


Figure 7.1: OML solutions to dust charge given by Allen for argon and hydrogen plasmas.

### 7.2.1 Shifted OML Theory

SOML was used as the basis for a theoretical model which could predict the levitation height of dust in the plasma. This was done by using the force balance equation between gravity, the ion drag force and the electric field force (equation 2.27). The force due to gravity is simple to calculate using $F_g = \rho_d V_d g$ where $\rho_d$ is the density of MF (1570 $kgm^{-3}$), $V_d$ is the volume of dust (mean radius 4.74 $\mu m$, $V_d$ = 4.37 $\times$ $10^{-6}$ $m^3$) and g is the acceleration due to gravity (9.81 $ms^{-1}$). The electric field is also relatively simple to measure in the sheath of the powered electrode by taking a vertical potential profile using an emissive probe (see Chapter 6).

The applicability of OML is limited by several factors relevant to this study. The ratio $r_d$ / $\lambda_D$ gives an indication of the validity of the thick sheath approximation which was determined by Willis *et. al.* to be 1.25 $(T_i$ / $T_e)^{0.4} < 50$ [170]. The ratio $T_i$ / $T_e$ will be given by $\beta$. Laframboise gives the limiting value of $\beta$ as approximately 3 [171]. The discrepancy may be explained by OML theory assumes spherical symmetry of the potential around the grain which is likely to not be valid in a flowing plasma.

In the literature, OML theory has been modified to account for flowing plasmas [24, 172, 173, 174]. This is done by using a shifted Maxwellian distribution instead of a stationary one. By using a shifted distribution in equation 2.25, the ion current becomes [24]:

$$I_i = 4\pi r^2 e n_i \left(\frac{k_b T_i}{2\pi m_i}\right)\left[\frac{\sqrt{\pi}}{4u}(1+2u^2)erf(u)+0.5exp(-u^2)-\frac{\sqrt{\pi}}{2u}erf(u)\frac{e\phi}{k_b T_i}\right] \tag{7.3}$$

where $u$ is the flow velocity normalised to the ion thermal velocity ($\sqrt{2kT_i/m_i}$) and $erf(u)$ is the error function of $u$. If the flow velocity tends to zero, the OML equation is recovered as

$erf(u) \approx 2u / \sqrt{\pi}$. By equating equation 7.2.1 to the electron current which is an unchanged Boltzmann distribution (due to the electrons being repelled by the grain) [175]:

$$I_e = I_i = -4\pi r_d^2 n_e e \left(\frac{k_b T_e}{2\pi m_e}\right)^{0.5} exp(\frac{e\phi}{k_b T_e}) \tag{7.4}$$

Within the sheath, there is a potential drop relative to the plasma potential ($\Delta\phi$). Consequently $\phi$ in these equations can be replaced by $\phi$ - $\Delta\phi$ to obtain the potential at a given distance into the sheath. The potential of an object immersed in a plasma according to SOML theory is then given by [24, 176]:

$$e^{-\phi} = \sqrt{\beta\frac{m_e}{m_i}}\left(\frac{\sqrt{2\pi\beta}}{4u}\left[1+\frac{u^2}{\beta}\right]erf\left[\frac{u}{\sqrt{2\beta}}\right] + 0.5exp\left[\frac{-u^2}{2\beta}\right] + \sqrt{\frac{\pi\beta}{2u^2}}erf\left[\frac{u}{\sqrt{2\beta}}\right]\frac{\phi-\Delta\phi}{\beta}\right) \tag{7.5}$$

This equation is identical to that given by Whipple [173], except with different normalisations. Equation 7.5 assumes the flow does not break the spherical symmetry assumed in OML. Hutchinson has found good agreement between the potentials given by SOML theory and a particle - in - cell code for an isolated sphere immersed in a plasma [174]. This was done with the SCEPTIC particle - in - cell code described in [177]. SCEPTIC solves the Poisson equation (with a Boltzmann distribution of electrons) for ion orbits in 3D and calculates the potential on an isolated sphere self - consistently. From this local potential the surface potential on a sphere could be calculated with equation 7.5. A code was written by the author using an in-built MATLAB solver to solve equation 7.5 for potential with increasing flow velocity. The resulting floating potentials ($\phi$), normalised to $T_e$ (eV), are plotted against flow velocity ($u$) and are shown in figure 7.2. The three curves are the solutions for increasing $\beta$ (0.01, 0.1 and 1). The simulations of Hutchinson *et. al.* were done for $\beta$ = 1 and 0.1 and are in good agreement with the solutions shown in figure 7.2. The figure also includes the situation relevant to the current experiments, where $T_e$ = 2.5 eV and $T_i$ = 0.025 eV ($\beta$ = 0.01). All the curves show a decrease in floating potential with increasing velocity reaching a minimum at around $2u$. This occurs at the point where $m_i u^2 \approx T_e$ where the kinetic energy of the ion and potential energy of the dust are approximately equal. Above this velocity the particle has enough kinetic energy to escape the potential well, reducing the collected charge. The potentials then increase again with flow velocity. The $\beta$ = 0.01 curve agrees very well with $\beta$ = 0.1 above $u \approx \sqrt{T_e/m_i}$. Below this velocity, the $\beta$ = 0.01 curve acquires a smaller charge and reaches a smaller negative potential.

Both curves increase to a maximum at $u = 0$. For $\beta = 1$ the curve is much more consistently flat and the velocity at the minimum increases slightly. At flow velocities $< 1$ the potential is more negative than for the other $\beta$ values.

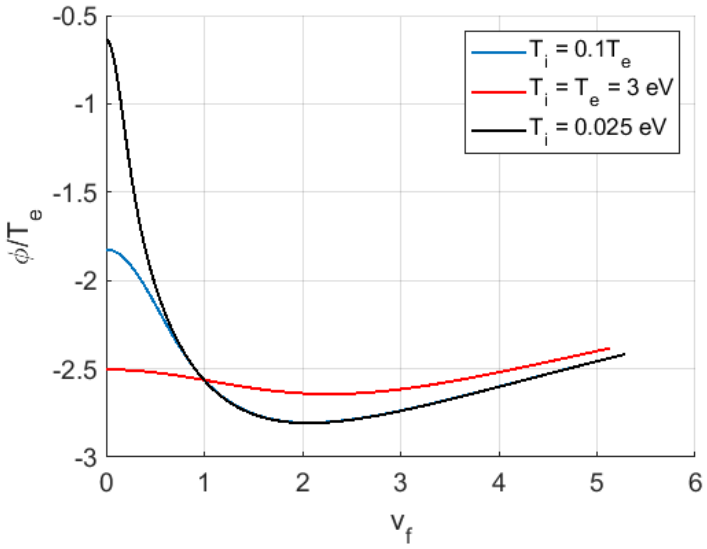


Figure 7.2: Computationally calculated floating potential of a dust particle with ion velocity. The values given by Hutchinson are included (for all curves $T_e = 3$ eV).

The number of electron charges on the dust grain was calculated using $Q_d = CT_e\phi$. Here, $C = 1/(4\pi\varepsilon_0 r_d)$ is the dust grain spherical capacitance and $\phi$ (normalised potential) was obtained from the solution of equation 7.5. This was done for both increasing ion velocity, $u$, (normalised to the ion thermal velocity) and the temperature ratio, $\beta$. The results are shown in figure 7.3 (a) and (b) respectively using a $T_e = 2.1$ eV, $r_d = 4.71$ $\mu$m and argon ions. In figure 7.3 (a) $\beta$ was kept constant, and in figure 7.3 (b) $u$ was kept constant. Note that the change in variable compared to figure 7.2 was done to ensure the results could easily be compared to the original authors. In figure 7.3 (a) $Q_d$ is initially approximately constant at $3.4 \times 10^4$ electron charges up to $u = 2$, before decreasing linearly with increasing velocity. The charge is more weakly dependent on $\beta$ but increases to a peak at around $\beta = 0.3$ for low flow velocities before decreasing again. When $u$ is increased, $Q_d$ becomes independent of $\beta$.

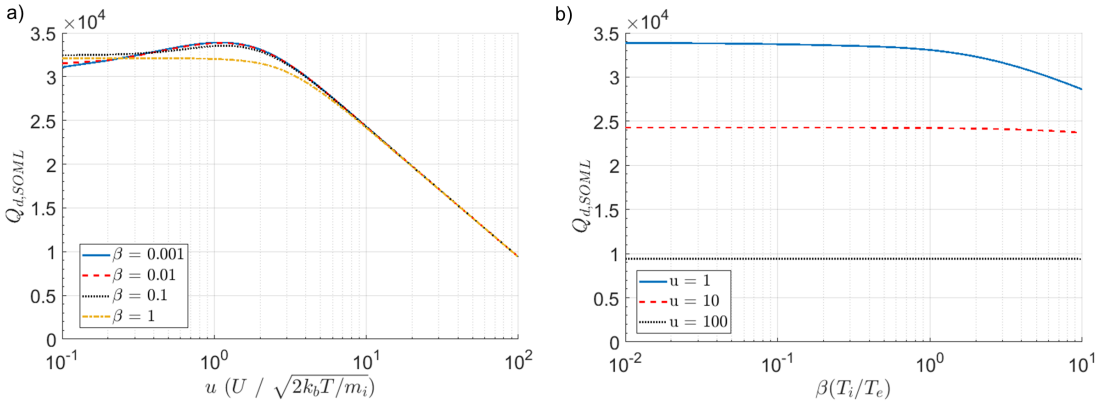


Figure 7.3: Calculated number of electron charges on a dust grain ($r_d$ = 4.71 $\mu$m, $T_e$ = 2.1 eV) as a function of (a) ion velocity and (b) ion to electron temperature ratio.

An example of the dust charge calculated using SOML is shown in figure 7.3 (b) with increasing ion velocity. This shows the case without magnetic field. By obtaining the charge at a velocity of $\mu E$, with $E$ obtained from the height of the polynomial fit where the forces balance, a total charge in terms of the electron charge was determined. For the plots which show the dust levitating in the bulk (figures 7.9, 7.10 and 7.12) this charge agrees with the conventional OML value to within 23 %.

### 7.2.2 Ion Drag Force

To determine the ion drag force ($F_i$), and compare the relative importance of $F_i$ to $F_g$ and $F_E$, the method employed by Khrapak *et. al.* was used [1]. After a lengthy derivation, the authors give the following equation for the ion drag force (in cgs units):

$$F_i = \sqrt{2\pi r_d^2} n_i m_i v_{th,i}^2 \left( \sqrt{\frac{\pi}{2}} erf \left[ \frac{u}{\sqrt{2}} [1 + u^2 + (1 - u^{-2}(1 + 2z\gamma) + 4z^2\gamma^2 u^{-2} ln\Lambda)] \right.\right.$$
$$\left.\left. + u^{-1}[1 + 2z\gamma + u^2 - 4z^2\gamma^2 ln\Lambda] exp\left(-\frac{u^2}{2}\right)\right]\right) \quad (7.6)$$

In this equation $\gamma = 1 / \beta = T_e / T_i$, $z$ is the normalised dust charge $Ze^2 / r_d T_e$, $u$ is the ion flow velocity normalised to the ion thermal velocity ($\sqrt{kT_i/m_i}$) and $ln\Lambda$ is the Coulomb logarithm which is given by [178]:

$$ln\Lambda = ln\left(\frac{\gamma + 1}{\gamma + (r_d/\lambda_{sc})}\right) \quad (7.7)$$

Where $\lambda_{sc} = (\lambda_{Di}^{-2}(1 + u^2)^{-1} + \lambda_{De}^{-2})^{-0.5}$ is the modified screening length taking ion flow into account. Khrapak *et. al.* used OML theory with a shifted Maxwellian velocity distribution to calculate the normalised dust charge $z$ as a function of $u$. This is applicable as long as the

flow velocity does not cause the potential to deviate significantly from the spherical symmetry assumed by OML. The other assumptions of SOML are still present in their analysis, including the particles being collisionless.

Equation 7.6 was solved by using the binary search method with increasing $z$ and the results are shown in figure 7.4. The ion density is calculated using the sheath model of Nitter [179]. The authors of [1] solved the equation only for $z = 3$, which agrees well with the results here. The shape of $F_i(u)$ does not change with increasing $z$, but all $z$ values converge above u = 12. Below this limit $F_i$ increases weakly with $z$. Three main regimes of $F_i(u)$ can be identified. The first is for $u < 1$ (the ion scattering regime), where $F_i \propto u$. The second, where $1 < u < \sqrt{\gamma}$, is the intermediate range where the regime switches from being dominated by ion scattering to being dominated by ion collection. In this regime the ion drag force is initially proportional to $u$ and after reaching a peak decreases proportional to $u^{-2}$. The third regime, where $F_i \propto u^2$, is the supersonic ion flow regime in which the ion drag force is dominated by ion collection [1].

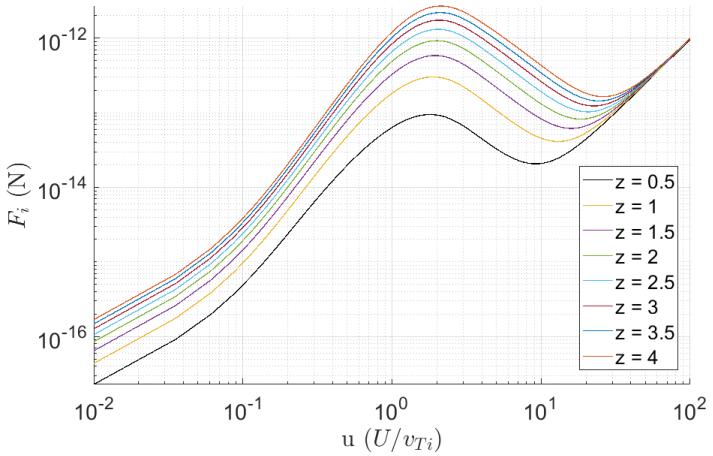


Figure 7.4: Computational code of force on a dust particle with increasing charge (z) based on work by Khrapak *et. al* [1].

### 7.2.3 Ion Collisionality

To investigate the effect of collisions in these experiments the mobility, $\mu(E)$, was calculated in order to use $U = \mu E$. The modified ion velocity was then used to solve the SOML equation (equation 7.5) and calculate the ion drag force (equation 7.6). This was done using the approximation of Frost [180]:

$$\mu(E) = \mu_0 \frac{p'}{T'} \left[1 + \frac{yE}{p}\right]^{-0.5} \tag{7.8}$$

Where $T'$ is the ratio of measured to standard temperature, $p'$ is ratio of measured to standard pressure, $p$ is the measured pressure in torr and $y$ and $\mu_0$ (the zero field mobility) are gas dependent constants. The zero field mobility must be corrected for temperature and pressure [181, 182]. For argon $y$ = 0.0264 and $\mu_0$ = 1460 $cm^2V^{-1}s^{-1}$ respectively. In order to use this equation to determine the effect of collisions the criteria for the validity of OML must be satisfied. These are that the ion mean free path must be greater than the radius of the dust grain and must also be smaller than the sheath width.

## 7.3 Dust Size Distribution

The imaging system setup used to acquire data in these experiments is described in section 3.3. The dust used in experiments is 9.47 $\mu$m diameter spherical MF particles. These have been imaged using a scanning electron microscope (SEM) to determine the size distribution. A typical SEM image is shown in figure 7.5. The sample was prepared by coating conductive tape with the dust and securing the tape to a sample holder whilst wearing gloves to minimise contamination. A range of magnifications were used between 100 $\times$ and 750 $\times$ with 10 images taken for each. However, during the analysis it was only possible to accurately distinguish particles inside of the range 450 $\times$ to 650 $\times$ magnification. Each image was taken at different parts of the dust sample within this magnification range. The size distribution was determined by analysis using ImageJ software (FIJI distribution) with distance calibrated to the scale shown in figure 7.5 using the built - in distance tool. The contrast of the image was then adjusted manually to a ”threshold” value which would only show the dust spheres and remove the background. ImageJ’s watershed tool was then used to determine the number of spheres along with their average Feret diameter, which are used to give the size distribution. In a given shape the Feret diameter is the maximum distance between two points within that shape. As most of the particles are spherical (as shown in figure 7.5) this provides a good measure of diameter.

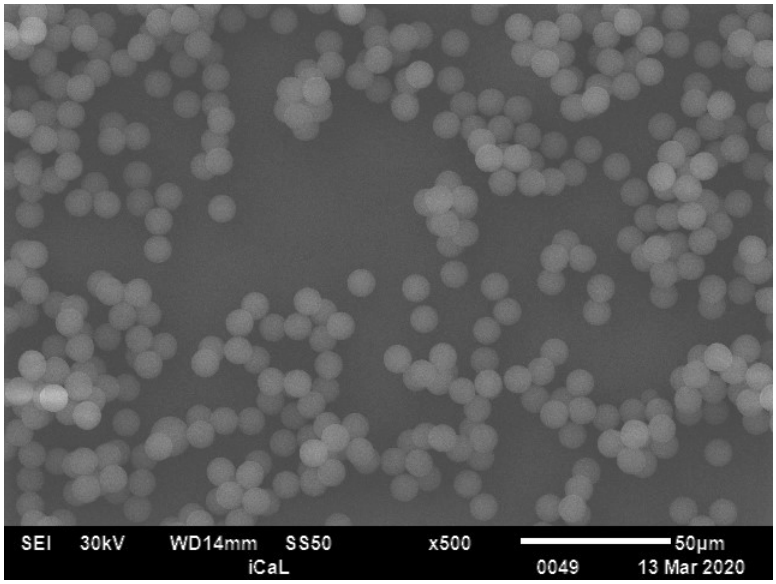


Figure 7.5: Scanning electron microscope image of 9.47 $\mu$m diameter MF particles at a magnification of $\times$ 450.

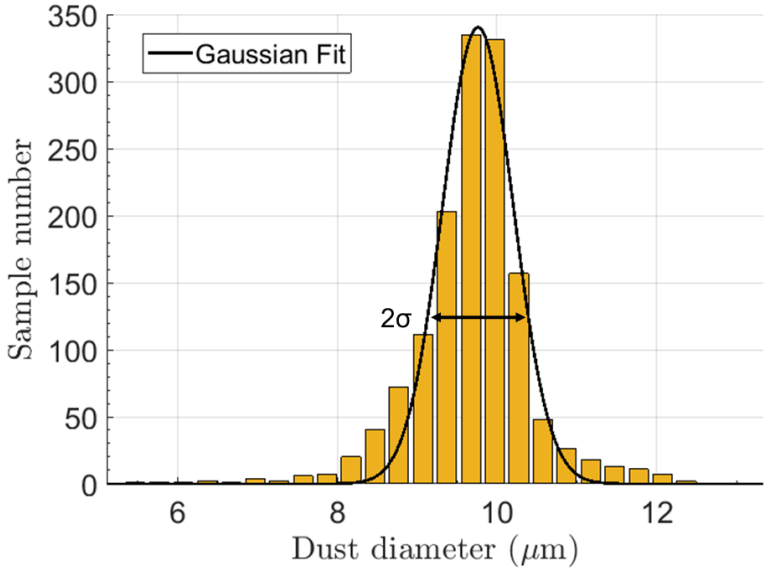


Figure 7.6: Distribution of of dust sizes measured using the SEM. Two standard deviations from the mean are indicated on the figure.

The size distribution of the combined number of particles from all of the images in the magnification range (450 - 650 $\times$) is shown in figure 7.6. As shown, the size distribution is approximately Gaussian with a mean value of 9.76 $\mu$m and a standard deviation ($\sigma$) of 0.445 $\mu$m. By taking the extremities of the size distribution, and thus the mass, ($\pm$ 2 $\sigma$ from the mean as indicated on the figure) the impact on the gravitational force can be determined. This gives $F_{g,min} = m_{d,min}g = 4.82 \times 10^{-12}$ N and $F_{g,max} = m_{d,max}g = 1.10 \times 10^{-11}$ N. The mean value of $F_g$ (using the mean obtained from the Gaussian fit) is $7.50 \times 10^{-12}$ N.

## 7.4 Dust Charging Results in Magnetised Plasmas

In this section the potential profiles measured using the emissive probe method, shown in section 6.6.3, are used to calculate the electric field. This is used along with the densities and temperatures measured by the OIS diagnostic (Chapter 5) to determine the levitation height of a dust grain. This was done by solving the force balance equation (equation 7.1) where levitation height was the only free parameter and all other parameters were known. The levitation height obtained with this method was then compared to the experimental measurement using a camera. The levitation height was measured using a Photron FastCam with the setup described in section 3.3. A laser sheet with a thickness of 1.3 mm was used to illuminate the dust. A conversion of pixels to mm was carried out using the dust confinement ring (thickness 2 mm). The number of pixels above the bottom of the ring to the illuminated dust was then measured and converted to mm. The emissive probe sheath profiles are shown in figure 6.34. At 0 mT, the sheath is wider and then collapses when a magnetic field is applied. The electric field was obtained from the derivative of the constrained polynomial fits in the figures. From these, the gravitational force and the ion drag force obtained in section 7.2.2 the force balance equation was solved for levitation height (i.e. the height at which the ion drag and gravitational forces were equal to the electrical force). Figure 7.7 shows the unmagnetised sheath profile in a 6 Pa, 10 W argon plasma. This figure also includes the measured dust levitation heights using the camera. The heights between which the gradient of the inflection point fit measured by the emissive probe changes sign are shown as vertical dashed lines which gives an indication of the sheath edge [136]. The edge of the sheath was also predicted by the Bohm velocity which is set as equal to the ion drift velocity, $\mu$E. The height, taken from the sheath profile, where the electric field was equal to that at $v_B$ was found to be 4.1 mm which agrees with the method of Wang and Hershkowitz [136]. This figure is a key result in an unmagnetised plasma, as the potential profile measured by the emissive probe allows the electric field at the location of the dust to be calculated, which is vital when determining the forces (and charge) on the dust particle (in conjunction with equation 7.1 and the previous results in this chapter). The evidence presented in this figure that this method works in unmagnetised plasmas allows further development in magnetised plasmas.

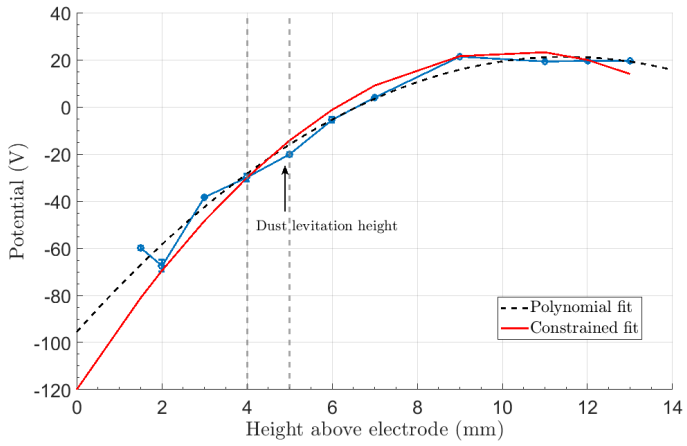


Figure 7.7: Unconstrained polynomial fit to the emissive sheath profile and constrained fit to the DC bias in a 0 mT magnetised plasma sheath. The vertical dashed lines indicate the heights where the gradient of the extrapolated fit changes sign (6 Pa, 10 W Ar).

The dependence of the main forces on ion velocity is shown in figure 7.8. Also shown is the constant gravitational force using the mean mass of the MF particles. The ion drag force is calculated using the method of Khrapak *et. al.* [1] and described in section 7.2. The sum of these two forces is shown by the dot - dashed line. The electrical force calculated using $Q_d E$ is also shown. The electrical force tends towards zero at higher fields as $Q_d$ decreases with increasing flow velocity as shown in figure 7.3. The kink in the electrical force arises as a result of the large sheath potential ($\Delta\phi$ in equation 7.5). The point where the forces balance is shown at the crossing point of $F_E$ and $F_i + F_g$ at $u = 10.1$ which is a typical value in these experiments. Consequently it cannot be assumed here that the ion drag force is negligible.

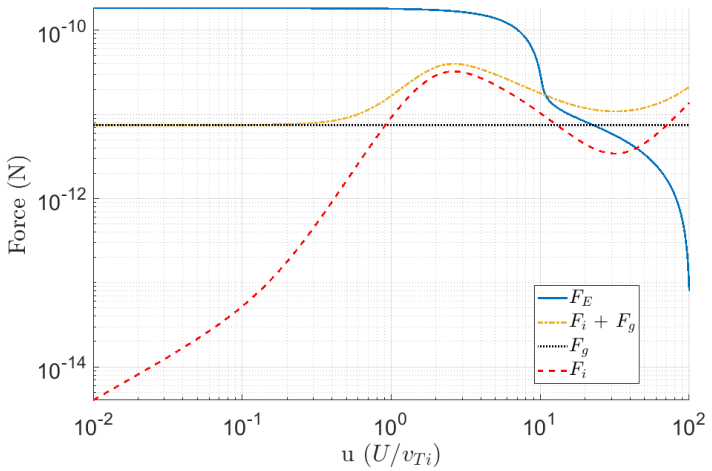


Figure 7.8: Dependence of ion drag force on ion velocity. The gravitational force (black dotted line) and calculated electrical force (red dashed line) needed to satisfy the force balance equation for an MF dust particle (as used in the experiments) are also shown.

Figures 7.9 - 7.12 show the sheath potential profiles with magnetic fields of 6 mT to 30 mT. These were also done with a 10 W RF, 6 Pa Ar plasma.

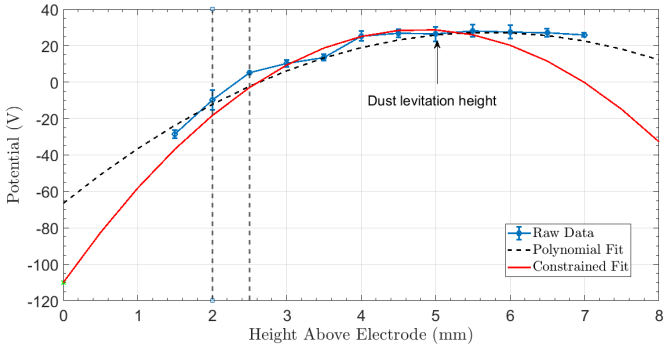


Figure 7.9: Unconstrained polynomial fit to the emissive sheath profile and constrained fit to the DC bias in a 6 mT magnetised plasma sheath. The vertical dashed lines indicate the heights where the gradient of the extrapolated fit changes sign (6 Pa, 10 W Ar).

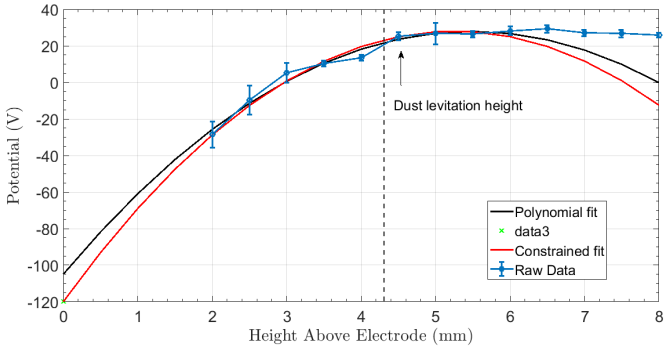


Figure 7.10: Unconstrained polynomial fit to the emissive sheath profile and constrained fit to the DC bias in a 10 mT magnetised plasma sheath. The vertical dashed lines indicate the heights where the gradient of the extrapolated fit changes sign (6 Pa, 10 W Ar).

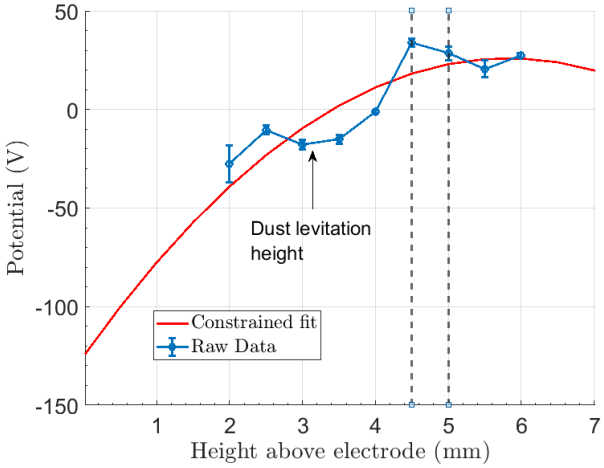


Figure 7.11: Unconstrained polynomial fit to the emissive sheath profile and constrained fit to the DC bias in a 20 mT magnetised plasma sheath. The vertical dashed lines indicate the heights where the gradient of the extrapolated fit changes sign (6 Pa, 10 W Ar).

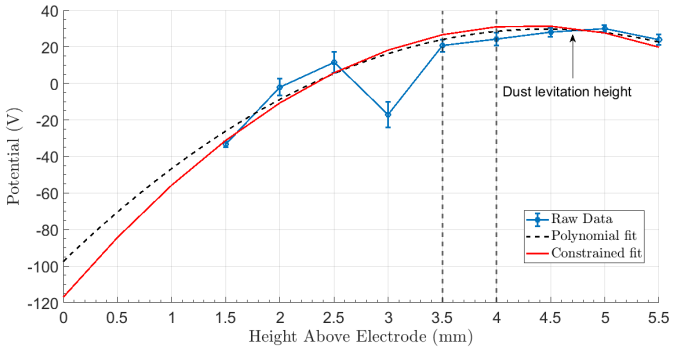


Figure 7.12: Unconstrained polynomial fit to emissive sheath profile and constrained fit to the DC bias in a 30 mT magnetised plasma sheath. The vertical dashed lines indicate the heights where the gradient of the extrapolated fit changes sign (6 Pa, 10 W Ar).

The black dashed curves in figures 7.7 - 7.12 are second order polynomial least - square fits to the measured potentials. The red solid curve is also a least - square polynomial fit, but is constrained to the DC bias on the powered electrode (i.e. at zero height). The two fits are in very good agreement (within 5 V) at the measured dust levitation heights for all magnetic fields used (although deviate by up to 33 V in the sheath). The good agreement between the fits at the dust levitation height means the constrained fit is used to obtain the electric field. This is done by fitting a quadratic equation (i.e. $V = ax^2 + bx + c$) using the in - built MATLAB functions which give a, b and c. Since a and b are both known the electric field can be calculated from $dV\ /\ dx = 2ax + b$. As shown in the figures, the dust levitates in the presheath at 6, 10 and 30 mT and in the sheath at 0 and 20 mT. This method was not possible for the 30 mT case as the polynomial fit becomes negative at the point where the dust levitates. Instead, the field was obtained from the gradient of the two adjacent data points around the levitation point.

A second order polynomial is not a good fit to the data points in the 20 mT sheath potential profile (figure 7.11) compared to the other magnetic fields used. A dip in the potential profile is observed between 2.5 and 4.5 mm and only three data points agree with the polynomial fit within error. Typically for this setup and wire diameter (50 $\mu$m) a heating current of between 200 - 300 mA is required to determine the plasma potential with the inflection point method. However, for the 20 mT case (and only the 20 mT case) the heating currents required to measure a shift in the position of the inflection point was sometimes as low as 100 mA. This is caused by the degradation of the probe wire with use which was consistently observed in experiments with the emissive probe. As well as indicating the probe is reaching the end of its life, this has the consequence of causing fluctuations in the heating current (by around $\pm$ 2 mA but with a downward trend). Since a scan with one point in the heating off - period takes approximately

5 minutes, this can lead to large fluctuations in the heating current (and therefore potential) which is likely the cause of the disagreement between the fit and data points in figure 7.11. The indicated sheath edge positions on figures 7.7 - 7.12 using the method of Wang and Hershkowitz [136] are generally in good agreement with the Bohm sheath model where the Bohm velocity is set to $\mu E$.

Just as for the unmagnetised case, the forces are plotted against ion velocity in magnetised plasmas. The 10 mT case is shown in figure 7.13 as an example and the forces are labelled as they are in figure 7.8. Due to the increase in density, the ion drag force has increased substantially compared to the unmagnetised case, which is counteracted by the electrical force so the crossing point occurs at a slightly lower velocity than with no magnetic field. This means the dust levitates slightly higher above the electrode at 10 mT field.

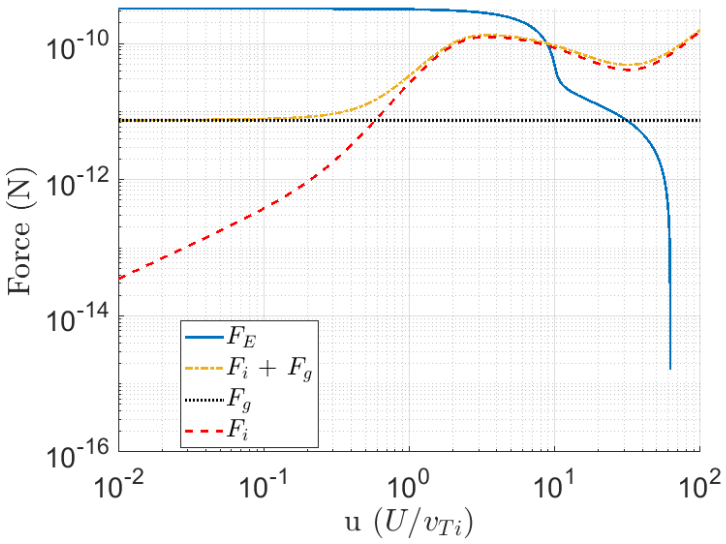


Figure 7.13: Dependence of ion drag force on ion velocity in a 10 mT magnetic field. The gravitational force (black dotted line) and calculated electrical force (red dashed line) needed to satisfy the force balance equation for an MF dust particle (as used in the experiments) are also shown.

In order to decide whether to assume collisional or collisionless ion motion for the SOML and ion drag calculations the ratio of the ion mean free path to sheath width, $s$, was calculated. Table 5.1 gives $\lambda_{i,mfp}$ = 94.8 $\mu$m and $s$ is typically about 5 mm, giving a ratio of $\lambda_{i,mfp}$ / $s$ = $1.9 \times 10^{-2}$. For these experiments, the sheath width was typically about 3 mm in magnetised plasmas giving a ratio of $\lambda_{i,mfp}$ / $s$ = $3.15 \times 10^{-2}$. The ions will therefore still be collisional in both unmagnetised and weakly magnetised sheaths so ions being accelerated to the dust grain will undergo collisions in all conditions used in experiments. To account for the collisions, the ion velocity will be given by $U = \mu(E)E$. Here the mobility $\mu(E)$ is based on the method of

Frost [180] described in section 7.2.3. An additional assumption is that the ion mean free path should be much greater than $r_d$. From table 5.1 $\lambda_{i,mfp}$ = 94.8 $\mu$m (assuming thermal velocity) and $r_d$ = 4.27 $\mu$m giving a ratio of $\lambda_{i,mfp}$ / $r_d$ = 22.2 so the assumption is justified in the bulk. In the sheath, the cross section changes so the mean free path will be longer so the ratio will increase. This means the plasma sheath is collisional but the ions do not undergo collisions in the vicinity of the dust which allows OML theory to be used.

The force balance equation (equation 7.1) was solved to obtain the predicted dust levitation height. This was done using the collisionless SOML charging model and the ion drag force theory of Khrapak [1] in the vicinity of the dust grain with collisional ion transport in the sheath. The predicted levitation heights (dashed line) are compared to the experimentally measured heights using the Photron FastCam (solid line) in figure 7.14 with increasing magnetic field. The densities and temperatures were measured using the OIS system (see section 5.6) to obtain the other parameters in equation 7.1. The figure, which is a key result of the work in this thesis, shows generally good agreement between measurement and theory, although they do not agree within error at 6 mT.

Both the experimentally measured dust levitation heights and those predicted by the collisional model are shown in the figure. With no magnetic field, the predicted and experimentally measured levitation heights agree well. When the magnetic field is initially applied, the collisional prediction is about 1 mm below the experimental measurement. After 10 mT, both experimental and the predicted heights decrease to about 3 mm above the electrode at 20 mT, before increasing again at 30 mT. The largest error is in the offset of the ends of the emissive probe tip which results in an uncertainty in the measurement position.

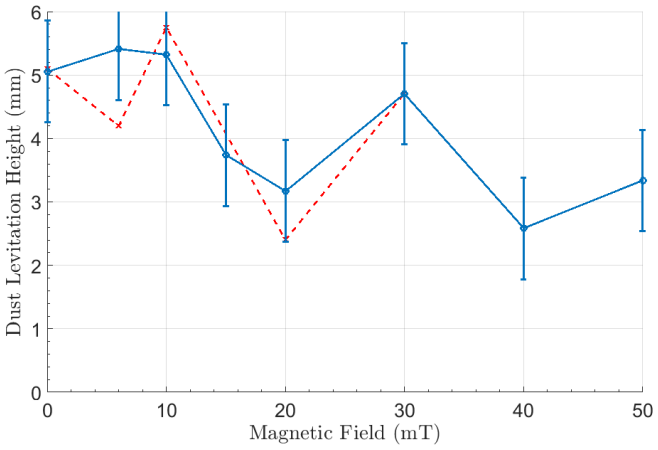


Figure 7.14: Dust levitation heights measured experimentally (solid line) and by a collisional model (dashed line) (6 Pa, 10 W Ar).

When the magnetic field is initially applied, the density in the central column above the electrode increases. This is expected to increase the ion drag force, decreasing the dust levitation height. However, as shown in figures 7.7 - 7.12 the sheath width decreases when the magnetic field is applied while the DC bias on the electrode is only slightly decreased (see figure 6.35). This increases the electric field force on a dust particle and causes the dust to levitate higher up (and decreases the ion drag force). When the magnetic field is initially applied (up to 10 mT) the dust levitates at approximately the same height (see figure 7.14) which shows the effects of the forces changing cancel at weak magnetic fields. Importantly, this means that the force balance method is still applicable in the (relatively weak) magnetic fields used in these experiments.

Bacharis *et. al.* [62] have investigated the effect of RF on dust charging in unmagnetised plasmas. The authors say the dust charge is less than that predicted by OML due to RF if the electric field is strong (i.e in the sheath). The agreement between levitation heights predicted using OML theory and experimental observations is good in the present work. This suggests RF effects are not important in the present experiments which could be because the RF voltage is small as the dust levitates in the plasma bulk in most of the experiments where the shielding will be strongest.

## 7.5 Conclusion

A theoretical model based on the principle of force balance between the electrical, gravitational and ion drag forces on a dust particle was used to predict the levitation height of a dust particle in RF plasmas. This was done in both unmagnetised and magnetised plasmas. The charge on the dust particle was calculated using both standard OML and using a shifted Maxwellian distribution to determine the importance of the ion flow in the sheath. These results were compared to experimentally measured levitation heights using a camera. Good agreement was generally found between the model and experiment with increasing magnetic field when SOML used to determine the dust charge. The experimentally measured dust levitation height (shown in figure 7.14) generally follows the trends in both DC bias on the powered electrode (see figure 6.35) and the bulk density measured by the OIS system described in Chapter 5.

In the literature, the thermophoretic force is often used to counteract gravity and move levitating dust particles into the plasma bulk in order to make OML charging theory applicable

[53] and to create 3D dust systems. This is done by heating the electrode to create a temperature gradient sufficient to offset gravity (see equation 2.28). Experiments have been performed in the literature in microgravity conditions to achieve a similar effect and allow the dust to levitate in the plasma bulk [59]. These are not always ideal as the temperature gradient may perturb plasma particles in the bulk and the requirement of taking measurements in space for microgravity is clearly not usually practical. An alternative method of making the dust levitate in the bulk has been proposed in these experiments. When a magnetic field is applied, the plasma collimates and the sheath width decreases. This means the dust will levitate in the presheath region where the electric field is weak but OML still applies. This offers a generally more practical method of performing dusty plasma experiments in which the basic plasma parameters can still be measured using the OIS method. In these experiments the theoretical prediction of Lange [19] and Willis *et. al.* [24] that the surface potential of an isolated spherical dust grain deviates from OML when $r_{L,e} \leq 10\ r_d$ was tested experimentally. The results, shown in figure 7.14, agree with theoretical prediction within this limit as OML agrees well with levitation heights observed using a camera. This key result provides some experimental verification of the simulations performed by Lange [19] which was a major motivation for this work. Experiments were not performed above this limit. It has also been shown in these experiments that, whether the dust is levitating in the dust or the sheath, the force balance equation is still applicable in magnetised complex plasmas. This is the case even though the dust consistently levitates in the bulk or presheath regions where the electric field and ion drag force are relatively weak. This may be subject to repeating experiments at 20 mT, where the agreement between a polynomial fit and the emissive probe sheath potential profile data is poorest and is the only magnetised case where the dust was found to levitate in the sheath.

An issue in this work is that a collisionless sheath model is used to determine $n_i$ in equation 7.6. This leads to an inconsistency in determining the ion density with a collisionless model and the ion velocity with a collisional model. This will only affect the unmagnetised and the 20 mT case in these results as these are the only two magnetic fields used in which the dust levitates in the sheath. For the other cases where the dust is in the presheath quasineutrality can be used and a sheath model is not needed. This can be solved in the future using a collisional RF sheath.

# Chapter 8

# Conclusions & Future Work

### 8.0.1 Conclusions

The two main topics covered in this work focussed on the issues of using Langmuir probes in RF plasmas and charge dynamics of a dust grain in magnetised RF plasma sheaths. Regarding the former, a comprehensive experimental study of RF compensation has been carried out to determine the effect of changing the level of RF compensation on plasma parameters obtained from IV curves. The input impedances given by a simulated circuit (using LT SPICE) were determined from a range of inductances. For some of these inductances, experiments were carried out to determine plasma parameters using a Langmuir probe with chokes. The values of plasma potential, floating potential, and electron temperature and density were used as a measure of the level of RF compensation. This was done in a small ($\approx 60 \times 60 \times 40$ mm chamber) capacitively coupled RF argon plasma. It has been shown in the literature that optimum compensation is obtained when $V_f$ is shifted most positively (in other words, the largest maximum value in the peak of $dI/dV$ for the same current at $V_p$). This was also observed in these experimental results in addition to other criteria not mentioned in the literature. It was found that the LT SPICE simulation gave impedances which generally agreed well with minima in temperature and maxima in floating potential. In addition, weaker local maxima were found in the density given using the standard OML theory. The chamber size was found to be of potential importance as the level of RF compensation decreases if there is a significant parasitic capacitance between the internal probe circuit and the chamber. This occurs when the inductor chain extends beyond the end of the plasma where there is no plasma shielding. In addition, in the small chamber used in these experiments, a compensation electrode of any sized or geometry used was found to perturb the plasma. Consequently, care must be taken when using passive

RF compensation in small chambers. The results show the importance of ensuring adequate RF compensation to obtain accurate measurements with passively compensated probes. The specific inductances needed will change for different setups, but it can be shown that a probe is sufficiently compensated when the criteria presented here are met. It is rare in the literature to show that a probe is compensated, except for the shift of $V_f$ previously mentioned, but these results give a number of relatively simple tests to determine optimum compensation.

An optical imaging spectroscopy diagnostic was developed (based on previous work, see Chapter 5) to measure density and temperature in both magnetised and unmagnetised plasmas. The diagnostic is based on the Corona model and provides line - averaged temperature and density maps of the plasma (over the area of the window). This was benchmarked against an RF - compensated Langmuir probe in unmagnetised RF plasmas before being used in magnetised plasmas up to 50 mT. Optical systems such as this have the advantage of not perturbing the plasma at the cost of more complex analysis techniques.

Emissive probe diagnostics were also used to measure the sheath potential profile in both unmagnetised and magnetised plasmas (Chapter 6). This has commonly been done in the literature in unmagnetised plasmas [137, 76, 144]. The width of the sheath was determined using the technique developed by Wang and Hershkowitz [136]. The sheath edge was determined as the point at which the gradient of an inflection point against heating current plot switches from decreasing with emission to increasing with emission.

A novel emissive probe setup was designed to reduce the measurement time and to improve the signal to noise ratio by reducing mains noise. This was achieved using a signal generator and an audio power amplifier. The signal generator allows frequencies other than the mains frequency to be used which makes measurements (taken in the heating off period) faster by increasing the heating signal frequency. This method was used in the plasma bulk and to measure potential profiles in unmagnetised and magnetised plasma sheaths shown in figures 6.30 and 6.34 respectively. A simple parabolic fit, which approximates several sheath models according to the literature [157], was plotted for each of these results and extrapolated to the DC bias on the powered electrode which was accurate to within 12 %. These fits had an $R^2$ of 0.9 or greater. To the author's knowledge, such an experiment has not been performed in a magnetised sheath in the literature, nor has an audio power amplifier and signal generator been used in combination to generate a low - noise signal. When using the IP method, the peak of the first derivative of IV curves was found to shift negatively instead of positively when moving

into the sheath which is in agreement with observations in the literature [136]. Although the novel method achieves a higher signal to noise ratio in the sheath (i.e. works at lower densities) than the conventional setup, the exact density limits are not known. The novel method is nevertheless preferable to the conventional method for emissive probe potential measurements in RF sheaths based on these results.

The OIS and novel emissive diagnostics were then used in to measure parameters ($E$, $n_e$, $T_e$) in magnetised plasmas to determine how dust charging dynamics are affected by magnetic fields. This was compared to conventional OML theory which has been predicted by simulations to be accurate up to $r_{L,e} < 10\ r_d$ [19, 24]. A shifted Maxwellian velocity distribution was used with conventional OML theory which has been done in the literature [24, 173, 174] (SOML). Images were taken of dust, illuminated by a 532 nm laser, levitating in a plasma and a pixel to mm calibration was used to determine the levitation height. A force balance equation was used to determine the predicted levitation height. This took into account the gravitational force of the dust particles, the ion drag force caused by accelerating ions in the sheath using the method of Khrapak *et. al.* [1], and the electric force obtained from emissive probe measurements. Good agreement was found between theory and experimental observations for the magnetic field range used as shown in figure 7.14. This has given experimental verification to the theoretical prediction of Lange [19] and Willis *et. al.* [24].

### 8.0.2 Future Work

In the determination of the level of RF compensation of a Langmuir probe, it would be useful to be able to measure the impedance of the probe circuit at the fundamental frequency and its harmonics directly. This would allow verification of the simulated impedance in LT SPICE. This was attempted using a network analyser, but the probe impedance could not be matched to the analyser at the relevant frequencies so the measurement was not reliable. In addition, taking the impedance of the circuit including the low pass filter would require a suitable sensitive instrument.

A further potential development to this work would be to use fusion - relevant magnetic fields (up to about 1 T) which the apparatus used in this work is capable of. The limit of applicability of OML predicted by Lange (when $r_{L,e} = 10\ r_d$) can then be verified experimentally as it should not apply above this limit. This would also involve investigating the effect of magnetised ions as well as electrons. This will require a much smaller diameter emissive probe

wire as the emission of electrons will not be accurately described by conventional theory if the wire diameter is approximately equal to the electron Larmor radius. Attempts have been made in these experiments to use smaller emissive probe wire diameters, but it was not possible to crimp such a small wire to the electrodes in the probe tip. Other plasma conditions, such as pressure, could also be varied to investigate the effects of increased collisions. In these experiments, the pressure used (6 Pa) results in a weakly collisional regime in which collisionality was not particularly significant. This may not be the case for increasing pressure.

Some further work is also possible in investigating the effect of probe degradation with persistent use (i.e. by assessing the repeatability of figures 7.9 - 7.12). If the results shown in these figures are repeatable, then in certain magnetic fields the prediction of Tomme *et. al.* [183] will fail in the conditions used in these experiments. If they are not repeatable then emissive probes must be regularly replaced when heated by an electric current.

An important development to this work is to use an appropriate collisional RF sheath model to determine the ion density in the sheath ($n_i$ in equation 7.6). In the present experiments a collisionless sheath model is used which leads to an error in determining the ion density with a collisionless model and the ion velocity with a collisional model. This will only affect the unmagnetised and the 20 mT case in these results as these are the only two magnetic fields used in which the dust levitates in the sheath. For the other cases where the dust is in the presheath quasineutrality can be used and a sheath model is not needed.

# Bibliography


[1] S.A. Khrapak *et. al.* Hybrid approach to the ion drag force. *Physics of plasmas*, 12(4), 2005.

[2] F. F. Chen. Lecture notes on langmuir probe diagnostics. In *Mini-Course on Plasma Diagnostics, IEEE-ICOPS meeting, Korea*, 2003.

[3] G. Y. Park *et. al.* Atmospheric-pressure plasma sources for biomedical applications. *Plasma Sources Science and Technology*, 21(4), 2012.

[4] F. F. Chen. *Introduction to plasma physics and controlled fusion*, volume 1. Springer, 1984.

[5] R. J Goldston. *Introduction to plasma physics*. CRC Press, 2020.

[6] J. W. Coburn and E. Kay. Positive-ion bombardment of substrates in rf diode glow discharge sputtering. *Journal of Applied Physics*, 43(12), 1972.

[7] V. A. Godyak, R. B. Piejak, and B. M. Alexandrovich. Electrical characteristics of parallel-plate rf discharges in argon. *IEEE Transactions on Plasma Science*, 19(4), 1991.

[8] S. Atzeni and J. Meyer-ter Vehn. *The physics of inertial fusion: beam plasma interaction, hydrodynamics, hot dense matter*, volume 125. OUP Oxford, 2004.

[9] P. K. Shukla and A.A. Mamun. *Introduction to dusty plasma physics*. CRC press, 2015.

[10] S. Bonazzola *et. al.* Jeans collapse in a turbulent medium. *Astronomy and Astrophysics*, 172, 1987.

[11] G. De Temmerman *et. al*. Dust creation and transport in MAST. *Nuclear Fusion*, 50(10), 2010.

[12] E. Thomas *et. al.* Initial measurements of two- and three-dimensional ordering, waves, and plasma filamentation in the magnetized dusty plasma experiment. *Physics of Plasmas*, 23(5), 2016.

[13] B.T. Draine and E.E. Salpeter. On the physics of dust grains in hot gas. *The Astrophysical Journal*, 231, 1979.

[14] J. P. Sheehan and N. Hershkowitz. Emissive probes. *Plasma Sources Science and Technology*, 20(6), 2011.

[15] I. D. Sudit and F. F. Chen. *Plasma Sources Science and Technology*, 3(2), 1994.

[16] H. M. Mott-Smith and Irving Langmuir. The theory of collectors in gaseous discharges. *Phys. Rev.*, 28, 1926.

[17] J E Allen. Probe theory - the orbital motion approach. *Physica Scripta*, 45(5), 1992.

[18] M. Klick, M. Kammeyer, W. Rehak, W. Kasper, P. Awakowicz, and G. Franz. Innovative plasma diagnostics and control of process in reactive low-temperature plasmas. *Surface and Coatings Technology*, 98(1), 1998. Papers presented at the Fifth International Conference on Plasma Surface Engineering.

[19] D. Lange. Floating surface potential of spherical dust grains in magnetized plasmas. *Journal of Plasma Physics*, 82(1), 2016.

[20] F. F. Chen. Time-varying impedance of the sheath on a probe in an RF plasma. *Plasma Sources Science and Technology*, 15(4), 2006.

[21] B. M. Annaratone and N. S. J. Braithwaite. *Measurement Science and Technology*, 2(8), 1991.

[22] A. Boschi and F. Magistrelli. Effect of a r.f, signal on the characteristic of a langmuir probe. *Il Nuovo Cimento (1955-1965)*, 29(2), 1963.

[23] A. Dyson *et al*. *Measurement Science and Technology*, 11(5), 2000.

[24] C. T. N. Willis *et. al.* Floating potential of large dust grains in a collisionless flowing plasma. *Phys. Rev. E*, 85, 2012.

[25] E. Thomas Jr *et. al.* Observations of imposed ordered structures in a dusty plasma at high magnetic field. *Physics of Plasmas*, 22(3), 2015.

[26] E. Thomas *et. al.* The magnetized dusty plasma experiment (mdpx). *Journal of Plasma Physics*, 81(2), 2015.

[27] chapter 11, Principles of Plasma Discharges and Materials Processing, pages 387–460. M. Lieberman and A. Lichtenberg, John Wiley & Sons, Ltd, 2005.

[28] T. Makabe and Z. L. Petrovic. *Plasma electronics: applications in microelectronic device fabrication*. CRC Press, 2006.

[29] K. Bera *et. al.* Frequency optimization for capacitively coupled plasma source. *IEEE Transactions on Plasma Science*, 33(2), 2005.

[30] F. F. Chen. Introduction to plasma physics. *Springer, New York1974)*, 4(6), 1974.

[31] E. V. Stenson *et. al.* Debye length and plasma skin depth: two length scales of interest in the creation and diagnosis of laboratory pair plasmas. *Journal of Plasma Physics*, 83(1), 2017.

[32] *Principles of Plasma Discharges and Materials Processing*, chapter 6, pages 165–206. M. Lieberman and A. Lichtenberg, John Wiley & Sons Ltd, 2005.

[33] H. Herold. Compton and thomson scattering in strong magnetic fields. *Phys. Rev. D*, 19, 1979.

[34] I. Langmuir. The pressure effect and other phenomena in gaseous discharges. *Journal of the Franklin Institute*, 196(6), 1923.

[35] Tsv. K. Popov, P Ivanova, J Stöckel, and R Dejarnac. Electron energy distribution function, plasma potential and electron density measured by langmuir probe in tokamak edge plasma. *Plasma Physics and Controlled Fusion*, 51(6), 2009.

[36] K.F. Al-Assadi *et. al.* Langmuir probe studies of oxygen and chlorine discharges in a 13.56 mhz plasma reactor. *Vacuum*, 42(15), 1991.

[37] J. Hopwood *et. al.* Langmuir probe measurements of a radio frequency induction plasma. *Journal of Vacuum Science & Technology A*, 11(1), 1993.

[38] J. E. Allen *et. al*. The collection of positive ions by a probe immersed in a plasma. *Proceedings of the Physical Society. Section B*, 70(3), 1957.

[39] G. Medicus. Simple way to obtain the velocity distribution of the electrons in gas discharge plasmas from probe curves. *Journal of Applied Physics*, 27(10), 1956.

[40] M. J. Druyvesteyn. Der niedervoltbogen. *Zeitschrift für Physik*, 64(11-12), 1930.

[41] K. Behringer and U. Fantz. Spectroscopic diagnostics of glow discharge plasmas with non-maxwellian electron energy distributions. *Journal of Physics D: Applied Physics*, 27(10), 1994.

[42] J. G. Laframboise. Ph.d thesis, university of toronto. 1966.

[43] P.M. Bryant. Theory of cylindrical langmuir probes in weakly ionized, non-thermal, stationary and moderately collisional plasmas. *Plasma Sources Science and Technology*, 18(1), 2008.

[44] L. Conde. An introduction to langmuir probe diagnostics of plasmas. *Madrid: Dept. Física. ETSI Aeronáut ngenieros Aeronáuticos Universidad Politécnica de Madrid*, 2011.

[45] I. D. Sudit and R. C. Woods. A study of the accuracy of various langmuir probe theories. *Journal of Applied Physics*, 76(8), 1994.

[46] J. Winter. Dust: A new challenge in nuclear fusion research? *Physics of Plasmas*, 7(10), 2000.

[47] J Winter. Dust in fusion devices—a multi-faceted problem connecting high- and low-temperature plasma physics. *Plasma Physics and Controlled Fusion*, 46(12B), 2004.

[48] L. Boufendi and A. Bouchoule. Industrial developments of scientific insights in dusty plasmas. *Plasma Sources Science and Technology*, 11(3A), 2002.

[49] C. R. James and F. Vermeulen. A microparticle plasma. *Canadian Journal of Physics*, 46(7), 1968.

[50] A. A. Sickafoose and J.E. Colwell. Experimental levitation of dust grains in a plasma sheath. *Journal of Geophysical Research: Space Physics*, 107(A11), 2002.

[51] S. Ratynskaia *et. al.* Experimental determination of dust-particle charge in a discharge plasma at elevated pressures. *Physical review letters*, 93(8), 2004.

[52] K. De Bleecker *et. al.* Role of the thermophoretic force on the transport of nanoparticles in dusty silane plasmas. *Phys. Rev. E*, 71, 2005.

[53] L. Talbot *et. al.* Thermophoresis of particles in a heated boundary layer. *Journal of Fluid Mechanics*, 101(4), 1980.

[54] P. S. Epstein. On the resistance experienced by spheres in their motion through gases. *Phys. Rev.*, 23, 1924.

[55] N. Kh. Bastykova *et. al.* Controlled levitation of dust particles in rf+ dc discharges. *Contributions to Plasma Physics*, 55(9), 2015.

[56] G.E. Morfill, V.N. Tsytovich, and H. Thomas. Complex plasmas: Ii. elementary processes in complex plasmas. *Plasma Physics Reports*, 29(1), 2003.

[57] V. N Tsytovich *et. al. Elementary physics of complex plasmas*, volume 731. Springer Science & Business Media, 2007.

[58] A. M. Ignatov. Basics of dusty plasma. *Plasma Physics Reports*, 31, 2005.

[59] V.N. Tsytovich *et. al.* Collision-dominated dust sheaths and voids-observations in micro-gravity experiments and numerical investigation of the force balance relations. *New Journal of Physics*, 5(1), 2003.

[60] H.M. Thomas *et. al.* Complex plasma laboratory pk-3 plus on the international space station. *New journal of physics*, 10(3), 2008.

[61] H. Thomas *et. al.* Plasma crystal: Coulomb crystallization in a dusty plasma. *Physical Review Letters*, 73(5), 1994.

[62] M. Bacharis, M. Coppins, and J. E. Allen. Dust grain charging in RF discharges. *Plasma Sources Science and Technology*, 19(2), 2010.

[63] N.N. Rao, P.K. Shukla, and M. Yu Yu. Dust-acoustic waves in dusty plasmas. *Planetary and space science*, 38(4), 1990.

[64] B. Pégourié *et. al.* Overview of the deuterium inventory campaign in tore supra: Operational conditions and particle balance. *Journal of Nuclear Materials*, 390-391, 2009. Proceedings of the 18th International Conference on Plasma-Surface Interactions in Controlled Fusion Device.

[65] B. J. Harris *et. al*. Ball pen probe in strongly magnetised rf plasmas. *Plasma Sources Science and Technology*, 2019.

[66] Leybold Vacuum. Leybold turbovac 50 operating instructions manual. 2004.

[67] M. A. Sobolewski. Electrical characterization of radio-frequency discharges in the gaseous electronics conference reference cell. *Journal of Vacuum Science & Technology A*, 10(6), 1992.

[68] F. F. Chen *et. al*. Electric probes. In *In Plasma Diagnostic Techniques, edited by Huddlestone, R.H. and Leornard, S.L.* Academic Press, 1965.

[69] J. V. Scanlan and M. B. Hopkins. Langmuir probe measurements of the electron energy distribution function in radio-frequency plasmas. *Journal of Vacuum Science & Technology A*, 10(4), 1992.

[70] M. Lampe. Limits of validity for orbital-motion-limited theory for a small floating collector. *Journal of Plasma Physics*, 65(3), 2001.

[71] R. Schrittwieser *et. al*. Application of emissive probes for plasma potential measurements in fusion devices. *Contributions to Plasma Physics*, 41(5), 2001.

[72] R. F. Kemp and J. M. Sellen. Plasma potential measurements by electron emissive probes. *Review of Scientific Instruments*, 37(4), 1966.

[73] J. P. Sheehan *et. al*. A comparison of emissive probe techniques for electric potential measurements in a complex plasma. *Physics of Plasmas*, 18(7), 2011.

[74] Kouta Kusaba and Haruo Shindo. A new emissive-probe method for electron temperature measurement in radio-frequency plasmas. *Review of Scientific Instruments*, 78(12), 2007.

[75] M. Cho *et. al.* Measurement of vacuum space potential by an emissive probe. *Review of Scientific Instruments*, 55(4), 1984.

[76] H. Yamada and D. L. Murphree. Electrostatic probe measurements in a collisionless plasma sheath. *The Physics of Fluids*, 14(6), 1971.

[77] J. R. Smith *et. al.* Inflection-point method of interpreting emissive probe characteristics. *Review of Scientific Instruments*, 50(2), 1979.

[78] J. W. Bradley *et. al.* Measurement of the plasma potential in a magnetron discharge and the prediction of the electron drift speeds. *Plasma Sources Science and Technology*, 10(3), 2001.

[79] D. Samsonov *et. al*. High speed laser tomography system. *Review of Scientific Instruments*, 79(3), 2008.

[80] PM Chung, L Talbot, and KJ Touryan. Electric probes in stationary and flowing plasmas: Theory and application springer. *New York p*, 3, 1975.

[81] N. Hershkowitz *et. al.* Enhancement of the plasma potential by fluctuating electric fields near the ion cyclotron frequency. *Phys. Rev. Lett.*, 55, 1985.

[82] B. M. Annaratone and N. S. J. Braithwaite. A comparison of a passive (filtered) and an active (driven) probe for RF plasma diagnostics. *Measurement Science and Technology*, 2(8), 1991.

[83] P. Bryant *et. al.* Langmuir probe measurements of weakly collisional electronegative RF discharge plasmas. *Journal of Physics D: Applied Physics*, 34(1), 2000.

[84] A. Dyson *et. al*. Multiple harmonic compensation of langmuir probes in rf discharges. *Measurement Science and Technology*, 11(5), 2000.

[85] A. Garscadden and K. G. Emeleus. Notes on the effect of noise on langmuir probe characteristics. *Proceedings of the Physical Society*, 79(3), 1962.

[86] B. M. Annaratone *et. al.* Ion currents to cylindrical langmuir probes in RF plasmas. *Journal of Physics D: Applied Physics*, 25(3), 1992.

[87] P Chabert and N Braithwaite. *Physics of Radio-Frequency Plasmas*. Cambridge University Press, 2011.

[88] J D Swift and M J.R. Schwar. chapter 1, pages 1 – 16. 1970.

[89] L. Oksuz *et. al*. Analysis of uncompensated langmuir probe characteristics in radio-frequency discharges revisited. *Journal of Applied Physics*, 99(1), 2006.

[90] V. A. Godyak and R. B. Piejak. Probe measurements of the space potential in a radio frequency discharge. *Journal of Applied Physics*, 68(7), 1990.

[91] K. Wiesemann. Characterisation of plasmas by advanced diagnostic methods. *Pure and applied chemistry*, 68(5), 1996.

[92] F. F Chen and J. P Chang. *Lecture notes on principles of plasma processing*. Springer Science & Business Media, 2012.

[93] V. A. Godiak and O. A. Popov. Probe diagnostics of an RF plasma. *Soviet Physics Technical Physics*, 22, 1977.

[94] R. R. J. Gagné and A. Cantin. Investigation of an rf plasma with symmetrical and asymmetrical electrostatic probes. *Journal of Applied Physics*, 43(6), 1972.

[95] N. St. J. Braithwaite *et. al.* An electrostatic probe technique for RF plasma. *Journal of Physics E: Scientific Instruments*, 20(8), 1987.

[96] H. Sabadil and S. Klagge. Probe measurements in a rf plasma-planar reactor at 27, 1 mhz in ar o 2, cf 2 cl 2 and cf 2 cl 2/o 2. In *XVII International Conference on Phenomena in Ionized Gases*, volume 1, page 322, 1985.

[97] T. I. Cox *et. al.* The use of langmuir probes and optical emission spectroscopy to measure electron energy distribution functions in RF-generated argon plasmas. *Journal of Physics D: Applied Physics*, 20(7), 1987.

[98] A. P. Paranjpe *et. al.* A tuned langmuir probe for measurements in rf glow discharges. *Journal of Applied Physics*, 67(11), 1990.

[99] B. M. Annaratone *et. al.* On the use of double probes in RF discharges. *Plasma Sources Science and Technology*, 1(4), 1992.

[100] P.A Chatterton *et. al.* A self-compensating langmuir probe for use in rf (13.56 mhz) plasma systems. *Vacuum*, 42(7), 1991.

[101] G. Dilecce *et. al.* Electron-energy distribution function measurements in capacitively coupled rf discharges. *Journal of Applied Physics*, 69(1), 1991.

[102] C. M. O. Mahony *et. al.* Structure observed in measured electron energy distribution functions in capacitively coupled radio frequency hydrogen plasmas. *Applied Physics Letters*, 75(3), 1999.

[103] K. Shimizu *et. al.* Noise elimination method using a transmission line for the diagnostics of radio frequency plasma. *Review of Scientific Instruments*, 68(4), 1997.

[104] A. E. Wendt. Passive external radio frequency filter for langmuir probes. *Review of Scientific Instruments*, 72(7), 2001.

[105] N. Mutsukura, K. Kobayashi, and Y. Machi. Monitoring of radio-frequency glow-discharge plasma. *Journal of Applied Physics*, 66(10), 1989.

[106] S. Linnane and M. B. Hopkins. Analysis of an uncompensated langmuir probe in a radio frequency plasma. *Plasma Sources Science and Technology*, 18(4), 2009.

[107] M Hannemann and F Sigeneger. *Czechoslovak Journal of Physics*, 56(2), 2006.

[108] J. F. Caneses and B. Blackwell. RF compensation of double langmuir probes: modelling and experiment. *Plasma Sources Science and Technology*, 24(3), 2015.

[109] Lt spice, analog devices. https://www.analog.com/en/design-center/design-tools-and-calculators/ltspice-simulator.html. Accessed: 2021-02-26.

[110] A. Savitzky and M. J.E. Golay. Smoothing and differentiation of data by simplified least squares procedures. *Analytical chemistry*, 36(8), 1964.

[111] U. Flender *et. al.* RF harmonic suppression in langmuir probe measurements in RF discharges. *Plasma Sources Science and Technology*, 5(1), 1996.

[112] M. Usoltceva *et. al*. Effective collecting area of a cylindrical langmuir probe in magnetized plasma. *Physics of Plasmas*, 25(6), 2018.

[113] W. Lochte-Holtegreven. *Plasma-diagnostics*. 1968.

[114] G. P. Davis and R. A. Gottscho. Measurement of spatially resolved gas-phase plasma temperatures by optical emission and laser-induced fluorescence spectroscopy. *Journal of Applied Physics*, 54(6), 1983.

[115] G. J. Tallents. *Collisional-Radiative Models*, page 226–254. Cambridge University Press, 2018.

[116] M. Tuszewski and J. A. Tobin. The accuracy of langmuir probe ion density measurements in low-frequency RF discharges. *Plasma Sources Science and Technology*, 5(4), 1996.

[117] R. Hippler *et. al. Low temperature plasma physics: fundamental aspects and applications*. 2001.

[118] T.M. Desai *et. al.* Electron temperature measurements in uhv systems by spectroscopic and langmuir probe techniques. *Vacuum*, 46(3), 1995.

[119] J. W. Coburn and M. Chen. Optical emission spectroscopy of reactive plasmas: A method for correlating emission intensities to reactive particle density. *Journal of Applied Physics*, 51(6), 1980.

[120] D.A.O. Hope, T.I. Cox, and V.G.I. Deshmukh. Langmuir probe and optical emission spectroscopic studies of ar and o2 plasmas. *Vacuum*, 37(3), 1987.

[121] B. Du *et. al.* A novel probe for spatially resolved emission spectroscopy in plasmas. *Plasma Sources Science and Technology*, 19(4), 2010.

[122] U. Fantz. Basics of plasma spectroscopy. *Plasma Sources Science and Technology*, 15(4), 2006.

[123] J. B. Boffard, C. C. Lin, and C. A. DeJoseph Jr. Application of excitation cross sections to optical plasma diagnostics. *Journal of Physics D: Applied Physics*, 37(12), 2004.

[124] S. Kotochigova *et. al.* Atomic reference data for electronic structure calculations. *at. Inst. Standards Technol*, 2005.

[125] G. Cristoforetti *et. al.* Local thermodynamic equilibrium in laser-induced breakdown spectroscopy: Beyond the mcwhirter criterion. *Spectrochimica Acta Part B: Atomic Spectroscopy*, 65(1), 2010.

[126] R. W. P. McWhirter. *Plasma Diagnostic Techniques*, 1965.

[127] P.J. Cullen and V. Milosavljević. Spectroscopic characterization of a radio-frequency argon plasma jet discharge in ambient air. *Progress of Theoretical and Experimental Physics*, 2015(6), 06 2015.

[128] AR Filippelli, Chun C Lin, and LW Anderson. Principles and methods for measurement of electron impact excitation cross sections for atoms and molecules by optical techniques. *Advances in Atomic, Molecular, and Optical Physics*, 33, 1994.

[129] A. Chutjian and D. C. Cartwright. Electron-impact excitation of electronic states in argon at incident energies between 16 and 100 ev. *Phys. Rev. A*, 23, 1981.

[130] J. B. Boffard *et. al.* Measurement of electron-impact excitation cross sections out of metastable levels of argon and comparison with ground-state excitation. *Phys. Rev. A*, 59, 1999.

[131] S. Tsurubuchi. Emission cross sections of ar+ measured in a wide range of electron impact energies. *Journal of the Physical Society of Japan*, 66(10), 1997.

[132] I. P. Zapesochnyi *et. al.* Experimental investigation of the excitation of ar ii and kr ii in electron-ion collisions. *Sov. Phys. JETP*, 36, 1973.

[133] D. Voloshin *et. al.* Evaluation of plasma density in rf ccp discharges from ion current to langmuir probe: experiment and numerical simulation. *The European Physical Journal D*, 69(1), 2015.

[134] T. Ott and M. Bonitz. Diffusion in a strongly coupled magnetized plasma. *Phys. Rev. Lett.*, 107, 2011.

[135] E.M. Lifshitz and L.P. Pitaevskii. Physical kinetics pergamon press, 1981.

[136] X. Wang and N. Hershkowitz. Simple way to determine the edge of an electron-free sheath with an emissive probe. *Review of Scientific Instruments*, 77(4), 2006.

[137] D. Diebold *et. al.* Emissive probe current bias method of measuring dc vacuum potential. *Review of Scientific Instruments*, 59(2), 1988.

[138] E. Y. Wang *et. al.* Techniques for using emitting probes for potential measurement in rf plasmas. *Review of Scientific Instruments*, 57(10), 1986.

[139] P. Coakley and N. Hershkowitz. Laboratory double layers. *The Physics of Fluids*, 22(6), 1979.

[140] P. Balan *et. al*. Emissive probe measurements of plasma potential fluctuations in the edge plasma regions of tokamaks. *Review of Scientific Instruments*, 74(3), 2003.

[141] L. Dorf, Y. Raitses, and N. J. Fisch. Electrostatic probe apparatus for measurements in the near-anode region of hall thrusters. *Review of Scientific Instruments*, 75(5), 2004.

[142] M. Y. Ye and S. Takamura. Effect of space-charge limited emission on measurements of plasma potential using emissive probes. *Physics of Plasmas*, 7(8), 2000.

[143] N. Hershkowitz *et. al.* Self-emissive probes. *Review of Scientific Instruments*, 54(1), 1983.

[144] H. Fujita and S. Yagura. Measurements of fast time evolutions of plasma potential using emissive probe. *Japanese Journal of Applied Physics*, 22(Part 1, No. 1), 1983.

[145] M. A. Makowski and G. A. Emmert. New method to measure plasma potential with emissive probes. *Review of Scientific Instruments*, 54(7), 1983.

[146] R. W. Schrittwieser *et. al.* A radially movable laser-heated emissive probe. *Journal of Plasma Fusion Research*, 8, 2009.

[147] G. D. Hobbs and J. A. Wesson. Heat flow through a langmuir sheath in the presence of electron emission. *Plasma Physics*, 9(1), 1967.

[148] T. Intrator *et. al.* The virtual cathode as a transient double sheath. *Journal of Applied Physics*, 64(6), 1988.

[149] S. Binwal *et. al.* Triple and emissive probe measurements of plasma parameters in a magnetized capacitive coupled discharge. In *44th EPS Conference on Plasma Physics*, 2017.

[150] R. Schrittwieser *et. al*. Measurements with an emissive probe in the CASTOR tokamak. *Plasma Physics and Controlled Fusion*, 44(5), 2002.

[151] S. Iizuka *et. al.* A method for measuring fast time evolutions of the plasma potential by means of a simple emissive probe. *Journal of Physics E: Scientific Instruments*, 14(11), 1981.

[152] L. A. Schwager. Effects of secondary and thermionic electron emission on the collector and source sheaths of a finite ion temperature plasma using kinetic theory and numerical simulation. *Physics of Fluids B: Plasma Physics*, 5(2), 1993.

[153] A. Fruchtman *et. al.* Potential of an emissive cylindrical probe in plasma. *Phys. Rev. E*, 84, 2011.

[154] A. Mishra, P. J. Kelly, and J. W. Bradley. The evolution of the plasma potential in a HiPIMS discharge and its relationship to deposition rate. *Plasma Sources Science and Technology*, 19(4), 2010.

[155] J. W. Bradley, S K Karkari, and A Vetushka. A study of the transient plasma potential in a pulsed bi-polar dc magnetron discharge. *Plasma Sources Science and Technology*, 13(2), 2004.

[156] Jian-quan *et. al* Li. Improved inflection point method of emissive probe for accurate measurement of plasma potential. *Journal of Vacuum Science & Technology A*, 34(6), 2016.

[157] E. B. Tomme *et. al. Plasma Sources Science and Technology*, 9(2), 2000.

[158] H. Fujita *et. al.* Potential measurements by an emissive probe in a magnetized plasma. *Physics Letters A*, 78(3), 1980.

[159] J. Adámek *et. al.* Comparative measurements of the plasma potential with the ball-pen and emissive probes on the castor tokamak. *Czechoslovak Journal of Physics*, 55(3), 2005.

[160] S. L. Cartier and R. L. Merlino. Anode-type double layers in a nonuniform magnetic field. *The Physics of Fluids*, 30(8), 1987.

[161] N. Hershkowitz, J. R. Smith, and H. Kozima. Electrostatic self-plugging of a picket fence cusped magnetic field. *The Physics of Fluids*, 22(1), 1979.

[162] C. Ionita *et. al.* The use of emissive probes in laboratory and tokamak plasmas. *Contributions to Plasma Physics*, 51(2-3), 2011.

[163] M. Mizumura *et. al.* Probe system with bias compensation using a laser heated emissive probe for RF discharge plasma diagnostics. *Journal of Physics D: Applied Physics*, 25(12), 1992.

[164] V. P. Kella *et. al.* A comparative study of sheath potential profile measurements with laser-heated and current-heated emissive probes. *Review of Scientific Instruments*, 87(4), 2016.

[165] D. B. Graves *et. al.* Charging, transport and heating of particles in radiofrequency and electron cyclotron resonance plasmas. *Plasma Sources Science and Technology*, 3(3), 1994.

[166] J. Liu and J.X. Ma. Effects of various forces on the distribution of particles at the boundary of a dusty plasma. *Physics of plasmas*, 4(8), 1997.

[167] L. Talbot. Thermophoresis of particles in a heated boundary layer. *Journal of fluid mechanics*, 101(4), 1980.

[168] L.M. Simons and M. Coppins. Floating potential of spherical dust in collisionless magnetised plasmas. *arXiv preprint arXiv:2003.14082*, 2020.

[169] J.E. Allen *et. al.* On the orbital motion limited theory for a small body at floating potential in a maxwellian plasma. *Journal of plasma physics*, 63(4), 2000.

[170] C. T. N. Willis *et. al.* The effect of dust grain size on the floating potential of dust in a collisionless plasma. *Plasma Sources Science and Technology*, 19(6), 2010.

[171] J. G. Laframboise. Theory of spherical and cylindrical langmuir probes in a collisionless, maxwellian plasma at rest. Technical report, TORONTO UNIV DOWNSVIEW (ONTARIO) INST FOR AEROSPACE STUDIES, 1966.

[172] D. M. Thomas and M. Coppins. Equilibrium probability distribution of a conductive sphere's floating charge in a collisionless, drifting maxwellian plasma. *Phys. Rev. E*, 88, 2013.

[173] E. C. Whipple. Potentials of surfaces in space. *Reports on Progress in Physics*, 44(11), 1981.

[174] I. H. Hutchinson. Ion collection by a sphere in a flowing plasma: 3. floating potential and drag force. *Plasma Physics and Controlled Fusion*, 47(1), 2004.

[175] C. T. N. Willis *et. al.* The effect of particle size on the floating potential of dust in a collisionless plasma. In *36th EPS Conference on Plasma Physics, Sofia E*, volume 33.

[176] O. Ishihara. Complex plasma: dusts in plasma. *Journal of Physics D: Applied Physics*, 40(8), 2007.

[177] I.H. Hutchinson. Ion collection by a sphere in a flowing plasma: 2. non-zero debye length. *Plasma physics and controlled fusion*, 45(8):1477, 2003.

[178] S. A. Khrapak *et. al.* Ion drag force in complex plasmas. *Phys. Rev. E*, 66, 2002.

[179] T Nitter. Levitation of dust in rf and dc glow discharges. *Plasma Sources Science and Technology*, 5(1), 1996.

[180] L. S. Frost. Effect of variable ionic mobility on ambipolar diffusion. *Phys. Rev.*, 105, 1957.

[181] A. Abedi *et. al.* Investigation of temperature, electric field and drift-gas composition effects on the mobility of nh4+ ions in he, ar, n2, and co2. *International Journal of Mass Spectrometry*, 370, 2014.

[182] E. W. McDaniel and E. A. Mason. Mobility and diffusion of ions in gases. 1973.

[183] E. B. Tomme *et. al.* Parabolic plasma sheath potentials and their implications for the charge on levitated dust particles. *Phys. Rev. Lett.*, 85, 2000.